

Numerical Method to Compute the Wave-Induced Rigid Body and Elastic Response of Ships at Forward Speed

Von der Fakultät für Ingenieurwissenschaften, Abteilung Maschinenbau
und Verfahrenstechnik

der
Universität Duisburg-Essen

zur Erlangung des akademischen Grades

eines

Doktors der Ingenieurwissenschaften

Dr.-Ing.

genehmigte Dissertation

von

Malte Riesner
aus
Heide

Gutachter: Prof. Dr.-Ing. Bettar el Moctar
Prof. Dr.-Ing. Yonghwan Kim
Prof. Dr.-Ing. Nikolai Kornev

Tag der mündlichen Prüfung: 28.01.2022

Abstract

Throughout the ship's operating life, the structural components of the ship hull have to withstand wave-induced loads. For the design of the steel structure, wave-induced global sectional loads, such as the vertical and horizontal bending moment or the torsional moment, play an important role. In some situations, resonant wave-induced hull girder vibrations, so-called springing, can occur, which is an important issue when addressing fatigue damage of the steel structure. The present work introduces a new numerical method that combines numerical efficiency with an accurate prediction of the global hydroelastic behaviour of ships in waves and is also able to predict higher order springing induced vibrations. Structural dynamics were computed based on a new beam element approach that considers vertical and horizontal bending as well as nonuniform torsion. The mass and stiffness matrices accounted for coupling effects between hull girder bending and torsion. A weakly-nonlinear time domain approach based on Rankine sources was developed to compute the ship's hydrodynamic properties and wave-induced forces and moments. The hydrodynamic solver coupled the fully nonlinear stationary forward speed flow problem with the oscillatory flow problem in waves and considered geometrical nonlinearities caused by the changing wetted surface due to the incident waves, ship motions and elastic deformation. New free surface and body boundary conditions were developed to account for elastic deformations of the ship structure. The new numerical method was systematically validated against model test data and CFD results of four different types of ships at forward speed in head and oblique waves. It was shown that the new numerical method is able to compute wave-induced hydrodynamic forces, wave-induced rigid body motions, the wave added resistance and wave-induced sectional loads of an elastic ship as well as higher order springing-induced vibrations with a good agreement to the model test and CFD results. Furthermore, it was shown that forward speed effects (the stationary wave system and dynamic trim and sinkage) and the wave steepness influences the hydroelastic response of ships in waves strongly.

Acknowledgements

I thank Professor Bettar Ould el Moctar for his supervision associated with my research work at the Institute for Ship Technology, Ocean Engineering and Transport Systems and I am grateful for his professional and personal support. Further acknowledgements are referred to Professor Yonghwan Kim and Professor Nikolai Kornev for their reviews of this thesis and their valuable comments.

I acknowledge the German Research Foundation (Deutsche Forschungsgemeinschaft, DFG) and the Federal Ministry for Economic Affairs and Energy (Bundesministerium für Wirtschaft und Energie, BMWi) for founding the research work associated with my thesis.

Many thanks go out to my colleagues and friends at the institute for having a great time together. In particular, I thank Sebastian Sigmund, Guillermo Chillcce, Mahdi Ghesmi and Jens Ley for long discussions, critical comments and support. Furthermore, I thank Alexander von Graefe und Vladimir Shigunov for great support during the early PhD-studies. Besides, I want to thank Thomas Schellin for reviewing my research work.

My warmest thank you go to my family, in particular to my wife Kristin and my daughter Hilda. You gave me a lot of strength and confidence! Thank you!

Content

List of Figures V

List of Tables XV

List of Variables XVII

1	Introduction	1
1.1	<i>Periodic Wave-Induced Forces and Rigid Body Motions</i>	<i>5</i>
1.2	<i>Wave-Induced Drift Forces and Corresponding Speed Loss</i>	<i>10</i>
1.3	<i>Sectional Loads and Springing-Induced Vibrations</i>	<i>14</i>
1.4	<i>Requirements for the New Numerical Method</i>	<i>18</i>
1.5	<i>Authors Contribution.....</i>	<i>20</i>
1.5.1	<i>Developments</i>	<i>20</i>
1.5.2	<i>Implementation of the New Numerical Method</i>	<i>22</i>
1.5.3	<i>Numerical Simulations and Model Tests for the Validation</i>	<i>23</i>
1.6	<i>Structure of the Present Work and Declaration</i>	<i>23</i>
2	Numerical Method to Compute the Rigid and Elastic Response of Ships in Wave	27
2.1	<i>Kinematic Relations.....</i>	<i>27</i>
2.2	<i>Weakly-Nonlinear Wave-Induced Rigid Body Motions</i>	<i>29</i>
2.2.1	<i>Nonlinear Motion Equations of a Rigid Body</i>	<i>30</i>
2.2.2	<i>Hydrodynamic Forces and Moments at the Ship Hull.....</i>	<i>32</i>
2.2.3	<i>Nonlinear Rigid Body Motion Equations with Weakly-Nonlinear Hydrodynamic Forces</i>	<i>47</i>
2.3	<i>Weakly-Nonlinear Wave-Induced Elastic Deformations</i>	<i>51</i>
2.3.1	<i>Strain and Kinetic Energy of an Elastic Vibrating Ship.....</i>	<i>56</i>
2.3.2	<i>Torsion-Induced Warping of Ship Cross Sections.....</i>	<i>65</i>
2.3.3	<i>Shape Functions to Compute Element Displacements</i>	<i>68</i>
2.3.4	<i>Linear Equation of Elastic Deformation</i>	<i>74</i>
2.3.5	<i>Characteristic System Equation to Compute Wet Natural Modes.....</i>	<i>77</i>
2.3.6	<i>Linear Elastic Deformation Equations with Weakly-Nonlinear Hydrodynamic Forces</i>	<i>81</i>

2.3.7	Computation of Sectional Loads	83
2.4	<i>Linear Frequency Domain Hydrodynamic Pressure</i>	84
2.4.1	Boundary value Problem	87
2.4.2	Computation of the Nonlinear Stationary Forward Speed Potential	89
2.4.3	Computation of the First Order Velocity Potential of an Elastic Vibrating Hull ..	90
2.4.4	Infinite Frequency Solution	101
2.4.5	First Oder Wave Theory	104
2.5	<i>Spatial Discretisation</i>	106
2.6	<i>Calculation Procedure</i>	109
3	Test Cases	113
3.1	<i>VLCC Tanker</i>	113
3.2	<i>Cruise Ship</i>	114
3.3	<i>Post-Panamax Containership A</i>	115
3.4	<i>Post-Panamax Containership B</i>	116
3.4.1	Structural and Mass Properties According to the Model Test Setup	117
3.4.2	Structural and Mass Properties According to a Realistic Full-Scale Setup	120
4	Verification and Validation	123
4.1	<i>Time and Spatial Discretisation Study</i>	123
4.1.1	Frequency Dependent Hydrodynamic Forces	125
4.1.2	Time Domain Hydrodynamic Forces and Rigid Body Motions	133
4.2	<i>Verification of the Convolution Integral to Compute Radiation Forces</i>	137
4.3	<i>Validation of Wave-Induced Forces</i>	146
4.3.1	Weakly-Nonlinear Hydrodynamic Force at a Fixed Ship	148
4.3.2	Weakly-Nonlinear Hydrodynamic Forces at a Moving Ship	165
4.3.3	Wave Added Resistance of a Fixed and Moving Ship	179
4.4	<i>Validation of Rigid Body Ship Motions in Steep Oblique Waves</i>	188
4.4.1	Viscous Roll Damping	189
4.4.2	Rigid Body Motions	191
4.5	<i>Validation of the Hydroelastic Reponse in Waves</i>	195
4.5.1	Grid Study for the Finite Beam Element Method	196
4.5.2	Validation of Wave Induced Sectional Loads	202
4.6	<i>Computational Performance</i>	234
5	Results	235
5.1	<i>Influence of the Wave Steepness on Ship Motions in Oblique Waves</i>	235

5.2	<i>Forward Speed and Wave Steepness Effects on Sectional Loads in Head Waves</i>	239
5.2.1	Forward Speed Effect on Wet Natural Frequencies.....	240
5.2.2	Effect of Wave Steepness on Sectional Loads.....	242
5.3	<i>Hydroelastic Response via Realistic Full-Scale Stiffness Properties.....</i>	249
5.3.1	Mid Ship Torsional Moments in Waves at 150deg and 120deg Encounter Angle	250
5.3.2	Mid Ship Bending Moments in Waves at 150deg and 120deg Encounter Angle	253
6	Summary	259
6.1	<i>Outlook.....</i>	263
7	Appendix	265
7.1	<i>Weakly-Nonlinear Hydrodynamic Forces at the Fixed VLCC Tanker</i>	265
7.1.1	Results for $\lambda/LPP = 1.62$	265
7.1.2	Results for $\lambda/LPP = 1.0$	268
7.1.3	Results for $\lambda/LPP = 0.54$	271
7.2	<i>Weakly-Nonlinear Hydrodynamic Forces at the Moving VLCC Tanker.....</i>	273
7.2.1	Results for $\lambda/LPP = 1.84$	274
7.2.2	Results for $\lambda/LPP = 1.0$	277
7.2.3	Results for $\lambda/LPP = 0.54$	280
8	Bibliography	283

List of Figures

Figure 1: Comparisons of the wave-induced longitudinal stress spectra at the main deck of a containership. The total stress spectrum is designated by the red curve. High frequency vibrations were eliminated by a low-pass filter (blue curve). Kahl and Menzel (2008).....	2
Figure 2: Attainable speed of a 355m long post-Panamax containership in bow quartering waves of 150deg encounter angle.	12
Figure 3: Visualization of the inertial $x = x; y; zT$ and the body fixed $x = x; y; zT$ coordinate system.	28
Figure 4: Visualization of the wave coordinate system.	43
Figure 5: Ship section with mean water level and instantiations wave elevation, Boese (1970)	45
Figure 6: Visualization of a ship's cross section with the body fixed coordinate system, bending coordinate system and shear center coordinate system (left). Visualization of bending and torsional coupling effects (right).	53
Figure 7: A typical beam element, showing the origin of its coordinate systems and the degrees of freedom of a node (left) and the applied external loads per unit length (right).	54
Figure 8: Geometric relations of a thin walled girder.	57
Figure 9: Free vibration of an unsupported U-Shape beam.	60
Figure 10: Torsion induced shear stress for an open (left) and closed (right) cross section.	60
Figure 11: Simplified ship cross section (left) and the associated warping function (right) distributed along structural components.	66
Figure 12: Visualization of the shape functions $N4, N7, N11$ and $N14$ over one element.	74
Figure 13: Forced deformation of a ship discretized with five beam elements	80
Figure 14: Illustration of the cross-section coordinate system.	92
Figure 15: Visualization of a linear wave with the wave coordinate system, $x(w) = [x(w), y(w), z(w)]$, the wave amplitude ζ_1 and the water depth D	104
Figure 16: Visualisation of the wave encounter angle, μ , and wave length, λ	105
Figure 17: Top view of the free surface and body grid and side view of the body grid for the stationary flow problem.	107
Figure 18: Illustration of the free surface grid used during frequency domain simulations, Graefe (2014).....	108
Figure 19: Side view of the time domain body grid.	109
Figure 20: Adjustment of the body grid to account for the instantaneous free surface.	109
Figure 21: Example of the hull surface treatment during time domain simulations.	109
Figure 22: Calculation procedure of the new numerical method.	111
Figure 23: Section plan of the VLCC tanker, Sigmund (2019).	114
Figure 24: Section plan of the Cruise ship, Sigmund (2019)	115
Figure 25: Section plan of the post Panamax Container ship A, Sigmund (2019).	116
Figure 26: Visualization of the cross section areas, S , effective shear cross section area, S_y, S_z , the area moment of inertia I_y and I_z , the torsional stiffness, IT , and the warping stiffness $I\omega$	120
Figure 27: Visualization of the vertical position (relative to keel line) of the neutral bending axis, Z_n , and shear center, ZS , the mass moment of inertia, j_y and j_z , the mass per unit length, μ , and j_x the torsional mass moment of inertia relative to the shear center	121
Figure 28: Medium grid discretizing the ship's hull up to its main deck.....	124

Figure 29: Transfer functions of the normalized hydrodynamic added mass resulting from the three different body discretization. nP designates the number of body panels.	126
Figure 30: Normalized hydrodynamic added mass for $\omega_e \approx 2.4\text{rad/s}$ plotted against the number of body panels nP	126
Figure 31: Transfer functions of the normalized hydrodynamic damping resulting from the three different body discretization. nP designates the number of body panels.....	127
Figure 32: Normalized hydrodynamic damping for $\omega_e \approx 2.4\text{rad/s}$ plotted against the number of body panels nP	127
Figure 33: Normalized transfer functions of the diffraction forces and moments for the three different body discretization. nP designates the number of body panels.....	128
Figure 34: Normalized diffraction roll moments for $\lambda/LPP = 0.58$ plotted against the number of body panels nP	129
Figure 35: Normalized transfer functions of the hydrodynamic added mass resulting from the three different free surface discretization, $\lambda/LP = 9; 19; 24$	130
Figure 36: Normalized hydrodynamic added roll mass for $\omega_e = 0.04\text{rad/s}$ plotted against λ/LP	130
Figure 37: Normalized transfer functions of hydrodynamic damping resulting from the three different free surface discretization, $\lambda/LP = 9; 19; 24$	131
Figure 38: Normalized hydrodynamic surge damping for $\omega_e = 0.64\text{rad/s}$ plotted against λ/LP	131
Figure 39: Normalized transfer functions of the diffraction forces and moments resulting from three different free surface discretization, $\lambda/LP = 9; 19; 24$	132
Figure 40: Normalized diffraction yaw moments for $\lambda/LPP = 0.58$ from three different free surface discretization, $\lambda/LP = 9; 19; 24$	132
Figure 41: Time histories of combined normalized Froude-Krylov and hydrostatic forces and moments for the fixed ship at $\lambda/Lpp = 0.110$	134
Figure 42: Normalized minimum combined Froude-Krylov and hydrostatic forces vertical forces for $\lambda/LPP = 0.110$ plotted against the number of body panels nP	134
Figure 43: Time histories of ship motions at $\lambda/Lpp = 0.984$ obtained from a time step of 0.2s, 0.075s and 0.025s.....	136
Figure 44: First harmonic amplitude of the roll motion against the time step.	137
Figure 45: Normalized hydrodynamic heave (B33) and pitch (B55) damping (left) and normalized hydrodynamic heave (A33) and pitch (A55) added mass (right).....	139
Figure 46: Normlaized heave impulse response functions (left) and pitch impulse response functions (right).....	139
Figure 47: Transfer functions of heave (left) and pitch (right) motions of the containership A in head waves computed with the linear time domain solver with impulse response functions based on hydrodynamic damping "linear D", based on the hydrodynamic added mass "linear M" and using the frequency domain solver "linear frq.".....	141
Figure 48: Transfer functions of heave (left) and pitch (right) motions of the VLCC tanker in head waves computed with the linear time domain solver with impulse response functions based on hydrodynamic damping "linear D", based on the hydrodynamic added mass "linear M" and using the frequency domain solver.	141

Figure 49: Transfer functions of heave (left) and pitch (right) motions of the cruise vessel in head waves computed with the linear time domain solver with impulse response functions based on hydrodynamic damping “linear D”, based on the hydrodynamic added mass “linear M” and using the frequency domain solver.	142
Figure 50: Transfer functions of heave (left) and pitch (right) motions of the containership A in head waves with a forward speed according to $F_n = 0.139$. “linear D” and “linear M” designates linear time domain simulations with impulse response functions based on hydrodynamic damping and hydrodynamic added mass “linear M”. “linear freq.” designates results from the linear frequency domain solver.	143
Figure 51: Transfer functions of heave (left) and pitch (right) motions of the VLCC tanker in head waves with a forward speed according to $F_n = 0.142$. “linear D” and “linear M” designates linear time domain simulations with impulse response functions based on hydrodynamic damping and hydrodynamic added mass “linear M”. “linear freq.” designates results from the linear frequency domain solver.	143
Figure 52: Transfer functions of heave (left) and pitch (right) motions of the cruise vessel in head waves with a forward speed according to $F_n = 0.166$. “linear D” and “linear M” designates linear time domain simulations with impulse response functions based on hydrodynamic damping and hydrodynamic added mass “linear M”. “linear freq.” designates results from the linear frequency domain solver.	144
Figure 53: : Transfer functions of heave (left) and pitch (right) motions of the containership A in head waves with a forward speed according to $F_n = 0.218$. “linear D” and “linear M” designates linear time domain simulations with impulse response functions based on hydrodynamic damping and hydrodynamic added mass “linear M”. “linear freq.” designates results from the linear frequency domain solver.	144
Figure 54: Normalized hydrodynamic damping $B_{55}(\omega_e)$ and normalized hydrodynamic added mass $M_{55}(\omega_e)$ of the pitch motion of containership A at $F_n = 0.218$ (left) and the impulse response function calculated using B_{55} and M_{55} (right).	146
Figure 55: Time histories of longitudinal forces for the fixed Containership A ($F_n = 0.139$) in head waves of $\lambda L = 2.50$ and a wave steepness $h = 0.011$. “FK+Hyd” denotes the combined Froude-Krylov and hydrostatic forces, “WL” denotes nonlinear waterline forces, “Dif” denotes diffraction forces and “nonlinear” denotes the total hydrodynamic force compared to the CFD result.	150
Figure 56: Time histories of vertical forces for the fixed Containership A ($F_n = 0.139$) in head waves of $\lambda L = 2.50$ and a wave steepness $h = 0.011$. “FK+Hyd” denotes the combined Froude-Krylov and hydrostatic forces, “WL” denotes nonlinear waterline forces, “Dif” denotes diffraction forces and “nonlinear” denotes the total hydrodynamic force compared to the CFD result.	151
Figure 57: Time histories of pitch moments for the fixed Containership A ($F_n = 0.139$) in head waves of $\lambda L = 2.50$ and a wave steepness $h = 0.011$. “FK+Hyd” denotes combined Froude-Krylov and hydrostatic moment, “WL” denotes nonlinear waterline moment, “Dif” denotes diffraction moment and “nonlinear” denotes the total hydrodynamic moment compared to the CFD result.	152
Figure 58: Time histories of longitudinal forces for the fixed Containership A ($F_n = 0.139$) in head waves of $\lambda L = 1.09$ and a wave steepness $h = 0.023$. “FK+Hyd” denotes combined Froude-Krylov and hydrostatic forces, “WL” denotes nonlinear waterline forces, “Dif” denotes diffraction forces and “nonlinear” denotes the total hydrodynamic force compared to CFD results.	154

Figure 59: Time histories of vertical forces for the fixed Containership A ($F_n = 0.139$) in head waves of $\lambda L = 1.09$ and a wave steepness $h = 0.023$. “FK+Hyd” denotes combined Froude-Krylov and hydrostatic forces, “WL” denotes nonlinear waterline forces, “Dif” denotes diffraction forces and “nonlinear” denotes the total hydrodynamic force compared to the CFD result.155

Figure 60: Time histories of wave induced pitch moments for the fixed containership A ($F_n = 0.139$) in head waves of $\lambda L = 1.09$ and a wave steepness $h = 0.023$. “FK+Hyd” denotes the combined Froude-Krylov and hydrostatic moment, “WL” denotes nonlinear waterline moment, “Dif” denotes diffraction moment and “nonlinear” denotes the total hydrodynamic moment compared to the CFD result.156

Figure 61: Time histories of longitudinal forces for the fixed Containership A ($F_n=0.139$) in head waves of $\lambda/L_{pp} = 0,6$ and a wave steepness $h = 0.028$. “FK+Hyd” denotes combined Froude-Krylov and hydrostatic forces, “WL” denotes nonlinear waterline forces, “Dif” denotes diffraction forces and “nonlinear” denotes the total hydrodynamic force compared to the CFD result.158

Figure 62: Time histories of vertical forces for the fixed Containership A ($F_n=0.139$) in head waves of $\lambda/L = 0.6$ and a wave steepness $h = 0.028$. “FK+Hyd” denotes the combined Froude-Krylov and hydrostatic force, “WL” denotes the nonlinear waterline force, “Dif” denotes the diffraction force and “nonlinear” denotes the total hydrodynamic force compared to the CFD result.159

Figure 63: Time histories of the pitch moment for the fixed containership A ($F_n = 0.139$) in head waves of $\lambda/L = 0.6$ and a wave steepness $h = 0.028$. “FK+Hyd” denotes combined Froude-Krylov and hydrostatic moments, “WL” denotes nonlinear waterline moments, “Dif” denotes diffraction moments and “nonlinear” denotes the total hydrodynamic moment compared to the CFD result.160

Figure 64: First, second, third and fourth harmonic amplitudes of the longitudinal force of the Containership A in head waves with a forward speed according to $F_n = 0.139$162

Figure 65: First, second, third and fourth harmonic amplitudes of the vertical force of the Containership A in head waves with a forward speed according to $F_n = 0.139$ 164

Figure 66: First, second, third and fourth harmonic amplitudes of the pitch moment of the Containership A in head waves with a forward speed according to $F_n = 0.139$165

Figure 67: Time histories of the longitudinal forces for the freely floating Containership A ($F_n=0.139$) in head waves of $\lambda/L = 2.5$ and a wave steepness $h = 0.011$. “FK+Hyd” denotes the combined Froude-Krylov and hydrostatic force, “WL” denotes nonlinear waterline forces, “Dif” denotes diffraction forces, “Rad” denotes the radiation force and “nonlinear” denotes the total hydrodynamic force.168

Figure 68: Time histories of the vertical forces for the freely floating Containership A ($F_n=0.139$) in head waves of $\lambda/L = 2.5$ and a wave steepness $h = 0.011$. “FK+Hyd” denotes the combined Froude-Krylov and hydrostatic force, “WL” denotes nonlinear waterline forces, “Dif” denotes diffraction forces, “Rad” denotes the radiation force and “nonlinear” denotes the total hydrodynamic force.169

Figure 69: Time histories of the pitch moment for the freely floating Containership A ($F_n=0.139$) in head waves of $\lambda/L = 2.5$ and a wave steepness $h = 0.011$. “FK+Hyd” denotes the combined Froude-Krylov and hydrostatic moment, “WL” denotes nonlinear waterline moment, “Dif” denotes diffraction moment, “Rad” denotes the radiation moment and “nonlinear” denotes the total hydrodynamic moment.170

Figure 70: Time histories of the longitudinal force (top), vertical forces (center) and pitch moment (bottom) for the freely floating Containership A ($F_n=0.139$) in head waves of $\lambda/LPP = 1.09$ and a wave steepness $h = 0.023$. “nonlinear” denotes results of the new numerical method and “CFD” denotes results from the CFD solver.	171
Figure 71: Time histories of the longitudinal force (top), vertical forces (center) and pitch moment (bottom) for the freely floating Containership A ($F_n=0.139$) in head waves of $\lambda/LPP = 0.6$ and a wave steepness $h = 0.0289$. “nonlinear” denotes results of the new numerical method and “CFD” denotes results from the CFD solver.	172
Figure 72: First, second, third and fourth harmonic amplitudes of the longitudinal force of the Containership A in head waves with a forward speed according to $F_n = 0.139$	175
Figure 73: First, second, third and fourth harmonic amplitudes of the vertical force of the Containership A in head waves with a forward speed according to $F_n = 0.139$	176
Figure 74: First, second, third and fourth harmonic amplitudes of the pitch moment of the Containership A in head waves with a forward speed according to $F_n = 0.139$	177
Figure 75: First harmonic amplitudes of the heave motion (left) and the pitch motion (right) for the Containership A at a forward speed of $F_n = 0.139$ in head waves.	178
Figure 76: Phase angle between the incident wave and heave (left) and pitch (right) motion of the Containership A at a forward speed of $F_n = 0.139$ in head waves.	179
Figure 77: Quadratic transfer function of the wave added resistance for the fixed Containership A at a forward speed of $F_n = 0.139$	181
Figure 78: Quadratic transfer function of the wave added resistance for the free Containership A at a forward speed of $F_n = 0.139$	182
Figure 79: Quadratic transfer function of the wave added resistance for the fixed VLCC tanker at a forward speed of ($F_n = 0.142$).	183
Figure 80: Normalized first harmonic amplitudes of the heave (left) and pitch motion (right) for the VLCC tanker with a forward speed according to $F_n = 0.142$ in head waves.	184
Figure 81: Phase angle between incident wave and heave (left) and pitch (right) motion of the VLCC tanker at a forward speed of $F_n = 0.142$ in head waves.	184
Figure 82: Quadratic transfer function of the wave added resistance for the moving VLCC tanker at a forward speed of $F_n = 0.142$	185
Figure 83: Percentage frictional wave added resistance for the Containership ($F_n = 0.139$) and the VLCC tanker ($F_n = 0.142$)	187
Figure 84: Quadratic transfer function of the wave added resistance including friction effects for the post-Panamax Containership A (left) at $F_n = 0.139$ and the VLCC tanker (right) at $F_n = 0.142$	188
Figure 85: Spring based mooring system used in model tests (el Moctar et al. (2016)).....	189
Figure 86: Roll decay tests from model test (Sprenger and Fathi (2015)) and nonlinear numerical simulation.....	190
Figure 87: Time histories of computed and measured rigid body motions of the Containership A at $F_n = 0.0523$ in 4.02m amplitude waves of $\lambda/Lpp = 1.09$ (wave steepness $h = 0.023$) at wave encounter angle of 30deg.	192
Figure 88: Comparisons of normalized first harmonic motions amplitudes computed with the new numerical method (nonlinear), a linear frequency domain method (linear frq.) and model test results (EXP) for the Containership A at $F_n = 0.0523$ and wave heading of 60deg.	194

Figure 89: Comparisons of normalized first harmonic motions amplitudes computed with the new numerical method (nonlinear), a linear frequency domain method (linear freq.) and model test results (EXP) for the Containership A at $F_n = 0.0523$ and wave heading of 30deg.	195
Figure 90: Natural modes of two-node vertical bending (top left), three-node vertical bending (top right), coupled one-node torsion-horizontal-bending (lower left), two-node torsion-horizontal-bending (lower center), and three-node torsion-horizontal-bending (lower right).	198
Figure 91: Normalized impulse response function for two-node, three-node and four-node vertical bending (left) and one-, two- and three-node coupled torsional-horizontal-bending modes (right).	198
Figure 92: Normalized decaying vibration of the one-node torsion-horizontal-bending mode (Mode 7) and two-node torsion-horizontal-bending mode (Mode 8).	202
Figure 93: Comparative decaying normalized vertical midship bending moments obtained from model tests (EXP Decay), from a fitted curve based on these model tests (curve fit), and from time domain simulations with the new numerical method (nonlinear).....	207
Figure 94: Comparative normalized first harmonic amplitudes of the heave (left) and pitch (right) motions for a wave encounter angle of 180deg and a forward speed of 15 kn.	209
Figure 95: Normalized two-node and three-node modal hydrodynamic vertical bending forces (left) and the vertical bending moments (right) for the wave of case 1 with $\omega_e = 0.562\text{rad/s}$ and 4.0m wave amplitude ($h = 0.0231$) for a wave encounter angle of 180deg and a forward speed of 15kn.....	210
Figure 96: Normalized two-node and three-node modal hydrodynamic vertical bending forces (left) and the vertical bending moments (right) for the wave of case 2 with $\omega_e = 0.590\text{rad/s}$ and 1.5m wave amplitude ($h = 0.00937$) for a wave encounter angle of 180deg and a forward speed of 15kn.....	211
Figure 97: Normalized two-node and three-node modal hydrodynamic vertical bending forces (left) and the vertical bending moments (right) for the wave of case 9 with $\omega_e = 0.985\text{rad/s}$ and 4.0m wave amplitude ($h = 0.055$) for a wave encounter angle of 180deg and a forward speed of 15kn.....	212
Figure 98: Normalized two-node and three-node modal hydrodynamic vertical bending forces (left) and the vertical bending moments (right) for the wave of case 10 with $\omega_e = 1.00\text{rad/s}$ and 2.5m wave amplitude ($h = 0.0354$) for a wave encounter angle of 180deg and a forward speed of 15kn.....	213
Figure 99: Normalized first ($My(1)$), second ($My(2)$), third ($My(3)$), and fourth ($My(4)$) harmonic amplitudes of the vertical bending moment vs. the encounter frequency for a wave encounter angle of 180deg and a forward speed of 15kn.....	215
Figure 100: Comparative normalized first harmonic amplitudes of the heave (left) and pitch (right) motions for a wave encounter angle of 180deg and a forward speed of 22 kn.	217
Figure 101: Normalized midship vertical bending moments for wave case 17 (left) with $\omega_e = 0.984\text{rad/s}$ and a wave steepness $h = 0.0167$ and for wave case 19 (right) with $\omega_e = 1.476\text{rad/s}$ and a wave steepness $h = 0.0295$	219
Figure 102: Amplitude spectra of vertical bending moment for wave case 19 with $\omega_e = 1.476\text{rad/s}$, a wave amplitude of 1.5m and a wave steepness $h = 0.0295$	219

Figure 103: Normalized first ($M_y(1)$), second ($M_y(2)$), third ($M_y(3)$), and fourth ($M_y(4)$) harmonic amplitudes of vertical bending moment vs. the encounter frequency for a wave encounter angle of 180deg and a forward speed of 22kn.	221
Figure 104: Comparative first harmonic amplitudes of heave (left), roll (centre), and pitch (right) for the ship, equipped with a backbone, in regular waves at 150deg heading at 15kn of forward speed.	223
Figure 105: Comparative time series (left) and amplitude spectra (right) of the torsional moment (top), vertical bending (mid) and horizontal bending moment (bottom) for the ship, equipped with a backbone, in waves of case 1 ($h = 0.0333$) at 150deg heading.....	225
Figure 106: Competitive time series (left) and amplitude spectra (right) of the midship torsional moment (top), vertical bending moment (mid) and horizontal bending moment (bottom) for the ship, equipped with a backbone, in waves of case 2 ($h = 0.0374$) at 150deg heading at 15kn of forward speed.	226
Figure 107: Comparative time series (left) and amplitude spectra (right) of the torsional moment (top), vertical bending moment (mid) and horizontal bending moment (bottom) for the ship, equipped with a backbone, in waves of case 3 ($h = 0.0411$) at 150deg heading.....	227
Figure 108: Comparative time series (left) and amplitude spectra (right) of the torsional moment (top), vertical bending moment (mid) and horizontal bending moment (bottom) for the ship, equipped with a backbone, in waves of case 4 ($h = 0.0303$) at 150deg heading.....	229
Figure 109: Comparative first harmonic amplitudes of heave (left), roll (centre), and pitch (right) for the ship, equipped with a backbone, in regular waves at 120deg heading and 15kn of forward speed	230
Figure 110: Comparative time series (left) and amplitude spectra (right) of the torsional moment (top), vertical bending moment (mid) and horizontal bending moment (bottom) for the ship, equipped with a backbone, in waves of case 1 ($h = 0.0532$) at 120deg heading at 15kn of forward.....	231
Figure 111: Comparative time series (left) and amplitude spectra (right) of the torsional moment (top), vertical bending moment (mid) and horizontal bending moment (bottom) for the Containership B, equipped with a backbone, in waves of case 2 ($h = 0.0341$) at 120deg heading and 15kn of forward speed.	232
Figure 112: Comparative time series (left) and amplitude spectra (right) of the torsional moment (top), vertical bending moment (mid) and horizontal bending moment (bottom) for the ship, equipped with a backbone, in waves of case 3 ($h = 0.0320$) at 120deg heading and 15kn of forward speed.	233
Figure 113: Time series of the normalized vertical bending moment of the Containership B in head waves with a wave encounter frequency of 3.25rad/s and a forward speed of 22kn.	234
Figure 114: Time histories of rigid body motions for the Containership A at $F_n = 0.139$ in waves of $\lambda/L_{pp} = 0.633$ and at wave encounter angle of 30deg for wave steepness $h = 0.01$, waves of $h = 0.02$, $h = 0.03$	237
Figure 115: Comparative normalized amplitude spectra of the surge motion for the Containership A at $F_n = 0.139$ in waves of $\lambda/L_{pp} = 0.633$ and at wave encounter angle of 30deg for wave steepness $h = 0.01$ and $h = 0.03$	237

Figure 116: Computed normalized first harmonic amplitudes of surge, sway, heave (top), roll, pitch, and yaw (bottom) for a forward speed according $F_n = 0.139$ and a wave heading of 30deg.....	239
Figure 117: Free surface elevations of the stationary wave systems for the ship at speeds of 10, 15, 22, and 30kn	241
Figure 118: Comparative two-node (left) and three-node (right) vertical bending natural frequencies obtained from the double body (DB) and the nonlinear (nonlinear) forward speed solution method.....	242
Figure 119: Comparisons of the normalized first ($My(1)$), second ($My(2)$), third ($My(3)$), and fourth ($My(4)$) harmonic amplitudes of the vertical bending moment in head waves for a wave steepness of 0.01 and 0.02 at 15kn of forward speed. The stationary forward speed solutions was based on double body free surface boundary condition (DB-0.01 and DB-0.02) and on the fully nonlinear free surface boundary conditions (SW-0.01 and SW-0.02).	244
Figure 120: Comparisons of normalized first harmonic amplitudes of the wave-induced modal hydrodynamic force of the two-node vertical bending mode at 15kn of forward speed, considering the fully nonlinear stationary forward speed solution (SW-0.02) and the stationary forward speed solution due to double body free surface boundary condition (DB-0.02).....	245
Figure 121: Comparisons of normalized second, third and fourth harmonic amplitudes of the wave-induced modal hydrodynamic force of the two-node vertical bending mode at 15kn of forward speed, considering the fully nonlinear stationary forward speed solution (SW-0.02) and the stationary forward speed solution due to double body free surface boundary condition (DB-0.02).....	246
Figure 122: : Comparisons of the normalized first ($My(1)$), second ($My(2)$), third ($My(3)$), and fourth ($My(4)$) harmonic amplitudes of the vertical bending moment for head waves with steepness of 0.01 and 0.02 at 22kn of forward speed. The stationary forward speed solutions were based on double body free surface boundary condition (DB-0.01 and DB-0.02) and on the fully nonlinear free surface boundary conditions (SW-0.01 and SW-0.02).	248
Figure 123: Normalized first, second, third and fourth harmonic amplitudes of the wave-induced modal hydrodynamic force of the two-node vertical bending mode for head waves with a steepness of 0.02 at 22kn of forward speed.....	249
Figure 124: Normalized torsional moments for the Containership B, its hull idealized with realistic full-scale stiffness properties, in regular waves at 150deg encounter angle.	252
Figure 125: Normalized torsional moments for the Containership B, its hull idealized with realistic full-scale stiffness properties, in regular waves at 120deg heading.....	253
Figure 126: Normalized amplitudes of the vertical the bending moment for the Containership B, its hull idealized with realistic full-scale stiffness properties, in regular waves at 150deg heading ..	255
Figure 127: Normalized amplitudes of the vertical bending moment for the Containership B, its hull idealized with realistic full-scale stiffness properties, in regular waves at 120deg heading ..	256
Figure 128: Normalized amplitudes of horizontal bending moments for the Containership B, its hull idealized with realistic full-scale stiffness properties, in regular waves at 150deg heading ..	257
Figure 129: Normalized amplitudes of horizontal bending moment for the containership B, with realistic full-scale stiffness properties, in regular waves at 120deg heading	258

Figure 130: Illustration of the radiation and diffraction induced changing wetted surface according to the waterline integral (left). Improved consideration of the changing wetted hull surface with the correct hull normal vectors (right). 264

Figure 131: Time histories of longitudinal forces for the fixed KVLCC2 tanker ($F_n = 0.142$) in head waves of $\lambda L = 1.62$ and a wave amplitude of 3m. “FK+Hyd” denotes combined nonlinear Froude-Krylov and hydrostatic forces, “Rad” denotes radiation forces, “Dif” denotes diffraction forces and “nonlinear” denotes the total hydrodynamic force compared to CFD results. 266

Figure 132: Time histories of vertical forces for the fixed KVLCC2 tanker ($F_n = 0.142$) in head waves of $\lambda L = 1.62$ and a wave amplitude of 3m. “FK+Hyd” denotes combined nonlinear Froude-Krylov and hydrostatic forces, “Rad” denotes radiation forces, “Dif” denotes diffraction forces and “nonlinear” denotes the total hydrodynamic force compared to CFD results. 266

Figure 133: Time histories of pitch moment for the fixed KVLCC2 tanker ($F_n = 0.142$) in head waves of $\lambda L = 1.62$ and a wave amplitude of 3m. “FK+Hyd” denotes combined nonlinear Froude-Krylov and hydrostatic forces, “Rad” denotes radiation forces, “Dif” denotes diffraction forces and “nonlinear” denotes the total hydrodynamic force compared to CFD results. 267

Figure 134: Time histories of longitudinal forces for the fixed KVLCC2 tanker ($F_n = 0.142$) in head waves of $\lambda L = 1.0$ and a wave amplitude of 3m. “FK+Hyd” denotes combined nonlinear Froude-Krylov and hydrostatic forces, “Rad” denotes radiation forces, “Dif” denotes diffraction forces and “nonlinear” denotes the total hydrodynamic force compared to CFD results. 268

Figure 135: Time histories of vertical forces for the fixed KVLCC2 tanker ($F_n = 0.142$) in head waves of $\lambda L = 1.0$ and a wave amplitude of 3m. “FK+Hyd” denotes combined nonlinear Froude-Krylov and hydrostatic forces, “Rad” denotes radiation forces, “Dif” denotes diffraction forces and “nonlinear” denotes the total hydrodynamic force compared to CFD results. 269

Figure 136: Time histories of pitch moment for the fixed KVLCC2 tanker ($F_n = 0.142$) in head waves of $\lambda L = 1.0$ and a wave amplitude of 3m. “FK+Hyd” denotes combined nonlinear Froude-Krylov and hydrostatic forces, “Rad” denotes radiation forces, “Dif” denotes diffraction forces and “nonlinear” denotes the total hydrodynamic force compared to CFD results. 270

Figure 137: Time histories of longitudinal forces for the fixed KVLCC2 tanker ($F_n = 0.142$) in head waves of $\lambda L = 0.54$ and a wave amplitude of 3m. “FK+Hyd” denotes combined nonlinear Froude-Krylov and hydrostatic forces, “Rad” denotes radiation forces, “Dif” denotes diffraction forces and “nonlinear” denotes the total hydrodynamic force compared to CFD results. 271

Figure 138: Time histories of vertical forces for the fixed KVLCC2 tanker ($F_n = 0.142$) in head waves of $\lambda L = 0.54$ and a wave amplitude of 3m. “FK+Hyd” denotes combined nonlinear Froude-Krylov and hydrostatic forces, “Rad” denotes radiation forces, “Dif” denotes diffraction forces and “nonlinear” denotes the total hydrodynamic force compared to CFD results. 272

Figure 139: Time histories of pitch moment for the fixed KVLCC2 tanker ($F_n = 0.142$) in head waves of $\lambda L = 0.54$ and a wave amplitude of 3m. “FK+Hyd” denotes combined nonlinear Froude-Krylov and hydrostatic forces, “Rad” denotes radiation forces, “Dif” denotes diffraction forces and “nonlinear” denotes the total hydrodynamic force compared to CFD results. 273

Figure 140: Time histories of longitudinal forces for the moving KVLCC2 tanker ($F_n = 0.142$) in head waves of $\lambda L = 1.84$ and a wave amplitude of 3m. “FK+Hyd” denotes combined nonlinear Froude-Krylov and hydrostatic forces, “Rad” denotes radiation forces, “Dif” denotes diffraction forces and “nonlinear” denotes the total hydrodynamic force compared to CFD results. 274

Figure 141: Time histories of vertical forces for the moving KVLCC2 tanker ($F_n = 0.142$) in head waves of $\lambda L = 1.84$ and a wave amplitude of 3m. “FK+Hyd” denotes combined nonlinear Froude-Krylov and hydrostatic forces, “Rad” denotes radiation forces, “Dif” denotes diffraction forces and “nonlinear” denotes the total hydrodynamic force compared to CFD results.275

Figure 142: Time histories of pitch moment for the moving KVLCC2 tanker ($F_n = 0.142$) in head waves of $\lambda L = 1.84$ and a wave amplitude of 3m. “FK+Hyd” denotes combined nonlinear Froude-Krylov and hydrostatic forces, “Rad” denotes radiation forces, “Dif” denotes diffraction forces and “nonlinear” denotes the total hydrodynamic force compared to CFD results.276

Figure 143: Time histories of longitudinal force for the moving KVLCC2 tanker ($F_n = 0.142$) in head waves of $\lambda L = 1.0$ and a wave amplitude of 3m. “FK+Hyd” denotes combined nonlinear Froude-Krylov and hydrostatic forces, “Rad” denotes radiation forces, “Dif” denotes diffraction forces and “nonlinear” denotes the total hydrodynamic force compared to CFD results.277

Figure 144: Time histories of vertical forces for the moving KVLCC2 tanker ($F_n = 0.142$) in head waves of $\lambda L = 1.0$ and a wave amplitude of 3m. “FK+Hyd” denotes combined nonlinear Froude-Krylov and hydrostatic forces, “Rad” denotes radiation forces, “Dif” denotes diffraction forces and “nonlinear” denotes the total hydrodynamic force compared to CFD results.278

Figure 145: Time histories of pitch moment for the moving KVLCC2 tanker ($F_n = 0.142$) in head waves of $\lambda L = 1.0$ and a wave amplitude of 3m. “FK+Hyd” denotes combined nonlinear Froude-Krylov and hydrostatic forces, “Rad” denotes radiation forces, “Dif” denotes diffraction forces and “nonlinear” denotes the total hydrodynamic force compared to CFD results.279

Figure 146: Time histories of longitudinal force for the moving KVLCC2 tanker ($F_n = 0.142$) in head waves of $\lambda L = 0.54$ and a wave amplitude of 3m. “FK+Hyd” denotes combined nonlinear Froude-Krylov and hydrostatic forces, “Rad” denotes radiation forces, “Dif” denotes diffraction forces and “nonlinear” denotes the total hydrodynamic force compared to CFD results.280

Figure 147: Time histories of vertical forces for the moving KVLCC2 tanker ($F_n = 0.142$) in head waves of $\lambda L = 0.54$ and a wave amplitude of 3m. “FK+Hyd” denotes combined nonlinear Froude-Krylov and hydrostatic forces, “Rad” denotes radiation forces, “Dif” denotes diffraction forces and “nonlinear” denotes the total hydrodynamic force compared to CFD results.281

Figure 148: Time histories of pitch moment for the moving KVLCC2 tanker ($F_n = 0.142$) in head waves of $\lambda L = 0.54$ and a wave amplitude of 3m. “FK+Hyd” denotes combined nonlinear Froude-Krylov and hydrostatic forces, “Rad” denotes radiation forces, “Dif” denotes diffraction forces and “nonlinear” denotes the total hydrodynamic force compared to CFD results.282

List of Tables

<i>Table 1: Cross section properties</i>	67
<i>Table 2: Comparisons of analytical computed and estimated distribution of the warping function</i>	67
<i>Table 3: Main particulars of the VLCC tanker</i>	113
<i>Table 4: Main particulars of the cruise ship</i>	114
<i>Table 5: Main particulars of the containership A.</i>	115
<i>Table 6: Main particulars of subject containership</i>	117
<i>Table 7: Sectional properties of the 333m long post-Panamax containership equipped with a backbone.</i>	119
<i>Table 8: Cross section properties of the containership under realistic full-scale conditions</i>	122
<i>Table 9: Investigated hull grid sizes</i>	124
<i>Table 10: First harmonic responses of each degree-of-freedom from simulations obtained from the time step study</i>	136
<i>Table 11: Wave length ratio, wave amplitude, and wave steepness for the considered cases</i>	161
<i>Table 12: Wave length ratio, wave amplitude, and wave steepness for the considered cases</i>	166
<i>Table 13: Critical roll damping coefficient against roll amplitude of the Containership A at zero speed</i>	190
<i>Table 14: Wave conditions</i>	191
<i>Table 15: Wave particulars investigated during model tests</i>	193
<i>Table 16: Elastic natural modes of the subjected containership B</i>	196
<i>Table 17: Comparative dry natural frequencies of the Containership B</i>	200
<i>Table 18: Comparative wet natural frequencies of the Containership B with real full-scale properties</i>	201
<i>Table 19: Comparative dry and wet natural frequencies of the Containership B with backbone structural properties</i>	204
<i>Table 20: Curve fitting results of the experimental decay tests</i>	206
<i>Table 21: Wet natural frequencies of the two and three-node vertical bending vibration for the ship at forward speeds of 0, 15, and 22kn</i>	207
<i>Table 22: Wave parameters of the 12 waves considered for the ship speed of 15kn and a wave encounter angle of 180deg</i>	208
<i>Table 23: Wave parameters of the investigated waves scenarios considered for the ship at 22kn.</i>	217
<i>Table 24: Wave parameters of the investigated waves scenarios at a wave encounter angle of 150deg and a ship forward speed of 22kn</i>	222
<i>Table 25: Comparative first harmonic amplitudes of heave (left), roll (center), and pitch (right) for the ship, equipped with a backbone, in regular waves at 120deg heading at 15kn of forward speed</i>	229
<i>Table 26: Dynamic trim, sinkage, and maxima of free surface wave elevation at bow and transom</i>	241

List of Variables

General variables

Variable	Description	Unit
β	scalar quantity	
$\hat{\beta}$	complex amplitude of a scalar quantity $\beta(t) = \text{Re}(\hat{\beta}e^{i\omega_e t})$	
$\vec{\beta}, \underline{\vec{\beta}}, \underline{\underline{\vec{\beta}}}, \underline{\underline{\underline{\vec{\beta}}}}$	vector quantity in inertial reference frame, in body fixed reference frame, in element reference frame, in shear centre reference frame, in modal coordinates	
$\hat{\vec{\beta}}$	complex amplitude of a vector quantity $\vec{\beta}(t) = \text{Re}(\hat{\vec{\beta}}e^{i\omega_e t})$	
$\alpha, \underline{\alpha}, \bar{\alpha}$	hydrodynamic matrix quantity in inertial coordinate system, body fixed coordinate system, modal coordinates	
$\mathbf{A}, \underline{\mathbf{A}}, \bar{\mathbf{A}}$	structural matrix quantity in inertial coordinate system, body fixed coordinate system, modal coordinates	
$\dot{\beta}$	$d\beta/dt$	
β'	$d\beta/dx$	
B	moulded ship breadth	[m]
D	draft	[m]
δ_n	damping ratio of natural mode n	[-]
Δ	Ship displacement	[m ³]
g	gravity constant	[m/s ²]
\vec{G}	Position vector of the ships centre of gravity	[m]
\mathbf{H}^{-1}	transformation matrix relating the angular velocity in body coordinates to the rate of change of the Euler angles	[-]
$\underline{\mathbf{I}}$	matrix including body inertia	[kg m ²]
L_{pp}	length between perpendiculars	[m]

m	ship mass	$[kg]$
\vec{n}	normal vector of the hull surface	$[-]$
$\tilde{\Omega}$	a skew symmetric tensor including angular velocities about body axes	$[rad/s]$
ϱ	model scale factor	$[-]$
ρ	fluid density	$[kg/m^3]$
t	time	$[s]$
Δt	time increment	$[s]$
ω	angular frequency	$[rad/s]$
ω_e	Wave encounter frequency	$[rad/s]$
\mathbf{T}	matrix transforming a vector from the body coordinate system to the inertial coordinate system	$[-]$
\mathbf{V}	matrix including elastic angular displacements	$[rad]$
∇	Nabla operator	
$\tilde{\varphi}$	normalized roll amplitude	$[-]$
$\tilde{\theta}$	normalized pitch amplitude	$[-]$
$\vec{\theta}$	$\vec{\theta} = (\varphi; \theta; \psi)^T$; vector of the Euler angles	$[rad]$
\tilde{x}	normalized surge amplitude	$[m/m]$
\tilde{y}	normalized sway amplitude	$[m/m]$
$\tilde{\psi}$	normalized yaw amplitude	$[-]$
\tilde{z}	normalized heave amplitude	$[m/m]$
$\vec{\Omega}$	angular velocity vector	$[rad/s]$

Variables describing properties for the finite element approach:

Variable	Description	Unit
$\vec{\alpha} = [\chi; \alpha; \beta]^T$	vector of cross section rotation	[rad]
B	structural damping matrix	[kg/s], [kg m/s], [kg m ² /s]
C	structural stiffness matrix	[N/m], [N/rad] [Nm/m], [Nm/rad]
E	youngth's modulus	[N/m ²]
$\varepsilon_x, \gamma_{xy}, \gamma_{xz}$	Longitudinal and shear strain	[-]
\vec{f}	vector of the generalized force of every nodal degree of freedom	[N], [Nm]
G	shear constant	[N/m ²]
I_y	Area moment of inertia around y-axis	[m ⁴]
I_{yz}	Area deviation moment	[m ⁴]
I_z	Area moment of inertia around z-axis	[m ⁴]
I_ω	Warping stiffness	[m ⁶]
$I_{y\omega}, I_{z\omega}$	sector centrifugal moments	[m ⁵]
I_T	Torsional stiffness	[m ⁴]
j_y, j_z, j_p	inertial moment per unit length	[kg m ² /m]
l	length of a finite beam element	[m]
λ_e	Matrix transforming properties from the element coordinate system into the inertial coordinate system	
M	structural mass matrix	[kg], [kg m], [kg m ²]
M_y, M_z	vertical and horizontal bending moment	[Nm]
$M_T, M_{St.V}, M_W$	total torsional moment, St. Venant torsional moment, warping torsional moment	[Nm]
$\tilde{M}_y^{(1)}, \tilde{M}_y^{(2)}$	first, second, third and fourth harmonic	[Nm/m]
$\tilde{M}_y^{(3)}, \tilde{M}_y^{(4)}$	amplitude of the bending moment normalized with the wave amplitude	
N_i	element shape function of the i th degree of freedom	[-]
ξ	Normalized longitudinal position; $\xi = \underline{x}/l$	[-]
μ	mass per unit length	[kg/m]
$\vec{P}_s = (P_{s,y}; P_{s,z})^T$	Position vector of the shear centre	[m]

q_t, q_x, q_y, q_z	external load per unit length (torsional, longitudinal, horizontal, vertical)	$[Nm/m]$, $[N/m]$
r_y, r_z	reduction factor to achieve the effective shear area	$[-]$
S	cross section area	$[m^2]$
$S_y; S_z$	area moments	$[m^3]$
T	kinetic energy	$[J]$
u_i	displacement of the i^{th} degree of freedom of a beam element	$[m]$, $[rad]$, $[rad/m]$
\vec{u}_j	vector of all unit degree of freedom displacements for the j^{th} natural mode (constant)	$[m]$, $[rad]$, $[rad/m]$
\vec{u}	vector of the time dependant displacements of all degrees of freedom (superposition of all considered mode shapes)	$[m]$, $[rad]$, $[rad/m]$
v_j	superposition factor for the response of the j^{th} mode shape	$[-]$
$\vartheta = d\chi/dx$	Rate of change of the torsion-induced twist angle	$[rad/m]$
V	strain energy	$[J]$
$\vec{w} = (w_x; w_y; w_z)^T$	vector of elastic displacements	$[m]$
w_M, w_B, w_S	displacement due to longitudinal tension, pure bending, shear bending	$[m]$
$\tilde{\omega}, \omega$	warping functions	$[m^6]$
Φ_y, Φ_z	Horizontal and vertical shear stiffness	$[-]$
$\psi = \gamma_{xs}^T / \vartheta$	relation of torsional shear strain and variation of the twist angle	$[m/rad]$
χ	torsion-induced twist angle	$[rad]$

Variables describing hydrodynamic properties

Variable	Description	Unit
$\mathbf{b}(\omega_e), \mathbf{b}(\infty)$	hydrodynamic damping matrix (frequency dependent and for infinite frequency)	$[kg/s]$, $[kg\ m/s]$, $[kg\ m^2/s]$
b_ϕ	relative damping coefficient	$[-]$
$\underline{\mathbf{b}}_{visc.}$	empirical viscous damping matrix (only roll damping)	$[kg\ m^2/s]$
\mathbf{c}	restoring forces coefficient matrix due to forward speed effects	$[N/m]$, $[N/rad]$ $[Nm/m]$, $[Nm/rad]$
$\tilde{\mathbf{c}}$	Estimated restoring matrix	$[N/m]$, $[N/rad]$ $[Nm/m]$, $[Nm/rad]$
C_B	block coefficient	$[-]$
ε	wave encounter angle	$[rad]$
$\vec{F}_E; \vec{M}_E$	excitation force and moment vector	$[N]$, $[Nm]$
$\vec{F}_{FK+Hyd};$ \vec{M}_{FK+Hyd}	combined Froude-Krylov and hydrostatic forces and moments	$[N]$, $[Nm]$
$\vec{F}_{Dif}, \vec{M}_{Dif}$	diffraction force and moment vector	$[N]$, $[Nm]$
$\vec{F}_{WL}, \vec{M}_{WL}$	vector of waterline forces and moments	$[N]$, $[Nm]$
Fn	Froude Number	$[-]$
h	wave steepness	$[-]$
k	wave number	$[-]$
\mathbf{k}	Matrix including impulse response functions	$[kg/s^2]$, $[kg\ m/s^2]$, $[kg\ m^2/s^2]$
λ	wave length	$[m]$
$\mathbf{m}(\omega_e), \mathbf{m}(\infty)$	hydrodynamic mass matrix (frequency dependent and for infinite frequency)	$[kg]$, $[kg\ m]$, $[kg\ m^2]$
$\tilde{\mathbf{m}}$	Estimated hydrodynamic added mass matrix	$[kg]$, $[kg\ m]$, $[kg\ m^2]$
$\vec{n}(\vec{x}, t)$	normal vector of the hull surface	$[-]$
$\vec{n}^0(\vec{x})$	normal vector of the stationary free surface	$[-]$
p_{FK+Hyd}	combined Froude-Krylov and hydrostatic pressure	$[Pa]$
p_{Rad}	Radiation pressure	$[Pa]$

\hat{p}^1	complex amplitude of first order pressure	[Pa]
\hat{p}_d^1	complex amplitude of the first order pressure (only frequency dependent component)	[Pa]
\hat{p}_{ind}^1	frequency independent component of the first order pressure	[Pa]
$p_{\overline{WL}}$	pressure at the time average waterline	[Pa]
ρ	fluid density	[kg/m ³]
ϕ^0	steady perturbation potential	[m ² /s]
ϕ^t	total velocity potential	[m ² /s]
$\hat{\phi}^1$	complex amplitude of the oscillating velocity potential	[m ² /s]
$\hat{\phi}_W^1$	velocity potential of the incoming wave	[m ² /s]
$\hat{\phi}_D^1$	diffraction velocity potential	[m ² /s]
$\hat{\phi}_R^1$	Radiation velocity potential	[m ² /s]
\mathbf{s}	matrix containing the result of the convolution integral (radiation forces) that is known from the past history	[N], [Nm]
ω_e	wave encounter frequency	[rad/s]
$\vec{U} = [-s; 0; 0]^T$	inflow velocity vector	[m/s]
ζ^0	stationary wave elevation; constant in body fixed reference frame	[m]
ζ^1	wave amplitude	[m]
ζ^t	Total wave elevation	[m]
s	ship forward speed	[m/s]
\vec{v}	fluid velocity vector	[m/s]

1 Introduction

Ship design and ship construction engineers have to solve difficult challenges to provide an ecologically friendly, safe and economic ship. One important challenge is the design of the hull structural scantling. The hull structure has to withstand ultimate loads and fatigue aging throughout the ship's operating life. Wave-induced loads are particularly relevant because they can introduce tremendous forces and moments into the ship structure. Furthermore, wave-induced loads basically occur over the entire operational time. Severe seas are more likely to affect the structure's ultimate strength, whereas small to moderate seas contribute significantly to fatigue damage because they occur frequently during service. Structural damage of the global steel structure of cargo ships due to fatigue aging was reported frequently. In a few cases, the entire ship sank. One recent example was the post-Panamax containership "MOL Comfort" that was build 2008 and broke into two pieces at the Arabian Sea in 2013. The hull of modern container ships is designed with large openings to allow efficient loading and unloading. However, these openings reduce significantly the vertical bending stiffness and torsional stiffness of the ship structure because the deck openings reduce the cross-sectional area strongly. For that reason, the deck of such ships is strongly reinforced by increasing the thickness of the deck plating and by using high tensile steel. In principle, high tensile steel is characterised by a higher yield strength resulting usually in a smaller plate thickness. However, high tensile steel is often more damageable due to fatigue. For example, high tensile steel was applied at the hull structure of the containership MOL Comfort and it can be assumed that fatigue aging of the ship structure contributed to structural failure of the hull.

Over the past few decades, full-scale measurements of wave-induced loads on ships were performed during research projects and by classification societies to gain a better understanding of the effect of wave-induced loads on ships, the associated load spectrum during the ship's lifetime and their contribution to fatigue aging of the steel structure. Such measurements showed that the ship structure can be excited to high frequency vibrations. The vibration frequency is

sometimes significantly higher than the wave encounter frequency and is often congruent with one of the elastic natural frequencies of the ship girder, e.g. the two-node vertical bending natural frequency.

The importance of accounting for the hull girder elasticity when computing ultimate sectional loads and fatigue aging is discussed in several research publications. Figure 1 plots the normalized sample spectra of the wave induced longitudinal stresses in the main deck of a containership, Kahl and Menzel (2008). The unfiltered data (red) comprises wave encountered and high frequency vibrations and the low-pass filtered data (blue) eliminated high frequency vibrations and included only contributions according to the wave encounter frequencies. It can be clearly seen that the unfiltered stress range exceeded the low-pass filtered stress range and thus affected the ship's ultimate strength. Furthermore, it was shown that the high frequency vibrations contributed approximately 50% to the total fatigue damage.

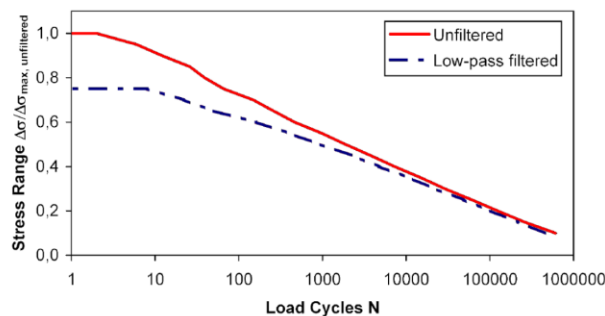


Figure 1: Comparisons of the wave-induced longitudinal stress spectra at the main deck of a containership. The total stress spectrum is designated by the red curve. High frequency vibrations were eliminated by a low-pass filter (blue curve). Kahl and Menzel (2008).

By comparing the contribution of elastic hull vibrations on fatigue damage for different sized containerships of load capacities between 2800 to 14000TEU, Storhaug (2014) reported that between 26 and 57% of the total fatigue damage was due to elastic hull girder vibration. Most of the research focus on vertical bending vibrations, because such vibrations were observed frequently during full-scale measurements. Further examples of full-scale measurements of the vertical bending moment of ships in waves can be found e.g. in Andersen and Jensen (2015). Horizontal bending and torsional vibrations were observed rarely, which might be explained by a higher damping rate of such vibration modes. However, recently, for example Storhaug and Kahl (2015) found that torsional vibration damage of an 8400TEU and an 8600TEU containership contributed up to 55% of

total fatigue damage. Furthermore, Mao et al. (2015) demonstrated that the combined horizontal bending and torsional warping significantly affected fatigue aging. In the deck region, they found that these combined loads contributed up to 15% of the total fatigue damage and up to 50% of the damage of structural details of a 4400TEU containership. Such results indicate that horizontal bending and torsional vibrations can occur in some specific situations and that the knowledge about such vibrations must be expanded in order to better understand these effects.

Generally, global elastic hull vibration can be classified into two phenomena. Initiated by an impulsive wave load, the hull girder starts to vibrate in one of its elastic natural modes. This transient vibration, so-called whipping, decays and finally disappears until a new wave-induced impulse leads to further vibrations. Resonant vibration, so-called springing, appears if the frequency of wave excitation is close to a natural frequency of the elastic hull girder. Due to small structural and hydrodynamic damping, the associated response amplitude can be significant and, due to the resonant excitation, the vibration can exist for a longer period.

The present work describes the development of a numerical method to compute springing induced vibrations of ship. Springing-induced vibrations are categorized into linear springing and higher order springing. In linear springing, the wave encounter frequency is close to the elastic natural frequency of the hull girder. Higher order springing occurs when the natural frequency of the hull girder coincides with a higher order component of wave-induced loads. Depending on whether second, third, or fourth order harmonic frequencies of these wave-induced loads are close to the natural frequency of the hull, it is referred to as second, third or fourth order springing. It is uncertain which springing effect contributes most to fatigue damage. In principle, it strongly depends not only on the type of ship, its loading condition and its forward speed, but also on the encountered sea states. Nevertheless, higher order springing can occur relatively more often because higher order components of wave induced forces are often closer to a ship's natural hull girder frequencies.

In the recent past, several research projects concerning springing induced vibrations were performed, see e.g. the EU founded project TULCS (e.g. Malenica and Derbanne (2012)), ExtremeSeas (Maron and Kapsenberg (2014)) or the international project WILS (see e.g. Hong, S., Y. et al. (2012) or Hong, S., Y. and

Kim, B., W. (2014)). During these research projects, springing induced vibrations were investigated within full-scale measurements, model tests and with numerical methods. As aforementioned, full-scale measurements were widely performed to investigate the effect of springing induced vibrations on fatigue aging of the ship structure. However, results of full-scale measurements can only slightly be used to investigate and optimize the springing behaviour of a new build ship during the design stage. Model tests are also widely used to investigate resonant vibrations of ships. However, it is challenging to scale the structural properties of ships. Often, an aluminium or steel backbone was used to simulate the stiffness properties of the hull, see e.g. Maron and Kapsenberg (2014) or Hong, S., Y. et al. (2012). This technique works well to model the vertical bending properties of the ship. However, the horizontal and torsional properties are often more complex and cannot be scaled correctly, if a simple backbone model is used. The steel structure of a ship is built out of thin plates (compared to the main dimensions of the ship). Referring to beam theory, such structure is called a "thin walled girder". As aforementioned, modern containerhips or bulk carrier are characterized by large deck openings to ensure efficient loading and unloading. Consequently, the "thin walled girder" consists of open and closed cells. Due to large deck openings, the shear centre of the cross section can be located far below the steel structure. In the present work, a 333m long containership will be investigated. Its shear centre is approximately 12m below the keel line (at the main frame). This phenomenon introduces strong coupling effects between torsion and horizontal bending. Such effects cannot be scaled correctly with a simple backbone model, because the location of the shear centre is often too high. Consequently, such experiments can be used to better understand the physical phenomenon of torsion and horizontal bending vibrations and to validate numerical methods, however, their use to investigate the springing behaviour of realistic ships is limited. More recently, researchers tried to overcome the drawbacks of a backbone and designed continuous models, e.g. Grammatikopoulos et al. (2020). With such technique, natural modes and frequencies of torsion could be achieved more accurate. However, the complexity and costs of such experimental techniques are high and so far, they are normally not applied during the ship design.

Efficient numerical methods to predict the springing behaviour of ships can overcome these issues. However, a reliable prediction of higher order springing-induced vibrations requires advanced numerical method that are able to consider

intricate details of the flow and structural behaviour. For that reason, an accurate and numerically efficient calculation at the same time is difficult to implement. The ship design request numerical method that are efficient regarding the computational time and that only need a minimum amount of engineering hours. Only such methods can be used effectively to optimise the ship design within an iterative procedure.

The present work presents a new numerical method that is intended to be numerically efficient and considers the most important nonlinear effects to compute higher order wave-induced springing. The diversity of numerical methods to determine the hydroelastic response of ships in waves is great and they do not always reliably predict springing induced vibrations, because they often cannot consider all important hydrodynamic and structural effects. For that reason, it must be differentiated precisely between the properties of the different methods and their applicability to determine global resonant vibrations. The following sections 1.1, 1.2 and 1.3 discuss the different methods to predict wave induced forces and moments as well as the corresponding rigid body motions, the determinations of wave-induced drift forces and the computations of wave-induced global elastic vibrations and associated sectional loads.

1.1 Periodic Wave-Induced Forces and Rigid Body Motions

The computation of wave-induced forces and moments as well as the corresponding rigid body ship motions is one of the classic subjects in marine hydrodynamics and concerns almost every seagoing vessel. Wave induced ship motions affect ship operations in many different aspects. Large motion amplitudes, high accelerations, and excessive wave loads must be avoided as they are detrimental to the performance of a ship and its crew as well as being a safety issue regarding not only the cargo carried on board, but also the strength of the ship's structure.

For a long time, model tests have been and are still the most reliable method to determine ship reactions in waves. E.g. Park et al. (2019) recently summarized experimental investigation of ship motion in head and oblique waves. Experimental investigations of ship motions in head waves have been established

as a common investigation during ship design for many years. Often, the port and starboard side of a ship are symmetric and consequently, the ship response in head waves is limited to surge, heave, roll (if parametric roll motions are expected) and pitch motion. Furthermore, surge motions are often assumed to be less important and are often not investigated, because the corresponding longitudinal accelerations are often smaller than the heave and pitch induced vertical accelerations. Consequently, the model is often only free to move in heave, roll and pitch. This procedure reduces the complexity of the test setup strongly.

In oblique waves the test setup becomes more complex, because the model will move in all six degrees of freedom. To avoid drift motion of degrees of freedom without restoring forces (surge, sway, yaw), the model is often moored by a system of soft springs. The spring stiffness need to be defined carefully. The natural frequency of the spring-system should be much lower than the wave encounter frequency to avoid that the first order harmonic amplitudes of the ship motions are affected by the springs. However, the spring stiffness should not be too low because strong drift motions and e.g. a large time average yaw angle need to be avoided, as well. Furthermore, the mooring system introduces often additional damping effects that might influence the ship response. Such model tests were performed e.g. during the project PerSee (Valanto and Hong (2015)) or SHOPERA (Lui et al. (2020)). However, they are expensive and intensive seakeeping measurements are often not feasible during a ship design.

Alternatively, numerical seakeeping computations can be used to reduce the amount of model tests. Advanced techniques to compute the flow surrounding ships exist, such as methods of Direct Numerical Simulation (DNS) and Large Eddy Simulation (LES) or field methods based on solving the Reynolds-averaged Navier-Stokes equations (RANSE). However, these techniques are beyond the capacity of readily available computational resources, especially those for the DNS and LES methods. Field methods based on solving the RANSE are less time consuming, but still it is not practical to perform a complete analysis within a reasonable time span. However, numerous simulations of ship motions in waves have been conducted to investigate specific features of ship-wave interactions; see, for example, Paik K.-J. et al. (2009), Seng S. and Jensen (2012), Stern et al. (2015), Craig et al. (2015), Robert et al. (2015), el Moctar et al. (2010) and Sigmund and el Moctar (2018b).

Wave-induced forces and moments and the corresponding ship motions are dominated by convection effects; thus, diffusion effects are relatively small. An exception is the roll motion, which is stronger affected by viscous effects. However, the corresponding viscous roll damping effects can be considered using empirical corrections. Consequently, seakeeping solvers based on potential theory became a useful tool because they are computationally efficient and accurate enough to predict wave-induced forces, moments and the corresponding ship motions.

A thorough overview of the development of seakeeping methods can be found in Beck R.F. and Reed A.M. (2001) and, more recently, in Schellin et al. (2015) as well as in the reports of the Seakeeping Committee of the International Towing Tank Conference (ITTC (2021)) and the Loads Committee of the International Ship and Offshore Structures Congress (ISSC (2018)). Two different kinds of potential theory solvers are mostly used, namely strip methods and three-dimensional (3D) boundary element methods. Under the assumption that hydrodynamic forces on slender hulls are smaller in the longitudinal direction, strip methods split the ship hull into individually separated transverse strips and the total loads are obtained by integrating the contribution of each strip. These methods are numerically more efficient than 3D solvers. However, strip methods are only valid for slender ships because three-dimensional effects and the influence of forward speed can only be estimated. Nevertheless, as the flow around each strip is computed individually, it is possible to consider certain nonlinear wave load components. One of the most widely used strip methods was introduced by Salvesen et al. (1970).

Three-dimensional boundary element methods account more accurately for the three-dimensional shape of the hull and can consider forward speed effects. First applications on seakeeping problems appeared in the late 1970s, solving the flow problem in the frequency domain based on the Neumann–Kelvin approach and linearized free surface and body boundary condition (Beck R.F. and Reed A.M. (2001)). Most widely, three-dimensional boundary element methods use either zero-speed Green functions to fulfil the boundary conditions (Telste and Noblesse (1986)) or Rankine sources (Söding and Bertram V. (2009)). The Green function method, although it needs additional analytic functions to fulfil the linear free surface condition, places singularities only at the body surface, whereas the Rankine source method distributes fundamental singularities at the body surface as well as at the free surface to fulfil the boundary conditions numerically. For zero-speed cases, zero-speed Green function methods are more efficient than

Rankine source methods. However, for ships with forward speed, it is more difficult to find an analytic function to fulfil the free surface boundary condition that is not prone to numerical instabilities. Consequently, Rankine source methods are nowadays more common when forward speed effects are considered. Chang (1977) introduced one of the first forward speed green function methods followed e.g. by Guevel and Bougis (1982), Wu and Eatock-Taylor (1987), Iwashita and Ito (1992) or Noblesse and Yang C. (2015). Detailed descriptions of zero speed green function methods are given by Telste and Noblesse (1986) or Papanikolaou and Schellin (1993). Good examples of Rankine source boundary element methods are given by Nakos and Sclavounos (1991), Bertram (1990) or Söding and Bertram V. (2009).

The above numerical tools provide quick solutions of linear wave-induced loads and linear ship motions with a relatively good engineering accuracy. Due to the linearization, these approaches neglect some nonlinear effects that become more important when the wave amplitude increases. First, the pressure integration is performed only over the time average wetted surface, neglecting changes of the wetted surface caused by waves and the corresponding ship motions (geometric nonlinearity). Second, due to the linearization, higher order pressure components are neglected (hydrodynamic nonlinearities). These simplifications are acceptable for flow problems dominated by first-order forces and moments and when the change of the wetted surface is moderate, for example, heave and pitch motions in small head waves. However, more complex investigations are often necessary to assess today's ship designs. For example, in steep oblique waves, nonlinear effects became more important and need to be considered when ship motions in all six degrees of freedom should be predicted accurately.

To account for hydrodynamic nonlinearities, e.g. Jensen and Dogliani (1996) or Wu and Moan (1996) investigated higher-order wave-induced forces and moments using second order strip theory. To account for geometrical nonlinearities, time domain approaches are often the preferred choice. Current time domain methods based on potential theory can be categorized into weakly-nonlinear, body exact, weak scattered and fully nonlinear methods. A weakly-nonlinear method assumes that an equivalent time domain solution exists for every frequency domain solution, Cummins (1962) and Ogilvie (1964). Convolution integrals based on Fourier transforms of frequency domain coefficients convert hydrodynamic forces and moments from the frequency domain into the time domain. The dominant geometrical nonlinearities result from the Froude-Krylov

and hydrostatic forces and moments. Assuming an undisturbed incident wave, these forces can be computed without solving a flow problem. Consequently, they can be computed efficiently in time domain considering the instantaneous wetted hull surface. For example, King (1987), Fonseca and Soares (1998) or Liu and Papanikolaou (2014) introduced weakly nonlinear hydrodynamic solvers. However, these methods are still based on linear hydrodynamic theory, and they split the total flow problem into a radiation and a diffraction term.

Body-exact methods try to account more accurately for the effect of radiation and diffraction on the changing wetted surface. Using a strip theory method, Rajendran et al. (2015) and Rajendran et al. (2016) developed a body-exact method to calculate nonlinear wave-induced forces of ships in waves. In principle, they resorted to convolution integrals to compute radiation and diffraction forces. However, to account for the effect of the changing wetted surface, they calculated the kernel functions for different drafts of each strip. Their technique still splits the flow problem into a radiation and diffraction part and they were not able to consider the stationary wave system due to forward speed.

This drawback can be avoided using the weak-scattered method of Pawlowski (1992). Based on the assumption that the effects of waves scattered from the body are relatively small, the boundary conditions are fulfilled on the instantaneous body surface and on the elevated free surface of the incident waves. In this approach, the flow problem has to be solved at every time step and, consequently, requires considerable computational effort. Examples of weak-scattered methods can be found in Huang (1998) or Kim et al. (2011). Kim et al. (2011) for example, used a precomputed double body forward speed solution to account for the stationary velocity potential.

A fully-nonlinear seakeeping solver fulfils the nonlinear free surface boundary condition at the instantaneous disturbed water surface and wetted hull surface. The latest publication of such method can be found in Söding (2020) or Ferreira González et al. (2020). The computational effort further increases compared to a weak-scattered method. The nonlinear boundary conditions are often solved iteratively. Furthermore, an accurate time domain computation of the interaction between the stationary wave system, incoming waves and scattered waves from the hull require a fine discretization of the free surface.

Based on the assumption of small motion amplitudes, the aforementioned approaches solve often a linear rigid body motion equation to compute ships position, velocities and accelerations. If larger amplitudes are expected, for example, in steep oblique waves or during manoeuvre simulations, the nonlinear motion equations should be solved to account for strong kinematic coupling effects. For example, Matusiak (2007, 2011) introduced a method to solve the nonlinear equations of motion using a ‘two-stage’ approach. In the first stage, he solved only the linear response (in frequency domain) of a rigid body and nonlinearities were introduced in the second stage in time domain. Bulian G. and Francescutto (2013) discussed different approaches to investigate numerically the intact stability of ships and presented an approach which integrates Froude–Krylov forces (undisturbed wave) over the instantaneous wetted surface and computes radiation forces by using a set of convolution integrals. Rigid body motions were solved based on the nonlinear equations of motion. Comparisons to experimental results of roll amplitudes in beam waves showed a good agreement. Söding (2020) solved the nonlinear equation of motion to computed wave-induced ship motions with a fully-nonlinear seakeeping solver.

1.2 Wave-Induced Drift Forces and Corresponding Speed Loss

As discussed in the previous section, wave induced forces and moments excite the ship to move periodically according to the wave encounter frequency. Deeper investigations of wave induced forces and moments show that the time average of a wave induced force is generally unequal zero and consequently initiates a drift motion of the ship. This time average force and moments are called drift force and moments and result from the nonlinear interaction between the incident wave and the moving ship geometry. The longitudinal drift force is called wave added resistance. The wave added resistance is an important component of the total resistance of ships in waves and play a significant role when computing the fuel consumption or speed loss in waves. Speed loss in waves must be considered not only to meet a ship's time schedule, but it has become also a safety issue because manoeuvrability has to be maintained under adverse weather conditions; see, e.g., Papanikolaou et al. (2015), Know (2008), Prpić-Oršić and Faltinsen (2012), Sigmund and el Moctar (2018b), Sigmund and el Moctar (2017), Kim et al. (2016) or Kim et al. (2015). The transverse drift force or the drift yaw moment are more

important for investigations of ships path during a stationary forward traveling, during manoeuvres or for dynamic positioning. The drift force in vertical direction, or the roll and pitch drift moment are less important for practical investigations. In extreme scenarios or during investigations of the dynamic stability, a time-averaged roll angle can affect the behaviour of the ship. However, for most scenarios, the corresponding time averaged heave, roll and pitch motions are small.

For springing-induced vibrations, the wave added resistance and the corresponding speed loss in waves is an important property, that cannot be neglected when computing the fatigue aging of the ship structure due to resonant vibration. The excitation forces and moments and the response of the structure depend on the forward speed of the ship. Consequently, when the ship cannot maintain service speed due to the wave conditions and the associated speed loss, the wave encounter frequency changes, which affects the wave-induced excitation forces and moments strongly. Furthermore, the ship speed affects the wet natural frequency of the vibrating hull due to a change of the stationary wave system and corresponding dynamic trim and sinkage and their effect on the hydrodynamic added mass. As a consequence, a change of the forward speed changes the natural frequency of the vibrating hull, the wave encounter frequency and the amplitude of the wave-induced excitation forces and moments.

The speed loss of a post-Panamax containership, a VLCC tanker and a cruise ship was investigated during a pre-study, see Riesner et al. (2018b). The ship speed was computed by solving a stationary equilibrium condition for the longitudinal and transverse forces and the yaw moment considering the propeller trust with engine dynamics, calm water and wave-induced drift forces and moments as well as rudder forces and moments. Wave-induced drift forces and moments for regular waves were computed using a linear frequency domain boundary element method and a Pierson-Moskowitz wave spectrum was applied to account for irregular seas. Figure 2 plots the attainable ship speed [m/s] of a post-Panamax containership for combinations of significant wave height, H_S , and zero up-crossing period T_z in bow quartering waves of 150deg encounter angle. It can be seen that the attainable ship speed reduces significantly with increasing significant wave height, especially for sea states near $T_z = 11s$. Such speed loss affects the wave encounter frequency and wave induced forces and moments strongly and should be considered for the computations of springing-induced resonant vibrations.

1.2 Wave-Induced Drift Forces and Corresponding Speed Loss

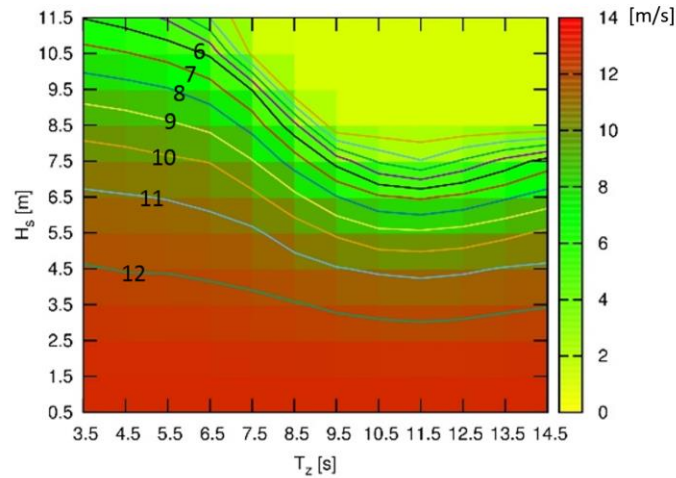


Figure 2: Attainable speed of a 355m long post-Panamax containership in bow quartering waves of 150deg encounter angle.

Conventional methods to compute the wave added resistance comprise model tests, empirical formulas, and numerical techniques. These methods differ significantly in accuracy and cost. To determine drift forces and moments, model tests are still one of the most reliable methods, exemplified by recent tests conducted within the framework of the European research projects Shopera (Sprenger et al. (2017), Papanikolaou et al. (2016)) and the German national research project PerSee (Valanto and Hong (2015)). However, model tests of drift forces are complex and expensive, especially in oblique waves when the ship should be free to move in all six degree of freedom but forces need to be measured.

Empirical formula for the prediction of drift forces are based on data bases of already investigated ships. Such formulas provide a quick estimation of drift forces for a wide range of different ship types and are useful at the preliminary design stage. However, they need constant updating. Consequently, they are of limited use for the design of new ship types. Some examples of recently developed empirical methods can be found in Liu and Papanikolaou (2016).

Numerical methods to compute drift forces in waves are generally based on the same technique used to compute ship motions in waves and can be split into field methods that solve the Reynolds-averaged Navier-Stokes equations (RANSE) or methods based on potential theory. However, drift forces and moments are so-called higher order phenomenon and are mainly dominated by second order wave-induced effects. Consequently, the numerical methods need to account for

such higher order wave force components. RANSE based field methods have been proven useful for the computation of drift forces because they account for most of the associated nonlinear flow effects, such as the changing wetted surface, breaking waves and viscous effects, see e.g. el Moctar et al. (2017) or Sigmund and el Moctar (2018b). Furthermore, they demonstrate that forward speed strongly affects the wave added resistance and that viscous effects influence wave added resistance in short waves. Others, notably Sportelli and Huijsmans (2012), Lyu and el Moctar (2017), Kim et al. (2017), Ley et al. (2014b), Guo et al. (2012), Sadat-Hosseini et al. (2010) and Sadat-Hosseini et al. (2013) also used this method to study the wave added resistance. In all cases, however, the computational effort was high and only an experienced user was able to obtain reliable results.

The obvious advantage of potential theory-based methods for the computation of drift forces is their computational efficiency. Generally, two different approaches exist to compute drift forces in waves, the so-called far field method and the near field method. The far field method assumes that drift forces can be related to the radiated and diffracted wave energy and the momentum flux at infinity. This method is widely used to compute the longitudinal drift force (wave added resistance) in head and following waves. However, when the ship is advancing in oblique waves and moves freely in all six degree of freedom it is difficult to associate the computed energy of radiated waves to each of the six degrees of freedom. The near field method is often called pressure integration method. The total force acting on the hull is computed by integrating the hydrodynamic pressure over the hull wetted surface and the drift forces and moments are the time averaged force or moment in each degree of freedom.

Maruo (1960, 1963) was one of the first to assess the wave added resistance using the far field method. Gerritsma and Beukelman (1972) and Journee (2001) modified this approach within a linear strip theory method and demonstrated the importance of bow wave diffraction for the prediction of the wave added resistance in short waves. Following Maruo's approach, Kashiwagi (1995, 2009, 2011) also accounted for the effect of bow wave diffraction. Salvesen (1978) used Gerritsma's and Beukelman's approach within a strip theory method. He showed the importance of an accurate prediction of ship motions when calculating the wave added resistance. Most of these potential theory based solvers, however, turned out to be unreliable to assess the wave added resistance in short waves. Boese (1970) tried to resolve this shortcoming by integrating hydrodynamic pressures (near field method). Later, Faltinsen et al. (1980) developed a more

accurate pressure integration method for short waves. Söding et al. (2014) introduced a frequency domain potential flow solver based on Rankine sources, which couples the effect of the nonlinear stationary forward speed problem with the linear seakeeping problem. His method directly integrates the pressure at the hull, accounts for the changing wetted surface (Boese's approach), and time averages the second order pressure field. Lyu and el Moctar (2017) compared results obtained with Söding's method to RANS based predictions and model test measurements and found generally favourable agreement. However, the wave added resistance in short waves was still underestimated strongly for several cases.

To consider the effect of the changing wetted surface more precisely, later developments were characterized by time domain potential flow solvers. Using such an approach, Kim et al. (2010), for example, calculated the wave added resistance from diffraction and radiation components, and Liu et al. (2011) employed a three-dimensional frequency domain panel method and a hybrid time domain Rankine source solver based on Green functions and a far-field approach to calculate the wave added resistance. At small Froude numbers, predictions from these methods compared well to experiments; however, at larger Froude numbers, errors increased.

1.3 Sectional Loads and Springing-Induced Vibrations

As aforementioned, springing-induced vibrations can be determined by experimental techniques. However, for model tests, a correct scaling of the ship structural properties is difficult. To compute springing induced resonant vibration numerically, the fluid-structure-interactions need to be considered. Generally, these numerical methods differ in complexity because different numerical methods to solve the fluid flow and the structural deformations of the ship exist. To compute the structural deformation, usually, finite element approaches are used. For example, el Moctar et al. (2017), el Moctar et al. (2011), Ley et al. (2014a) and Oberhagemann (2016) introduced an accurate procedure that is able to account for intricate details of the entire ship structure as well as complex flow phenomena. Their techniques couple a three-dimensional finite element method (structural response) with a field method that solves the Reynolds-averaged Navier-Stokes equations (RANSE). However, to predict global elastic vibrations, a detailed discretization of the ship's structure is often unnecessary. Beam theory

approaches lead to accurate results with significantly less numerical effort; see, e.g., Lakshmyanarayanana et al. (2015), Lakshmyanarayanana and Temarel (2019), Ley and el Moctar (2014), Craig et al. (2015), Robert et al. (2015) and el Moctar et al. (2011) who coupled a RANSE solver with a finite beam element approach. The computational effort to compute the structural response can be further reduced by decomposing the overall deformation of the structure into basic vibration modes. The final result is then obtained by superposing the result of every basic vibration mode (modal super positioning technique).

The available numerical methods to compute wave induced forces were already discussed in section 1.1. Usually, these methods are applied also for hydroelastic investigations of ships in waves. As aforementioned, the numerical effort and the associated engineering hours to apply RANSE based field methods are large, which is why such methods are not often used in industry to calculate elastic vibrations of ships. For that reason, methods based on potential theory are widely used for the computation of global resonant vibrations, as well. Although widely used, potential theory-based methods do not always reliably predict springing induced vibrations, because they often cannot consider every of the necessary flow phenomena, such as the nonlinearities of wave-induced forces and the influence of the ship's forward speed with its stationary wave system that causes dynamic trim and sinkage.

Bishop and Price (1979) introduced one of the first hydroelastic approaches for ship vibrations by solving the hydroelastic equations of motion in the frequency domain. They focused on vertical bending deflections, and their technique is based on strip theory to describe the flow around the ship and a beam model to calculate the elastic response. Hirdaris et al. (2003), Senjanović et al. (2007a) and Senjanović et al. (2007b) intensively investigated hydroelasticity of ships in waves using a frequency domain method. They focused on vertical bending, horizontal bending, and torsion, whereas Senjanović et al. (2007a) and Senjanović et al. (2007b) used beam theory coupled with a boundary element method. In conjunction with beam theory, Hirdaris et al. (2003) used a three-dimensional finite element model. However, their method split the hull into individually strips and does not consider three-dimensional effects. Furthermore, they do not consider effects of forward speed and the associated steady wave system and pressure distribution at the hull.

Söding (2009b) developed a hydroelastic method that accounts for the fully nonlinear stationary forward speed problem. He relied on a three-dimensional

frequency domain boundary element method to compute the flow around the vibrating ship hull advancing at constant forward speed. To account for high wave encounter frequencies and to analyse linear springing-induced vertical bending vibrations, he simplified the free surface boundary condition by satisfying it analytically without panelising the free surface. However, damping effects due to radiated waves are then not captured. Riesner et al. (2018c) introduced a similar method that does account for hydrodynamic damping by coupling the nonlinear forward speed problem with the linear oscillating vibration problem. At low frequencies, they discretized the free surface numerically. At high frequencies, they computed damping by combining the low frequency solution with an infinite frequency solution. Their approach obtained results that compared favourably to RANSE based computations. However, such linear frequency domain methods are limited to predict linear springing and are not able to predict higher order springing.

To numerically predict higher order springing, nonlinearities and three-dimensional effects need to be considered. Hänninen (2014), for example, investigated second order springing-induced vibrations and highlighted the necessity to carefully predict three-dimensional effects. As aforementioned, potential theory allows splitting the nonlinearities into geometrical nonlinearities and hydrodynamic nonlinearities. Among others, Jensen and Dogliani (1996) and Wu et al. (1997) investigated higher order hydroelastic responses considering hydrodynamic nonlinearities by using a second order strip theory method. As already discussed, to account for geometrical nonlinearities, time domain methods such as weakly nonlinear, body-exact, weak-scattered or fully-nonlinear methods can be applied. Jiao and Yu (2019), Lee et al. (2014) and Malenica et al. (2007) introduced weakly nonlinear hydroelastic solvers. However, additional methods need to be used to account for the effect of the changing wetted surface due to radiation and diffraction, as described in section 1.1 and 1.2. A body-exact method based on strip theory was recently introduced by Rajendran et al. (2015) and Rajendran et al. (2016) to calculate the elastic vertical bending response of ships in waves. However, this method does not account for three dimensional effects and for the effect of stationary forward speed. Usually, resonant vibrations occur at higher forward speeds because the natural frequency of the hull and the wave encounter frequency are close together (at least in head or head quartering waves). At higher forward speed the associated stationary wave system and the dynamic trim and sinkage influence springing induced vibrations significantly

because these phenomena influence the wetted hull surface. This affects the wave induced forces as well as the wet natural frequencies and mode shapes of the elastic ship, see e.g. Orlowitz and Brandt (2014). More accurately but with more computational effort, Kim et al. (2011), for example, developed a hydroelastic method based on the weak-scattered approach considering the effect of the stationary forward speed double body flow. Fully-nonlinear potential flow methods do not split the solution into the stationary forward speed and oscillatory solution and solve the total flow in one system. However, fully-nonlinear hydroelastic methods have not been yet applied for hydroelastic solvers. Recently, Söding (2020) introduced a fully-nonlinear seakeeping solver and computed vertical bending moments considering a rigid hull.

As already discussed, springing-induced horizontal bending moments and torsional moments are being examined more and more frequently. Because of their relatively weak torsional stiffness, large container ships or bulk carrier are investigated often. These ships are characterized by large hatch openings and a shear centre located below the keel, i.e., outside of the hull's cross section. When beam theory computes vibrations of such cross sections, warping effects and coupling of horizontal bending and torsion becomes essential. Pedersen (1985) or Wu and Ho (1987) were one of the first to introduce coupling effects of horizontal bending and torsion for ship structures. Wu and Ho (1987) applied their beam element approach to determine wave-induced vibrations of simplified ship cross section (U-shape and rectangular cross sections). They considered coupling terms in the mass matrix, but neglected shear coupling effects in the stiffness matrix. Kim et al. (2009) introduced a hydroelastic method that coupled a similar finite element beam approach with a higher-order B-spline Rankine panel method, and Kim et al. (2011) improved the hydroelastic solver by coupling the same finite element approach with a weak-scattered method. To accurately compute dry and wet natural frequencies, the finite beam element approach should consider shear coupling effects of bending and torsion. Pavazza (2005) introduced a beam theory that considers shear coupling effects, and he applied his theory on a simple I-shape beam. Senjanović et al. (2011) used a similar technique to compute dry natural modes of a large containership by also accounting for the effects of bulkheads. However, they did not consider wave-induced fluid-structure interaction and, consequently, they were unable to determine sectional hull girder loads.

1.4 Requirements for the New Numerical Method

The discussion of the current state of research showed an overview of existing methods for the computation of wave-induced forces (periodic components and time average drift force), wave-induced rigid body motions and wave-induced resonant vibrations of ships. This section discusses the requirements for the newly developed numerical method and it will be gradually work out which theoretical approaches are necessary to fulfil these requirements. The following list summarizes the requirements for the new hydrodynamic method:

- [1] The new numerical method is intended to be used during the ship design process and must be numerically efficient.
- [2] Based on the literature study, considering the stationary forward speed problem including the steady wave system and dynamic trim and sinkage is essential for the computation of the wave-induced forces, corresponding rigid body motions and elastic vibrations of ships at forward speed. Consequently, the developed numerical method should account for the fully-nonlinear stationary forward speed problem.
- [3] The literature study showed that the consideration of nonlinear wave-induced force components is essential for the computation of wave-induced drift forces and higher order elastic resonant hull girder vibrations. However, to meet the requirement of being numerically efficient, only the most dominant nonlinear wave-induced force components should be considered.
- [4] Sigmund and el Moctar (2018) showed that viscous effects play a significant role for the wave added resistance in short waves, consequently, such effects should be considered.
- [5] Most of the seakeeping and hydroelastic solvers rely on the assumption of small rigid body motions (body rotations smaller than 5deg). Therefore, they often linearized the equations of rigid body motions. However, in steep oblique waves, ship rotations can be significantly higher than 5deg. Consequently, a linearization of the equation of rigid body motion is not valid for such scenarios.

To fulfil the requirement of being numerical efficient, the newly developed numerical method is based on potential theory. As aforementioned, wave-induced forces and moments are only marginally affected by diffusion effects. Thus,

methods based on potential theory are well established to predict wave induced loads. Diffusion effects that affect rigid body ship motions, the drift forces and elastic vibrations slightly stronger, e.g. viscous effect on the wave added resistance in short waves and hydrodynamic damping of the roll motions and resonant elastic vibrations, empirical methods will be applied to account for these effects. As it was shown in the discussion of the current state of research, three-dimensional potential flow methods based on Rankine sources are the most common choice when the stationary forward speed problem is considered. For that reason, the newly developed method uses Rankine sources to fulfil the boundary conditions for the stationary forward speed problem and the periodic rigid body and elastic problem in waves. As already discussed in the literature study, different time domain approaches exist to consider geometrical nonlinear wave force and moments. According to the literature study, the most important nonlinear contributions result from Froude-Krylov forces and moments. Nonlinear Froude-Krylov forces can be efficiently computed with a weakly-nonlinear time domain approach. As already mentioned, the weakly nonlinear time domain solver relies on linear hydrodynamic theory to compute radiation and diffraction forces. Consequently, radiation and diffraction forces are only integrated over the mean wetted surface. However, to overcome this drawback, a waterline integral will be applied to account for the effect of the changing wetted surface on radiation and diffraction forces. Such waterline integral was already sufficiently used in frequency domain seakeeping solvers to predict the drift forces and moments, e.g. Söding et al. (2014). For the new numerical method, it is intended to use such waterline integral to compute nonlinear radiation and diffraction effects in time domain. To allow large rigid body motions due to steep oblique waves and to compute roll and torsional moments accurately, the nonlinear equation of rigid body motions will be used to compute rigid body ship motions, velocities and accelerations.

To predict global elastic resonant vibrations accurately, the fluid-structure-interaction of the elastic hull in waves need to be accounted. The new numerical method computes the fluid-structure-interaction by coupling the hydrodynamic solver with a finite-element-method that computes the structural response. This finite-element-method needs to fulfil the following relevant requirements:

- [1] Similar to the flow solver, although the structural solver must be numerically efficient to enable its use during the ship design.

[2] As already discussed, ships are thin walled structures and some ship types are characterized by large deck opening. The newly developed numerical method needs to be able to account for the warping effects of thin walled structures and the coupling effects of bending and torsion for ships in oblique waves

The new numerical method is intended to predict global elastic vibrations of ships in oblique waves. The literature study showed that finite element approaches based on beam theory can adequately predict global deformations of the hull girder. Additionally, such method need only a small amount of computationally time. Consequently, the new numerical method will be based on beam theory to compute the elastic behaviour of the ship. To further reduce the computational time, the modal superpositioning technique will be applied to decouple the total elastic system into basic vibration modes. As aforementioned, some ship types, e.g. container ships and bulk carrier have large deck opening, and consequently these ships are characterized by a relatively weak torsional stiffness and large torsion related warping effects. Furthermore, bending and torsional displacements are coupled. To account for such effects the newly developed beam element method will account for nonuniform torsion induced warping (restrained warping) and furthermore couples bending and torsion. A ship cross section consists of closed and sometimes open cells. To compute coupling effects of torsion and bending, detailed information about cross section properties and time-consuming precomputations of the corresponding beam element properties are usually necessary. To avoid such complicated computations, the beam element method is optimized for ship like cross sections.

1.5 Authors Contribution

1.5.1 Developments

The developments within this work can be spitted into the following three main approaches :

[1] A weakly-nonlinear hydrodynamic method was developed that couples the fully nonlinear forward speed problem with the periodic

hydroelastic flow problem in waves using the Hachmann approach, Hachmann (1991). The following development have been made

- a. Development of new linear boundary conditions at the free surface and the hull to account for elastic vibrations of the ship at forward speed.
- b. Development of a numerical method to compute the infinite frequency solution of the hydrodynamic added mass and hydrodynamic damping.
- c. A semi-analytical integration method to compute the impulse response function base on the integration of the hydrodynamic damping or hydrodynamic added mass.
- d. An adaptive body grid approach to capture the instantaneous wetted hull surface in time domain.
- e. Nonlinear equations of rigid body motion defined in the inertial coordinate system. These equations solve directly the Euler angles associated with roll, pitch, yaw and the body translations using an implicit time-integration method. Radiation forces of the moving ship are related to the body acceleration and velocity. Consequently, these force components are included in the homogeneous part of the partial differential equations.
- f. Development of a time domain waterline integral to compute the effect of the changing wetted hull surface on radiation and diffraction forces. The radiation pressure at the mean waterline is computed based on convolution integrals. Thus, the waterline integral can be solved in every time instance during the time domain simulation. Furthermore, the interactions between radiation, diffraction and combined Froude-Krylov and hydrostatic forces is accounted.
- g. Empirical correction method to account for viscous (friction) effects on the wave added resistance of ships in head waves.

[2] A structural finite element beam method to compute the global elastic response of a ship due to torsion, horizontal and vertical bending and the associated coupling effect was developed. The following developments have been made:

- a. Development of a new finite beam element approach to account for coupling effects of torsion induced nonuniform deformations

(restrained warping) and vertical and horizontal bending. This method, considers coupling effects in the mass and stiffness matrix of the equation system to describe elastic ship deformation.

- b. The coupling effects of torsion and bending normally require an extensive number of precomputations to determine all necessary structural properties. To overcome this drawback, the new finite beam element approach is optimised for the use of ship like structures.

[3] A hydroelastic method to compute the fluid-structure-interaction of ships in waves was developed. The following developments have been made:

- a. Development of a numerical method to compute wet natural modes. As aforementioned, the elastic response is computed using the modal superpositioning technique. Thus, the natural modes need to be precomputed. In principle, the fluid around the ship affects the mode shape. To compute the hydroelastic response accurately, the wet natural modes need to be considered for the modal superpositioning technique. Basically, the hydrodynamic properties, namely hydrodynamic added mass, damping and restoring, depend on the mode shape. To ensure that the wet natural modes are orthogonal, they are computed based on estimated, frequency independent hydrodynamic properties.
- b. Development of a frequency independent hydroelastic method to compute free vibrations of ships in waves (weakly-nonlinear).
- c. To couple the fluid flow solver with the nonlinear rigid body motion solver and the linear elastic deformation, a two-way coupled algorithm was developed.

1.5.2 Implementation of the New Numerical Method

The new numerical method was implemented in the programming language C++.

1.5.3 Numerical Simulations and Model Tests for the Validation

All numerical simulations with the new numerical method were performed by the author. For the verification and validation study, numerical simulations with a frequency domain boundary element method were performed by the author as well. CFD results that were used for the validation of the new numerical method were not performed by the author. The CFD results were taken from public literature and provided by Sebastian Sigmund. The specific source is given when the data is discussed. During the validation study, the new numerical method was validated also against experimental data. The experiments were performed by project partners, see references. Often the raw data of the experiments were available and the new numerical method was directly compared to the measured time series. Furthermore, Fourier transformations of the time series were performed to compare harmonic response amplitudes. The data processing and the Fourier transformations of experimental results for the validation of rigid body ship motions in steep oblique waves, see section 4.4, were performed by Guillermo Chillcce. The processing of the raw data of the model test used to validate the hydroelastic response in waves, see section 4.5, was performed by the author. When experimental data is used for validation, the source is provided during the discussion.

1.6 Structure of the Present Work and Declaration

The following chapters describe the developed approaches and the new numerical method to compute the rigid and elastic response of a ship in oblique waves.

The theoretical description of the new numerical method begins with the description of the kinematic relations of a moving and vibrating ship hull in section 2.1. The total response of the ship was split into the rigid body response (rigid body motions) and the elastic response (elastic deformation) of the hull. Section 2.2 introduces the procedure to compute rigid body motions and discuss hydrodynamic forces and moments acting at the ship hull. Afterwards, the new beam element approach to compute the elastic deformation of the ship is described in section 2.3. Subsections discuss systematically the definition of the strain and kinematic energy of a vibrating beam (section 2.3.1), torsion induced warping effects at ships cross sections (section 2.3.2), shape functions to compute

element displacements (section 2.3.3) and the definition of the linear equation of elastic deformations (section 2.3.4). As aforementioned, the elastic response of the ship was computed based on the modal superpositioning technique. This requires a precomputation of the natural modes. The new method to compute wet natural modes is described in Section 2.3.5. Finally, the new weakly-nonlinear elastic deformation equations are introduced in section 2.3.6.

Section 3 describes the investigated ships and provides all properties that are necessary for the simulations performed in this work.

A verification and validation study of all developed approaches is given in chapter 4. The verification and validation is split into a time and spatial discretisation study (section 4.1), the verification of convolution integrals to compute radiation forces and moments (section 4.2), the validation of nonlinear wave-induced forces and moments on a fixed and moving ship (section 4.3), the validation of rigid body ship motions in steep oblique waves (section 4.4) and the validation of the hydroelastic response in waves of varying wave encounter angle and varying ship speeds (section 4.5).

Section 5 discuss investigations of the rigid and elastic response of ships in waves with special attention on the effect of the wave steepness and forward speed on rigid body motions and elastic vibrations (section 5.1 and 5.2). The validation study of the elastic ship response in waves was performed with structural properties of a backbone model. A backbone cannot simulate realistic structural properties of a ship. To investigate the hydroelastic properties of a ship with realistic structural properties, further simulations of a post-Panamax containership with realistic full-scale structural properties were performed and compared to results based on backbone structural properties, see section 5.3.

Content of this dissertation has previously been published in the following references:

- [1] Riesner, M., von Graefe, A., Shigunov, V., el Moctar, O., 2016, "Prediction of Non-Linear Ship Responses in Waves Considering Forward Speed Effects", *Ship Technology Research*, Vol. 64, pp. 135-145.
- [2] Riesner, M.; Chillce, G.; el Moctar, O. (2018): Rankine source time domain method for nonlinear ship motions in steep oblique waves. *Ships and Offshore Structures*,. DOI: 10.1080/17445302.2018.1498568.

- [3] Riesner, M.; el Moctar, O. (2018): A time domain boundary element method for wave added resistance of ships taking into account viscous effects. *Ocean Engineering*, Vol:162, pp. 290–303.
- [4] Riesner, M.; Ley, J.; el Moctar, O. (2018): An Efficient Approach to Predict Wave-Induced Global Hydroelastic Ship Response. 8th International Conference on HYDROELASTICITY IN MARINE TECHNOLOGY,,
- [5] Riesner, M.; el Moctar, O. (2021): Assessment of Wave Induced Higher Order Resonant Vibrations of Ships at Forward Speed,(under review). *Journal of Fluids and Structures*, Vol: 103, <https://doi.org/10.1016/j.jfluidstructs.2021.103262>.
- [6] Riesner, M.; el Moctar, O. (2021), A Numerical Method to Compute Global Resonant Vibrations of Ships at Forward Speed in Oblique Waves”, *Applied Ocean Research*, Vol:108, <https://doi.org/10.1016/j.apor.2020.102520>.

2 Numerical Method to Compute the Rigid and Elastic Response of Ships in Wave

This chapter includes a theoretical description of the new numerical method for the computation of the rigid body and elastic deformation response of ships in waves. Section 2.1 describes the kinematic relation between rigid body motions and elastic deformations. Afterwards section 2.2 describes the new mathematical model to compute the rigid body motions due to weakly-nonlinear wave induced hydrodynamic forces and moments. Section 2.3 describes the mathematical model to compute the hydroelastic response due to weakly-nonlinear wave-induced loads. Section 2.4 describes the hydrodynamic method to frequency domain wave-induced forces and moments considering the fully nonlinear stationary forward speed solution with the stationary wave system and the dynamic trim and sinkage. Section 2.5 discusses the spatial discretisation of the frequency domain solver and time domain solver. Section 2.6 describes the computational procedure of the new numerical hydroelastic solver.

2.1 Kinematic Relations

Some content of this section was published in Riesner and el Moctar (2021a, 2021b).

As discussed in the introduction, it is established practice to split the total response of the hull into basic modes. This technique separates the total response into rigid body motions and elastic hull girder deformations. In the present work, the total response is determined by superposing the response of all rigid body motions and all considered elastic deformation modes. Rigid body motions were based on the assumption that the motion of a rigid body can be described as translational motions of the body's center of gravity plus rotational motions of the body around the body's center of gravity. For a wetted hull this technique is only an approximation. Due to the influence of the fluid and the associated hydrodynamic forces, the body does not rotate exactly around the center of gravity. For example, the roll axis is often slightly below the center of gravity. This effect is mainly caused by hydrodynamic forces due to roll accelerations

2.1 Kinematic Relations

(hydrodynamic added mass). However, the magnitude of the hydrodynamic added mass of the roll motion is usually relatively small compared to the total inertial properties of the ship structure. For that reason, the distance between the correct roll axis and the center of gravity is often small and thus assuming that the ship is rotating around its center of gravity is usually a reasonable assumption.

To analyse the body response of ships in waves, two coordinate systems were applied to describe the position of a point at the hull. The first coordinate system, a right-handed inertial coordinate system with the origin O , $\vec{x} = [x; y; z]^T$, follows the time-averaged longitudinal velocity of the ship at constant forward speed. The second coordinate system is a right-handed coordinate system fixed to the ship with its origin placed at the ship's center of gravity (G), $\vec{\underline{x}} = [\underline{x}; \underline{y}; \underline{z}]^T$. Figure 3 shows exemplary both coordinate systems.

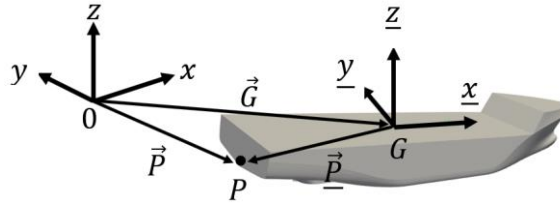


Figure 3: Visualization of the inertial ($\vec{x} = [x; y; z]^T$) and the body fixed ($\vec{\underline{x}} = [\underline{x}; \underline{y}; \underline{z}]^T$) coordinate system.

The position of a point \vec{P} at the ship hull in the inertial coordinate system is expressed as follows:

$$\vec{P} = \vec{G} + \mathbf{T}(\vec{\theta})\vec{\underline{P}} + \vec{w} \quad (1)$$

The first two components on the r.h.s. comprises contribution from rigid body motions, where \vec{G} is the position of ship's center of gravity in inertial coordinate system, $\vec{\underline{P}}$ is the position of the point in body fixed coordinate system and \mathbf{T} is the transformation matrix relating a vector in the body fixed coordinate system into the inertial coordinate system. Applying Tait-Bryans x-y-z sequence rotation order, \mathbf{T} follows from

$$\mathbf{T}(\vec{\theta}) = \begin{bmatrix} c(\theta)c(\psi) & -c(\theta)s(\psi) & s(\theta) \\ c(\varphi)s(\psi) + s(\varphi)s(\theta)c(\psi) & c(\varphi)c(\psi) - s(\varphi)s(\theta)s(\psi) & -s(\varphi)c(\theta) \\ s(\varphi)s(\psi) - c(\varphi)s(\theta)c(\psi) & s(\varphi)c(\psi) + c(\varphi)s(\theta)s(\psi) & c(\varphi)c(\theta) \end{bmatrix} \quad (2)$$

With $c(\theta) := \cos(\theta)$ and $s(\theta) := \sin(\theta)$. Due to Tait-Bryans x-y-z sequence rotation order, the vector of body rotations, $\vec{\theta} = (\varphi, \theta, \psi)^T$, includes the roll, pitch and yaw motion of the ship, respectively.

The third component, \vec{w} , on the r.h.s. of (1) is the displacement of the point \vec{P} due to elastic deflections of the ship structure in the inertial coordinate system. The following section describe the computation of the rigid body motions \vec{G} and $\vec{\theta}$ by applying a new weakly-nonlinear seakeeping solver.

2.2 Weakly-Nonlinear Wave-Induced Rigid Body Motions

The content in this section was published in Riesner et al. (2018a).

Often, seakeeping solvers based on potential theory solve the linear rigid body motions equations. The linearized equation of motion is based on the assumption that the rigid body rotations are small (less than 5deg). This assumption is often valid for wave induced ship motions in head waves. If the ship hull is port-starboard symmetric, only pitch motions but no roll and yaw motions occur (assuming no periodic roll motion). In such scenario the pitch motion is often less than 5deg. However, the presented new numerical method is intended to compute wave-induced forces and moments and the corresponding ship response in steep oblique waves. In such scenarios, coupled roll, pitch and yaw motions occur and their amplitudes, especially the roll amplitude, can exceed 5deg. A precise computation of the roll motion is important for the prediction of higher order resonant vibrations, because higher order wave induced forces and moments play a major role. For that reason, the new numerical method solved the nonlinear rigid body motion equations. From a mathematical point of few, superposing the nonlinear rigid body response with the linear hydroelastic response is questionable, because the superposition technique requires a linear system. However, using the nonlinear equation of motion improves the pressure

computation during roll motions, which is important for the computation of the torsional moment. A similar technique was applied by el Moctar et al. (2011), who coupled a Rans based CFD solver with a linear Timoshenko beam element model.

2.2.1 Nonlinear Motion Equations of a Rigid Body

The following kinematic and dynamic relation of a rigid body can be found in Woernle (2011). The motions of a rigid body in the inertial coordinate system is described by Newton's second law (Euler rigid body equation) as follows:

$$\frac{d}{dt}(m\dot{\vec{G}}) = \sum \vec{F} \quad (3)$$

$$\frac{d}{dt}(\mathbf{I}\vec{\Omega}) = \sum \vec{M} \quad (4)$$

where m is the ship's mass, \mathbf{I} is the ship's inertia tensor, $\dot{\vec{G}}$ is the velocity vector of rigid body translations, $\vec{\Omega}$ is the angular velocity vector of rigid body rotation, \vec{F} is the external force vector, \vec{M} is the external moment vector, and t is the time. Equation (4) relates the inertia tensor to the moments calculated about the ship's centre of gravity expressed in the inertial coordinate system. The ship's inertia tensor is only constant when expressed in the body coordinate system. The transformation matrix \mathbf{T} (see eq. (2)) relates the inertia tensor $\underline{\mathbf{I}}$ (in the body coordinate system) and the inertia tensor \mathbf{I} (in the inertial coordinate system) as follows:

$$\mathbf{I} = \mathbf{T}\underline{\mathbf{I}}\mathbf{T}^T \quad (5)$$

The angular momentum is then written as follows:

$$\mathbf{I}\vec{\Omega} = \mathbf{T}(\underline{\mathbf{I}}\vec{\Omega}) \quad (6)$$

$\underline{\vec{\Omega}} = \mathbf{T}^T\vec{\Omega}$ is the angular velocity in the body coordinate system. Inserting (6) into (4) results in

$$\frac{d}{dt}(\underline{\mathbf{I}}\underline{\dot{\boldsymbol{\Omega}}}) = \frac{d}{dt}(\underline{\mathbf{T}}\underline{\mathbf{I}}\underline{\dot{\boldsymbol{\theta}}}) = \dot{\underline{\mathbf{T}}}(\underline{\mathbf{I}}\underline{\dot{\boldsymbol{\theta}}}) + \underline{\mathbf{T}}\underline{\dot{\mathbf{I}}}\underline{\dot{\boldsymbol{\theta}}} \quad (7)$$

The angular velocity in body coordinates, $\underline{\dot{\boldsymbol{\Omega}}}$, can be described by the rate of change of the Euler angles, $\underline{\dot{\boldsymbol{\theta}}}$

$$\underline{\dot{\boldsymbol{\Omega}}} = \underline{\mathbf{H}}^{-1}\underline{\dot{\boldsymbol{\theta}}} \quad (8)$$

Here, $\underline{\mathbf{H}}^{-1}$ is a transformation matrix relating the angular velocity in body coordinates with the rate of change of the Euler angle

$$\underline{\mathbf{H}}^{-1}(\underline{\dot{\boldsymbol{\theta}}}) = \begin{bmatrix} 1 & 0 & -\sin(\theta) \\ 0 & \cos(\varphi) & \sin(\varphi)\cos(\theta) \\ 0 & -\sin(\varphi) & \cos(\varphi)\cos(\theta) \end{bmatrix} \quad (9)$$

The time derivative of $\underline{\dot{\boldsymbol{\Omega}}}$ follows from

$$\underline{\ddot{\boldsymbol{\Omega}}} = \underline{\dot{\mathbf{H}}}\underline{\dot{\boldsymbol{\theta}}} + \underline{\mathbf{H}}^{-1}\underline{\ddot{\boldsymbol{\theta}}} \quad (10)$$

Inserting (10) into (7) results in

$$(\dot{\underline{\mathbf{T}}}\underline{\mathbf{H}}^{-1} + \underline{\mathbf{T}}\underline{\dot{\mathbf{H}}}\underline{\mathbf{H}}^{-1})\underline{\dot{\boldsymbol{\theta}}} + \underline{\mathbf{T}}\underline{\mathbf{H}}^{-1}\underline{\ddot{\boldsymbol{\theta}}} = \sum \underline{\vec{M}} \quad (11)$$

Using matrix notation, equation (3) and (4) can be combined and result in the nonlinear equations of rigid body motions (in the inertial coordinate system)

$$\begin{bmatrix} m\underline{\mathbf{I}}_{3 \times 3} & \underline{\mathbf{0}}_{3 \times 3} \\ \underline{\mathbf{0}}_{3 \times 3} & \underline{\mathbf{T}}\underline{\mathbf{H}}\underline{\mathbf{H}}^{-1} \end{bmatrix} \begin{pmatrix} \underline{\ddot{\mathbf{G}}} \\ \underline{\ddot{\boldsymbol{\theta}}} \end{pmatrix} + \begin{bmatrix} \underline{\mathbf{0}}_{3 \times 3} & \underline{\mathbf{0}}_{3 \times 3} \\ \underline{\mathbf{0}}_{3 \times 3} & \dot{\underline{\mathbf{T}}}\underline{\mathbf{H}}\underline{\mathbf{H}}^{-1} + \underline{\mathbf{T}}\underline{\dot{\mathbf{H}}}\underline{\mathbf{H}}^{-1} \end{bmatrix} \begin{pmatrix} \underline{\dot{\mathbf{G}}} \\ \underline{\dot{\boldsymbol{\theta}}} \end{pmatrix} = \begin{pmatrix} \underline{\vec{F}} \\ \underline{\vec{M}} \end{pmatrix} \quad (12)$$

Where $\mathbf{I}_{3 \times 3}$ is the 3x3 identity matrix and $\mathbf{0}_{3 \times 3}$ a 3x3 zero matrix. The external force vector, \vec{F} , and moment vector, \vec{M} , are the hydrodynamic and hydrostatic forces and moments due to the incident wave and ship motions. The mathematical models to describe these forces and moments are described in the next subsection.

2.2.2 Hydrodynamic Forces and Moments at the Ship Hull

As discussed in the section 1.1, a weakly nonlinear hydrodynamic solver is based on linear hydrodynamic theory because it transfers linear frequency domain hydrodynamic coefficients into time domain using convolution integrals. After linearizing the governing equations for the computation of wave induced pressures at the hull, the total system can be split into the motion induced pressure and into the pressure induced by the incident wave. The forces and moments corresponding to the motion induced pressure are called radiation force and moments, \vec{F}_{Rad} and \vec{M}_{Rad} , and the forces and moments corresponding to the wave induced pressure are called excitation forces and moments, \vec{F}_E and \vec{M}_E . These force and moment components can further subdivide. The radiation forces and moments include components according to the ship acceleration, the ship velocity and the ship position. The two former components are hydrodynamic forces and moments and the latter are hydrostatic forces and moments (also called restoring force). To compute the hydrodynamic components, a flow problem has to be solved to fulfill the boundary conditions at the free surface and at the hull. The hydrostatic components can be computed without solving a flow problem. From here, the hydrodynamic radiation forces and moments are denoted as \vec{F}_{Rad} and \vec{M}_{Rad} . The hydrostatic radiation forces and moments are denoted as \vec{F}_{Hyd} and \vec{M}_{Hyd} . The excitation forces and moments can be divided into two components. The first component is called diffraction forces and moments, \vec{F}_{Dif} and \vec{M}_{Dif} , and results from the disturbance of the wave velocity field at the ship hull. The second component are called Froude-Krylov forces and moments, \vec{F}_{FK} and \vec{M}_{FK} , and accounts for the periodical change of the pressure underneath the free surface due to crest and trough of an undisturbed incoming waves. To compute diffraction forces and moments, the boundary conditions at the free surface and at the hull need to be fulfilled and thus a flow problem need to be solved. Assuming that Froude-Krylov forces and moments are computed based on an undisturbed wave, they can be computed without solving a flow

problem. Due to the above decomposition of forces and moments, the total hydrodynamic forces and moments follow from

$$\begin{aligned}\vec{F} &= \vec{F}_{Rad} + \vec{F}_{Dif} + \vec{F}_{FK+Hyd} \\ \vec{M} &= \vec{M}_{Rad} + \vec{M}_{Dif} + \vec{M}_{FK+Hyd}\end{aligned}\quad (13)$$

Here \vec{F}_{FK+Hyd} and \vec{M}_{FK+Hyd} comprises the forces and moments that can be computed without solving a flow problem, namely the hydrostatic and the Froude-Krylov forces and moments. The following subsections discuss the computation of each force and moment component.

2.2.2.1 Radiation Forces and Moments

As aforementioned, radiation forces and moments result from ship motions and thus can be interpreted as a response force or moment. If linear hydrodynamic theory and linear wave theory is applied (a theoretical description of linear hydrodynamic theory and linear wave theory is given in section 2.4), the free surface elevation oscillates harmonically and the ship respond with harmonic motions (if only the time average wetted hull surface is considered). For harmonic oscillations, radiation forces \vec{F}_{Rad} and moments \vec{M}_{Rad} can be computed by splitting the total force into one component due to body accelerations and one component due to the body velocity. In the body coordinate system, it follows

$$\begin{pmatrix} \vec{F}_{Rad} \\ \vec{M}_{Rad} \end{pmatrix} = -\underline{\mathbf{m}}(\omega_e) \begin{pmatrix} \ddot{\vec{G}} \\ \ddot{\vec{\Omega}} \end{pmatrix} - \underline{\mathbf{b}}(\omega_e) \begin{pmatrix} \dot{\vec{G}} \\ \dot{\vec{\Omega}} \end{pmatrix}\quad (14)$$

The first component on the r.h.s. describes forces and moments associated with the ship acceleration with $\underline{\mathbf{m}}(\omega_e)$ being the hydrodynamic added mass matrix. The second component on the r.h.s. describes forces and moments due to the ship velocity with $\underline{\mathbf{b}}(\omega_e)$ being the hydrodynamic damping matrix.

The hydrodynamic added mass and hydrodynamic damping are frequency dependent, consequently, equation (14) formally can only be applied for harmonic oscillations with a constant wave encounter frequency. However, as

aforementioned, the new numerical method considered nonlinear Froude-Krylov and hydrostatic forces and moments. Consequently, the ship response is not necessarily harmonic. Furthermore, such frequency dependent definition of radiation forces and moments cannot be applied for the computation of elastic vibrations because the vibration frequency is necessarily not equal to the wave encounter frequency.

Cummins (1962) and Ogilvie (1964) applied a convolution integral to model radiation forces of non-harmonic ship motions. Following this technique, the frequency independent radiation force was described by

$$\begin{pmatrix} \vec{F}_{Rad} \\ \vec{M}_{Rad} \end{pmatrix} = -\underline{\mathbf{C}}_1 \begin{pmatrix} \ddot{\vec{G}} \\ \dot{\vec{\Omega}} \end{pmatrix} - \underline{\mathbf{C}}_2 \begin{pmatrix} \dot{\vec{G}} \\ \vec{\Omega} \end{pmatrix} - \int_{-\infty}^t \underline{\mathbf{k}}(t - \tau) \begin{pmatrix} \dot{\vec{G}}(\tau) \\ \vec{\Omega}(\tau) \end{pmatrix} d\tau \quad (15)$$

Here, the convolution integral (third term on the r.h.s.) modelled the so-called memory effect of the radiation forces and moments and $\underline{\mathbf{k}}$ is a matrix including the impulse response functions, also called retardation functions, which includes the history of the radiation forces and moments at time t caused by a past ship motions at time τ . $\underline{\mathbf{C}}_1$ and $\underline{\mathbf{C}}_2$ are constants that describe components depending on the body acceleration and body velocity.

$\underline{\mathbf{C}}_1$, $\underline{\mathbf{C}}_2$ and $\underline{\mathbf{k}}$ were elaborated by assuming that for a pure harmonic oscillation, equation (15) and (14) give equivalent solutions. Applying a Fourier transformation on equation (14) and (15), it was shown by Ogilvie (1964) that the following relation holds true

$$\omega_e^2 \underline{\mathbf{m}}(\omega_e) - i\omega_e \underline{\mathbf{b}}(\omega_e) = \omega_e^2 \underline{\mathbf{C}}_1 - i\omega_e \underline{\mathbf{C}}_2 - i\omega_e \mathcal{F}_c\{\underline{\mathbf{k}}(t)\} - \omega_e \mathcal{F}_s\{\underline{\mathbf{k}}(t)\} \quad (16)$$

The Fourier transformation was split into the real and complex component by splitting the solution of the convolution integral into the sine, $\mathcal{F}_s\{\underline{\mathbf{k}}(t)\} = \frac{i}{\sqrt{2\pi}} \int \underline{\mathbf{k}}(t) \sin(\omega_e t) dt$, and cosine, $\mathcal{F}_c\{\underline{\mathbf{k}}(t)\} = \frac{1}{\sqrt{2\pi}} \int \underline{\mathbf{k}}(t) \cos(\omega_e t) dt$, solution. Comparing the real and complex components in equation (16) gives the following relations

$$\underline{\mathbf{m}}(\omega_e) = \underline{\mathbf{C}}_1 - \frac{1}{\omega_e} \mathcal{F}_s\{\underline{\mathbf{k}}(t)\} \quad (17)$$

$$\underline{\mathbf{b}}(\omega_e) = \underline{\mathbf{C}}_2 + \mathcal{F}_c\{\underline{\mathbf{k}}(t)\} \quad (18)$$

Computing the limit for $\lim_{\omega_e \rightarrow \infty} \underline{\mathbf{m}}(\omega_e)$ it follows

$$\underline{\mathbf{C}}_1 = \underline{\mathbf{m}}(\infty) \quad (19)$$

Applying the Riemann-Lebesgue lemma, it can be shown that

$$\lim_{\omega_e \rightarrow \infty} \int_0^{\infty} \underline{\mathbf{k}}(t) \cos(\omega_e t) dt = 0 \quad (20)$$

And from $\lim_{\omega_e \rightarrow \infty} \underline{\mathbf{b}}(\omega_e)$ follows that

$$\underline{\mathbf{C}}_2 = \underline{\mathbf{b}}(\infty) \quad (21)$$

Often, $\underline{\mathbf{b}}(\infty)$ was assumed to be zero, see e.g. King (1987), what is true for zero forward speed. However, it will be shown in section 2.4 that under forward speed, $\underline{\mathbf{b}}(\infty)$ is not necessarily zero.

Inserting equation (19) and (21) into (15) results in the frequency independent radiation forces and moments:

$$\begin{pmatrix} \vec{F}_{Rad} \\ \vec{M}_{Rad} \end{pmatrix} = -\underline{\mathbf{m}}(\infty) \begin{pmatrix} \ddot{\vec{G}} \\ \dot{\vec{\Omega}} \end{pmatrix} - \underline{\mathbf{b}}(\infty) \begin{pmatrix} \dot{\vec{G}} \\ \vec{\Omega} \end{pmatrix} - \int_{-\infty}^t \underline{\mathbf{k}}(t - \tau) \begin{pmatrix} \dot{\vec{G}} \\ \vec{\Omega} \end{pmatrix} d\tau \quad (22)$$

Here, $\underline{\mathbf{m}}(\infty)$ is a matrix including the hydrodynamic added mass for infinite frequency and $\underline{\mathbf{b}}(\infty)$ is a matrix including the hydrodynamic damping for infinite frequency.

Applying an inverse Fourier transformation on equation (17) and (18), $\underline{\mathbf{k}}$ can be computed based on hydrodynamic damping

$$\underline{\mathbf{k}}_{ij}(t) = \frac{2}{\pi} \int_0^{\infty} [\underline{\mathbf{b}}_{ij}(\omega_e) - \underline{\mathbf{b}}_{ij}(\infty)] \cos(\omega_e t) d\omega \quad (23)$$

or based on the hydrodynamic added mass

$$\underline{\mathbf{k}}_{ij}(t) = -\frac{2}{\pi} \int_0^{\infty} \omega_e [\underline{\mathbf{m}}_{ij}(\omega_e) - \underline{\mathbf{m}}_{ij}(\infty)] \sin(\omega_e t) d\omega \quad (24)$$

Thus, the impulse response function can be computed based on transfer functions of the hydrodynamic added mass or hydrodynamic damping. It will be explained in section 2.4 that Rankine sources were used to fulfil the boundary conditions at the hull and free surface. Consequently, the free surface was panelized and the grid needed to be refined according to increasing wave encounter frequencies. For that reason, the Rankine source boundary element method is limited to a certain maximum wave encounter frequency. At higher wave encounter frequencies, the computational time increases strongly and the computation becomes inefficient. For the present method computations were limited to a wave encounter frequency of approximately 2.5rad/s. However, to compute the impulse response function accurately, the upper integration limit in eq. (23) and (24) should be higher than 2.5rad/s. To account for higher wave encounter frequencies, equation (23) and (24) were split into a numerical integrated part for low and medium wave encounter frequencies and into an analytically integrated part up to infinite frequency. The analytical integration was based on Perez and Fossen (2008), who propose an expression for the asymptotic behavior of the damping coefficients and hydrodynamic added masses at high frequencies:

$$\underline{\mathbf{b}}_{ij}(\omega_e) - \underline{\mathbf{b}}_{ij}(\infty) \rightarrow \bar{\mathbf{b}}_{ij} \omega_e^{-2} - \bar{\bar{\mathbf{b}}}_{ij} \omega_e^{-4} \quad (25)$$

and

$$\underline{\mathbf{m}}_{ij}(\omega_e) - \underline{\mathbf{m}}_{ij}(\infty) \rightarrow \overline{\mathbf{m}}_{ij}\omega_e^{-2} - \overline{\overline{\mathbf{m}}}_{ij}\omega_e^{-4} \quad (26)$$

respectively. $\overline{\mathbf{b}}$, $\overline{\overline{\mathbf{b}}}$, $\overline{\mathbf{m}}$ and $\overline{\overline{\mathbf{m}}}$ are real constant coefficients describing the asymptotic behavior of hydrodynamic damping and hydrodynamic added mass up to infinite frequencies. In the present work, only the first and dominant term on the r.h.s. of equations (25) and (26) was used to develop an analytical integration for high wave encounter frequencies. Inserting the respective terms into equations (23) and (24) resulted in

$$\begin{aligned} \underline{\mathbf{k}}_{ij}(t) = & -\frac{2}{\pi} \int_0^{\omega_{max}} [\underline{\mathbf{m}}_{ij}(\omega_e) - \underline{\mathbf{m}}_{ij}(\infty)] \omega_e \sin(\omega_e t) d\omega \\ & + \frac{2}{\pi} \omega_{max}^2 [\underline{\mathbf{m}}_{ij}(\omega_{max}) - \underline{\mathbf{m}}_{ij}(\infty)] \left[Si(\omega_{max}t) - \frac{\pi}{2} \right] \end{aligned} \quad (27)$$

and

$$\begin{aligned} \underline{\mathbf{k}}_{ij}(t) = & \frac{2}{\pi} \int_0^{\omega_{max}} [\underline{\mathbf{b}}_{ij}(\omega_e) - \underline{\mathbf{b}}_{ij}(\infty)] \cos(\omega_e t) d\omega \\ & + \frac{2}{\pi} \omega_{max}^2 [\underline{\mathbf{b}}_{ij}(\omega_{max}) - \underline{\mathbf{b}}_{ij}(\infty)] \left[t Si(\omega_{max}t) - \frac{\pi t}{2} \right. \\ & \left. + \frac{\cos(\omega_{max}t)}{\omega_{max}} \right] \end{aligned} \quad (28)$$

Here, ω_{max} denotes the highest encounter angular frequency used in the frequency domain computations (approximately 2.5 rad/s). In equations (27) and (28), the calculation of $\underline{\mathbf{k}}_{ij}(t)$ was split into a numerically integrated part from $0 \leq \omega_e \leq \omega_{max}$ and an analytically integrated part for $\omega_e > \omega_{max}$. With the sine integral: $Si(x) = \int_0^x \sin(t)/t dt$.

Equation (22) describes radiation forces in the body fixed coordinate system. As aforementioned, rigid body motions were computed in the inertial coordinate system using equation (12). In the following paragraph, the radiation force in equation (22) is transferred from the body fixed coordinate system into the inertial coordinate system, starting with the first term of equation (22)

$$\begin{pmatrix} \underline{\vec{F}}_{Rad,1} \\ \underline{\vec{M}}_{Rad,1} \end{pmatrix} = -\underline{\mathbf{m}}(\infty) \begin{pmatrix} \underline{\dot{\vec{G}}} \\ \underline{\dot{\vec{\Omega}}} \end{pmatrix} \quad (29)$$

The translational body velocity expressed in the inertial coordinate system is related to the body velocity in the body fixed coordinate system through matrix transformation, $\underline{\dot{\vec{G}}} = \mathbf{T}\underline{\dot{\vec{G}}}$. The time derivative of this expression yields the relation between the translational accelerations expressed in the inertial coordinate system, $\underline{\ddot{\vec{G}}}$, and the accelerations expressed in body coordinate system, $\underline{\ddot{\vec{G}}}$:

$$\underline{\ddot{\vec{G}}} = \mathbf{T}^T \underline{\ddot{\vec{G}}} - \mathbf{T}^T \dot{\mathbf{T}} \mathbf{T}^T \underline{\dot{\vec{G}}} \quad (30)$$

The Matrix product $\dot{\mathbf{T}}\mathbf{T}^T$ can be replaced by a skew symmetric tensor

$$\underline{\tilde{\Omega}} = \dot{\mathbf{T}}\mathbf{T}^T = \begin{bmatrix} 0 & -\underline{\Omega}_z & \underline{\Omega}_y \\ \underline{\Omega}_z & 0 & -\underline{\Omega}_x \\ -\underline{\Omega}_y & \underline{\Omega}_x & 0 \end{bmatrix} \quad (31)$$

where $\underline{\Omega}_x$, $\underline{\Omega}_y$, and $\underline{\Omega}_z$ are angular velocities respect the body's axis \underline{x} , \underline{y} and \underline{z} . The relation between the rate of change of the Euler angles, $\underline{\dot{\theta}} = (\dot{\varphi}, \dot{\theta}, \dot{\psi})^T$, and the angular velocities in body coordinates, $\underline{\vec{\Omega}} = (\underline{\Omega}_x, \underline{\Omega}_y, \underline{\Omega}_z)^T$, was already given in equation (8), and, for the time derivative of the angular velocity in body coordinates, $\underline{\dot{\vec{\Omega}}}$, in equation (10). Inserting the above into (29) and using the transformation matrix to transform both from body coordinates to inertial coordinates results in

$$\begin{aligned} \begin{bmatrix} \underline{\vec{F}}_{Rad,1} \\ \underline{\vec{M}}_{Rad,1} \end{bmatrix} &= - \begin{bmatrix} \mathbf{T}\underline{\mathbf{m}}_{11}(\infty)\mathbf{T}^T & \mathbf{T}\underline{\mathbf{m}}_{12}(\infty)\mathbf{H}^{-1} \\ \mathbf{T}\underline{\mathbf{m}}_{21}(\infty)\mathbf{T}^T & \mathbf{T}\underline{\mathbf{m}}_{22}(\infty)\mathbf{H}^{-1} \end{bmatrix} \begin{bmatrix} \underline{\ddot{\vec{G}}} \\ \underline{\dot{\theta}} \end{bmatrix} \\ &\quad - \begin{bmatrix} -\mathbf{T}\underline{\mathbf{m}}_{11}(\infty)\mathbf{T}^T \underline{\tilde{\Omega}} & \mathbf{T}\underline{\mathbf{m}}_{12}(\infty)\mathbf{H}^{-1} \\ -\mathbf{T}\underline{\mathbf{m}}_{21}(\infty)\mathbf{T}^T \underline{\tilde{\Omega}} & \mathbf{T}\underline{\mathbf{m}}_{22}(\infty)\mathbf{H}^{-1} \end{bmatrix} \begin{bmatrix} \underline{\dot{\vec{G}}} \\ \underline{\dot{\theta}} \end{bmatrix} \end{aligned} \quad (32)$$

In equation (32), the hydrodynamic added mass matrix was split as follows

$$\underline{\mathbf{m}}(\infty) = \begin{bmatrix} \underline{\mathbf{m}}_{11}(\infty) & \underline{\mathbf{m}}_{12}(\infty) \\ \underline{\mathbf{m}}_{21}(\infty) & \underline{\mathbf{m}}_{22}(\infty) \end{bmatrix} \quad (33)$$

The second and third terms of (22) represents forces that depend on body velocities:

$$\begin{pmatrix} \vec{F}_{Rad,2} \\ \vec{M}_{Rad,2} \end{pmatrix} = -\underline{\mathbf{b}}(\infty) \begin{pmatrix} \dot{\underline{G}} \\ \dot{\underline{\Omega}} \end{pmatrix} - \int_{-\infty}^t \underline{\mathbf{k}}(t-\tau) \begin{pmatrix} \dot{\underline{G}}(\tau) \\ \dot{\underline{\Omega}}(\tau) \end{pmatrix} d\tau \quad (34)$$

Transforming equation (34) into the inertial coordinate system by applying the matrix transformation of equation (5) and the relation between the angular velocity in body coordinates and the rate of change of the Euler angles ,equation (8), it follows

$$\begin{pmatrix} \vec{F}_{Rad,2} \\ \vec{M}_{Rad,2} \end{pmatrix} = - \begin{bmatrix} \underline{\mathbf{T}}\underline{\mathbf{b}}_{11}(\infty)\mathbf{T}^T & \underline{\mathbf{T}}\underline{\mathbf{b}}_{12}(\infty)\mathbf{H}^{-1} \\ \underline{\mathbf{T}}\underline{\mathbf{b}}_{21}(\infty)\mathbf{T}^T & \underline{\mathbf{T}}\underline{\mathbf{b}}_{22}(\infty)\mathbf{H}^{-1} \end{bmatrix} \begin{bmatrix} \dot{\underline{G}} \\ \dot{\underline{\theta}} \end{bmatrix} - \int_{-\infty}^t \begin{bmatrix} \underline{\mathbf{T}}\underline{\mathbf{k}}_{11}(t-\tau)\mathbf{T}^T & \underline{\mathbf{T}}\underline{\mathbf{k}}_{12}(t-\tau)\mathbf{H}^{-1} \\ \underline{\mathbf{T}}\underline{\mathbf{k}}_{21}(t-\tau)\mathbf{T}^T & \underline{\mathbf{T}}\underline{\mathbf{k}}_{22}(t-\tau)\mathbf{H}^{-1} \end{bmatrix} \begin{bmatrix} \dot{\underline{G}}(\tau) \\ \dot{\underline{\theta}}(\tau) \end{bmatrix} d\tau \quad (35)$$

Combining equation (32) and (35), the total radiation force and moment vector in the inertial coordinate system follows as

$$\begin{pmatrix} \vec{F}_{Rad} \\ \vec{M}_{Rad} \end{pmatrix} = - \begin{bmatrix} \underline{\mathbf{T}}\underline{\mathbf{m}}_{11}(\infty)\mathbf{T}^T & \underline{\mathbf{T}}\underline{\mathbf{m}}_{12}(\infty)\mathbf{H}^{-1} \\ \underline{\mathbf{T}}\underline{\mathbf{m}}_{21}(\infty)\mathbf{T}^T & \underline{\mathbf{T}}\underline{\mathbf{m}}_{22}(\infty)\mathbf{H}^{-1} \end{bmatrix} \begin{bmatrix} \ddot{\underline{G}} \\ \ddot{\underline{\theta}} \end{bmatrix} - \begin{bmatrix} -\underline{\mathbf{T}}\underline{\mathbf{m}}_{11}(\infty)\mathbf{T}^T\tilde{\underline{\Omega}} + \underline{\mathbf{T}}\underline{\mathbf{b}}_{11}(\infty)\mathbf{T}^T & \underline{\mathbf{T}}\underline{\mathbf{m}}_{12}(\infty)\mathbf{H}^{-1} + \underline{\mathbf{T}}\underline{\mathbf{b}}_{12}(\infty)\mathbf{H}^{-1} \\ -\underline{\mathbf{T}}\underline{\mathbf{m}}_{21}(\infty)\mathbf{T}^T\tilde{\underline{\Omega}} + \underline{\mathbf{T}}\underline{\mathbf{b}}_{21}(\infty)\mathbf{T}^T & \underline{\mathbf{T}}\underline{\mathbf{m}}_{22}(\infty)\mathbf{H}^{-1} + \underline{\mathbf{T}}\underline{\mathbf{b}}_{22}(\infty)\mathbf{H}^{-1} \end{bmatrix} \begin{bmatrix} \dot{\underline{G}} \\ \dot{\underline{\theta}} \end{bmatrix} - \int_{-\infty}^t \begin{bmatrix} \underline{\mathbf{T}}\underline{\mathbf{k}}_{11}(t-\tau)\mathbf{T}^T & \underline{\mathbf{T}}\underline{\mathbf{k}}_{12}(t-\tau)\mathbf{H}^{-1} \\ \underline{\mathbf{T}}\underline{\mathbf{k}}_{21}(t-\tau)\mathbf{T}^T & \underline{\mathbf{T}}\underline{\mathbf{k}}_{22}(t-\tau)\mathbf{H}^{-1} \end{bmatrix} \begin{bmatrix} \dot{\underline{G}} \\ \dot{\underline{\theta}} \end{bmatrix}(\tau) d\tau \quad (36)$$

As already discussed, the new numerical method couples the fully nonlinear stationary forward speed flow with the oscillatory flow of a moving and vibration ship in waves. Based on Hachmann's approach (Hachmann (1991)), it was assumed that the stationary velocity field is attached to the ship hull and, thus, the stationary flow is constant in the body fixed coordinate system. Consequently, the stationary velocity field moves with the ship motion and generates restoring forces and moments additional to the classical hydrostatic restoring forces and moments. An additional component, based on a restoring matrix \underline{c} multiplied with the body translation and Euler angles, needs to be added to equation (36). A detailed explanation of the computation of \underline{c} is given in section 2.4.

As aforementioned, it was assumed that radiation forces and moments are dominated by convection effects and thus are pressure dominated. This assumption is not correct for roll-induced hydrodynamic moments. The roll-induced moment is affected by viscous damping. Such roll damping moment can be considered based on empirical approaches. Piehl (2016) gives a good summary of existing empirical roll damping approaches. The simplest approach is a linear damping model which computes the viscous roll damping moment with one damping coefficients multiplied with the roll angular velocity. More accurate but also more complex are higher order roll damping models that use further higher order components of a polynomial to describe the viscous roll moment. Some approaches additionally split the damping coefficients into individual contributions from different physical phenomena (Ikeda et al. (1978)) , e.g. friction, generation of eddies, contribution from bilge keels, etc..

Often, roll decay tests are performed and the damping coefficients are computed from a regression analysis of the measured decaying roll oscillation. In the present work, investigations of roll motions were performed for a 333m and 355m long container ship. It will be shown in chapter 4.4.1 that a linear roll damping approach is a good representation of the roll damping behaviour for such container ships. Similar was shown by Liu and Papanikolaou (2014). For the present method, the actual roll damping is related the critical roll damping. The critical roll damping coefficient follows from

$$b_{cr}(\omega) = 2\omega_{roll}(\underline{\mathbf{I}}_{11} + \underline{\mathbf{m}}_{44}(\omega_{roll})) \quad (37)$$

With the natural angular roll frequency, ω_{roll} , and the hydrodynamic added mass for roll, $\underline{\mathbf{m}}_{44}$. In equation (37), $\underline{\mathbf{m}}_{44}$ depends on the natural angular roll frequency. Usually the hydrodynamic added mass varies significantly for low angular frequencies and less strongly for moderate and high frequencies (asymptotic behavior of the hydrodynamic added mass for high frequencies). Thus, the actual frequency independent roll damping coefficient was computed based on the hydrodynamic added mass at infinite frequency and follows from

$$b_{roll} = 2b_{\phi}\omega_{roll}(\underline{\mathbf{I}}_{11} + \underline{\mathbf{m}}_{44}(\infty)) \quad (38)$$

b_{ϕ} describes the relation between the critical roll damping and the actual roll damping. For seagoing ships b_{ϕ} is often between 0.01 and 0.05, depending on the forward speed (higher forward speed results in higher damping). In chapter 4.4.1, b_{ϕ} will be computed explicitly for a 355m long container ship. To include viscous damping into equation (35), a viscous damping matrix was defined:

$$\underline{\mathbf{b}}_{visc.} = \begin{bmatrix} b_{roll} & 0 & 0 \\ 0 & 0 & 0 \\ 0 & 0 & 0 \end{bmatrix} \quad (39)$$

Combining equation (36) and (39) and including the additional restoring component based on the restoring matrix $\underline{\mathbf{c}}$ results in the following expression for the radiation forces and moments in the inertial coordinate system

$$\begin{aligned} \vec{F}_{Rad} &= - \begin{bmatrix} \underline{\mathbf{Tm}}_{11}(\infty)\mathbf{T}^T & \underline{\mathbf{Tm}}_{12}(\infty)\mathbf{H}^{-1} \\ \underline{\mathbf{Tm}}_{21}(\infty)\mathbf{T}^T & \underline{\mathbf{Tm}}_{22}(\infty)\mathbf{H}^{-1} \end{bmatrix} \begin{bmatrix} \ddot{\vec{G}} \\ \ddot{\vec{\theta}} \end{bmatrix} \\ &- \begin{bmatrix} \underline{\mathbf{Tb}}_{11}(\infty)\mathbf{T}^T - \underline{\mathbf{Tm}}_{11}(\infty)\mathbf{T}^T\tilde{\mathbf{\Omega}} & \underline{\mathbf{Tb}}_{12}(\infty)\mathbf{H}^{-1} + \underline{\mathbf{Tm}}_{12}(\infty)\mathbf{H}^{-1} \\ \underline{\mathbf{Tb}}_{21}(\infty)\mathbf{T}^T - \underline{\mathbf{Tm}}_{21}(\infty)\mathbf{T}^T\tilde{\mathbf{\Omega}} & \underline{\mathbf{T}}(\underline{\mathbf{b}}_{22}(\infty) + \underline{\mathbf{b}}_{visc.})\mathbf{H}^{-1} + \underline{\mathbf{Tm}}_{22}(\infty)\mathbf{H}^{-1} \end{bmatrix} \begin{bmatrix} \dot{\vec{G}} \\ \dot{\vec{\theta}} \end{bmatrix} \\ &- \int_{-\infty}^t \begin{bmatrix} \underline{\mathbf{Tk}}_{11}(t-\tau)\mathbf{T}^T & \underline{\mathbf{Tk}}_{12}(t-\tau)\mathbf{H}^{-1} \\ \underline{\mathbf{Tk}}_{21}(t-\tau)\mathbf{T}^T & \underline{\mathbf{Tk}}_{22}(t-\tau)\mathbf{H}^{-1} \end{bmatrix} \begin{bmatrix} \dot{\vec{G}} \\ \dot{\vec{\theta}} \end{bmatrix}(\tau)d\tau - \begin{bmatrix} \vec{0} & \underline{\mathbf{Tc}}_{12}\mathbf{T}^T \\ \vec{0} & \underline{\mathbf{Tc}}_{22}\mathbf{T}^T \end{bmatrix} \begin{bmatrix} \vec{G} \\ \vec{\theta} \end{bmatrix} \end{aligned} \quad (40)$$

2.2.2.2 Diffraction Forces and Moments

Diffraction forces and moments, \vec{F}_{Dif} and \vec{M}_{Dif} , were calculated using the complex diffraction force amplitudes, $\hat{F}_{Dif}(\omega)$ and $\hat{M}_{Dif}(\omega)$, resulting from the linear hydrodynamic flow problem of the incident wave. A description of the computation of the linear wave induced pressure acting at the ship hull is given in section 2.4. To calculate complex diffraction force and moment amplitudes in frequency domain, the ship is fixed. However, in time domain simulations, the ship will oscillate relative to the incident waves. Average low-frequency motions (drift motions) are avoided by the combined action of a system of soft springs. As a result, the ship executes these low-frequency motions at the beginning of a simulation until the time average hydrodynamic forces and time average spring forces attain about the same magnitude acting in opposite directions. The time average position of the ship then differs from its initial position, and the relative motion between the incident waves and the ship results in a time dependent shift of phase angle shift, $\Delta\varphi_D$, between the incident wave and the diffraction forces acting on the hull.

Figure 4 illustrates the position of the ship with its body fixed coordinate system relative to the incoming wave. The inertial coordinate system is at the position, where the ship's centre of gravity (origin of the body fixed coordinate system) was located at the beginning of the simulation. A wave coordinate system, $\vec{x}_w = (x_w, y_w, z_w)^T$ defines the direction of wave traveling. Its origin is identical to the origin of the inertial coordinate system, but its x-axis points in the direction of wave propagation. The vector $\vec{r}_w = (r_{w,x}, r_{w,y}, r_{w,z})^T$ is the position vector of the ship's centre of gravity expressed in the wave's coordinate system and λ is the wave length.

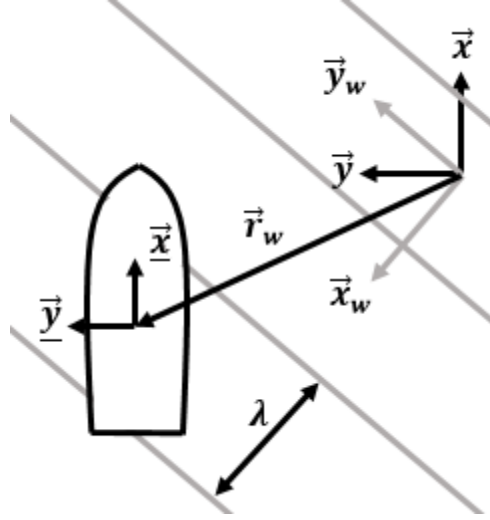


Figure 4: Visualization of the wave coordinate system.

Phase angle shift, $\Delta\varphi_D(t)$, is related to wave length, λ , and to the x -component of ship position vector, $r_{w,x}$, expressed in the wave coordinate system. $\Delta\varphi_D(t)$ results from

$$\Delta\varphi_D = 2\pi \frac{r_{w,x}}{\lambda} \quad (41)$$

The diffraction force vector in inertial coordinates, $\vec{F}_{Dif}(t)$, results from

$$\vec{F}_{Dif}(t) = \mathbf{T} \operatorname{Re} \left[\hat{\vec{F}}_{Dif} e^{i\omega_e t + \Delta\varphi_D} \right] \quad (42)$$

and the diffraction moment vector, $\vec{M}_{Dif}(t)$ from

$$\vec{M}_{Dif}(t) = \mathbf{T} \operatorname{Re} \left[\hat{\vec{M}}_{Dif} e^{i\omega_e t + \Delta\varphi_D} \right] \quad (43)$$

Re designates that only the real component of the content in brackets was applied.

2.2.2.3 Combined Froude-Krylov and Hydrostatic Forces and Moments

The combined Froude–Krylov and hydrostatic forces, \vec{F}_{FK+Hyd} , and moments, \vec{M}_{FK+Hyd} , were determined by integrating the pressure, p_{FK+Hyd} , under an undisturbed wave (considering the Smith effect) over the instantaneous wetted surface, taking into account the wave elevation, the rigid and elastic ship motions, and the stationary wave system caused by the steady forward speed in calm water. Consequently, \vec{F}_{FK} and \vec{M}_{FK} were calculated as follows:

$$\vec{F}_{FK+Hyd} = \mathbf{T} \int_S p_{FK+Hyd} \vec{n} dS \quad (44)$$

$$\vec{M}_{FK+Hyd} = \mathbf{T} \int_S p_{FK+Hyd} (\vec{x} \times \vec{n}) dS \quad (45)$$

The pressure, p_{FK} , due to an incoming wave was calculated based on linear wave theory, see equation (210). The ship hull was discretised by triangular panels and equation (44) and (45) were numerically integrated by assuming a constant pressure p_{FK+Hyd} over one body panels. An adaptive grid technique was developed to account for panels that intersect with the free surface. A detailed description of the spatial discretization is given in section 2.5.

2.2.2.4 Radiation and Diffraction Forces due to the Changing Wetted Surface

It was already discussed in the literature study that geometrical nonlinearities have a significant influence on higher order wave induced force and moment components and affect the rigid body and elastic response strongly. As aforementioned, a linear frequency domain boundary element method yielded radiation and diffraction pressures (see section 2.4), which are then transferred into the time domain. Consequently, the corresponding forces and moments were computed by integrating the radiation and diffraction pressure over the mean wetted surface of the hull, neglecting variations of hull submergence caused by the incident wave and the ship motions an elastic deformation. To account for the effect of the changing wetted surface on radiation and diffraction force and

moments, a modified approximation of the changing wetted surface according to Boese (1970) was developed.

Relative motions between the free surface and the hull as well as the associated pressure distribution on the hull surface were approximated from the first order pressure at the mean waterline. Söding et al. (2014) implemented a similar approach into a linear frequency domain boundary element method to successfully calculate time average drift forces. However, the present technique calculates the effect of the changing wetted surface in time domain. At a typical ship section shown in Figure 5, the relative motion between the free surface and the hull is the distance d measured from the mean water surface, \overline{WL} , to the instantaneous wave elevation, WL . The pressure at the hull is p ; the pressure at the mean water line, $p_{\overline{WL}}$. A linear frequency domain calculation neglects pressures within the red colored triangle.

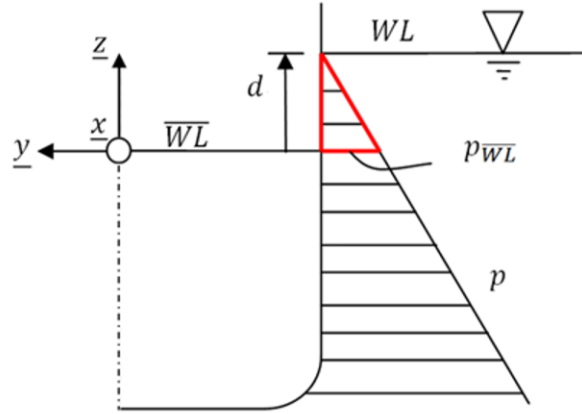


Figure 5: Ship section with mean water level and instantaneous wave elevation, Boese (1970)

Assuming a linear pressure distribution between the mean water surface, \overline{WL} , and the instantaneous wave elevation, WL , the corresponding force, \vec{F}_{WL} , and moment, \vec{M}_{WL} , summed over all waterline panels are calculated as follows, see e.g. Söding et al. (2014):

$$\vec{F}_{WL} = \sum_{WL_Panels} \frac{p_{\overline{WL}}^2 \vec{s} \times (\vec{n} \times \vec{s})}{2 \rho g (\vec{n} \times \vec{s})_3} \quad (46)$$

$$\vec{M}_{WL} = \sum_{WL_Panels} \vec{P} \times \frac{p_{WL}^2 \vec{s} \times (\vec{n} \times \vec{s})}{2 \rho g (\vec{n} \times \vec{s})_3} \quad (47)$$

A waterline panel (*WL_Panel*) is a triangular body panel having two of its three corners at the mean waterline, \vec{s} is the vector between these two corners, and index 3 designates the third component (vertical) of the resulting vector. In a linear frequency domain method, p_{wl} is the sum of the pressure contributions from radiation (including restoring), diffraction, and Froude-Krylov. However, the new numerical weakly nonlinear time domain method already integrates Froude-Krylov and hydrostatic pressures over the instantaneous wetted surface. Therefore, only coupling effects between these pressure contributions were considered in the waterline integral, and this leads to the following expression:

$$p_{WL}^2 = p_{Rad}^2 + p_{Dif}^2 + 2 p_{Rad} p_{Dif} + 2 p_{Rad} p_{FK+Hyd} + 2 p_{Dif} p_{FK+Hyd} \quad (48)$$

The first two terms on the right hand side of (48) result directly from radiation and diffraction and, had linear Froude-Krylov forces been used (instead of the nonlinear Froude-Krylov forces integrated over the instantaneous wetted surface), (48) would also include a term p_{FK+Hyd}^2 . The last three terms on the right hand side of (48) account for coupling effects between pressures caused by radiation, diffraction, and the combined Froude-Krylov and hydrostatic effects. Pressure p_{Dif} is calculated from the frequency domain results (see section 2.4), similar to equation (42) applied over every waterline panel and p_{Rad} is the radiation pressure. Pressure $p_{Rad}(t)$ is calculated using convolution integrals in a manner similar to the calculation of total radiation forces and moments acting on the ship; see (22). Accounting for contributions from all six rigid body motions, p_{Rad} is calculated as follows:

$$\vec{p}_{Rad} = -\vec{\tilde{m}}(\infty) \cdot \left(\frac{\ddot{\vec{G}}}{\dot{\vec{\Omega}}} \right) - \vec{\tilde{b}}(\infty) \cdot \left(\frac{\dot{\vec{G}}}{\dot{\vec{\Omega}}} \right) - \int_0^t \vec{\tilde{k}}(t - \tau) \cdot \left(\frac{\dot{\vec{G}}}{\dot{\vec{\Omega}}} \right) (\tau) d\tau \quad (49)$$

The radiation forces and moments in (22) act over the entire ship, whereas (49) stands for the radiation pressure acting at a single water line panel. Therefore,

$\underline{\tilde{m}}(\infty) \cdot \begin{pmatrix} \ddot{\vec{G}} \\ \dot{\vec{\Omega}} \end{pmatrix}$ and $\underline{\tilde{b}}(\infty) \cdot \begin{pmatrix} \dot{\vec{G}} \\ \vec{\Omega} \end{pmatrix}$ are here pressure-induced components of added mass and damping and $\underline{\tilde{k}}(t)$ accounts for the time history of the pressure. Here $\underline{\tilde{m}}(\infty)$, $\underline{\tilde{b}}(\infty)$, and $\underline{\tilde{k}}(t)$ are vectors and multiplied by the velocity and acceleration vector using the scalar product. The computation of $\underline{\tilde{m}}$ and $\underline{\tilde{b}}$ based on a frequency domain boundary element method is explained in section 2.4.

The impulse response function $\underline{\tilde{k}}(t)$ is calculated similarly to (27) and (28). The memory storage necessary to calculate pressures acting on one waterline panel is six times less than the memory storage to calculate the radiation forces and moments acting on the hull using (22). Nevertheless, the coefficients in (49) need to be stored for every waterline panel, whereas (22) already includes the radiation response of the complete ship.

2.2.3 Nonlinear Rigid Body Motion Equations with Weakly-Nonlinear Hydrodynamic Forces

The nonlinear equation of rigid body motions was discussed in section 2.2.1, see equation (12), and the external hydrodynamic forces and moments were discussed in section 2.2.2. The diffraction force and moments and the combined Froude-Krylov and hydrostatic forces and moments were treated as external forces on the r.h.s. of the equation of motion. However, the radiation forces and moments can be interpreted as a system response and, thus, are introduced to the l.h.s. of the equation of motions. Inserting the radiation forces on the l.h.s. of equation (12) results in

$$\begin{aligned} \mathbf{m}(\vec{\theta}) \begin{pmatrix} \ddot{\vec{G}} \\ \ddot{\vec{\theta}} \end{pmatrix} + \mathbf{b}(\vec{\theta}) \begin{pmatrix} \dot{\vec{G}} \\ \dot{\vec{\theta}} \end{pmatrix} + \int_{-\infty}^t \mathbf{k}(\vec{\theta}, t - \tau) \begin{pmatrix} \dot{\vec{G}} \\ \dot{\vec{\theta}} \end{pmatrix}(\tau) d\tau + \mathbf{c}(\vec{\theta}) \begin{pmatrix} \vec{G} \\ \vec{\theta} \end{pmatrix} \\ = \begin{pmatrix} \vec{F}_{Dif} \\ \vec{M}_{Dif} \end{pmatrix} + \begin{pmatrix} \vec{F}_{WL} \\ \vec{M}_{WL} \end{pmatrix} + \begin{pmatrix} \vec{F}_{FK+Hyd} \\ \vec{M}_{FK+Hyd} \end{pmatrix} \end{aligned} \quad (50)$$

The coefficient matrixes \mathbf{m} , \mathbf{b} , \mathbf{k} and \mathbf{c} depend on the current Euler angles $\vec{\theta}$ with

$$\mathbf{m}(\vec{\theta}) = \begin{bmatrix} \mathbf{T} \left(m\mathbf{I}_{3 \times 3} + \underline{\mathbf{m}}_{11}(\infty) \right) \mathbf{T}^T & \underline{\mathbf{Tm}}_{12}(\infty) \mathbf{H}^{-1} \\ \underline{\mathbf{Tm}}_{21}(\infty) \mathbf{T}^T & \mathbf{T} \left(\mathbf{I} + \underline{\mathbf{m}}_{22}(\infty) \right) \mathbf{H}^{-1} \end{bmatrix} \quad (51)$$

$$\mathbf{b}(\vec{\theta}) = \begin{bmatrix} \mathbf{b}_{11} & \mathbf{b}_{12} \\ \mathbf{b}_{21} & \mathbf{b}_{22} \end{bmatrix} \quad (52)$$

$$\mathbf{k}(\vec{\theta}, t) = \begin{bmatrix} \underline{\mathbf{T}}\mathbf{k}_{11} \mathbf{T}^T & \underline{\mathbf{T}}\mathbf{k}_{12} \mathbf{H}^{-1} \\ \underline{\mathbf{T}}\mathbf{k}_{21} \mathbf{T}^T & \underline{\mathbf{T}}\mathbf{k}_{22} \mathbf{H}^{-1} \end{bmatrix} \quad (53)$$

$$\mathbf{c}(\vec{\theta}) = \begin{bmatrix} \vec{0} & \underline{\mathbf{T}}\mathbf{c}_{12} \mathbf{T}^T \\ \vec{0} & \underline{\mathbf{T}}\mathbf{c}_{22} \mathbf{T}^T \end{bmatrix} \quad (54)$$

The components of matrix \mathbf{b} are read as follows

$$\mathbf{b}_{11} = \underline{\mathbf{T}}\mathbf{b}_{11}(\infty) \mathbf{T}^T - \underline{\mathbf{Tm}}_{11}(\infty) \mathbf{T}^T \tilde{\mathbf{\Omega}} \quad (55)$$

$$\mathbf{b}_{12} = \underline{\mathbf{T}}\mathbf{b}_{12}(\infty) \mathbf{H}^{-1} + \underline{\mathbf{Tm}}_{12}(\infty) \mathbf{H}^{-1} \quad (56)$$

$$\mathbf{b}_{21} = \underline{\mathbf{T}}\mathbf{b}_{21}(\infty) \mathbf{T}^T - \underline{\mathbf{Tm}}_{21}(\infty) \mathbf{T}^T \tilde{\mathbf{\Omega}} \quad (57)$$

$$\mathbf{b}_{22} = \dot{\underline{\mathbf{T}}}\mathbf{H}^{-1} + \underline{\mathbf{T}}\dot{\mathbf{H}}^{-1} + \underline{\mathbf{T}}(\mathbf{b}_{22}(\infty) + \underline{\mathbf{b}}_{visc.}) \mathbf{H}^{-1} + \underline{\mathbf{Tm}}_{22}(\infty) \mathbf{H}^{-1} \quad (58)$$

Equation (50) was solved using the implicit Euler method. Consequently, the convolution integral includes one component, $\underline{\mathbf{k}}_{ij}^0$, that depends on the next unknown time step $n + 1$ and all other components, $\underline{\mathbf{k}}_{ij}^{a-d}$, that can be precomputed based on the solution of the previous time steps. Thus, the convolution integral can be numerically computed as follows

$$\int_{-\infty}^t \mathbf{k} \begin{pmatrix} \dot{\vec{G}} \\ \dot{\vec{\theta}} \end{pmatrix} (\tau) d\tau = \begin{bmatrix} \Delta t \mathbf{T}\underline{\mathbf{k}}_{11}^{(0)} \mathbf{T}^T & \Delta t \mathbf{T}\underline{\mathbf{k}}_{12}^{(0)} \mathbf{H}^{-1} \\ \Delta t \mathbf{T}\underline{\mathbf{k}}_{21}^{(0)} \mathbf{T}^T & \Delta t \mathbf{T}\underline{\mathbf{k}}_{22}^{(0)} \mathbf{H}^{-1} \end{bmatrix} \begin{pmatrix} \dot{\vec{G}} \\ \dot{\vec{\theta}} \end{pmatrix} + \vec{s} \quad (59)$$

The first component in equation (59) includes contributions of the next, unknown time step. The second component on the r.h.s. comprises the solution of the precomputed convolution integral that considers all contributions of the past:

$$\vec{s} = \Delta t \sum_{d=lu}^{lo-1} \begin{bmatrix} \mathbf{T}\underline{\mathbf{k}}_{11}^{(a-d)} \mathbf{T}^T & \mathbf{T}\underline{\mathbf{k}}_{12}^{(a-d)} \mathbf{H}^{-1} \\ \mathbf{T}\underline{\mathbf{k}}_{21}^{(a-d)} \mathbf{T}^T & \mathbf{T}\underline{\mathbf{k}}_{22}^{(a-d)} \mathbf{H}^{-1} \end{bmatrix} \begin{pmatrix} \dot{\vec{G}} \\ \dot{\vec{\theta}} \end{pmatrix}_{(j-a+1)} \quad (60)$$

Δt is the time step size, a is the length of the impulse response function $\underline{\mathbf{k}}$ divided by Δt , lu is the furthest time instant of the past considered by the convolution integral, and lo is the current instant of time.

The component of the convolution integral that includes the contribution of the next time step has to be included on the l.h.s. of the equation of motion and will later be part of the coefficient matrix to solve the system of equations. The precomputed components, \vec{s} , can be placed on the r.h.s. of the equation of motion. Combining all above force components, the nonlinear equation of motion reads as

$$\begin{aligned} \mathbf{m}(\vec{\theta}) \begin{pmatrix} \ddot{\vec{G}} \\ \ddot{\vec{\theta}} \end{pmatrix} + \mathbf{b}(\vec{\theta}) \begin{pmatrix} \dot{\vec{G}} \\ \dot{\vec{\theta}} \end{pmatrix} + \mathbf{c}(\vec{\theta}) \begin{pmatrix} \vec{G} \\ \vec{\theta} \end{pmatrix} \\ = -\vec{s}(\vec{\theta}) + \begin{pmatrix} \vec{F}_{Dif} \\ \vec{M}_{Dif} \end{pmatrix} + \begin{pmatrix} \vec{F}_{WL} \\ \vec{M}_{WL} \end{pmatrix} + \begin{pmatrix} \vec{F}_{FK+Hyd} \\ \vec{M}_{FK+Hyd} \end{pmatrix} \end{aligned} \quad (61)$$

The components of \mathbf{b} were now extended with the contribution from the convolution integral and reads as follows

$$\mathbf{b}_{11} = \mathbf{T}\underline{\mathbf{b}}_{11}(\infty) \mathbf{T}^T + \Delta t \mathbf{T}\underline{\mathbf{k}}_{11}^{(0)} \mathbf{T}^T - \mathbf{T}\underline{\mathbf{m}}_{11}(\infty) \mathbf{T}^T \tilde{\Omega} \quad (62)$$

$$\mathbf{b}_{12} = \mathbf{T}\underline{\mathbf{b}}_{12}(\infty)\mathbf{H}^{-1} + \Delta t \mathbf{T}\underline{\mathbf{k}}_{12}^{(0)}\mathbf{H}^{-1} + \mathbf{T}\underline{\mathbf{m}}_{12}(\infty)\dot{\mathbf{H}}^{-1} \quad (63)$$

$$\mathbf{b}_{21} = \mathbf{T}\underline{\mathbf{b}}_{21}(\infty)\mathbf{T}^T + \Delta t \mathbf{T}\underline{\mathbf{k}}_{21}^{(0)}\mathbf{T}^T - \mathbf{T}\underline{\mathbf{m}}_{21}(\infty)\mathbf{T}^T\tilde{\boldsymbol{\Omega}} \quad (64)$$

$$\begin{aligned} \mathbf{b}_{22} = \mathbf{T}(\underline{\mathbf{b}}_{22}(\infty) + \underline{\mathbf{b}}_{visc.})\mathbf{H}^{-1} + \Delta t \mathbf{T}\underline{\mathbf{k}}_{22}^{(0)}\mathbf{H}^{-1} + \dot{\mathbf{T}}\underline{\mathbf{I}}\mathbf{H}^{-1} + \mathbf{T}\underline{\mathbf{I}}\dot{\mathbf{H}}^{-1} \\ + \mathbf{T}\underline{\mathbf{m}}_{22}(\infty)\mathbf{H}^{-1} \end{aligned} \quad (65)$$

As aforementioned, equation (61) was solve using the implicit Euler method. The displacement and velocity of the body are the sum of the result of the last time step, n , and the product of the time step size with a function depending on the parameters of the next time step $n + 1$:

$$\begin{pmatrix} \vec{G} \\ \vec{\theta} \end{pmatrix}_{n+1} = \begin{pmatrix} \vec{G} \\ \vec{\theta} \end{pmatrix}_n + \Delta t f(t_{n+1}, \vec{G}_{n+1}, \vec{\theta}_{n+1}) \quad (66)$$

$$\begin{pmatrix} \dot{\vec{G}} \\ \dot{\vec{\theta}} \end{pmatrix}_{n+1} = \begin{pmatrix} \dot{\vec{G}} \\ \dot{\vec{\theta}} \end{pmatrix}_n + \Delta t f(t_{n+1}, \dot{\vec{G}}_{n+1}, \dot{\vec{\theta}}_{n+1}) \quad (67)$$

Using the linear numerical derivative of the accelerations and velocities to obtain the displacements it follows

$$\begin{pmatrix} \dot{\vec{G}} \\ \dot{\vec{\theta}} \end{pmatrix}_{n+1} = \frac{1}{\Delta t} \left[\begin{pmatrix} \vec{G} \\ \vec{\theta} \end{pmatrix}_{n+1} - \begin{pmatrix} \vec{G} \\ \vec{\theta} \end{pmatrix}_n \right] \quad (68)$$

$$\begin{pmatrix} \ddot{\vec{G}} \\ \ddot{\vec{\theta}} \end{pmatrix} = \frac{1}{\Delta t} \left[\begin{pmatrix} \dot{\vec{G}} \\ \dot{\vec{\theta}} \end{pmatrix}_{n+1} - \begin{pmatrix} \dot{\vec{G}} \\ \dot{\vec{\theta}} \end{pmatrix}_n \right] \quad (69)$$

The system of equations to solve displacements and velocities follows as

$$\begin{bmatrix} \mathbf{I}_{6 \times 6} & -\Delta t \mathbf{I}_{6 \times 6} \\ \mathbf{c} & I_{6 \times 6} + \Delta t \mathbf{m}^{-1} \mathbf{b} \end{bmatrix} \begin{pmatrix} \begin{pmatrix} \vec{G} \\ \vec{\theta} \end{pmatrix}_{n+1} \\ \begin{pmatrix} \dot{\vec{G}} \\ \dot{\vec{\theta}} \end{pmatrix}_{n+1} \end{pmatrix} = \begin{pmatrix} \begin{pmatrix} \vec{G} \\ \vec{\theta} \end{pmatrix}_n \\ \begin{pmatrix} \dot{\vec{G}} \\ \dot{\vec{\theta}} \end{pmatrix}_n \end{pmatrix} \quad (70)$$

$$+ \begin{pmatrix} \vec{0} \\ \Delta t \mathbf{m}^{-1} \left[-\vec{s} + \begin{pmatrix} \vec{F}_{Dif} \\ \vec{M}_{Dif} \end{pmatrix} + \begin{pmatrix} \vec{F}_{WL} \\ \vec{M}_{WL} \end{pmatrix} + \begin{pmatrix} \vec{F}_{FK+Hyd} \\ \vec{M}_{FK+Hyd} \end{pmatrix} \right] \end{pmatrix}$$

Displacements and velocities are solved simultaneously, thus the matrix on the l.h.s. of equation (70) is of size 12 x 12. $I_{6 \times 6}$ is the 6x6 identity matrix. The waterline forces and moments and the combined Froude-Krylov and hydrostatic forces and moments depend on the current body displacement. An internal iteration loop ensures an accurate convergence. Usually, more than three iterations were not necessary. Recall that \mathbf{m} , \mathbf{b} and \mathbf{c} includes transformation matrixes $\mathbf{T}(\vec{\theta})$, $\mathbf{H}^{-1}(\vec{\theta})$, $\dot{\mathbf{T}}(\vec{\theta})$ and $\dot{\mathbf{H}}^{-1}(\vec{\theta})$ and that all of these matrixes depend on the instantaneous Euler angles ($\vec{\theta}$). Consequently, the system of equations is nonlinear. To solve equation (70), all transformation matrixes were computed based on the Euler angles of the previous time step. During the internal iteration loop, the transformation matrixes were updated and an accurate convergence was ensured. After the new displacements and velocities of the time step n+1 were solved, the new accelerations were computed applying equation (69).

2.3 Weakly-Nonlinear Wave-Induced Elastic Deformations

The following chapter describes the new mathematical formulation to compute global elastic structural deformation of ships. The content of this section was published in Riesner and el Moctar (2021a, 2021b).

The structural behavior of local ship components, e.g. single hull plates, affect the global elastic response only minimally. For that reason, as already discussed in the literature study (see chapter 0), finite element beam theory was applied for the new hydroelastic solver. Finite element beam theory was proven to

adequately represent the global ships structural behavior and to allow a numerically efficient computation of springing induced vibrations.

A ship hull is a so-called thin-walled girder (in beam theory terminology), consisting of thin plates that are typically combined to closed or open cells. The left side of Figure 11 shows the portside of a simplified ship cross section, where the double body is made of two closed cells and the side wall is a so-called open cell. To describe the structural properties of such cross sections, advanced beam theory has to be applied.

The left side of Figure 6 shows the portside of a simplified container ship cross section that is loaded with containers. G designates the center of gravity of the ship considering cargo. As aforementioned, rigid body rotations are described by rotations around the center of gravity. Elastic deformations are usually not described respect the center of gravity. According to the Euler-Bernoulli or Timoshenko beam theory of straight beams (Timoshenko and Goodier (1970)), bending deformations are often described respect the neutral bending axis of the cross section. The coordinate system N with its longitudinal, \underline{x} , horizontal, \underline{y} and vertical, \underline{z} , axis designates the neutral bending axis of the simplified ship cross section. Based on torsional theory for thin-walled girder, see e.g. Vlasov (1961), the shear center is the pole of torsion induced twist. Thus, elastic deformations induced by torsion are usually described respect a coordinate system located at the shear center of the cross section. Recall that ship cross sections are characterized by open and closed cells and that the shear center can be located significantly below the keel line. The coordinate system, S , with its longitudinal, \underline{x} , horizontal, \underline{y} , and vertical, \underline{z} , axis designates the shear center of the simplified ship cross section. χ is the torsion induced twist angle. The right side of Figure 6 illustrates the new position of the center of gravity, G' , the intersection of the neutral bending axis, N' , and the shear center S' due to a combined torsion induced twist, χ , and horizontal bending induced translation, $w_{B,y+S,y}$ (in this case negative for a clear visualization), of the cross section. It can be seen that a twist motion initiates a horizontal displacement of N and G . Vice versa a horizontal bending motion initiates a torsional moment. The corresponding coupling terms contribute to the kinetic energy and strain energy of the deformed beam and thus are part of the mass matrix and stiffness matrix., see also Senjanović et al. (2009) and Pavazza (2005).

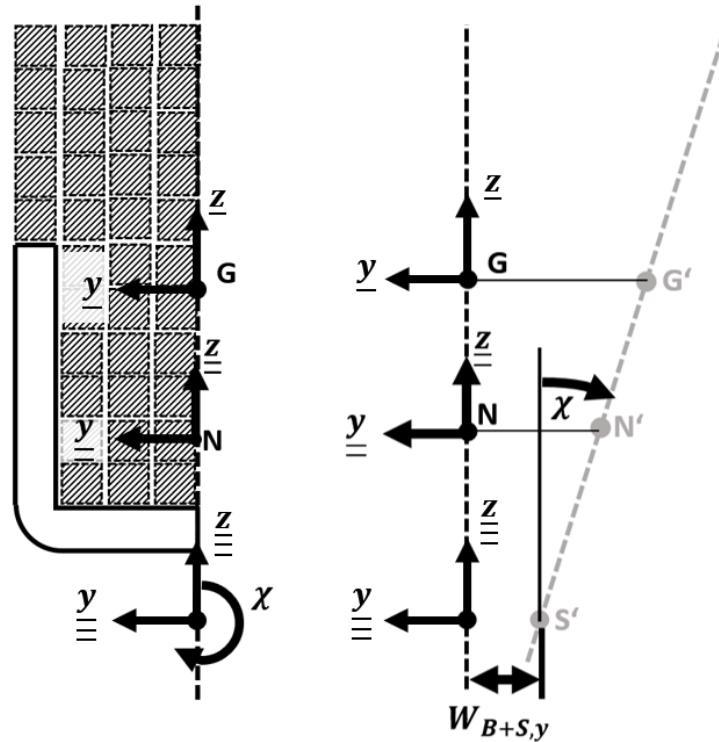


Figure 6: Visualization of a ship's cross section with the body fixed coordinate system, bending coordinate system and shear center coordinate system (left). Visualization of bending and torsional coupling effects (right).

To compute elastic deformations of the ship structure, a two-node fourteen-degrees-of-freedom beam element model was developed. The left side of Figure 7 shows the definition of the coordinate systems as well as the nodal displacements (colored blue). The origin of the element coordinate system, $\underline{\underline{\vec{x}}} = \begin{bmatrix} \underline{\underline{x}} \\ \underline{\underline{y}} \\ \underline{\underline{z}} \end{bmatrix}^T$, is placed at the first node coincident with the intersection of the neutral bending axis (see also Figure 6). The displacement u_i describes the displacement of the i^{th} degree of freedom. Indices $i = 1,2,3$ identify the translations of the first node in the $\underline{\underline{x}}$ -, $\underline{\underline{y}}$ - and $\underline{\underline{z}}$ -directions, respectively, and indices $i = 5,6$ mark the rotations of the first node about the $\underline{\underline{y}}$ -axis - and $\underline{\underline{z}}$ -axes, respectively. As already introduced, an additional coordinate system at the shear center defined the pole of torsion induced twist, $\underline{\underline{\vec{x}}} = \begin{bmatrix} \underline{\underline{x}} \\ \underline{\underline{y}} \\ \underline{\underline{z}} \end{bmatrix}^T$. The index $i = 4$ marks the twist angle due to torsion of the first node about the $\underline{\underline{x}}$ -axis and index $i = 7$ denotes the variation

2.3 Weakly-Nonlinear Wave-Induced Elastic Deformations

of the twist angle about the \underline{x} -axis, $u_7 = du_4/dx$. Similar to the indices 1 to 7, indices 8 to 14 denote the corresponding displacements of the second node. The element length is designated l .

The right side of Figure 7 shows a side and a top view of the beam element with q_x [N/m] being the external longitudinal force, q_y [N/m] the external horizontal force, q_z [N/m] the external vertical force, and q_t [Nm/m] the external torsional moment per unit length.

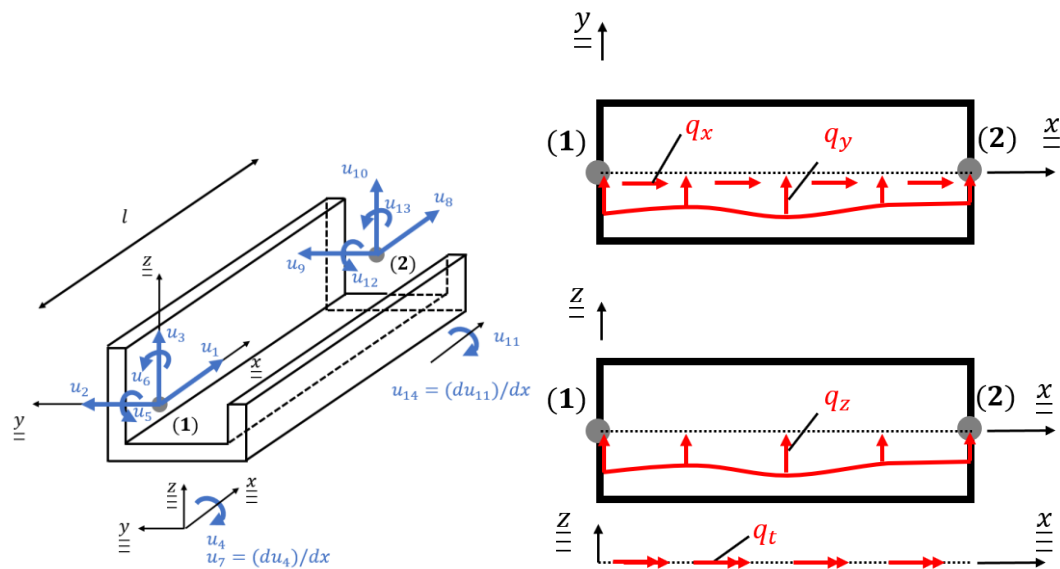


Figure 7: A typical beam element, showing the origin of its coordinate systems and the degrees of freedom of a node (left) and the applied external loads per unit length (right).

Simplified torsional theory (St. Venant torsion) assumes that the variation of the twist angle, $u_7 = du_4/dx$, is constant over one element (Vlasov (1961)) and the sevens degree of freedom ($i = 7$) could then be avoided. Considering here that the variation of the twist angle varies over the element length is the most important difference between the present torsional theory and the simplified torsional theory due to St. Venant. St. Venant torsional theory is of often referred to as pure torsion or uniform torsion and the torsional theory with a varying variation of the twist angle is often referred to as Vlasov's torsional theory or non-uniform torsion. Further simplifications can be applied for some specific cross section. For cross sections with two symmetry plains, e.g. rectangular cross sections, the shear centre, is coincident with the neutral bending axis and if no further non-structural masses are applied, it is also coincident with the centre of

gravity. For such cross section, coupling effects between torsion and bending disappear. Further simplifications can be made for rotationally symmetrical cross section as cylinders or pipes, because they don't show torsion induced warping effects.

Based on the assumption that the total elastic response can be approximated by superposing all basic vibration modes, the overall elastic structural response is calculated using the modal superposition technique in time domain. Let \vec{u}_j be the unified response vector for all degrees of freedom for the j^{th} natural mode and $v_j(t)$ a superposition factor for the response of that mode due to excitation forces and moments. The total response is described as follows:

$$\vec{u} = \sum_{j=7}^J \vec{u}_j v_j \quad (71)$$

Using this technique, the complete elastic ship response was decoupled into basic ship vibrations that can be solved separately. The first natural modes describe generally rigid body motion. Recall that rigid body motions were computed with a nonlinear rigid body motion solver and not with the linear finite element solver, the loop in equation (71) neglect the first six modes. When computing the elastic natural modes, it is important to consider that the ship is freely floated in water. As a result, vibration induced hydrodynamic forces act at the hull and affect the natural frequency and mode shape. In this case both parameters are referred to as wet natural frequency and wet natural mode.

The linear motion equations to describe the nodal displacements, \vec{u}_j , was derived based on the strain energy, V , and kinetic energy, T , of a vibrating beam using the Lagrange formalism (Bathe, 1996):

$$\frac{d}{dt} \left(\frac{\partial L}{\partial \dot{u}_j} \right) - \frac{\partial L}{\partial u_j} = f_j \quad (72)$$

Where L is the Lagrange Operator

$$L = T - V \quad (73)$$

and f_j are generalized external forces.

The following subsection 2.3.1 describe the mathematical formulation of the strain and kinetic energy of the vibrating hull to describe the Lagrange Operator in equation (73) and to derive the equation of nodal displacements from equation (72). As aforementioned, the new beam element approach considers torsion-induced warping. Ships cross section are complex structures with thin walled open and closed cells. Computing the warping properties of such structures is a complicate and time-consuming procedure, especially during the design state. To reduce the complexity, the warping characteristics of the structure were simplified to adequately represent ship-like structure but to simplify the computation procedure of the ship's structural properties. This procedure is discussed in subsection 2.3.2. Afterwards, subsection 2.3.3 discusses the element shape functions to describe displacements of the structure inside the beam element due to nodal displacement. Subsection 2.3.4 connect the content of the previous three subsections and describes the derivation of the linear equations of nodal displacements. Subsection 2.3.5 discuss the procedure of computing wet natural modes and subsection 2.3.6 explains the derivation of the frequency independent equation of nodal displacements including all considered hydrodynamic forces. Finally, subsection 2.3.7 describes the computation of the sectional loads, namely the torsional moment and the vertical and horizontal bending moment.

2.3.1 Strain and Kinetic Energy of an Elastic Vibrating Ship

Figure 8 exemplary shows a small segment of a cross section structure (colored grey) and their geometrical relationships to the element coordinate system, $\underline{\underline{\vec{x}}} = \begin{bmatrix} x \\ y \\ z \end{bmatrix}^T$, and the shear center coordinate system, $\underline{\underline{\vec{x}}} = \begin{bmatrix} x \\ y \\ z \end{bmatrix}^T$. Furthermore, an additional coordinate system was introduced that describes the position on the cross section, with the distance s measured from an arbitrary starting point 0.

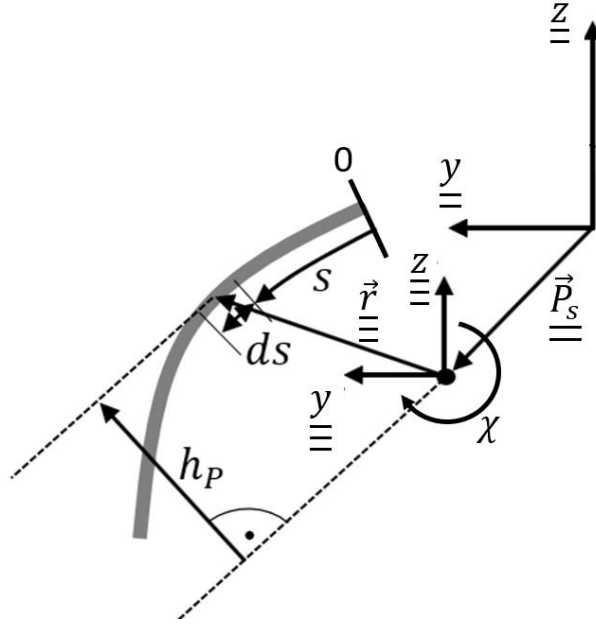


Figure 8: Geometric relations of a thin walled girder.

As introduced in equation (1), the vector $\vec{w}(x, y, z) = (w_x; w_y; w_z)^T$ describes the elastic longitudinal, horizontal and vertical displacements of a point on the cross section, respectively, and $\dot{\vec{w}} = (\dot{w}_x; \dot{w}_y; \dot{w}_z)^T$ is the velocity of that point. $\underline{\underline{P}}_s = (\underline{\underline{P}}_{s,y}; \underline{\underline{P}}_{s,z})^T$ is the position vector of the shear center coordinate system in the beam element coordinate system.

The kinetic energy of the vibrating structure follows from

$$T = \frac{1}{2} \int_V \rho \vec{w}^2(\vec{x}) dV \quad (74)$$

For a thin walled girder, the strain energy follows from

$$V = \frac{1}{2} \int_V \left(E \varepsilon_x^2(\vec{x}) + G \gamma_{xy}^2(\vec{x}) + G \gamma_{xz}^2(\vec{x}) \right) dV \quad (75)$$

Where E and G are the Young's modulus and the shear modulus, respectively. The longitudinal strain, ε_x , and the shear strain, γ_{xy} and γ_{xz} , follows from

$$\varepsilon_x = \frac{dw_x}{dx}; \quad \gamma_{xy} = \frac{dw_x}{dy} + \frac{dw_y}{dx}; \quad \gamma_{xz} = \frac{\partial w_x}{\partial z} + \frac{\partial w_z}{\partial x} \quad (76)$$

The longitudinal displacement due to elongation, torsion, vertical and horizontal bending can be described as follows, see e.g. Pavazza (2005)

$$w_x = w_M - \theta_z \underline{y} + \theta_y \underline{z} - \vartheta \int_0^s h_p ds + \int_0^s \gamma_{xs}^T ds + \int_0^s \gamma_{xs}^{vS} ds + \int_0^s \gamma_{xs}^{hS} ds \quad (77)$$

where w_M is the longitudinal displacement due to pure longitudinal elongation or compression, θ_z is the cross-section rotation due to horizontal bending, and θ_y the cross-section rotation due to vertical bending. Here, $\vartheta = d\chi/dx$ is the variation of torsion induced twist angle, h_p is the shortest distance between the torsional pole and the considered point on the cross section (see Figure 8), and γ_{xs}^T , γ_{xs}^{vS} and γ_{xs}^{hS} are the shear strains due to torsion, vertical bending and horizontal bending. There are different theories with different levels of complexity to model warping effects. In principle, warping describes the out of plain displacement (displacement in x direction), perpendicular on the cross section. The upper picture in Figure 9 shows exemplary the cross section of a U-Beam with the shear center coordinate system located below the beam structure. The lower picture in Figure 9 illustrates the one-node torsion mode. On both ends of the beam the longitudinal displacements due to torsion-induced warping can clearly be seen and can be computed by the $-\vartheta \left(\underline{x} \right) \omega(s)$. $\omega(s)$ is the torsional warping function for open girders that depends only on geometrical properties of the cross section $\omega(s) = \int_0^s h_p ds$, Vlasov (1961). For the new numerical method, it was assumed that the cross section is constant along one beam element. Consequently, ω did not depend on the longitudinal position \underline{x} over an element. The present example shows the free vibration of the beam without any boundary conditions at the beam ends. In this scenario, $\vartheta \left(\underline{x} \right)$ is constant along the total beam length and it follows $d\vartheta(\underline{x})/dx = 0$. Consequently, warping do not contribute to the longitudinal strain, see equation (76), and as described later in equation (108) and (109), it does not contribute to the total torsional moment. In

that case, the torsional moment can be computed according to St. Venant torsion theory, see e.g. Vlasov (1961). Even if it is often neglected for such scenario, warping contributes to the kinetic energy and should be considered for dynamic analysis.

In a real application, often boundary conditions at the beam ends prevent free warping of the cross section. Such effect also occurs if the total structure is made of beams with a different warping stiffness (see the later explanation at equation (87)), which is the case for ship structures due to large hatch opening and relatively stiff compartments between the hatch openings. In this case, the stiff compartment prevents free warping of the weaker compartments which results in a longitudinal variation of $\vartheta(\underline{x})$ over each element. This effect is called non-uniform warping (often also called restrained warping) and affects the modes and natural frequencies of torsional vibrations significantly.

For cross sections with open cells, the torsion induced shear flow $T(s) = \int \tau dt$, which is the integral of the torsion induced shear stress over the plate thickness, t , is zero. Figure 10 left illustrates this effect. Consequently, the integral of the torsion induced shear strain in equation (77), $\int_0^S \gamma_{xs}^T ds$, is zero and does not contribute to the longitudinal displacement. Often, this term, and also the integral of the bending induced shear strain, $\int_0^S \gamma_{xs}^{vS} ds$ and $\int_0^S \gamma_{xs}^{hS} ds$, are neglected also when computing the longitudinal displacement of closed section, Vlasov (1961). However, the torsion induced shear flow at closed sections is unequal zero, see Figure 10 right, and consequently $\int_0^S \gamma_{xs}^T ds$ contributes to the longitudinal displacements. In the new numerical method, $\int_0^S \gamma_{xs}^T ds$ and also its coupling effects with $\int_0^S \gamma_{xs}^{vS} ds$ and $\int_0^S \gamma_{xs}^{hS} ds$ were considered. The definition of the longitudinal displacement differs to the classical Vlasov theory, see. Vlasov (1961), because the shear strain γ_{xs}^T , γ_{xs}^{vS} and γ_{xs}^{hS} were neglected by Vlasov.

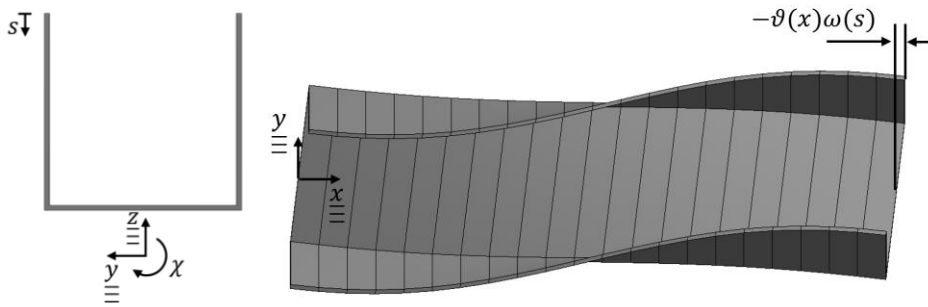


Figure 9: Free vibration of an unsupported U-Shape beam.

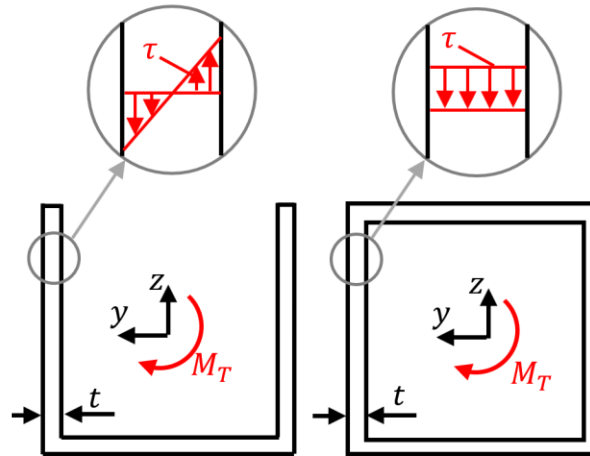


Figure 10: Torsion induced shear stress for an open (left) and closed (right) cross section.

For a simple cross section, such as an U-Profile in Figure 10 (left), all the necessary geometrical information can be easily calculated to compute each term of equation (77). However, cross sections of ships are often complicated as they include open and closed cells of changing plate thickness. Integrating all geometrical properties over the entire cross section is a time-consuming procedure, and often such detailed cross-sectional information is unavailable at the early design stage. Therefore, equation (77) was simplified to be applicable for practical engineering calculations. First, the vertical and horizontal shear strain was simplified using a linear warping approach (according to Timoshenko's beam theory) to describe the bending shear strain. Consequently, as the bending shear strain is considered to be constant over the complete cross section, the longitudinal displacement due to, e.g., horizontal bending strain was substituted as follows:

$$\int_0^s \gamma_{xs}^{hs} ds = \frac{dw_{s,y}}{dx} y(s) = w'_{s,y} y(s) \quad (78)$$

Here $w_{s,y}$ is the horizontal shear bending and the apostrophe designates the derivative with respect x . Combining the cross-sectional rotation due to horizontal bending with the bending shear strain results in the following relationship:

$$-\theta_z y + \int_0^s \gamma_{xs}^{hs} ds = -(w'_{B,y+s,y} - w'_{s,y}) y = -w'_{B,y} y \quad (79)$$

where $w_{B,y+s,y}$ is the total horizontal bending (pure bending plus shear bending), and $w_{B,y}$ is the horizontal displacement due to pure bending. Consequently, the bending shear strain does not generate a longitudinal displacement; see, e.g., Timoshenko and Goodier (1970). The same applies to vertical bending.

Figure 11 shows exemplarily a simplified symmetric ship cross section. The lower part (double bottom) consists of closed cells, and the side part is an open structure. To simplify the contribution of the torsional shear strain, the relation of the torsional shear strain and the variation of the twist angle was described by $\psi = \gamma_{xs}^T / \vartheta$. The warping function, $\tilde{\omega}$, of closed girders was defined as follows:

$$\tilde{\omega} = \int_0^s (h_p - \psi) ds \quad (80)$$

For an open thin walled beam, the warping function reduces to the classical warping function of Vlasov (1961), i.e., $\omega = \int_0^s h_p ds$. Based on the above simplification, the longitudinal displacement of a thin walled beam of open or closed cells was computed as follows:

$$w_x = w_M - w'_{B,y} y - w'_{B,z} z - \vartheta \tilde{\omega} \quad (81)$$

According to the geometrical relations in Figure 8, vertical and horizontal displacements are written as follows:

$$w_z = w_{B,z} + w_{S,z} + \left(\underline{y} - \underline{\underline{P}}_{S,y} \right) \chi = w_{B,z} + w_{S,z} + \underline{\underline{y}} \chi \quad (82)$$

$$w_y = w_{B,y} + w_{S,y} - \left(\underline{z} - \underline{\underline{P}}_{S,z} \right) \chi = w_{B,y} + w_{S,y} - \underline{\underline{z}} \chi \quad (83)$$

Equations (81), (82) and (83) were inserted into (76) to finally compute the strain energy. However, it was assumed that the longitudinal displacement, w_M , due to a pure longitudinal elongation represents only a minor contribution to elastic ship dynamics and that the coupling effect between w_M and the remaining longitudinal displacements is even smaller. Therefore, the longitudinal strain was simplified as follows:

$$\varepsilon_x^2 = (w'_M)^2 + \left(-w''_{B,y} \underline{\underline{y}} - w''_{B,z} \underline{\underline{z}} - \vartheta' \tilde{\omega} \right)^2 \quad (84)$$

The above procedure results in the following expression of the strain energy:

$$\begin{aligned} V = \frac{1}{2} \int_l \left(E \left((w'_M)^2 S + (w''_{Pz})^2 \underline{\underline{I}}_y + (w''_{Py})^2 \underline{\underline{I}}_z + (\vartheta')^2 \underline{\underline{I}}_\omega + 2w''_{Py} w''_{Pz} \underline{\underline{I}}_{yz} \right. \right. \\ \left. \left. + 2w''_{Pz} \vartheta' \underline{\underline{I}}_{y\omega} + 2w''_{Py} \vartheta' \underline{\underline{I}}_{z\omega} \right) \right. \\ \left. + G \left((w'_{S,y})^2 r_y S + (w'_{S,z})^2 r_z S \right) + G \vartheta^2 I_T \right. \\ \left. + 2G \vartheta \left(w'_{S,z} \int_s \left(-\frac{d\tilde{\omega}}{dz} + \underline{\underline{y}} \right) dA \right. \right. \\ \left. \left. - w'_{S,y} \int_s \left(\frac{d\tilde{\omega}}{dy} + \underline{\underline{z}} \right) dA \right) \right) dx \quad (85) \end{aligned}$$

Here, S is the cross sectional area, r_y and r_z coefficients to reduce the cross sectional area to the effective shear area in y and z direction, $\underline{\underline{I}}_y$ and $\underline{\underline{I}}_z$ are the area moment of inertia about the $\underline{\underline{y}}$ - and $\underline{\underline{z}}$ -axes, respectively, $\underline{\underline{I}}_\omega$ is the warping stiffness, $\underline{\underline{I}}_{yz}$ is the deviation moment, $\underline{\underline{I}}_{y\omega}$ and $\underline{\underline{I}}_{z\omega}$ are the sector centrifugal

moments, and I_T is the torsional stiffness. Moments $\underline{\underline{I}}_y$, $\underline{\underline{I}}_z$, $\underline{\underline{I}}_{yz}$, and I_T are known from classical beam theory:

$$\begin{aligned}\underline{\underline{I}}_y &= \int \underline{\underline{z}}^2 dA \\ \underline{\underline{I}}_z &= \int \underline{\underline{y}}^2 dA \\ \underline{\underline{I}}_{yz} &= \int \underline{\underline{yz}} dA \\ I_T &= \int \left(\left(-\frac{d\tilde{\omega}}{dy} - \frac{\underline{\underline{z}}}{\underline{\underline{z}}} \right)^2 + \left(-\frac{d\tilde{\omega}}{dz} + \frac{\underline{\underline{y}}}{\underline{\underline{z}}} \right)^2 \right) dA\end{aligned}\tag{86}$$

The deviation moment becomes zero when the cross section has at least one symmetric plain. Consequently, $\underline{\underline{I}}_{yz}$ is often zero for ship cross sections. The warping stiffness, $\underline{\underline{I}}_\omega$, is obtained as follows:

$$\underline{\underline{I}}_\omega = \int \tilde{\omega}^2 dA\tag{87}$$

The centrifugal moments $\underline{\underline{I}}_{y\omega}$ and $\underline{\underline{I}}_{z\omega}$ of a sector read as follows:

$$\begin{aligned}\underline{\underline{I}}_{y\omega} &= \int \underline{\underline{z}}\tilde{\omega} dA \\ \underline{\underline{I}}_{z\omega} &= \int \underline{\underline{y}}\tilde{\omega} dA\end{aligned}\tag{88}$$

These moments are zero when referred to the principle coordinates (shear center).

To describe the kinetic energy, see equation (74), it is important to consider that not only the ship's structure itself, but also its non-structural components contribute to the total kinetic energy. This comprises e.g. all kinds of cargo masses.

This is important e.g. for containerships, especially when containers are stacked high on deck, thereby exceeding the cross-sectional dimensions of the ship's steel structure, see e.g. Figure 6 left. Here, all cargo was treated as solid masses. In addition, it was assumed that cargo motions followed the general motions and deflections of the ship. Based on equations (81), (82) and (83), the total velocity was separated into a longitudinal component:

$$\frac{dw_x}{dt} = \dot{w}_M - \dot{w}'_{B,y} \underline{\underline{y}} - \dot{w}'_{B,z} \underline{\underline{z}} - \dot{\vartheta} \tilde{\omega} \quad (89)$$

and a horizontal and vertical component:

$$\begin{aligned} \frac{dw_z}{dt} &= \dot{w}_z + \dot{\chi} \underline{\underline{y}} \\ \frac{dw_y}{dt} &= \dot{w}_y - \dot{\chi} \underline{\underline{z}} \end{aligned} \quad (90)$$

Inserting equations (89) and (90) into equation (74), the total kinetic energy was defined as follows:

$$\begin{aligned} T = \frac{1}{2} \int_{x=0}^l \left[\underline{\underline{j}}_p \dot{\chi}^2(x) + \mu \dot{w}_x^2 + \mu \dot{w}_y^2 + \mu \dot{w}_z^2 + \underline{\underline{j}}_z (\dot{w}'_{B,y})^2 + \underline{\underline{j}}_y (\dot{w}'_{B,z})^2 \right. \\ \left. + \frac{\mu}{S} \underline{\underline{I}}_{\omega} \dot{\vartheta}^2 - 2 \frac{\mu}{S} \underline{\underline{I}}_{y\omega} \dot{\vartheta} \dot{w}'_{B,z} - 2 \frac{\mu}{S} \underline{\underline{I}}_{z\omega} \dot{\vartheta} \dot{w}'_{B,y} + 2 \mu \underline{\underline{y}}_{cog} \dot{\chi} \dot{w}_z \right. \\ \left. - 2 \mu \underline{\underline{z}}_{cog} \dot{\chi} \dot{w}_y \right] dx \quad (91) \end{aligned}$$

Here, $\underline{\underline{j}}_p$ is the polar inertial moment per unit length with respect to the shear centre, μ is the mass per unit length, and $\underline{\underline{j}}_y$ and $\underline{\underline{j}}_z$ are the inertial moments per unit length about the neutral bending $\underline{\underline{y}}$ - and $\underline{\underline{z}}$ - axes, respectively. $\underline{\underline{y}}_{cog}$ and $\underline{\underline{z}}_{cog}$ are the horizontal and vertical position of the center of gravity respect the shear center. Recall that warping induced longitudinal velocities were considered by $\dot{\vartheta} \tilde{\omega}$

in equation (89). However, \tilde{w} describes only the warping induced displacement of the ship structure. The warping induced displacement of cargo (e.g. containers) cannot be described by \tilde{w} , because some important properties, e.g. the stiffness of the lashing, are unknown. In the present method, the kinetic energy due to warping induced cargo motions was computed by distributing the total mass per unit length over the structural cross section by introducing the term μ/S in equation (91).

2.3.2 Torsion-Induced Warping of Ship Cross Sections

The computation of the strain energy in equation (85) is complex for ship structures. This is particularly true for the last two terms on the r.h.s., that represent the shear coupling effect of bending and torsion:

$$2G\vartheta \left(w'_{s,z} \int_s \left(-\frac{d\tilde{w}}{dz} + \underline{y} \right) dA - w'_{s,y} \int_s \left(\frac{d\tilde{w}}{dy} + \underline{z} \right) dA \right) \quad (92)$$

To integrate the derivative of the warping function over the entire cross-sectional area, detailed sectional properties have to be known. To avoid such complicated computations, a simplified approach was developed. Equation (92) was split into separate components, where $\underline{S}_z = \int_s \underline{y} dA$ and $\underline{S}_y = \int_s \underline{z} dA$ are the area moments of the cross section relative to the shear center:

$$2G\vartheta \left(w'_{s,z} \underline{S}_z - w'_{s,y} \underline{S}_y - w'_{s,z} \int_s \frac{d\tilde{w}}{dz} dA - w'_{s,y} \int_s \frac{d\tilde{w}}{dy} dA \right) \quad (93)$$

The terms $\int \frac{d\tilde{w}}{dz} dA$ and $\int \frac{d\tilde{w}}{dy} dA$ can be estimated for the parallel mid ship assuming that the ship cross section is made of only vertical and horizontal plates. Although this neglects the bilge radius, it is a reasonable assumption considering its relatively minor effect on the remaining ship structure. With this simplification, $h_p = \underline{z}$ is constant for horizontal plates, and $h_p = \underline{y}$ is constant for vertical plates. For thin walled girders, the cross-section area of horizontal plates can be related to the effective horizontal shear area, and the cross-section area of vertical plates

2.3 Weakly-Nonlinear Wave-Induced Elastic Deformations

can be related to the effective vertical shear area. Based on this simplification, the following holds true:

$$\int_S \frac{d\tilde{\omega}}{dy} dA = \int_{S_{horiz.}} \underline{\underline{z}} dA \approx -r_y S \underline{\underline{P}}_{S,z} \quad (94)$$

and for vertical plates,

$$\int_S \frac{d\tilde{\omega}}{dz} dA = \int_{S_{vertical}} \underline{\underline{y}} dA \approx -r_z S \underline{\underline{P}}_{S,y} \quad (95)$$

where $\underline{\underline{P}}_{S,z} = (\underline{\underline{P}}_{S,y}; \underline{\underline{P}}_{S,z})^T$ is the vector extending from the element coordinate system (situated at the neutral axis) to the shear center; see Figure 8.

Equation (94) and (95) was verified with a simplified ship cross section. Figure 11 (left) shows a drawing of this simplified cross section and the associated dimensions in meter. The plate thickness is $t = 0.02m$. Figure 11 (right) shows this cross section and the warping function, $\tilde{\omega}$, distributed along its structural members.

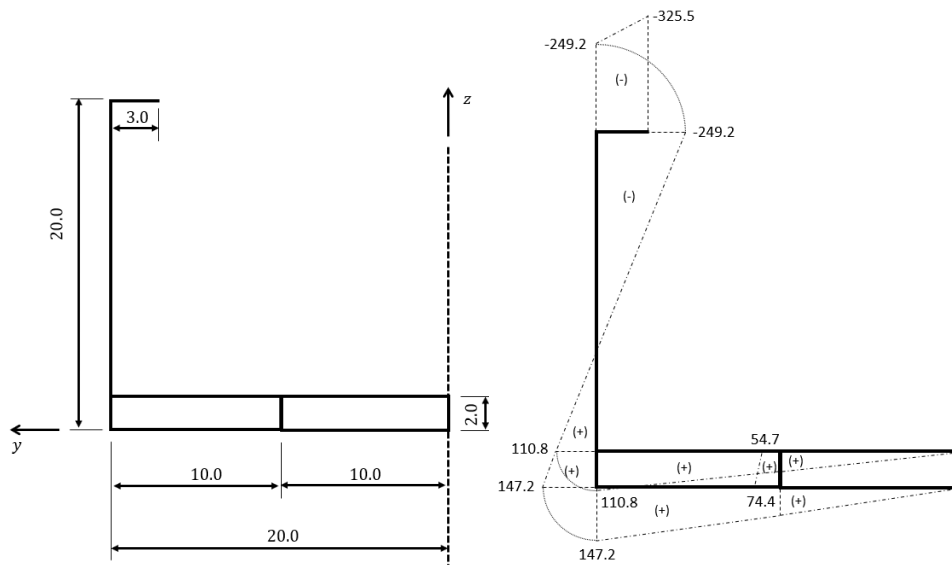


Figure 11: Simplified ship cross section (left) and the associated warping function (right) distributed along structural components.

Table 1 lists the geometrical properties of this simplified cross section and Table 2 compares the analytical and estimated solution based on equations (94) and (95). The analytically computed result of $\int_S (d\tilde{\omega}/dz) dA = 0 m^3$ and estimated equivalent $r_z S P_y = 0.0 m^3$ indicate that this cross section is symmetric about the x-z plain. Furthermore, comparing the analytically computed $\int_S (d\tilde{\omega}/dy) dA = 12.72 m^3$ and estimated $-r_y S \underline{\underline{P}}_z = 12.53 m^3$ shows a good agreement. Consequently, the following relations $\int_S (d\tilde{\omega})/dy dA \approx -r_y S \underline{\underline{P}}_z$, was assumed to be accurate enough for ship structure.

Table 1: Cross section properties

$$\begin{aligned} S &= 2.64 m^2 & z_M &= 4.59 m & y_M &= 0.0 m \\ S_y &= 1.25 m^2 & z_s &= -5.45 m & y_s &= 0.0 m \\ S_z &= 0.61 m^2 & P_z &= -10.0 m & P_y &= 0 m \end{aligned}$$

Table 2: Comparisons of analytical computed and estimated distribution of the warping function

analytical solution	estimated solution
$\int_S \frac{d\tilde{\omega}}{dz} dA = 0.0 m^3$	$-r_z S \underline{\underline{P}}_y = 0.0 m^3$
$\int_S \frac{d\tilde{\omega}}{dy} dA = 12.72 m^3$	$-r_y S \underline{\underline{P}}_z = 12.53 m^3$

Inserting the above simplifications into equation (85) results in the following definition of the strain energy of the new beam element approach:

$$\begin{aligned} V &= \frac{1}{2} \int_l \left(E \left((w'_M)^2 S + (w''_{B,z})^2 \underline{\underline{I}}_y + (w''_{B,y})^2 \underline{\underline{I}}_z + (\vartheta')^2 \underline{\underline{I}}_\omega + \right. \right. \\ &2w''_{B,y} w''_{B,z} \underline{\underline{I}}_{yz} + 2w''_{B,z} \vartheta' \underline{\underline{I}}_{y\omega} + 2w''_{B,y} \vartheta' \underline{\underline{I}}_{z\omega} \left. \right) + GS \left((w'_{S,y})^2 r_y + \right. \\ &\left. (w'_{S,z})^2 r_z \right) + G\vartheta^2 I_T + 2GS\vartheta w'_{S,z} P_z (r_z - 1) + 2GS\vartheta w'_{S,y} P_y (r_y + 1) \left. \right) dx \end{aligned} \quad (96)$$

2.3.3 Shape Functions to Compute Element Displacements

As already shown in Figure 7, the current deformation of the system of finite beam elements were described by nodal displacements, u_i . The translations and rotations of the cross section at the position \underline{x} inside the beam element (between two element node) were described by the summation of shape functions, $N(\underline{x})$, multiplied with the associated nodal displacements, u_i . The three translations w_M , $w_{B,y+S,y}$ and $w_{B,z+S,z}$ (bending +shear) point in the \underline{x} -, \underline{y} - and \underline{z} -directions, respectively, and the three rotations χ , α and β rotate about the \underline{x} -, \underline{y} - and \underline{z} -axes, respectively, were computed as follows:

$$\begin{pmatrix} \vec{w}_P \\ \vec{\alpha} \end{pmatrix} = \begin{pmatrix} w_M \\ w_{B,y+S,y} \\ w_{B,z+S,z} \\ \chi \\ \alpha \\ \beta \end{pmatrix} = \begin{pmatrix} \sum_{i=1,8} [N_i(\underline{x}) u_i] \\ \sum_{i=2,6,9,13} [N_i(\underline{x}) u_i] \\ \sum_{i=3,5,10,12} [N_i(\underline{x}) u_i] \\ \sum_{i=4,7,11,14} [N_i(\underline{x}) u_i] \\ - \sum_{i=3,5,10,12} \left[\frac{dN_i(\underline{x})}{dx} u_i \right] \\ \sum_{i=2,6,9,13} \left[\frac{dN_i(\underline{x})}{dx} u_i \right] \end{pmatrix} \quad (97)$$

The shape function to describe pure longitudinal elongation or compression and the shape functions to describe vertical and horizontal bending displacements were taken from existing literature. The shape functions to describe torsion induced displacements have been derived within this work.

The longitudinal displacement of a point on the beam centre due to pure longitudinal elongation or compression were described by two linear shape functions N_1 and N_8 , Przemieniecki (2012)

$$\begin{aligned} N_1(\xi) &= 1 - \xi \\ N_8(\xi) &= \xi \end{aligned} \quad (98)$$

where $\xi = \underline{x}/l$ is the normalized longitudinal position.

The four shape functions N_3 , N_5 , N_{10} and N_{12} described vertical displacements due to vertical bending. They account for the effect of bending and a linear shear deflection according to Timoshenko's beam theory, Przemieniecki (2012):

$$N_3(\xi) = \frac{1}{1 + \Phi_z} [1 - 3\xi^2 + 2\xi^3 + (1 - \xi)\Phi_z] \quad (99)$$

$$N_5(\xi) = \frac{l}{1 + \Phi_z} \left(\xi - 2\xi^2 + \xi^3 + \frac{1}{2}(\xi - \xi^2)\Phi_z \right) \quad (100)$$

$$N_{10}(\xi) = \frac{1}{1 + \Phi_z} (3\xi^2 - 2\xi^3 + \xi\Phi_z) \quad (101)$$

$$N_{12}(\xi) = \frac{l}{1 + \Phi_z} \left(-\xi^2 + \xi^3 - \frac{1}{2}(\xi - \xi^2)\Phi_z \right) \quad (102)$$

where Φ_z is a shear deformation parameter that describes the relation between bending and shear stiffness

$$\Phi_z = \frac{12 EI_y}{r_z G S l^2} \quad (103)$$

and r_z is a factor reducing the cross-sectional area, S , to the effective shear cross sectional area in the z -direction. Similar to equations (99), deflections in the horizontal direction are described by the four shape functions N_2 , N_6 , N_9 and N_{13} . However, according to the coordinate conventions defined in Figure 7, the sign of the rotations is changed. Applying the shear deformation parameter in horizontal direction, $\Phi_y = (12 EI_y)/(r_z G S l^2)$ instead of Φ_z , the shape functions for horizontal bending follow as:

$$N_2(\xi) = \frac{1}{1 + \Phi_y} [1 - 3\xi^2 + 2\xi^3 + (1 - \xi)\Phi_y] \quad (104)$$

$$N_6(\xi) = -\frac{l}{1 + \Phi_y} \left(\xi - 2\xi^2 + \xi^3 + \frac{1}{2}(\xi - \xi^2)\Phi_y \right) \quad (105)$$

$$N_9(\xi) = \frac{1}{1 + \Phi_y} (3\xi^2 - 2\xi^3 + \xi\Phi_y) \quad (106)$$

$$N_{13}(\xi) = -\frac{l}{1 + \Phi_y} \left(-\xi^2 + \xi^3 - \frac{1}{2}(\xi - \xi^2)\Phi_y \right) \quad (107)$$

Cross section rotations α and β follow from the derivatives of their shape function with respect to \underline{x} ; see equation (97).

The four shape functions N_4 , N_7 , N_{11} and N_{14} describe the torsion induced twist. The mathematical model to describe torsion with nonuniform warping separates the total torque, M_T , into one component due to the St. Venant torsion, $M_{St.V}$, and another component due to the warping related torque, M_W , as follows (see e.g. Vlasov (1961)):

$$M_T = M_{St.V} + M_W \quad (108)$$

where

$$\begin{aligned} M_{St.V} &= G I_T \vartheta \\ M_W &= -E \underline{I_\omega} \vartheta'' \end{aligned} \quad (109)$$

Hence, the general differential equation of nonuniform torsion is expressed as follows, see e.g. Vlasov (1961):

$$\vartheta''(\underline{x}) - \alpha^2 \vartheta(\underline{x}) = -\frac{M_T}{E \underline{I}_\omega} \quad (110)$$

with

$$\alpha^2 = \frac{G I_T}{E \underline{I}_\omega} \quad (111)$$

The shape functions to describe torsion-induced twist were determined using an analytical solution of equation (110) similar to the procedure of Dvorkin et al. (1989). The analytical solution consists of solving the following equation:

$$\chi(\xi) = D_1 + D_2 l\xi + D_3 e^{\alpha l\xi} + D_4 e^{-\alpha l\xi} \quad (112)$$

where D_1, D_2, D_3 and D_4 are constants that depend on the boundary conditions of the finite beam element. Shape functions of the same kind as in equation (112) were chosen. Consequently, the four constants are obtained separately for each shape function.

The following boundary conditions describe the relation between the nodal degrees of freedom (only torsional degrees of freedom) and the torsion induced twist angle at the beginning and the end of the beam element

$$\begin{aligned} \chi(\underline{x} = 0) &= u_4 \\ \frac{d\chi(\underline{x} = 0)}{dx} &= \vartheta(\underline{x} = 0) = u_7 \\ \chi(\underline{x} = l) &= u_{11} \end{aligned} \quad (113)$$

$$\frac{dw_4\left(\underline{\underline{x}} = l\right)}{dx} = w_7(l) = u_{14}$$

The first two boundary conditions define that the twist angle of the cross section at the position $\underline{\underline{x}} = 0$ is equal to the nodal displacement u_4 and that the variation of twist angle at $\underline{\underline{x}} = 0$ is equal to the degree of freedom u_7 . Furthermore, the last two boundary conditions define that the twist angle and the variation of the twist angle at the position $\underline{\underline{x}} = l$ are equal to the nodal displacements u_{11} and u_{14} , respectively.

Using the normalized longitudinal position $\xi = \underline{\underline{x}}/l$, the following system of equations was obtained to determine the constants $D_{i,1}$, $D_{i,2}$, $D_{i,3}$ and $D_{i,4}$ for each shape function denoted by the index i :

$$\begin{bmatrix} 1 & 0 & 1 & 1 \\ 0 & 1 & \alpha & -\alpha \\ 1 & l & e^{\alpha l} & e^{-\alpha l} \\ 0 & 1 & \alpha e^{\alpha l} & -\alpha e^{-\alpha l} \end{bmatrix} \begin{pmatrix} D_{i,1} \\ D_{i,2} \\ D_{i,3} \\ D_{i,4} \end{pmatrix} = \vec{b}_i \quad (114)$$

with

$$\vec{b}_4 = \begin{pmatrix} 1 \\ 0 \\ 0 \\ 0 \end{pmatrix}; \vec{b}_7 = \begin{pmatrix} 0 \\ 1 \\ 0 \\ 0 \end{pmatrix}; \vec{b}_{11} = \begin{pmatrix} 0 \\ 0 \\ 1 \\ 0 \end{pmatrix}; \vec{b}_{14} = \begin{pmatrix} 0 \\ 0 \\ 0 \\ 1 \end{pmatrix} \quad (115)$$

The four shape functions to describing torsion induced displacements follow as:

$$N_4(\xi) = \frac{-e^{-\alpha l(\xi-1)} + e^{\alpha l\xi} + (\alpha l(1-\xi) - 1)e^{\alpha l} + 1 + \alpha l(1-\xi)}{c} \quad (116)$$

$$\begin{aligned}
 N_7(\xi) & \\
 &= \frac{(-\alpha l + 1)e^{-\alpha l(\xi-2)} - e^{-\alpha l(\xi-1)} + e^{\alpha l(\xi+1)} - 1e^{2\alpha l}}{(e^{\alpha l} - 1)\alpha c} \\
 &+ \frac{\alpha l(1 - \xi)e^{2\alpha l} + (-\alpha l - 1)e^{\alpha l\xi} + 2\alpha l\xi e^{\alpha l} + 1 + (1 - \xi)\alpha l}{(e^{\alpha l} - 1)\alpha c}
 \end{aligned} \tag{117}$$

$$N_{11}(\xi) = \frac{e^{-\alpha l(\xi-1)} - e^{\alpha l\xi} + (\alpha l\xi - 1)e^{\alpha l} + \alpha l\xi + 1}{c} \tag{118}$$

$$\begin{aligned}
 N_{14}(\xi) &= \frac{(\alpha l + 1)e^{-\alpha l(\xi-1)} - e^{-\alpha l(\xi-2)} + (\alpha l - 1)e^{\alpha l(\xi+1)}}{(e^{\alpha l} - 1)\alpha c} \\
 &+ \frac{(1 - \alpha l\xi)e^{2\alpha l} + e^{\alpha l\xi} + (2\xi - 2)\alpha l e^{\alpha l} - \alpha l\xi - 1}{(e^{\alpha l} - 1)\alpha c}
 \end{aligned} \tag{119}$$

with

$$c = \alpha l e^{\alpha l} + \alpha l - 2e^{\alpha l} + 2 \tag{120}$$

Figure 12 plots exemplary the shape functions N_4 , N_7 , N_{11} and N_{14} along an element with $\alpha = 1$. $\xi = 0$ designates the beginning of the element and the location of the first element node. $\xi = 1$ designates the end of the element and the location of the second node. It can be seen, that the shape functions N_4 and N_{11} are symmetric and the shape functions N_7 and N_{14} are antimetric respect the middle of the element ($\xi = 0.5$).

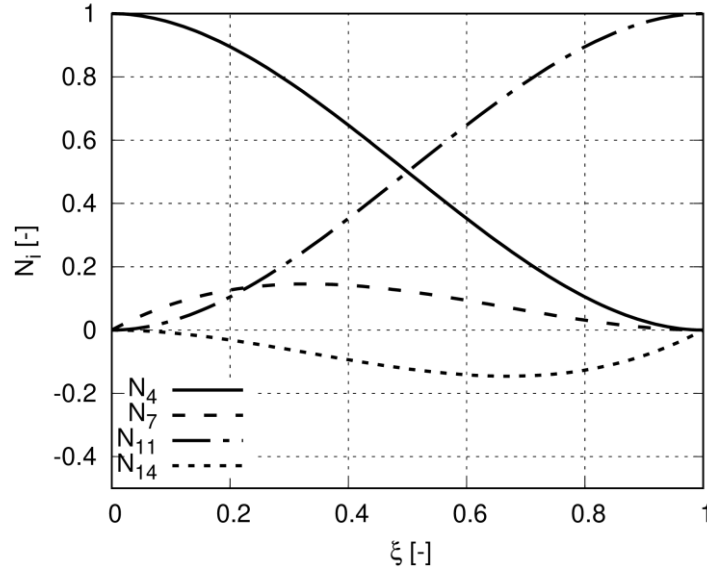


Figure 12: Visualization of the shape functions N_4 , N_7 , N_{11} and N_{14} over one element.

2.3.4 Linear Equation of Elastic Deformation

The shape functions N_i described in the previous subsection 2.3.3 were applied to describe the displacements of the ship structure in the strain energy (equation (96)) and the velocity of the ship structure and nonstructural masses in the kinetic energy (equation (91)). Afterwards, the strain energy and kinetic energy were computed and the Lagrange formalism (equation (72)) was solved to obtain the linear equations of nodal displacements. The linear equation of nodal displacements reads as

$$\mathbf{M}\ddot{\vec{u}}(t) + \mathbf{B}\dot{\vec{u}}(t) + \mathbf{C}\vec{u}(t) = \vec{f} \quad (121)$$

\mathbf{M} is the structural mass matrix and results from the kinetic energy of the vibrating beam element. \mathbf{C} is the structural stiffness matrix and results from the strain energy of the deformed beam element. \mathbf{B} is the structural damping matrix. The definition of the structural damping matrix is discussed later. For one element, \mathbf{M} , \mathbf{C} and \mathbf{B} are matrixes of size 14x14. Due to the coupling effect between torsion and bending, the matrixes are relatively dense and have 68 entries unequal zero.

\vec{f} is the generalized vector of nodal forces and results from the external loads per unit length acting along the element, see Figure 7. The calculation of the generalized nodal forces was based on the virtual work approach, e. g., Bathe (1996). The generalized nodal forces for vertical bending degrees of freedom follow from

$$\vec{f}_i = \int_0^l p_z(x) N_i(x) dx. \quad (122)$$

Similar was applied for vertical bending and torsional degrees of freedom.

During the pre-processing, the ship structure could be discretized with an arbitrary number of beam element and afterwards, the total system of equations was set up. Usually, the axis of the element coordinate system and the inertial coordinate system are not parallel due to the dynamic trim resulting from the stationary forward speed solution or due to the trim according to the load case, e.g. ballast load case. The relation between the element coordinate system and inertial coordinate system was expressed by the transformation matrix λ_e . λ_e is defined in the same way as the transformation matrix $\mathbf{T}(\vec{\theta})$. However, \mathbf{T} depends on the current Euler angles, whereas λ_e is computed based on the initial trim angle.

Elastic body displacements in the element coordinate system were transferred to the inertial coordinate system by

$$\vec{w} = \lambda_e \underline{\underline{\vec{w}}} \quad (123)$$

Coefficient matrixes in the element coordinate system were also transferred into the inertial coordinate system by applying the transformation matrix λ_e . E.g. for the structural mass matrix it follows:

$$\mathbf{M} = \lambda_e \underline{\underline{\mathbf{M}}} \lambda_e^T \quad (124)$$

The same procedure can be applied for all other coefficient matrixes.

For numerical computations, the structural damping matrix, \mathbf{B} , is often assumed to be proportional to the structural mass matrix, \mathbf{M} , or to the structural stiffness matrix, \mathbf{C} , see e.g. Przemieniecki (2012). If the structural damping matrix is proportional to the mass matrix, the damping forces are inversely proportional to the vibration frequency and thus, the structural damping is decreasing with increasing frequency. If the structural damping matrix is proportional to the stiffness matrix, the damping force is linearly proportional to the vibration frequency and thus increases with increasing frequency. Consequently, the damping forces depend on the vibration frequency in both approaches. Often, Rayleigh damping is applied (Przemieniecki (2012)), where the actual damping matrix is the sum of a mass proportional and a stiffness proportional term:

$$\mathbf{B} = \alpha\mathbf{M} + \beta\mathbf{C} \quad (125)$$

Here, α and β are constants of proportionality. Usually, the damping ratio can be measured from a decaying vibration, where the structure is usually vibrating in one of its natural modes and the vibration frequency is consequently the natural frequency of that natural modes. From such tests, the damping ratio for the first and second natural mode and the natural frequency of that modes can often be computed accurately, however, it is difficult to identify the damping ratio of higher natural modes and frequencies or for scenarios, when the structure is oscillating with a frequency different to the natural frequency (forced excitation).

Additional to Rayleigh damping, the structural damping matrix can also be related to the critical damping ratio (similar to the viscous roll damping approach for a rigid body discussed in section 2.2.2.1). The structural damping matrix then follows from

$$\mathbf{B} = 2\delta\mathbf{M} \quad (126)$$

δ is a proportionality factor that relates the actual damping to the critical damping. Both damping techniques, Rayleigh damping and critical damping, were implemented to the new numerical method. However, it was assumed that the structural damping is almost constant for the range of investigated frequencies. Thus, only critical damping was applied in the present work.

2.3.5 Characteristic System Equation to Compute Wet Natural Modes

Content of this section was published in Riesner et al. (2018c) and Riesner and el Moctar (2021a, 2021b).

The natural modes of an elastic system can be computed from the eigen vectors of the characteristic equation of the system, see e.g. Przemieniecki (2012). Assuming an unsuppressed system without any excitation force, the characteristic equation of the system follows from the homogeneous part of the linear differential equations elastic node displacements, equation (121). However, the hydrodynamic and hydrostatic pressure at the vibrating hull affects the natural modes significantly and need to be considered. To account for the hydrodynamic effects, equation (121) was extended with the hydrodynamic added mass matrix, $\mathbf{m}(\omega)$, hydrodynamic damping matrix, $\mathbf{b}(\omega)$, and hydrostatic restoring matrix \mathbf{c}

$$(\mathbf{M} + \mathbf{m}(\omega))\ddot{\vec{u}} + (\mathbf{B} + \mathbf{b}(\omega))\dot{\vec{u}} + (\mathbf{C} + \mathbf{c})\vec{u} = \vec{f} \quad (127)$$

Thus, equation (127) combines structural and hydrodynamic properties of the elastic system. Matrixes in capital letters are related to the structural behaviour and matrixes in small letters to the hydrodynamic behaviour. Assuming harmonic oscillations $u_i = Re(\hat{u}_i e^{i\omega t})$, where the hat symbol designates a complex amplitude, the characteristic equation of the elastic system follows as

$$\left(-\omega^2(\mathbf{M} + \mathbf{m}(\omega)) + i\omega(\mathbf{B} + \mathbf{b}(\omega)) + (\mathbf{C} + \mathbf{c})\right)\hat{\vec{u}} = \vec{0} \quad (128)$$

For nonzero solutions of $\hat{\vec{u}}$, the wet natural frequencies can be computed from

$$\left|-\omega^2(\mathbf{M} + \mathbf{m}(\omega)) + i\omega(\mathbf{B} + \mathbf{b}(\omega)) + (\mathbf{C} + \mathbf{c})\right| = 0 \quad (129)$$

The wet natural modes can be computed e.g. by the method introduced by Duncan (1956). To simplify the solution of (128), the following identity was introduced

$$i\omega(\mathbf{M} + \mathbf{m}(\omega)) - i\omega(\mathbf{M} + \mathbf{m}(\omega)) = \vec{0} \quad (130)$$

This results in the following equation system:

$$\begin{aligned} & \begin{bmatrix} \mathbf{0} & (\mathbf{M} + \mathbf{m}(\omega)) \\ (\mathbf{M} + \mathbf{m}(\omega)) & (\mathbf{B} + \mathbf{b}(\omega)) \end{bmatrix} \begin{pmatrix} -\omega^2 \hat{\mathbf{u}} \\ i\omega \hat{\mathbf{u}} \end{pmatrix} \\ & + \begin{bmatrix} -(\mathbf{M} + \mathbf{m}(\omega)) & \mathbf{0} \\ \mathbf{0} & (\mathbf{K} + \mathbf{k}) \end{bmatrix} \begin{pmatrix} i\omega \hat{\mathbf{u}} \\ \hat{\mathbf{u}} \end{pmatrix} = \begin{pmatrix} \vec{0} \\ \vec{0} \end{pmatrix} \end{aligned} \quad (131)$$

Using the following expressions

$$\begin{aligned} \mathbf{A} &= \begin{bmatrix} \mathbf{0} & (\mathbf{M} + \mathbf{m}(\omega)) \\ (\mathbf{M} + \mathbf{m}(\omega)) & (\mathbf{B} + \mathbf{b}(\omega)) \end{bmatrix} \\ \mathbf{D} &= \begin{bmatrix} -(\mathbf{M} + \mathbf{m}(\omega)) & \mathbf{0} \\ \mathbf{0} & (\mathbf{K} + \mathbf{k}) \end{bmatrix} \\ \hat{\mathbf{U}} &= \begin{pmatrix} i\omega \hat{\mathbf{u}} \\ \hat{\mathbf{u}} \end{pmatrix} \end{aligned} \quad (132)$$

and solving only the complex amplitudes of $\hat{\mathbf{U}}$ based on the harmonic motion assumption, the characteristic equation was transformed into a standard form as follows:

$$(i\omega\mathbf{A} + \mathbf{D})\hat{\mathbf{U}} = \begin{pmatrix} \vec{0} \\ \vec{0} \end{pmatrix} \quad (133)$$

Matrices \mathbf{A} and \mathbf{D} and the vector $\hat{\mathbf{U}}$ in (133) are twice as large as their corresponding matrices and vectors in equation (128). The eigenvectors and corresponding eigenvalues are described by complex numbers. The lower halves of the resulting eigenvectors include the natural modes; the upper halves, the natural modes multiplied by $i\omega$. The imaginary part of the eigenvalue includes the natural frequency; the real part, the decay rate depending on the natural mode and the natural frequency due to structural and hydrodynamic damping. This technique was applied in Riesner et al. (2018c) to compute wet, damped natural

modes that were used to compute linear springing induced vertical bending vibrations of ships in waves using a frequency domain method.

Damped and thus complex natural modes can be easily used within frequency domain solvers. However, for a time-domain method, using complex natural modes increase the complexity of the computation because the final result needs to be a real number. A method to achieve a real time domain solution by using complex natural modes is described by O'Kelly (1961). Generally, natural modes became complex numbers because structural and hydrodynamic damping is considered. However, damping affects the mode shapes only minimally. To avoid the complicate procedure of considering the complex natural modes during time domain simulations, damping was neglected for the computation of the wet natural modes.

Furthermore, it has to be considered that the hydrodynamic matrixes in equation (128) are frequency dependant and generally differ depending on the vibration frequency and the mode shape. Consequently, wet natural modes are generally not orthogonal. To compute all wet natural modes and wet natural frequencies correctly from equation (128) would have required an iterative procedure that computes the hydrodynamic matrices corresponding to their mode shape and natural frequency. To avoid this time-consuming procedure and to provide orthogonal natural modes, the hydrodynamic added mass matrix and the hydrostatic restoring matrix were estimated and assumed to be constant for the computation of all considered wet natural modes. For the final time domain simulations, hydrodynamic coefficient matrixes were recomputed and updated according to the pre-computed wet natural mode shape.

The wet natural modes for the time domain simulations followed from

$$(-\omega^2(\mathbf{M} + \tilde{\mathbf{m}}(\infty)) + (\mathbf{C} + \tilde{\mathbf{c}}(\infty)))\hat{\mathbf{u}} = \vec{0} \quad (134)$$

With $\tilde{\mathbf{m}}$ being the estimated hydrodynamic added mass matrix and $\tilde{\mathbf{c}}$ the estimated hydrostatic restoring matrix. To estimate the hydrodynamic coefficient matrices $\tilde{\mathbf{m}}$ and $\tilde{\mathbf{c}}$, the body was forced to oscillate in specific modes. The hydrodynamic added mass and restoring matrix were than determined from the computed radiation forces. Technically, the contribution of node translations and rotations are coupled, and the coefficient matrices were not necessarily diagonal.

2.3 Weakly-Nonlinear Wave-Induced Elastic Deformations

However, diagonal matrices were assumed, which decoupled linear translations and node rotations. Furthermore, the coefficient matrixes in equation (134) remain symmetric, which ensures that the resulting natural modes are orthogonal.

The hydrodynamic coefficients for longitudinal, horizontal and vertical nodal displacements were estimated similarly to the classical seakeeping radiation problem by allocating a surge, sway and heave motion to the hydroelastic model. To obtain the hydrodynamic coefficients for nodal rotations about the \underline{x} -, \underline{y} - and \underline{z} -axis, each node was forced to rotate opposite to its neighboring nodes. Figure 13 shows exemplarily the forced deformation to estimate the hydrodynamic effect of nodal rotations around the y-axis (vertical bending) of a ship discretized with five beam elements.

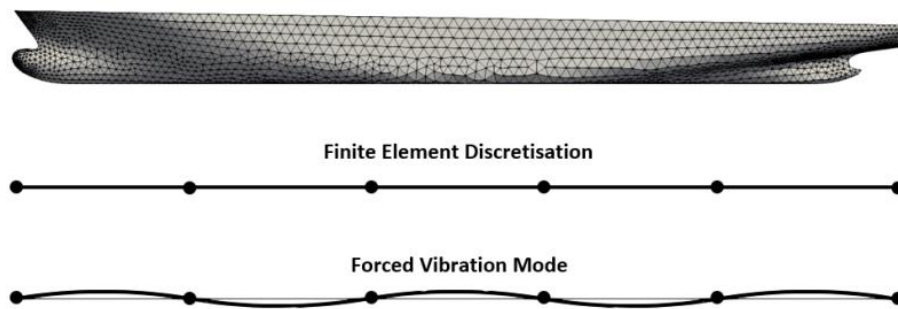


Figure 13: Forced deformation of a ship discretized with five beam elements

The wet natural frequencies of elastic ship vibrations are relatively high. The hydrodynamic coefficients depend generally strongly on the vibration frequency at low and moderate frequencies. However, they are almost constant at high frequencies. For that reason, the simplified infinite frequency boundary condition was applied to estimate the hydrodynamic added mass in equation (134). Thus, hydrodynamic matrixes were constant and the wet natural modes were orthogonal. Once the wet natural modes were computed, modal transfer functions of hydrodynamic added mass and damping were computed again specifically for each wet natural mode.

2.3.6 Linear Elastic Deformation Equations with Weakly-Nonlinear Hydrodynamic Forces

The new numerical method is intended to simulate higher order springing induced vibrations of ships at forward speed in waves. It was discussed in the previous subsections that the superpositioning technique was applied to compute the total response by superposing the response of every elastic wet natural mode. The wet natural modes were computed based on a frequency dependant equation of motion, see equation (127). This equation is frequency dependant because the hydrodynamic matrixes, namely hydrodynamic added mass and hydrodynamic damping, depend on the vibration frequency. However, such frequency dependant equation of elastic deformation cannot be used for the computation of higher order springing-induced vibrations. Higher order springing, e.g. second order springing occurs when the frequency of the second harmonic amplitude of the wave induced force is equal to e.g. the natural frequency of the two-node vertical bending mode. In that situation, the ship is performing rigid body motions with a frequency equal to the wave encounter frequency and elastic vibrations of the two-node vertical bending mode with a frequency twice the wave encounter frequency. Additionally, further high frequency vibrations can occur. This scenario indicates that a frequency dependant equation of motion is not applicable for higher order springing computations.

To solve frequency independent elastic vibrations, the l.h.s. of equation (127) needs to be frequency independent. A frequency independent equation of motions can be achieved by computing radiation forces based on convolution integrals, similar to the procedure that was applied for the nonlinear rigid body motion equations in section 2.2.2.1. Applying this procedure to equation (127) and splitting external forces into diffraction forces, combined Froude-Krylov and hydrostatic forces and the waterline force (see also section 2.2.2), the frequency independent equations of elastic deformation follows as:

$$\bar{\mathbf{M}}_T \ddot{\vec{v}} + \bar{\mathbf{B}}_T \dot{\vec{v}} + \int_0^t \bar{\mathbf{k}}(t - \tau) \dot{\vec{v}}(\tau) d\tau + \bar{\mathbf{C}}_T \vec{v} = \bar{\vec{F}}_{Dif} + \bar{\vec{F}}_{FK+R} + \bar{\vec{F}}_{WL} \quad (135)$$

Based on the modal superposition, equation (135) was already transferred into modal coordinates, denoted by the over bars. Relying on the orthogonality between the mode shape vectors and coefficient matrixes, the following transformation on matrixes were applied:

$$\begin{aligned}
 \bar{\mathbf{M}}_{Tjj} &= \vec{u}_j^T (\mathbf{M} + \mathbf{m}(\infty)) \vec{u}_j \\
 \bar{\mathbf{B}}_{Tjj} &= \vec{u}_j^T (\mathbf{B} + \mathbf{b}(\infty)) \vec{u}_j \\
 \bar{\mathbf{k}}_{jj} &= \vec{u}_j^T (\mathbf{k}) \vec{u}_j \\
 \bar{\mathbf{C}}_{Tjj} &= \vec{u}_j^T (\mathbf{C} + \mathbf{c}) \vec{u}_j
 \end{aligned} \tag{136}$$

The generalized node force vectors, $\bar{\mathbf{F}}_j$, was transformed as follows:

$$\bar{\mathbf{F}}_j = \vec{u}_j^T \vec{f} \tag{137}$$

As the system is decoupled, all matrixes in modal coordinates are diagonal matrixes. The left side of equation (135) represents the structural behaviour of the ship and the radiation forces due to elastic deformations of the wetted hull. According to the modal superpositioning technique, equation (135) is a linear equation of motion because the coefficient matrixes are constant. However, the r.h.s. of equation (135) includes the same nonlinear hydrodynamic forces as already discussed for the nonlinear rigid body motion solver, see equations (42), (44) and (46).

The generalized vector of nodal forces, $\vec{f}(t)$, was computed according to equation (122). The loads per unit length (q_x , q_y , q_z and q_t) were computed by integrating the pressure from diffraction, radiation, combined Froude-Krylov and hydrostatic as well as the waterline integral over the associated hull segment of each element, considering the change of hull normal due to rigid body motions and elastic deformation. The integral in equation (122) was simplified by assuming a constant load per unit length along each element. Consequently, the computational time could be reduced by precomputing the integral by applying an unified load and the actual generalized nodal force was computed during the simulation by multiplying the unified nodal force with the computed load per

length. Although considering a constant load per unit length is a strong simplification, it will be shown in a validation study that this simplification is justified when the ship is subdivided into at least 18 elements.

2.3.7 Computation of Sectional Loads

The new numerical method computed vertical and horizontal bending moments as well as torsional moments. Following classical beam theory, vertical and horizontal bending moments were determined from the second derivative of the horizontal ($w_{B,y+S,y}$) and the vertical ($w_{B,z+S,z}$) displacement, Timoshenko and Goodier (1970):

$$M_y(\underline{x}) = EI \frac{d^2 w_{B,z+S,z}(\underline{x})}{dx^2} \quad (138)$$

$$M_z(\underline{x}) = -EI \frac{d^2 w_{B,y+S,y}(\underline{x})}{dx^2}$$

where $w''_{B,y+S,y}$ and $w''_{B,z+S,z}$ represent a summation of the response of every considered mode shape j as follows:

$$\frac{d^2 w_{B,z+S,z}(\underline{x})}{dx^2} = \sum_{i=3,5,10,12} \left[\frac{d^2 N_i(\underline{x})}{dx^2} \sum_{j=7}^J \vec{u}_{ij} v_j \right] \quad (139)$$

$$\frac{d^2 w_{B,y+S,y}(\underline{x})}{dx^2} = \sum_{i=2,6,9,13} \left[\frac{d^2 N_i(\underline{x})}{dx^2} \sum_{j=7}^J \vec{u}_{ij} v_j \right]$$

The outer loop superposes the result of each of the four degrees of freedom, i . The inner loop superposes the contribution of every considered mode shape, j . Recall that indices $i = 2, 6, 9, 13$ refer to horizontal bending and indices $i = 3, 5, 10, 12$ to vertical bending.

The torsional moment was computed according to equations (108) and (109). The variation of the twist angle, $\vartheta\left(\underline{x}\right) = d\chi/dx$ and $\vartheta''\left(\underline{x}\right)$, is computed as follows:

$$\begin{aligned}\vartheta\left(\underline{x}\right) &= \sum_{i=4,7,11,14} \left[\frac{dN_i\left(\underline{x}\right)}{dx} \sum_{j=7}^J u_{ij} v_j \right] \\ \vartheta''\left(\underline{x}\right) &= \sum_{i=4,7,11,14} \left[\frac{d^3 N_i\left(\underline{x}\right)}{dx^3} \sum_{j=7}^J u_{ij} v_j \right]\end{aligned}\tag{140}$$

2.4 Linear Frequency Domain Hydrodynamic Pressure

To compute rigid body motions, see equation (61), and hydroelastic deformations, see equation (135), hydrodynamic forces and moments due to the incoming wave and due to rigid as well as elastic ship oscillations need to be computed. For the present work, the fluid properties were simplified by assuming an ideal fluid. Thus, the fluid was assumed to be incompressible, inviscid and the flow irrotational. For the present investigations, the ship speed is low compared to the speed of sound waves in the fluid (less than 0.3 times the speed of sound waves), which allows to assume a constant fluid density (incompressible). In principle, water and air are viscous fluids. However, wave induced forces and moments as well as radiation forces and moments can be categorised as pressure dominated because the fluid viscosity influences these forces and moments only minimally. Thus, the assumption of an inviscid fluid is reasonable for the present new numerical method. Assuming the flow to be irrotational is a strong simplification, because effects such as, e.g. breaking waves or recirculation at the hull cannot be considered. However, as described in this section, this simplification allows to describe the velocity field based on a velocity potential and thus reduces the computational effort of the new numerical method significantly. In some scenarios breaking waves can occur, e.g. for ships at high speed in steep waves.

These scenarios can play a role for the ship design and the computation of the structure's strength. However, the present method focuses on springing induced vibrations, which usually occur in moderate wave conditions. Thus, assuming an irrotational flow is a reasonable simplification.

Water (Newtonian fluid) is modelled as a continuum and its properties, such as pressure and velocity field can be described by the continuity equation (mass conservation) and the Navier-Stokes equation (momentum conservation), see e.g. Ferziger and Peric (2010) or el Moctar et al. (2021).

The continuity equation follows as

$$\frac{\partial \rho}{\partial t} + \nabla \cdot (\rho \vec{v}) = 0 \quad (141)$$

Here, ρ is the density and \vec{v} the velocity vector of the fluid. For an incompressible fluid the density is constant. The continuity equation then simplifies to

$$\nabla \cdot \vec{v} = 0 \quad (142)$$

Assuming that the fluid is irrotational, it follows

$$\nabla \times \vec{v} = \vec{0} \quad (143)$$

If this condition is fulfilled, the velocity field \vec{v} can be expressed as the gradient of a scalar field ϕ_t , the so-called velocity potential:

$$\vec{v} = \nabla \phi_t \quad (144)$$

Inserting equation (144) into (142) results in the Laplace equation

$$\Delta \phi_t = \frac{\partial^2 \phi}{\partial^2 x} + \frac{\partial^2 \phi}{\partial^2 y} + \frac{\partial^2 \phi}{\partial^2 z} = 0 \quad (145)$$

which has to be fulfilled in the whole domain.

The Navier-Stokes equation read as follows, Ferziger and Peric (2010) or el Moctar et al. (2021):

$$\frac{\partial(\rho\vec{v})}{\partial t} + \nabla \cdot (\rho\vec{v}\vec{v}) = \nabla \cdot \mathbf{T} + \rho\vec{g} \quad (146)$$

In equation (146) \mathbf{T} is the stress tensor and \vec{g} is the gravity acceleration vector. Please note that $\vec{v}\vec{v}$ describes the outer product of the velocity vector and itself. In principle, water and air are viscous fluids. For that reason, the stress tensor \mathbf{T} includes components depending on the pressure p and the dynamic viscosity μ . However, for an inviscid fluid, \mathbf{T} depends only on the pressure. The Navier-Stokes equation for an incompressible and inviscid fluid simplifies to

$$\frac{\partial\vec{v}}{\partial t} + \nabla \cdot (\vec{v}\vec{v}) = -\frac{\nabla p}{\rho} + \vec{g} \quad (147)$$

Describing the velocity vector based on a velocity potential, $(\partial\vec{v})/\partial t = \nabla\dot{\phi}$ and defining the gravity vector as $\vec{g} = [0,0,g]^T$, equation (147) can be further simplified to

$$\nabla \left(\frac{\partial\phi_t}{\partial t} + \frac{1}{2}|\vec{v}|^2 + \frac{p}{\rho} - gz \right) = 0 \quad (148)$$

From this expression, the Bernoulli equation follows as

$$\frac{\partial\phi_t}{\partial t} + \frac{1}{2}|\nabla\phi_t|^2 + \frac{p}{\rho} - gz = C(t) \quad (149)$$

with an arbitrary constant $C(t)$ that can only depend on time but not on space variables.

2.4.1 Boundary value Problem

The time average ship velocity is described by the velocity vector $\vec{U} = (-s; 0; 0)^T$, where s is the forward speed. The total potential was split into the known and constant potential due to the forward speed, $-sx$, and into the unknown potential, ϕ , due to the disturbance of the hull and the incoming wave.

$$\phi_t = -sx + \phi \quad (150)$$

The flow around the oscillating and elastic ship hull is described by a boundary value problem. In the complete domain, the Laplace equation, equation (145), has to be fulfilled. The numerical calculations performed within this work were made in unrestricted (no bank or channel effects), deep water, thus, no boundary condition for the bottom or side walls needed to be applied. Furthermore, it was assumed that a sharp free surface separates air and water and that the air phase contributes only minimally to the forces and moments on the ship hull. For that reason, the air phase was neglected and the free surface built the top boundary of the domain. At the free surface, two boundary conditions have to be fulfilled. The dynamic boundary condition states that the total pressure at the free surface is equal to the atmospheric pressure. Inserting this relation into equation (149) results in the dynamic boundary condition on the free surface $z = \zeta_t$, from which the free surface elevation, ζ_t , can be computed:

$$\frac{\partial \phi}{\partial t} + \frac{1}{2} |\nabla \phi_t|^2 + g\zeta_t = \frac{1}{2} s^2 \quad (151)$$

The kinematic boundary condition at the free surface states that the vertical velocity of the fluid is equal to the vertical velocity of the free surface

$$\left(\frac{\partial}{\partial t} + (\nabla \phi_t) \cdot \nabla \right) \zeta_t = \frac{\partial \phi_t}{\partial z} \quad (152)$$

On the hull surface the body boundary condition, no flow through the hull surface, has to be fulfilled:

$$\nabla\phi_t \cdot \vec{n} = (\vec{U} + \nabla\phi) \cdot \vec{n} = 0 \quad (153)$$

Where \vec{n} is the normal vector of the hull surface.

Except for low speed, it can be assumed that the lower edge of the transom acts as a trailing edge, thus, the transom remains dry. In this scenario, the vertical position of the lower transom edge defines the height of the free surface directly behind the transom. This effect is not fulfilled by the dynamic free surface condition. An additional transom condition was applied to ensure that the transom contour defines the free surface elevation behind the transom. More details about the transom condition can be found in Graefe (2014).

The boundary conditions in equation (151), (152) and (153) were fulfilled numerically applying a boundary element method. General descriptions of boundary elements methods can be found e.g. in Gaul et al. (2003) or Schanz and Steinbach (2007). The free surface was panelised by a structured grid based on flat quadrangular panels and the wetted part of the hull was panelised with an unstructured grid based on flat triangular panels. Behind each panel (outside of the domain) Rankine sources were located (desingularisation method) at points $\vec{\gamma}_j$. The potential at a point \vec{x} due to a Rankine source j was described by

$$G(\vec{x}, \vec{\gamma}_j) = |\vec{x} - \vec{\gamma}_j|^{-1} \quad (154)$$

With the unknown source strength, q_j , the superposition of all sources result in the following expression:

$$\phi(\vec{x}) = \sum_{j=1}^n q_j G(\vec{x}, \vec{\gamma}_j) \quad (155)$$

Equation (154) automatically fulfil the Laplace equation. Consequently, only the free surface and body boundary conditions need to be fulfilled numerically by choosing proper source strengths. The new numerical method used the patch method, whereby the boundary conditions were satisfied on the average over each panel instead of at their collocation points. A detailed description of the

patch method can be found in Söding (1993) or Graefe (2014). As aforementioned, the new numerical method coupled the fully nonlinear stationary forward speed problem with the oscillatory flow problem of the elastic hull in waves. The velocity potential ϕ in equation (150) was split into the disturbance potential due to the fully nonlinear stationary forward speed problem, ϕ^0 , and into the linear (first order) oscillatory potential, ϕ^1 .

$$\phi = \phi^0 + \phi^1 \quad (156)$$

ϕ^0 was solved individually during a fully nonlinear stationary computation by solving the fully nonlinear stationary wave system and the dynamic trim and sinkage of the hull due to the ships forward speed. Afterwards, ϕ^1 was computed in the frequency domain.

Waves generated by the ship (stationary wave system as well as radiation and diffracted waves) travel usually downstream. This behaviour is ensured by the radiation condition. The source shifting method was applied to numerically fulfil the radiation condition. Thus, free surface sources were shifted backwards by the length of one free surface panel. For the oscillatory flow in waves, the source shifting was applied only if the following relation kept true:

$$\frac{s\omega_e}{g} \leq 0.25 \quad (157)$$

More details of the radiation condition and the applied source shifting method can be found in Graefe (2014).

2.4.2 Computation of the Nonlinear Stationary Forward Speed Potential

The computation of the nonlinear stationary forward speed potential was based on the work of Söding (2009a) and Graefe (2014). An existing numerical method (Graefe (2014)) provided the nonlinear stationary forward speed potential.

The body and the dynamic and kinematic free surface boundary conditions were already introduced in equation (151), (152) and (153) (153). For the stationary flow problem, the total potential in equation (150) simplifies to

$$\phi_t(\vec{x}) = -sx + \phi_0 \quad (158)$$

For the stationary flow problem, it follows $\partial\phi_t/\partial t = 0$. Inserting equation (158) into the dynamic free surface boundary condition (equation (151)), the stationary free surface elevation, ζ^0 , follows as

$$\zeta^0 = -\frac{1}{g}\left(\vec{U}\nabla\phi^0 + \frac{1}{2}|\nabla\phi^0|^2\right) \quad (159)$$

The dynamic boundary condition requires an iterative solution. After each iteration step, the source strengths as well as trim and sinkage of the ship are updated. Then the wave elevation on the free surface is determined. For the kinematic boundary condition in equation (152), the time derivative of the free surface elevation is zero, $\partial\zeta/\partial t = 0$. Thus, the kinematic boundary condition at the free surface simplifies to

$$(\vec{U} + \nabla\phi_0) \cdot \vec{n} \quad (160)$$

and is identical to the body boundary condition in equation (153).

2.4.3 Computation of the First Order Velocity Potential of an Elastic Vibrating Hull

In the present work, new linear boundary conditions at the body and the free surface were developed to consider the elastic deflection of the hull due to torsion as well as vertical and horizontal bending. The new developed boundary conditions were derived based on the method of Söding et al. (2012). They introduced a linear boundary element solver for the computation of wave induced forces and motions on a rigid ship in waves. Their technique couples the fully

nonlinear stationary forward speed flow problem with the linear oscillatory flow problem of a rigid body in waves.

The result of the stationary flow solver defined the new time average position of the ship for the periodic computations in waves. The time average wetted hull surface was updated according to the stationary wave system and the dynamic trim and sinkage. Thus, the kinematic boundary condition at the oscillating elastic ship hull was fulfilled at the updated wetted hull. The linearized kinematic and dynamic boundary condition at the free surface for the oscillating elastic ship were fulfilled at the elevated free surface according to the stationary wave system.

There are essentially two different methods to formulate the coupling of the stationary velocity potential and the oscillating velocity potential in waves. The first method is based on the assumption that the stationary velocity potential is constant in the inertial coordinate system. Then the body boundary condition contains second order derivatives of the stationary velocity potential, the so-called m -terms (Ogilvie and Tuck (1969)), because the ship in waves moves relative to the stationary velocity potential. The second method of Hachmann (1991) assumes that the stationary velocity potential is constant in the body-fixed coordinate system. Then the kinematic and dynamic boundary conditions at the free surface contain second order derivatives of the stationary velocity potential because the velocity potential moves relative to the free surface. Söding et al. (2012), Söding (1993) or Graefe (2014) discuss additional details of this technique. In general, second order derivatives are difficult to compute numerically and can, therefore, lead to inaccuracies (Bertram and Thiart (1998), Bertram (2000) or Zaho and Faltinsen (1989)). However, to calculate the oscillating velocity potential and, finally, the pressure on the ship's hull, the influence of second derivatives of the stationary velocity potential is less when these derivatives are included in the kinematic and dynamic free surface boundary conditions and not in the body boundary condition. Therefore, the method of Hachmann was applied for the present work.

The frequency domain solver used the same coordinate systems as previously introduced in section 2.1, Figure 3, where \vec{x} denotes a vector in the inertial coordinate system and $\underline{\vec{x}}$ denotes a vector in the body fixed coordinate system.

Furthermore, a cross section coordinate system was used, $\vec{r} = \{\gamma; \varepsilon; \delta\}^T$ to describe the rotation of a cross section due to an elastic deformation, see Figure 14.

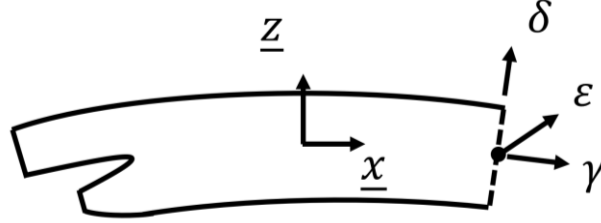


Figure 14: Illustration of the cross-section coordinate system.

For the computation of frequency dependant hydrodynamic coefficient of rigid body motions and elastic ship deformations, harmonic oscillations were assumed. Thus, the oscillating first order potential follows as

$$\phi^1(t) = Re(\hat{\phi}^1 e^{i\omega_e t}) \quad (161)$$

The hat symbol designates a complex amplitude and i is the unit imaginary number. Re denotes that the real component of the complex number. The linearization of the periodic velocity potential allows to compute ϕ^1 as the superposition of the potential of the incoming wave $\hat{\phi}_W^1$, the diffraction potential $\hat{\phi}_D^1$ and the radiation potential $\hat{\phi}_{R,j}^1$ due to the rigid body motion or natural elastic mode j . Inserting the above expressions into equation (156) and finally into the expression of the total potential in equation (150) results in the following expression of the total potential

$$\begin{aligned} \phi^t(\vec{x}, t) = & -sx + \phi^0(\underline{x}, \varepsilon, \delta) + Re\left(\left(\hat{\phi}_W^1 + \hat{\phi}_D^1\right)e^{i\omega_e t}\right) \\ & + \sum_{j=0}^{jmax} Re\left(\hat{\phi}_{R,j}^1 e^{i\omega_e t}\right) \end{aligned} \quad (162)$$

The sum over the radiation potential superpose the contribution of every rigid body motion and elastic natural mode. The first six modes designated rigid body motions and the further modes designated elastic modes.

To derive the linear dynamic and kinematic boundary condition at the free surface and the linear body boundary condition, equation (162) was inserted into the boundary conditions in equations (151), (152) and (153). The new linear boundary conditions for an elastic vibrating hull were derived by following the procedure of Graefe (2014), who derived boundary conditions for rigid ships to compute ship-ship interaction. Applying a first order Taylor expansion for the stationary potential it follows

$$\phi^0(\underline{\vec{x}}) = \phi^0(\underline{\vec{x}}) - \nabla\phi^0(\underline{\vec{x}}) \cdot \widehat{\underline{\vec{w}}} \quad (163)$$

$\widehat{\underline{\vec{w}}}$ is the complex amplitude vector of the displacement of a point due to rigid and elastic ship motions. For elastic vibrations the motion of a point $\underline{\vec{p}}$ on the body surface can be described as follows (linearized):

$$\widehat{\underline{\vec{w}}} = \widehat{\underline{\vec{w}}}_p + \widehat{\underline{\alpha}}_b \times \underline{\vec{p}} + \widehat{\underline{\alpha}}_T \times \underline{\vec{p}} \quad (164)$$

The first term on the r.h.s accounts for the longitudinal, horizontal and vertical translation due to pure longitudinal strain and horizontal and vertical bending $\widehat{\underline{\vec{w}}}_p = (\widehat{w}_M; \widehat{w}_{B,y+S,y}; \widehat{w}_{B,y+S,z})^T$, see equation (97). The second term accounts for the displacement due to bending-induced cross sections rotations with $\widehat{\underline{\alpha}}_b = (0; \widehat{\alpha}; \widehat{\beta})^T$. The third term accounts for the displacement due to torsion induced cross section rotations with $\widehat{\underline{\alpha}}_T = (\widehat{\chi}; 0; 0)^T$. For rigid body motions, the displacement of $\underline{\vec{p}}$ follows from

$$\widehat{\underline{\vec{w}}} = \widehat{\underline{G}} + \widehat{\underline{\theta}} \times \underline{\vec{p}} \quad (165)$$

Were $\widehat{\underline{G}}$ is the complex amplitude vector of the body translations, surge, sway and heave and $\widehat{\underline{\theta}}$ is the complex amplitude vector of the body rotations, roll, pitch and yaw.

Inserting equation (163) into equation (162) result in the following expression of the total velocity potential:

$$\begin{aligned} \phi^t(\vec{x}, t) = & -sx + \phi^0(\vec{x}) - Re[\nabla\phi^0(\vec{x}) \cdot \widehat{w}e^{i\omega_e t}] \\ & + Re \left[\left(\widehat{\phi}_W^1 + \widehat{\phi}_D^1 + \sum_{j=0}^{j_{max}} \widehat{\phi}_{R,j}^1 \right) e^{i\omega_e t} \right] \end{aligned} \quad (166)$$

The following derivation steps will discuss the computation of the gradient of the total potential, $\nabla\phi^t(\vec{x}, t)$. The gradient of the total potential results from the gradient of each term in equation (166). The gradient of the term $\nabla\phi^0(\vec{x}) \cdot \widehat{w}$ has to be examined more detailed. It follows

$$\begin{aligned} \nabla(\nabla\phi^0(\vec{x}) \cdot \widehat{w}) & = (\nabla\phi^0 \cdot \nabla)\widehat{w} + (\widehat{w} \cdot \nabla)\nabla\phi^0 + \nabla\phi^0 \times (\nabla \times \widehat{w}) \\ & + \widehat{w} \times (\nabla \times \nabla\phi^0) \end{aligned} \quad (167)$$

The first term on the r.h.s. of equation (167) follows from

$$(\nabla\phi^0 \cdot \nabla)\widehat{w} = \begin{bmatrix} \frac{\partial\widehat{w}_x}{\partial x} & \frac{\partial\widehat{w}_x}{\partial y} & \frac{\partial\widehat{w}_x}{\partial z} \\ \frac{\partial\widehat{w}_y}{\partial x} & \frac{\partial\widehat{w}_y}{\partial y} & \frac{\partial\widehat{w}_y}{\partial z} \\ \frac{\partial\widehat{w}_z}{\partial x} & \frac{\partial\widehat{w}_z}{\partial y} & \frac{\partial\widehat{w}_z}{\partial z} \end{bmatrix} \begin{pmatrix} \nabla\phi_x^0 \\ \nabla\phi_y^0 \\ \nabla\phi_z^0 \end{pmatrix} \quad (168)$$

The matrix on the r.h.s. of equation (168) includes the derivatives of the displacement. According to the finite element approach that was introduced in section 2.3, elastic displacements were computed using element shape functions according to equation (97). The derivative of the longitudinal displacements follow as

$$\frac{\partial\widehat{w}_x}{\partial x} = \sum_{i=1,8} \left[\frac{\partial N_i(x)}{\partial x} \widehat{u}_i \right] + \frac{\partial\alpha(x)}{\partial x} \underline{z} - \frac{\partial\beta(x)}{\partial x} \underline{y} \quad (169)$$

$$\frac{\partial \hat{w}_x}{\partial y} = -\beta(x) \quad (170)$$

$$\frac{\partial \hat{w}_x}{\partial z} = \alpha(x) \quad (171)$$

the derivatives of the transverse displacements follow as

$$\frac{\partial \hat{w}_y}{\partial x} = \sum_{i=2,6,9,13} \left[\frac{\partial N_i(x)}{\partial x} \hat{u}_i \right] - \frac{\partial \chi(x)}{\partial x} \underline{\underline{z}} \quad (172)$$

$$\frac{\partial \hat{w}_y}{\partial y} = 0 \quad (173)$$

$$\frac{\partial \hat{w}_y}{\partial z} = -\chi(x) \quad (174)$$

and the derivatives of the vertical displacements result from

$$\frac{\partial \hat{w}_z}{\partial x} = \sum_{i=3,5,10,12} \left[\frac{\partial N_i(x)}{\partial x} \hat{u}_i \right] + \frac{\partial \chi(x)}{\partial x} \underline{\underline{y}} \quad (175)$$

$$\frac{\partial \hat{w}_z}{\partial y} = \chi \quad (176)$$

$$\frac{\partial \hat{w}_z}{\partial z} = 0 \quad (177)$$

Inserting the derivatives of the displacements into equation (168) results in

$$(\nabla\phi^0 \cdot \nabla)\hat{v} = \begin{bmatrix} \sum_{i=1,8} \left[\frac{\partial N_i}{\partial x} \hat{u}_i \right] + \frac{\partial \alpha}{\partial x} \underline{z} - \frac{\partial \beta}{\partial x} \underline{y} & -\beta & \alpha \\ \beta - \frac{\partial \chi}{\partial x} \underline{z} & 0 & -\chi \\ -\alpha + \frac{\partial \chi}{\partial x} \underline{y} & \chi & 0 \end{bmatrix} \nabla\phi^0 \quad (178)$$

The second term on the r.h.s. of equation (167) can be substituted by

$$(\hat{w} \cdot \nabla)\nabla\phi^0 = \nabla\nabla\phi^0\hat{w} \quad (179)$$

The third term on the r.h.s. of equation (167) follows from

$$\nabla\phi^0 \times (\nabla \times \hat{w}) = \begin{pmatrix} -2\chi \\ -2\alpha + \frac{\partial \chi}{\partial x} \underline{y} \\ -2\beta + \frac{\partial \chi}{\partial x} \underline{z} \end{pmatrix} \times \nabla\phi^0 \quad (180)$$

The last term on the r.h.s. of equation (167) follows as

$$\hat{w} \times (\nabla \times \nabla\phi^0) = \hat{w} \times \begin{pmatrix} \frac{\partial^2 \phi^0}{\partial y \partial z} - \frac{\partial^2 \phi^0}{\partial z \partial y} \\ \frac{\partial^2 \phi^0}{\partial z \partial x} - \frac{\partial^2 \phi^0}{\partial x \partial z} \\ \frac{\partial^2 \phi^0}{\partial x \partial y} - \frac{\partial^2 \phi^0}{\partial y \partial x} \end{pmatrix} = \vec{0} \quad (181)$$

Inserting above expressions in equation (167) results as

$$\nabla(\nabla\phi^0(\vec{x}) \cdot \hat{w}) = \nabla\nabla\phi^0\hat{w} + \mathbf{V}\nabla\phi^0 - \hat{\alpha} \times \nabla\phi^0 \quad (182)$$

With the matrix \mathbf{V} being

$$\mathbf{v} = \begin{bmatrix} \sum_{i=1,8} \left[\frac{\partial N_i}{\partial x} \hat{u}_i \right] + \frac{\partial \alpha}{\partial x} \underline{z} - \frac{\partial \beta}{\partial x} \underline{y} & -\frac{\partial \chi}{\partial x} \underline{z} & \frac{\partial \chi}{\partial x} \underline{y} \\ 0 & 0 & 0 \\ 0 & 0 & 0 \end{bmatrix} \quad (183)$$

The gradient of the total potential then results in

$$\begin{aligned} \nabla \phi^t(\vec{x}, t) = & \vec{U} + \nabla \phi^0(\vec{x}) - Re[(\nabla \nabla \phi^0 \hat{w} + \mathbf{V} \nabla \phi^0 - \hat{\alpha} \times \nabla \phi^0) e^{i\omega_e t}] \\ & + Re \left[\left(\nabla \hat{\phi}_W^1 + \nabla \hat{\phi}_D^1 + \sum_{j=0}^{jmax} \nabla \hat{\phi}_{R,j}^1 \right) e^{i\omega_e t} \right] \end{aligned} \quad (184)$$

Here $\hat{\alpha} = \hat{\alpha}_b + \hat{\alpha}_T$. The time derivative of the total potential follows as

$$\dot{\phi}^t(\vec{x}, t) = Re \left[i\omega_e \left(\nabla \phi^0(\vec{x}) \cdot \hat{w} + \hat{\phi}_W^1 + \hat{\phi}_D^1 + \sum_{j=0}^{jmax} \hat{\phi}_{R,j}^1 \right) e^{i\omega_e t} \right] \quad (185)$$

Applying above technique on the definition of the total wave elevation results in

$$\zeta^t(\vec{x}, t) = \zeta^0(\vec{x}) + Re[(\zeta^1 - \hat{w} \nabla \zeta^0) e^{i\omega_e t}] \quad (186)$$

And the gradient of the total wave elevation follows from

$$\nabla \zeta^t(\vec{x}, t) = \nabla \zeta^0(\vec{x}) + Re[\nabla \zeta^1 + \hat{\alpha} \times \nabla \zeta^0 - \mathbf{V} \nabla \zeta^0 - \nabla \zeta^0 \hat{w}] e^{i\omega_e t} \quad (187)$$

Above expressions were inserted into equation (151) to achieve the dynamic boundary condition. After linearization the linear dynamic boundary condition at the free surface reads as

$$\begin{aligned}
 & (\vec{U} + \nabla\phi^0(\vec{x})) (\nabla\phi^1 + \hat{\alpha} \times \nabla\phi^0 - \mathbf{V}\nabla\phi^0 - \nabla\nabla\phi^0\hat{w}) \\
 & + i\omega_e (\phi^1 - \hat{w}\nabla\phi^0(\vec{x})) + g(\zeta^1 - \hat{w}\nabla\zeta^0) = 0
 \end{aligned} \tag{188}$$

From equation (152), the kinematic boundary condition reads as:

$$\begin{aligned}
 & i\omega_e [\zeta^1 - \hat{w}\nabla\zeta^0] + \vec{n}^o [\nabla\phi^1 - \mathbf{V}\nabla\phi^0] + (\vec{U} + \nabla\phi^0)(\nabla\zeta^1 - \mathbf{V}\nabla\zeta^0) \\
 & + \begin{bmatrix} -\phi^0/\partial y \\ \phi^0/\partial x \\ u \cdot \partial\zeta^0/\partial y \end{bmatrix} \hat{\alpha} + \hat{A} = 0
 \end{aligned} \tag{189}$$

Here, \hat{A} includes all second order derivatives of the stationary potential and the stationary wave system:

$$\hat{A} = \frac{-\hat{w}\vec{n}^o}{|\vec{n}^o|^2} \vec{n}^o [(\nabla^2\phi^0)\vec{n}^o + (\nabla^2\zeta^0)(\nabla\phi^0 - \vec{U})] \tag{190}$$

\vec{n}^o is the normal vector of the stationary free surface. A detailed explanation of the numerical calculation of equation (190) is given by Graefe (2014).

The body boundary condition was already introduced, see equation (153). Assuming a harmonic oscillating displacement of the body surface due to rigid body motions or elastic deformations, the body boundary condition can be expressed as

$$Re[(\nabla\phi^t(\vec{x}, t) - i\omega_e\hat{w}) \cdot \hat{\vec{n}}(\vec{x})e^{i\omega_e t}] = 0 \tag{191}$$

In contrast to a classical seakeeping analysis (rigid body), the change of hull normal vector depends on time and on the longitudinal position, which is expressed as follows:

$$\hat{\vec{n}}(\vec{x}) = \underline{\vec{n}}(\vec{x}) + \hat{\alpha} \times \underline{\vec{n}}(\vec{x}) \tag{192}$$

Accordingly, the elastic body boundary condition is written as follows:

$$\vec{n} \cdot (\nabla\phi^1 - \hat{\alpha} \times \vec{U} - \mathbf{V}\nabla\phi^0 - i\omega_e \hat{w}) = 0 \quad (193)$$

The implementation of the boundary conditions and the solving procedure of the equation system follows the procedure described by Graefe (2014).

The periodic first order pressure at the hull can be computed from the Bernoulli equation, equation (149), as follows

$$\frac{p - p_a}{\rho} = \frac{1}{2} s^2 - \frac{1}{2} |\nabla\phi^t(\vec{x}, t)|^2 - \frac{\partial\phi^t(\vec{x}, t)}{\partial t} - gz \quad (194)$$

Inserting equation (184) and (185) into equation (194), the complex amplitude of the first order pressure, \hat{p}^1 , was computed from

$$\frac{\hat{p}^1}{\rho} = - \left(\vec{U} + \nabla\phi^0(\vec{x}) \right) \left[\nabla\hat{\phi}^1 + \hat{\alpha} \times \nabla\phi^0 - \mathbf{V}\nabla\phi^0 \right] - i\omega_e (\hat{\phi}^1 - \hat{w}\nabla\phi^0) \quad (195)$$

with ρ being the fluid density. The contributions from the hydrostatic pressure is not included in equation (195), because the hydrostatic pressure was directly computed in time domain, see section 2.2.2.1. For the elastic modes, $\hat{\alpha} = (\hat{\chi}; \hat{\alpha}; \hat{\beta})^T$ and \mathbf{V} in the above equations vary depending on the longitudinal coordinate. For the elastic modes, $\hat{\chi}$, $\hat{\alpha}$ and $\hat{\beta}$ as well as their derivatives in \mathbf{V} were computed based on element shape functions according to equation (97). If equations (187), (188), (189), (193) and (195) were applied for rigid body motions, the vector of cross section rotations is substituted by the vector of rigid body rotation (roll, pitch and yaw) with $\hat{\alpha} = \hat{\theta}$. The rigid body rotations are constant over the complete ship. In this case, the derivative of the cross-section rotation respect x are zero, $(\partial\hat{\theta})/\partial x = \vec{0}$. Consequently, all components of the matrix \mathbf{V} are zero. Then the equation (187), (188), (189), (193) and (195) simplify to the same equations introduced by Söding et al. (2012) for a rigid ship.

The radiation-induced first order pressure and the diffraction-induced first order pressure were computed separately. For the computation of the radiation-induced first order pressure, the potential of the incoming wave, $\hat{\phi}_W^1$, and diffraction potential, $\hat{\phi}_D^1$, were zero. In this case, the frequency dependent part of equation (195) was used to calculate hydrodynamic added mass (real part) and hydrodynamic damping (imaginary part) due to all rigid and elastic vibration modes. Hydrodynamic damping, $\underline{\mathbf{b}}_i$, of the i^{th} body panel is proportional to the imaginary part of the frequency dependent hydrodynamic first order pressure divided by $-\omega_e$

$$\underline{\mathbf{b}}_i(\omega_e) \approx - \frac{Im \left(- \left(\vec{U} + \nabla \phi^0(\vec{x}) \right) \nabla \hat{\phi}^1 - i \omega_e \left(\hat{\phi}^1 - \hat{w} \nabla \phi^0 \right) \right)}{\omega_e} \quad (196)$$

The hydrodynamic added mass, $\underline{\mathbf{A}}_i$, of the i^{th} body panel is proportional to the real part of the frequency dependent hydrodynamic first order pressure divided by ω_e^2

$$\underline{\mathbf{m}}_i(\omega_e) \approx \frac{Re \left(- \left(\vec{U} + \nabla \phi^0(\vec{x}) \right) \nabla \hat{\phi}^1 - i \omega_e \left(\hat{\phi}^1 - \hat{w} \nabla \phi^0 \right) \right)}{\omega_e^2} \quad (197)$$

The components of equation (195) that are frequency independent follow from

$$\frac{\hat{p}_{ind}^1}{\rho} = - \left(\vec{U} + \nabla \phi^0(\vec{x}) \right) \left[\hat{\alpha} \times \nabla \phi^0 - \mathbf{V} \nabla \phi^0 \right] \quad (198)$$

This component results from the assumption that the stationary flow is constant in body coordinate system (Hachmann's approach). As mentioned above, \mathbf{V} includes the first derivatives of the body surface rotations, and it was assumed that its contribution in equation (198) is small compared to the rotation angles $\hat{\alpha}$. Therefore, the term $\mathbf{V} \nabla \phi^0$ was neglected. The remaining components in equation (198) depend only on the cross-sectional rotation angle, $\hat{\alpha}$. This pressure component was interpreted as an additional restoring pressure component and the corresponding restoring forces and moments were modeled using the

restoring matrix \mathbf{c} in the nonlinear rigid body motion solver (see equation (61) and the elastic deformation solver (see equation (135))).

For the computation of the diffraction potential and diffraction-induced first order pressure, the body was fixed (no rigid body motion or elastic deformation). Consequently, the radiation potential, $\hat{\phi}_{R,j}^1$, was zero. The definition of the velocity potential of the incoming wave, $\hat{\phi}_W^1$, is described in section 2.4.5.

2.4.4 Infinite Frequency Solution

In section 2.2.2.1 it was shown that the hydrodynamic added mass and damping at infinite frequency is required to compute the radiation forces, see equations (22), (27) and (28). To determine these hydrodynamic coefficients for infinite frequency, a simplified boundary value problem was solved. The free surface boundary conditions were substituted by the high-frequency condition:

$$\hat{\phi}^1 = 0 \text{ (on the free surface)} \quad (199)$$

Söding (2009b) investigated linear springing induced vibrations of the two-node and three-node vertical bending modes in frequency domain by coupling a boundary element flow solver and a finite beam element solver. The length of waves that excited linear springing-induced vibrations of the three-node vertical bending mode was so small that the free surface discretization would have had to be refined significantly. To avoid such refinements, he applied the high-frequency free surface condition to compute the frequency dependent excitation and radiation forces.

For the new numerical method, this high frequency boundary condition was applied to compute the hydrodynamic added mass and hydrodynamic damping for infinite frequency. Usually, this condition is analytically fulfilled by placing image sources with opposite source strengths symmetrically with respect to the plane $z = 0$. However, to fulfill this condition on the nonlinear stationary free surface with its elevation $z = \zeta^0$, the image sources were mirrored at the elevated free surface due to the stationary wave system. In this way, the boundary condition is not fulfilled exactly, but to a sufficient level of accuracy, see Söding (2009b). Because the high frequency condition on the free surface was fulfilled

using mirrored sources, only the boundary conditions on the body surfaces must be treated numerically during the computation.

As aforementioned, equation (197) and (198) was applied to computed the frequency dependant hydrodynamic added mass and hydrodynamic damping. For the computation of the hydrodynamic added mass and hydrodynamic damping for infinite frequency, the complex amplitude of the first order potential was normalized with the wave encounter frequency, $\hat{\phi}^1(\omega_e) = \hat{\phi}^1/\omega_e$. Following this procedure the hydrodynamic damping of a body panel i results from

$$B_i(\omega_e) = \rho \underline{\vec{n}}_i \int_{S_i} \text{Im} \left[\left(\vec{U} + \nabla \phi^0(\vec{x}) \right) \nabla \hat{\phi}^1 + i \omega_e \hat{\phi}^1 - i \widehat{\vec{w}}_i \nabla \phi^0 \right] dA \quad (200)$$

And the hydrodynamic added mass results from

$$A_i(\omega_e) = \rho \underline{\vec{n}}_i \int_{S_i} \text{Re} \left[-\frac{1}{\omega_e} \left(\vec{U} + \nabla \phi^0(\vec{x}) \right) \nabla \hat{\phi}^1 - i \left(\hat{\phi}^1 - \frac{\widehat{\vec{w}}_i \nabla \phi^0}{\omega_e} \right) \right] dA \quad (201)$$

Applying the patch method (see e.g. Graefe (2014)) on equation (155), the body boundary condition of the rigid and elastic body surface was solved numerically

$$\sum_i^N q_i \int_{S_i} \underline{\vec{n}}_i \nabla G_i dA = \sum_{i=1}^N S_i \underline{\vec{n}}_i \left(\hat{\vec{\alpha}} \times \vec{U} + \mathbf{V} \nabla \phi^0 + i \omega_e \widehat{\vec{w}}_i \right) \quad (202)$$

Substituting $H_i = \int_{S_i} \underline{\vec{n}}_i \nabla G_i dA$ and dividing all by ω_e results in

$$\sum_i^N \tilde{q}_i(\omega_e) H_i = \sum_{i=1}^N S_i \underline{\vec{n}}_i \left(\frac{\hat{\vec{\alpha}} \times \vec{U}}{\omega_e} + \frac{\mathbf{V} \nabla \phi^0}{\omega_e} + i \widehat{\vec{w}}_i \right) \quad (203)$$

With $\tilde{q}_i(\omega_e) = q_i(\omega_e)/\omega_e$. Applying $\omega_e \rightarrow \infty$ in equation (203) it follows

$$\sum_i^N \tilde{q}_i(\infty) H_i = \sum_{i=1}^N i S_i \underline{\vec{n}}_i \widehat{w}_i \quad (204)$$

Recall that the first order potential was computed as $\widehat{\phi}^1(\vec{x}) = \sum_i^N \tilde{q}_i(\infty) H_i$. In equation (204) the panel area S_i and the panel normal vector $\underline{\vec{n}}_i$ are real numbers. The total motion of the panel is described by a complex amplitude, \widehat{w}_i , however, the motion is predefined according to the rigid body motion or the elastic deformation of the hull and only the real part is unequal zero. Consequently, for \tilde{q}_i and the corresponding normalized first order potential, $\widehat{\phi}^1$, only the imaginary part contributes and is unequal zero. For that reason, the term $i\omega_e \widehat{\phi}^1$ in equation (200) has only a real component and does not contribute to the hydrodynamic damping at infinite frequency. Simplifying the integral by assuming that $\widehat{\phi}^1$ and $\nabla\phi^0$ are constant over one panel, the hydrodynamic damping for infinite frequency follows as

$$B_i(\infty) = \rho S_i \underline{\vec{n}}_i \left[\left(\vec{U} + \nabla\phi^0(\vec{x}) \right) \nabla\widehat{\phi}^1(\infty) - i \widehat{w}_i \nabla\phi^0 \right] \quad (205)$$

Similarly, the hydrodynamic added mass for infinite frequency follows from

$$A_i(\infty) = \lim_{\omega_e \rightarrow \infty} \rho S_i \underline{\vec{n}}_i \operatorname{Re} \left[-\frac{1}{\omega_e} \left(\vec{U} + \nabla\phi^0(\vec{x}) \right) \nabla\widehat{\phi}^1(\omega_e) - i \left(\widehat{\phi}^1 - \frac{\widehat{w}_i \nabla\phi^0}{\omega_e} \right) \right] \quad (206)$$

Which finally results in

$$A_i(\infty) = -\rho S_i \underline{\vec{n}} \operatorname{Re} \left[i \widehat{\phi}^1(\infty) \right] \quad (207)$$

Equation (205) and (206) shows that the hydrodynamic added mass and hydrodynamic damping for infinite frequency is bounded and unequal zero.

2.4.5 First Order Wave Theory

Natural seaway, often called irregular sea, is characterised by varying wave amplitudes, wave frequencies and direction of wave propagation (spreading angle). However, investigation of wave induced rigid body ship motions and elastic vibrations are often performed in regular waves (constant wave amplitude, wave frequency and propagation direction) to gain an insight of the general nature of wave-induced ship responses. Furthermore, regular waves can be reproduced easily, which is of particular importance for the validation of e.g. numerical results with experimental data. For that reason, regular waves were applied to validate the new numerical method. To describe the free surface elevation, a coordinate system located at the calm water surface was introduced, $\vec{x}^{(w)} = (x^{(w)}; y^{(w)}; z^{(w)})^T$ with $z^{(w)}$ pointing upwards. Figure 15 illustrates the location of the coordinate system, the time averaged free surface and the instantaneous free surface elevation due to an incoming wave with a wave amplitude ζ^1 . The wave height is $2\zeta^1$. Figure 15 also shows the bottom and the water depth, L . For the present work, water of infinite depth was applied only. Consequently, a bottom condition (no flow through the bottom) was not applied. Furthermore, Figure 15 illustrates that the Laplace-Equation (equation (145)) is fulfilled in the whole domain.

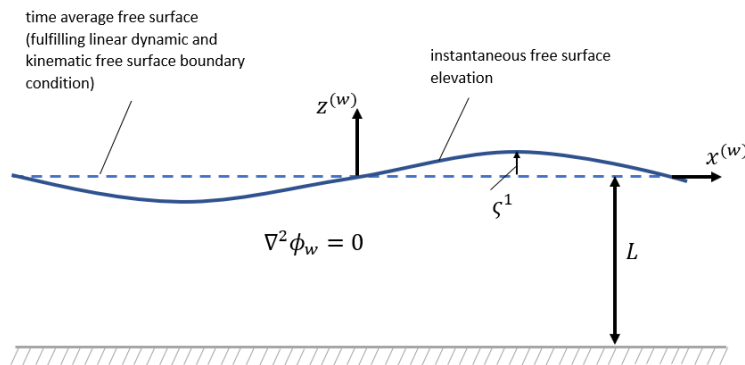


Figure 15: Visualization of a linear wave with the wave coordinate system, $\vec{x}^{(w)} = [x^{(w)}, y^{(w)}, z^{(w)}]$, the wave amplitude ζ^1 and the water depth D .

Figure 16 shows the ship and its body fixed coordinate system relative to the wave coordinate system. The angle μ is called the wave encounter angle or wave heading angle. $\varepsilon = 0^\circ$ denotes following waves and $\varepsilon = 180^\circ$ denotes head waves. Furthermore, Figure 16 shows the definition of the wave length λ .

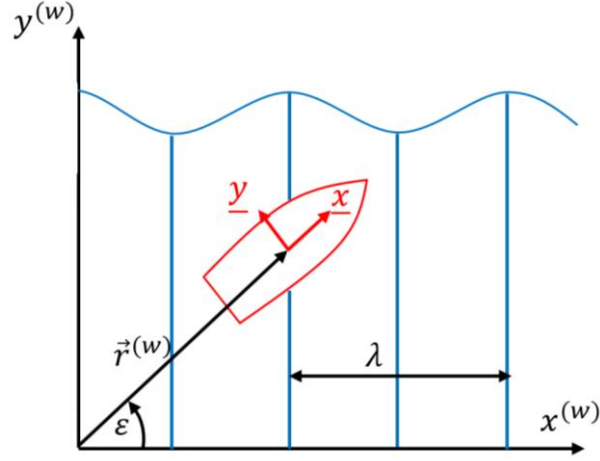


Figure 16: Visualisation of the wave encounter angle, μ , and wave length, λ .

Linear wave theory is based on the assumption that the wave steepness are small. Mathematically, linear wave theory can be applied when the wave steepness $h = H/\lambda$ is smaller than 0.007, Le Méhauté (1976). However, in practice, linear wave theory is often used for higher wave steepnesses. The later validation study will show that for the computation of rigid body ship motions and elastic vibrations the maximum wave height is often limited due to an immersed deck and the corresponding generation of breaking waves. An extensive derivation of the governing equations of linear waves can be found in Dean and Dalrymple (1991) or Mei et al. (2005). In the present work, the most important properties of linear waves are summarized. The potential of a linear deep water wave reads as

$$\phi_w(\vec{x}, t) = \text{Re} \left(\hat{\zeta}^1 \frac{i\omega}{k} e^{kz^{(w)}} e^{i(\omega t - \vec{k}\vec{x}^{(w)})} \right) \quad (208)$$

$\hat{\zeta}^1$ is the complex wave amplitude, i the imaginary number, ω the wave angular frequency, $k = 2\pi/\lambda$ the wave number and t the time.

Due to ships forward speed, s , the wave encounter frequency, ω_e , follows from

$$\omega_e = \omega - sk \cos \mu \quad (209)$$

The pressure under a linear wave can be computed by inserting ϕ_w in the Bernoulli equation, equation (149). The integration of the wave induced pressure, p_{FK} , over the instantaneous wetted hull surface results in the combined Froude-Krylov and hydrostatic forces and moments according to equation (44), which was computed in time domain. Substituting $\hat{\zeta}^1 e^{i(\omega t - \vec{k}\vec{x})}$ by $\zeta(\vec{x}, t)$ and considering that the new numerical method coupled the stationary free surface elevation, $\zeta^0(\vec{x})$, with the incoming wave, p_{FK} follows from

$$p_{FK+Hyd}(\vec{x}, \vec{k}, \omega_e, t) = \rho g \left[-z^{(w)} + \zeta^0(\vec{x}) + \zeta(\vec{x}, t) e^{kz^{(w)}} \right] \quad (210)$$

The wave induced velocity potential from equation (208), and the wave-induced pressure from equation (210) were derived by fulfilling the free surface boundary conditions at the time average free surface position (due to the stationary free surface elevation). For locations below the time average free surface, $z^{(w)}$ is negative and it follows $e^{kz^{(w)}} \leq 1.0$ in equation (210). However, for locations above the time average free surface $z^{(w)}$ becomes positive and $e^{kz^{(w)}}$ would introduce increasing pressure amplitudes. Consequently, equation (210) can only be used to compute the pressure at locations below the time average free surface. However, the new numerical method integrates p_{FK} over the instantaneous wetted surface and thus has to integrate the pressure also at hull locations above the time average wetted hull surface. To avoid the use of higher order wave theory, stretching method can be applied to stretch the time average free surface to the instantaneous free surface due to the incoming wave. In the present work, the Wheeler stretching method was applied, Wheeler (1970), and the pressure at the instantaneous wetted hull surface then follows from

$$p_{FK+Hyd}(\vec{x}, \vec{k}, \omega_e, t) = \rho g \left[-z^{(w)} + \zeta^0(\vec{x}) + \zeta^1(\vec{x}, t) e^{k(z^{(w)} - \zeta^1(\vec{x}^{(w)}, t))} \right] \quad (211)$$

2.5 Spatial Discretisation

The new numerical method used two different types of hull grids and three different types of free surface grids. For the computation of the stationary wave

system and the dynamic trim and sinkage, the free surface was panelized with a structured grid based on rectangular panels. The hull was discretized with triangles. The top image in Figure 17 shows exemplary a top view of the stationary free surface grid and the hull grid. As discussed in section 2.4, an interactive procedure solved the stationary wave system as well as dynamic trim and sinkage. During each iteration, the body grid was adjusted according to the computed free surface elevation. The lower image in Figure 17 shows exemplary a side view of the adjusted body grid according to the stationary wave elevation.

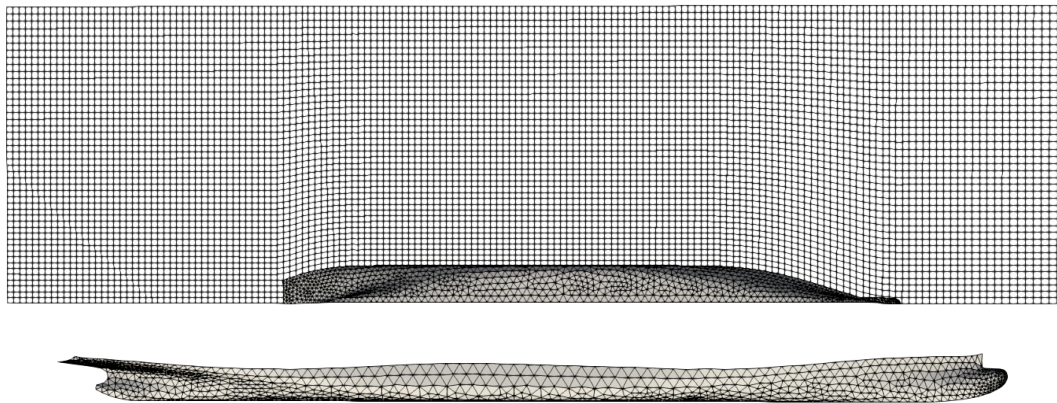


Figure 17: Top view of the free surface and body grid and side view of the body grid for the stationary flow problem.

The final result of the stationary flow problem defined the contour of the boundaries for the frequency domain simulation. The body grid was used for the frequency domain simulations with out any further changes. The free surface grid for the frequency domain simulations differed from the free surface grid used during the stationary simulation. The free surface grid for the frequency domain simulations was divided into one inner grid, one front grid, one aft grid and two side grids, see the illustration in Figure 18. Recall that the stationary wave elevation defined the time averaged free surface elevation for the frequency domain simulations. Thus, the stationary wave elevation was mapped on the frequency domain free surface grid. The outer grids are used to ensure that generated waves travel away from the ship and being damped. This is achieved by using modified boundary conditions and an additional damping approach. More details about this technique can be found in Graefe (2014). For the computation of the hydrodynamic coefficients, the size of inner grid panels is important and should be adjusted to the length of the incoming wave. A detailed grid study is

presented in section 4. Further details about the stationary and frequency domain spatial discretisation can be found in Graefe (2014).

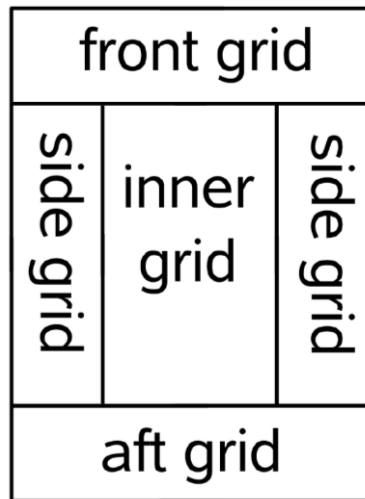


Figure 18: Illustration of the free surface grid used during frequency domain simulations, Graefe (2014)

As discussed in section 2, combined Froude-Krylov and hydrostatic forces and moments can be computed in time domain without solving a flow problem. Consequently, no free surface grid needs to be treated during the time domain simulations. However, combined Froude-Krylov and hydrostatic force and moments were integrated over the instantaneous wetted hull surface. The body grid that was used during the stationary and frequency domain simulation reached only up to the time average wetted hull surface. Consequently, an additional body grid was necessary to compute the combined Froude-Krylov and hydrostatic forces and moments during the time domain simulations. This time domain body grid covered the complete hull surface up to the main deck. Figure 19 shows exemplarily a side view of the time domain body grid. In time domain, the free surface intersects some body panels. The panels of the time domain body grid were based on triangles. For panels that are intersected by the free surface, the upper nodes of the panels were shifted downwards to the current free surface in the plane of the original panel. This procedure ensured that the correct wetted surface was considered at any time. Figure 20 indicates this procedure for a segment of a body grid. The grey line represents the instantaneous free surface, the dotted lines the initial grid and the solid lines the modified grid. Figure 21 shows exemplarily the instantiations wetted surface (dark grey colored) and correspondingly adjusted panels at the bow region of a container ship.

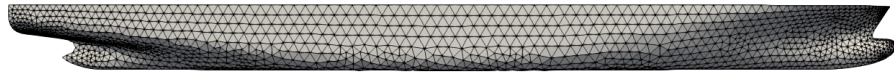


Figure 19: Side view of the time domain body grid.

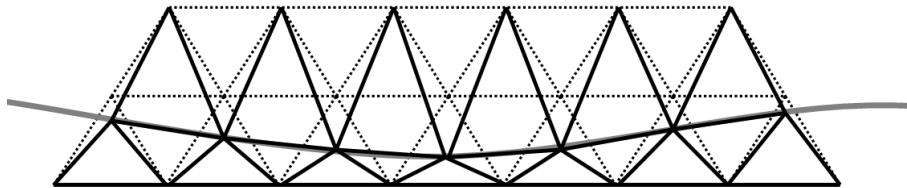


Figure 20: Adjustment of the body grid to account for the instantaneous free surface.

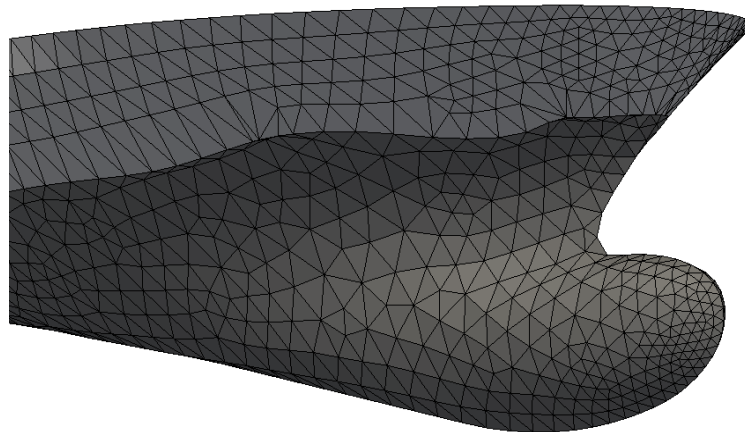


Figure 21: Example of the hull surface treatment during time domain simulations.

2.6 Calculation Procedure

Before computing wave-induced rigid body motions and elastic deformations, pre-computations were performed. During these pre-computations, the stationary flow problem was solved first, followed by solving for the wet natural modes. Next, transfer functions of hydrodynamic added mass and hydrodynamic damping were computed as well as their infinite frequency solution. Then the impulse response functions were determined.

2.6 Calculation Procedure

After the pre-computations, time domain calculations were started. As described above, the diffraction forces were based on the linear solution of the incident wave diffraction. The linear diffraction pressures were obtained for the undeformed/fixed hull and, consequently, the diffraction pressure was independent of the natural mode or rigid body motion. Therefore, the complex diffraction force amplitude according to the wave scenario was calculated first.

Due to the modal superposition technique, radiation pressures during the time domain simulation were individually computed for every rigid body motion and elastic mode, based on the hydrodynamic added mass, the hydrodynamic damping, and the convolution integral. Thus, the radiation forces were part of the coefficient matrix on the l.h.s. of the equation of motions (except for the part of the convolution integral that describes the memory effect). Thus, radiation forces are referred as being strongly coupled. The combined nonlinear Froude-Krylov and hydrostatic forces were calculated by considering the instantaneous rigid body motions and the elastic deformation. That means that the result of all considered rigid body motions and elastic deformations were superposed to compute the new hull position and the new normal vectors of the hull surface panels when computing the Froude-Krylov and hydrostatic pressures. This procedure was embedded in an internal iteration loop (two-way coupling). Finally, the rigid body motions, elastic deformations and associated sectional loads were obtained before continuing with the next time step. Figure 22 visualizes this calculation procedure.

2 Numerical Method to Compute the Rigid and Elastic Response of Ships in Wave

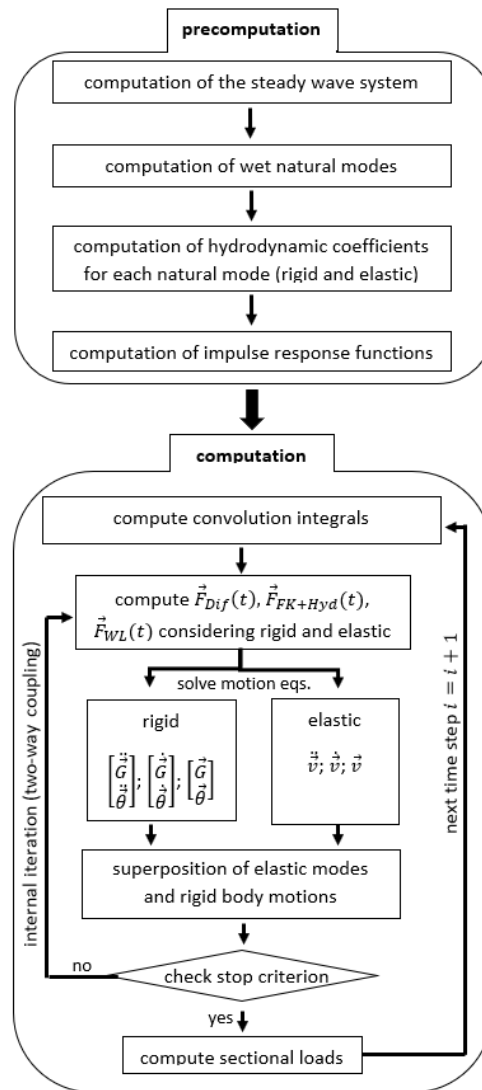


Figure 22: Calculation procedure of the new numerical method.

3 Test Cases

In the present work, four different ships were analysed during the validation and result study. Investigations of rigid body ship motions were performed for a VLCC tanker, a 220m long cruise ship and a 355m long post-Panamax container ship. Hydroelastic investigations were performed for a 333m long post-Panamax container ship. The following section describe the properties of each ship.

3.1 VLCC Tanker

The VLCC tanker was investigated for the verification of the convolution integral for the computation of radiation forces, see section 4.2, and for the validation of the computed wave added resistance in section 4.3.3. The main particulars of the VLCC tanker are listed in Table 3 and Figure 23 shows its section plan.

Table 3: Main particulars of the VLCC tanker

Description	Symbol	Unit	Values
Length between perpendiculars	L_{pp}	[m]	320
Moulded breadth	B	[m]	58
Draft	D	[m]	20.8
Displacement	Δ	[m ³]	312622
Block coefficient	C_B	[-]	0.81
Vertical centre of gravity	KG	[m]	18.60
Metacentric height	GM	[m]	5.71
Radius of gyration about x	r_{xx}	[m]	23.2
Radius of gyration about y	r_{yy}	[m]	80.0
Radius of gyration about z	r_{zz}	[m]	80.0

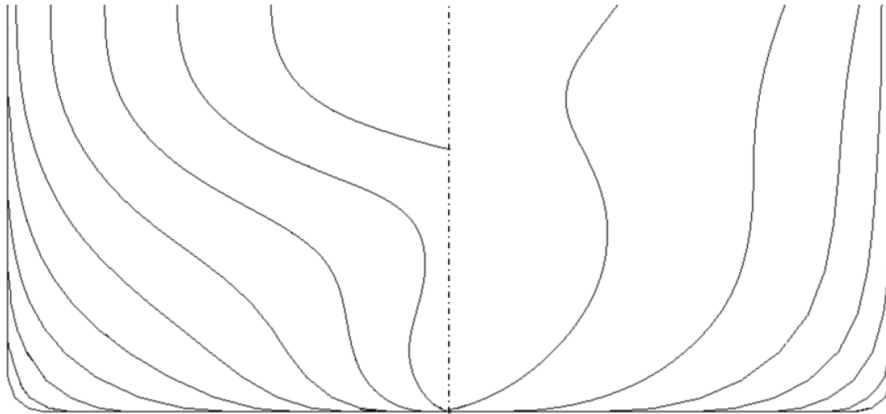


Figure 23: Section plan of the VLCC tanker, Sigmund (2019).

3.2 Cruise Ship

The cruise ship was investigated for the verification of the convolution integral for the computation of radiation forces, see section 4.2. The main particulars of the cruise ship are listed Table 4 and Figure 24 shows its section plan.

Table 4: Main particulars of the cruise ship

Description	Symbol	Unit	Values
Length between perpendiculars	L_{pp}	[m]	220.2
Moulded breadth	B	[m]	32.2
Draft	D	[m]	7.2
Displacement	Δ	[m ³]	33229
Block coefficient	C_B	[–]	0.65
Vertical centre of gravity	KG	[m]	14.94
Metacentric height	GM	GM	2.754
Radius of gyration about x	r_{xx}	[m]	13.14
Radius of gyration about y	r_{yy}	[m]	58.18
Radius of gyration about z	r_{zz}	[m]	58.18

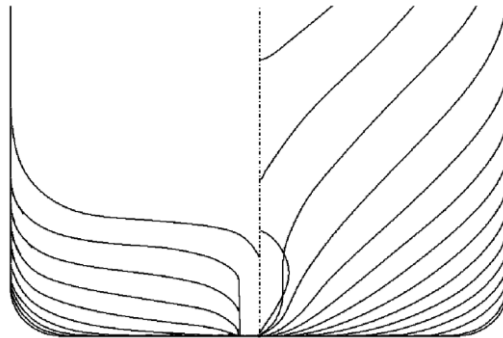


Figure 24: Section plan of the Cruise ship, Sigmund (2019)

3.3 Post-Panamax Containership A

The 355m long post-Panamax Containership was investigated in the time and spatial discretisation study in section 4.1, in the verification study of the convolution integral for the computation of radiation forces in section 4.2 and in the validation study of wave induced forces 4.3, where the nonlinear hydrodynamic forces at the fixed ship, the freely moving ship and the wave added resistance were investigated. Furthermore, the containership A was investigated regarding the influence of the wave steepness on ship motion in oblique waves, see section 5.1. The main particulars of this container ship are listed in Table 5.

Table 5: Main particulars of the containership A.

Description	Symbol	Unit	Values
Length between perpendiculars	L_{pp}	[m]	355
Moulded breadth	B	[m]	51
Draft	D	[m]	14.5
Displacement	Δ	[m ³]	173467
Block coefficient	C_B	[-]	0.661
Vertical centre of gravity	KG	[m]	19.85
Metacentric height	GM	[m]	5.1
Radius of gyration about x	r_{xx}	[m]	20.3
Radius of gyration about y	r_{yy}	[m]	87.3
Radius of gyration about z	r_{zz}	[m]	87.4

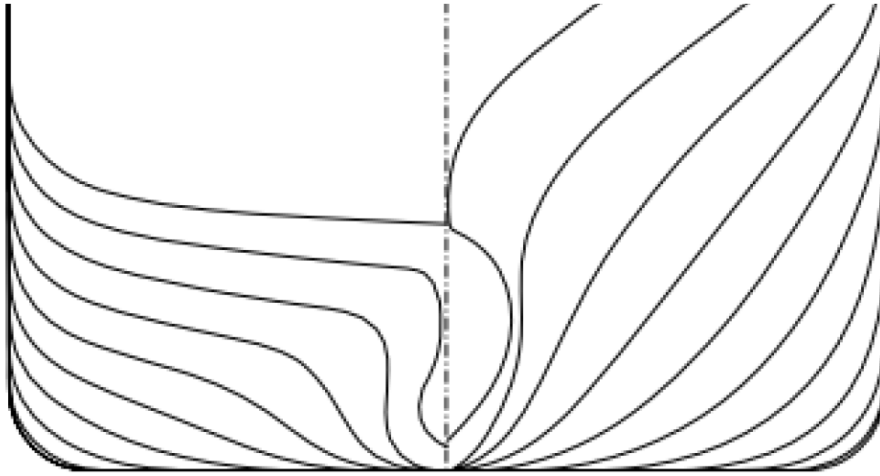


Figure 25: Section plan of the post Panamax Container ship A, Sigmund (2019).

3.4 Post-Panamax Containership B

The 333m long post-Panamax containership (Containership B) was investigated in the validation study on the hydroelastic solver. The validation study comprises comparisons of rigid body ship motions and sectional loads (torsional moments, vertical and horizontal bending moments) at the main frame of the ship. Further results of the influence of the wave steepness and forward speed effect on wave-induced sectional load of the Containership B are discussed in section 5.2. This ship was already investigated within the framework of the EU founded projects ExtremeSeas and TULCS, see e.g. Maron and Kapsenbeerg (2014). Table 6 lists main particulars. The section plan of the post-Panamax Containership B is similar to the section plan of post-Panamax Containership A shown in Figure 25.

Table 6: Main particulars of subject containership

Description	Symbol	Unit	Value
Length between perpendiculars	L_{pp}	[m]	333.44
Moulded breadth	B	[m]	42.80
Draft	D	[m]	13.1
Displacement	Δ	[m ³]	125604
Block coefficient	C_B	–	0.62
Vertical centre of gravity	KG	[m]	19.2
metacentric height	GM	[m]	2.280
Radius of gyration about x	r_{xx}	[m]	18.4
Radius of gyration about y	r_{yy}	[m]	84.0
Radius of gyration about z	r_{zz}	[m]	84.0

Model test results of the containership were available from the project ExtremeSeas. During that model test, the structural properties of the ship were modelled with an aluminum backbone. The structural properties of the backbone model are discussed in the section 3.4.1. To validate the new numerical method, the model test scenarios were numerically computed and the obtained results were compared with the measured results. As aforementioned, the backbone model did not simulate the full-scale structural properties of the real ship correctly. Especially the location of the shear center and the warping stiffness differed. For that reason, additional simulations of the 333m long post-Panamax containership with realistic full-scale structural properties were performed. The full-scale ship properties are discussed in chapter 3.4.2.

3.4.1 Structural and Mass Properties According to the Model Test Setup

The containership was tested at the Canal de Experiencias Hidrodinámicas de El Pardo (CEHIPAR) (Maron and Kapsenberg (2014)) during the project ExtremeSeas. The results have not been published, however, time series of measured values were available from the project and were used to validate the new numerical method. Structural properties of the ship were simulated by a rectangular backbone made of aluminum. Cutouts in the upper face of the backbone were used to reduce the location of the shear center and to introduce warping effects. A detailed description of the model test setup is given by Maron and Kapsenberg (2014). For the present work, the numerical model was constructed accordingly to the model test setup. However, during the

experiments, the backbone did not reach completely from the transom to the bow. It started approximately 44m (full scale) in front of the aft perpendicular and ended 5m before the forward perpendicular. To account for ships inertial correctly and to transfer hydrodynamic pressures at the bow and transom to the beam element model, the numerical beam element model was extended to reach from the transom to the foremost point of the bulbous bow. This can have an effect on the structural behaviour, especially for higher modes when the vibration nodes become closer to the ends of the backbone. As in the experiments, the model was divided into six segments. Table 7 lists the structural properties of each segment. The shear center was assumed to be constant over the total ship length and located 1.368m below the keel line. The full-scale young's module was $6.4 \times 10^{12} \text{ N/m}^2$.

Table 7: Sectional properties of the 333m long post-Panamax containership equipped with a backbone.

Property	Symbol	Unit	Segment					
			1	2	3	4	5	6
Segment length	l	$[m]$	96.58	36.0	36.0	59.2	76.0	45.22
Effective transverse shear cross section area	$S_{y,eff}$	$[m^2]$	4.16	4.16	4.16	4.16	4.16	4.16
Effective vertical shear cross section area	$S_{z,eff}$	$[m^2]$	2.10	2.10	2.10	2.10	2.10	2.10
Mass per unit length	μ	$[kg/m]$	238130	468282	460259	455466	359149	242769
Section area moment of inertia about y-axis	$\underline{\underline{I_y}}$	$[m^4]$	35.41	35.41	35.41	35.41	35.41	35.41
Section area moment of inertia about z-axis	$\underline{\underline{I_z}}$	$[m^4]$	80.47	80.47	80.47	80.47	80.47	80.47
Torsional stiffness	$\underline{\underline{I_T}}$	$[m^4]$	3.54	3.54	3.54	3.54	3.54	3.54
Warping stiffness	$\underline{\underline{I_{\omega}}}$	$[m^6]$	220	220	220	220	220	220
Mass moment of inertia per unit length about y-axis	$\underline{\underline{j_y}}$	$[kgm^2/m]$	2.07e8	5.96e7	2.37e8	1.63e8	1.92e8	4.19e7
Mass moment of inertia per unit length about z-axis	$\underline{\underline{j_z}}$	$[kgm^2/m]$	1.78e8	1.00e8	1.34e8	2.10e8	2.00e8	5.57e8
Mass moment of inertia per unit length about x-axis	$\underline{\underline{j_t}}$	$[kgm^2/m]$	2.28e8	2.50e8	3.18e8	3.31e8	2.01e8	6.12e7
Vertical position of neutral bending axis from keel	Z_n	$[m]$	10.0	10.0	10.0	10.0	10.0	10.0
Vertical position of shear centre from keel	Z_s	$[m]$	-1.368	-1.368	-1.368	-1.368	5.0	13.0

3.4.2 Structural and Mass Properties According to a Realistic Full-Scale Setup

The structural properties of the 333m long post-Panamax containership cannot be simulated correctly by using the simplified properties of a backbone model. For that reason, additional simulations of springing-induced vibrations with realistic full scale structural and mass properties were performed. The applied full scale structural and mass properties are plotted in Figure 26 and Figure 27 as functions of its longitudinal position x , where $x = 0$ represents the ship's transom.

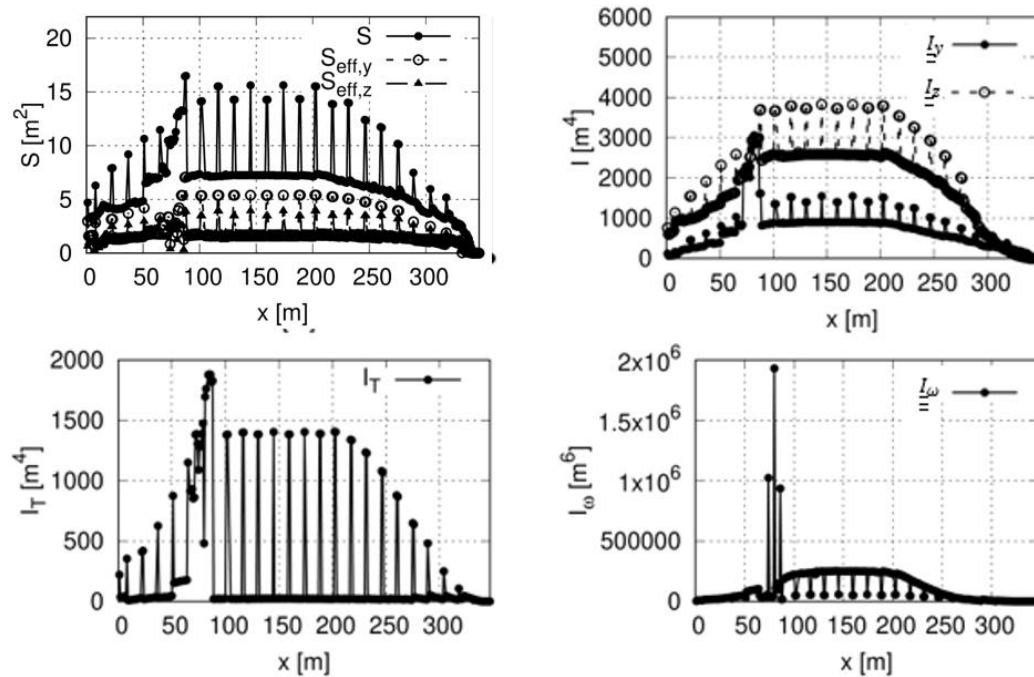


Figure 26: Visualization of the cross section areas, S , effective shear cross section area, S_y , S_z , the area moment of inertia I_y and I_z , the torsional stiffness, I_T , and the warping stiffness I_ω

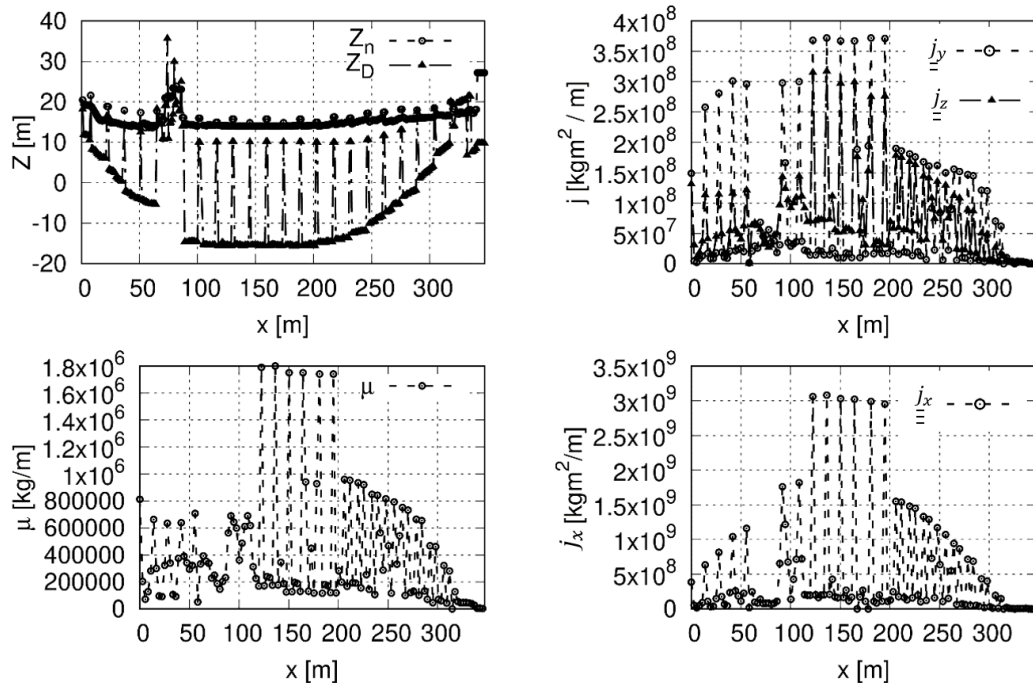


Figure 27: Visualization of the vertical position (relative to keel line) of the neutral bending axis, Z_n , and shear center, Z_s , the mass moment of inertia, j_y and j_z , the mass per unit length, μ , and j_x the torsional mass moment of inertia relative to the shear center

Following the procedure of the model test with a back bone, the hull structure was subdivided into six segments and the cross-section properties of each segment were determined from the full-scale properties plotted in Figure 26 and Figure 27. All hull properties were assumed constant over the length of each segment. Furthermore, linear elastic material properties were assumed with a Young's modulus of $2.06 \times 10^{11} \text{ N/m}^2$. Table 8 lists the cross-section properties for each segment, beginning with segment 1 at the transom and ending with segment 6 at the bow.

3.4 Post-Panamax Containership B

Table 8: Cross section properties of the containership under realistic full-scale conditions

Property	Symbol	Unit	Segment					
			1	2	3	4	5	6
Segment length	l	[m]	96.58	36.0	36.0	59.2	76.0	45.22
Cross section area	S	[m ²]	6.704	8.143	8.261	8.104	8.104	2.658
Shear reduction factor y	r_y	[-]	0.305	0.257	0.257	0.253	0.278	0.288
Shear reduction factor z	r_z	[-]	0.260	0.245	0.243	0.247	0.291	0.353
Section area moment of inertia about y-axis	$\underline{\underline{I_y}}$	[m ⁴]	777	940	972	945	615	194
Section area moment of inertia about z-axis	$\underline{\underline{I_z}}$	[m ⁴]	1548	2693	2746	2695	1811	201
Torsional stiffness	I_T	[m ⁴]	433.33	192.44	212.25	182.89	133.5	26.30
Warping stiffness	$\underline{\underline{I_\omega}}$	[m ⁶]	87418	202064	222255	212026	55879	2188
Mass per unit length	μ	[kg/m]	307607	525142	452315	467831	393057	93709
Mass moment of inertia per unit length about y-axis	$\underline{\underline{j_y}}$	[kgm ² /m]	5.48e7	9.37e7	7.21e7	8.46e7	6.88e7	1.38e7
Mass moment of inertia per unit length about z-axis	$\underline{\underline{j_z}}$	[kgm ² /m]	5.05e7	1.06e8	1.08e8	9.18e7	6.85e7	7.21e6
Mass moment of inertia per unit length about x-axis	$\underline{\underline{j_t}}$	[kgm ² /m]	1.76e8	7.38e8	5.98e8	6.28e8	4.21e8	3.57e7
Vertical position of neutral bending axis from keel	Z_n	[m]	16.92	14.41	14.25	14.31	15.67	18.61
Vertical position of shear centre from keel	Z_s	[m]	7.02	-11.93	-11.94	-12.23	-5.18	11.49

4 Verification and Validation

The main goal of the validation study was to compare wave-induced forces and moments, ship motions and elastic vibrations obtained with the new numerical method with model test results and CFD results. However, before the actual validation study, a time and spatial discretisation study was performed to minimize the numerical error, see section 4.1. Afterwards, a verification study of the convolution integral was performed to investigate the accuracy of the convolution integral to compute ship induced radiation forces, see section 4.2. After the verification study, the actual validation of the new numerical method was performed. The validation study was split into three validation steps. The first validation step focus on the computation of wave induced hydrodynamic forces, see section 4.3. The second validation step focused on the computation of wave induced rigid body ship motions, see section 4.4. The third validation step focused on the computation of wave-induced sectional loads and springing-induced resonant elastic vibrations of the hull girder, see section 4.5. Content of the verification and validation study was already published in Riesner et al. (2016); Riesner and el Moctar (2018); Riesner et al. (2018a); Riesner and el Moctar (2021a) and Riesner and el Moctar (2021b).

In the validation study, results of the new numerical method were also compared to results of a linear frequency domain boundary element method, which computed wave-induced rigid body motions. The linear frequency domain method is based on the approach of Söding et al. (2012), Söding et al. (2014) and Graefe (2014). It couples the fully nonlinear stationary forward speed problem with the linear periodic flow problem in waves.

4.1 Time and Spatial Discretisation Study

To minimize the numerical error, a spatial and time discretization study was performed for the 355 meter long post-Panamax Containership A, see section 3.3.

The present work focus on the computation of wave-induced hydrodynamic forces and moments and the rigid body and elastic response. As aforementioned, the solution of the stationary forward speed potential is required for the computation of wave-induced forces and moments. As a consequence, differences in the stationary forward speed solution due to a changing spatial discretization will affect wave-induced forces and moments as well.

4.1 Time and Spatial Discretisation Study

However, specific results of the stationary solution, such as the calm water resistance, are not of particular interest for the present study. Consequently, an individual discretization study for the stationary forward speed solution was not performed. A systematic grid study of the stationary forward speed solution can be found in Graefe (2014) and in Söding (2009a).

Recall that two different body grids were used, one frequency domain body grid that reached up to the time averaged free surface and one time domain body grid that covered the total hull. In general, the panel dimensions for both grids were similar. To investigate the influence of the panel size on time domain and frequency domain results, three different grids for each discretization were generated, namely, a coarse, a medium, and a fine grid. Table 9 lists the number of panels for these grids. The mid column presents the number of panels used to discretize the ship's hull up to its mean wetted surface; the right column, the number of panels used to discretize the ship's hull up to its main deck. Figure 28 shows exemplary the medium size time domain grid comprising 3880 panels used to discretizes the ship's hull up to its main deck. During the variation of the body discretization, the length of a free surface panel was approximately 1/19 of the wavelength. After the body grid study, the free surface panel length was varied, whereas the number of body panels was kept constant (medium grid). The free surface panel length varied between 1/9, 1/19, 1/22 and 1/24 of the wave length. All computations for the discretization study were performed at a constant velocity of $Fn = 0.052$. The hydrodynamic added mass and damping are independent of the wave encounter angle, the excitation forces were computed for a wave encounter angle of 120 degrees.



Figure 28: Medium grid discretizing the ship's hull up to its main deck

Table 9: Investigated hull grid sizes

grid description	frequency domain grid	Time domain grid
Coarse grid	1174	1836
Medium grid	2306	3880
Fine grid	4078	6794

4.1.1 Frequency Dependent Hydrodynamic Forces

As already discussed in section 2.3, radiation forces (more specific the hydrodynamic added mass and hydrodynamic damping) and diffraction forces (complex diffraction force amplitude) were precomputed using the frequency domain solver. Figure 29 shows the normalized hydrodynamic added mass for each rigid body motion (diagonal components of the added mass matrix). According to equation (27) and (28), transfer functions of the hydrodynamic added mass and damping were integrated over the wave encounter frequency to obtain the impulse response function. For that reason, transfer functions of the hydrodynamic added mass and hydrodynamic damping are plotted against the wave encounter frequency. Figure 29 compares transfer functions of the normalized hydrodynamic added mass resulting from the three different body discretization. n_p designates the number of body panels. The results were normalized with the maximum amplitude of the fine grid with 4078 panels. In principle, the hydrodynamic added mass matrix and hydrodynamic damping matrix are 6x6 matrixes. However, the diagonal terms of these matrixes usually dominate the hydrodynamic response. For that reason, only the diagonal terms, $\tilde{\mathbf{M}}_{ii}$ with $i = 1; 2; 3; 4; 5; 6$, are compared. For all hydrodynamic added mass components in Figure 29, except the roll added mass $\tilde{\mathbf{M}}_{44}$, only small differences were found. For the surge, $\tilde{\mathbf{M}}_{11}$, heave, $\tilde{\mathbf{M}}_{33}$, and pitch, $\tilde{\mathbf{M}}_{55}$, added mass, all three discretization gave almost identical results. For the sway, $\tilde{\mathbf{M}}_{22}$, and yaw, $\tilde{\mathbf{M}}_{66}$, added mass, the coarse body grid with 1174 panels underestimated the result slightly. For the roll added mass, $\tilde{\mathbf{M}}_{44}$, strong differences between the coarse grid and the medium and fine grid were found. The biggest differences occurred for a wave encounter frequency of approximately 2.4 rad/s . Figure 30 compares the hydrodynamic added mass for $\omega_e \approx 2.4 \text{ rad/s}$ plotted against the number of body panels n_p . The hydrodynamic added mass in Figure 30 were normalized with the results of the fine grid. It can be seen that with 1174 body panels, the hydrodynamic added mass was underestimated by approximately 28% compared to the result based on 4078 body panels. Using 2306 panels improved the results significantly and underestimated the hydrodynamic added mass by approximately 2.5%.

Figure 31 compares the transfer function of the hydrodynamic damping for all three body grids. Again, the roll hydrodynamic damping, $\tilde{\mathbf{B}}_{44}$, differed the most, whereas all other degrees of freedom showed only marginally deviations. Figure 32 compares the normalized hydrodynamic damping (normalized with the result of the fine grid) from all three grids for a wave encounter frequency of approximately 2.4 rad/s , where the highest deviations were found. With 1174 panels, the roll hydrodynamic damping was overestimated by approximately 34% compared to the result based on 4078 body panels.

4.1 Time and Spatial Discretisation Study

Increasing the number of body panels to 2306 reduced the divergences to approximately 5%.

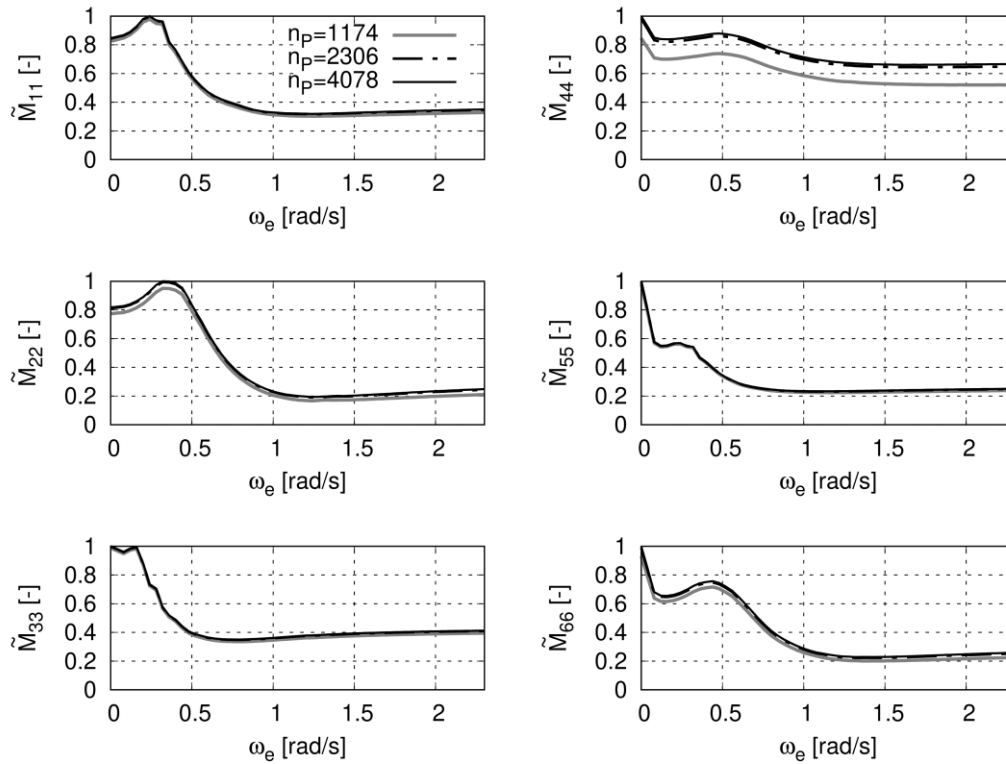


Figure 29: Transfer functions of the normalized hydrodynamic added mass resulting from the three different body discretization. n_p designates the number of body panels.

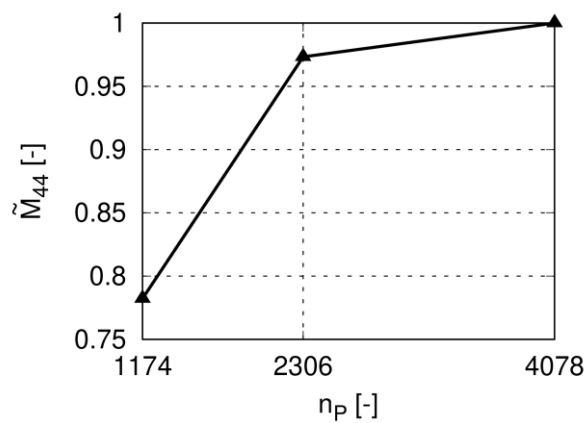


Figure 30: Normalized hydrodynamic added mass for $\omega_e \approx 2.4 \text{ rad/s}$ plotted against the number of body panels n_p .

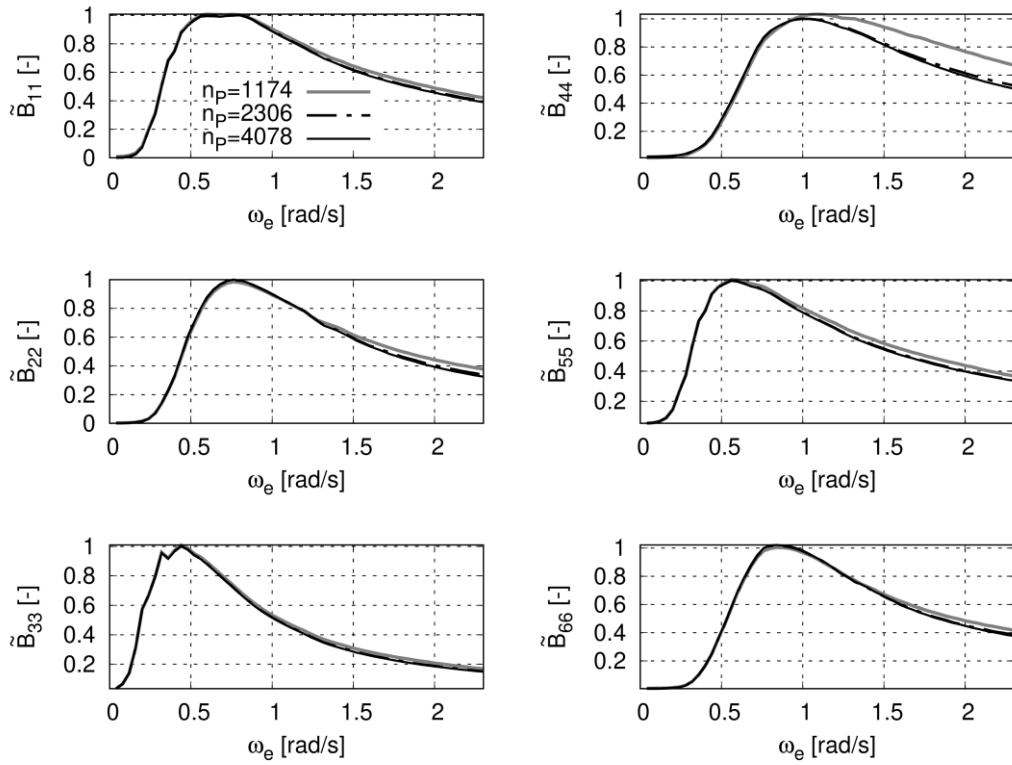


Figure 31: Transfer functions of the normalized hydrodynamic damping resulting from the three different body discretization. n_p designates the number of body panels.

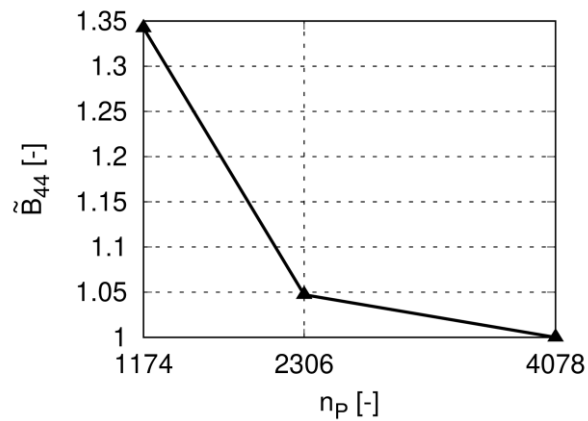


Figure 32: Normalized hydrodynamic damping for $\omega_e \approx 2.4$ rad/s plotted against the number of body panels n_p .

4.1 Time and Spatial Discretisation Study

Figure 33 compares normalized transfer functions of the diffraction forces and moments for all three body grids plotted against λ/L_{PP} . Again, the highest deviations were found for the roll moment, $\tilde{M}_{Dif,x}$, at $\lambda/L_{PP} = 0.58$. Figure 34 compares the normalized diffraction roll moments from all three body discretization for $\lambda/L_{PP} = 0.58$. With 1174 body panels, the roll moment was underestimated with approximately 38% and using 2306 body panels reduced the underestimation to approximately 1.5%.

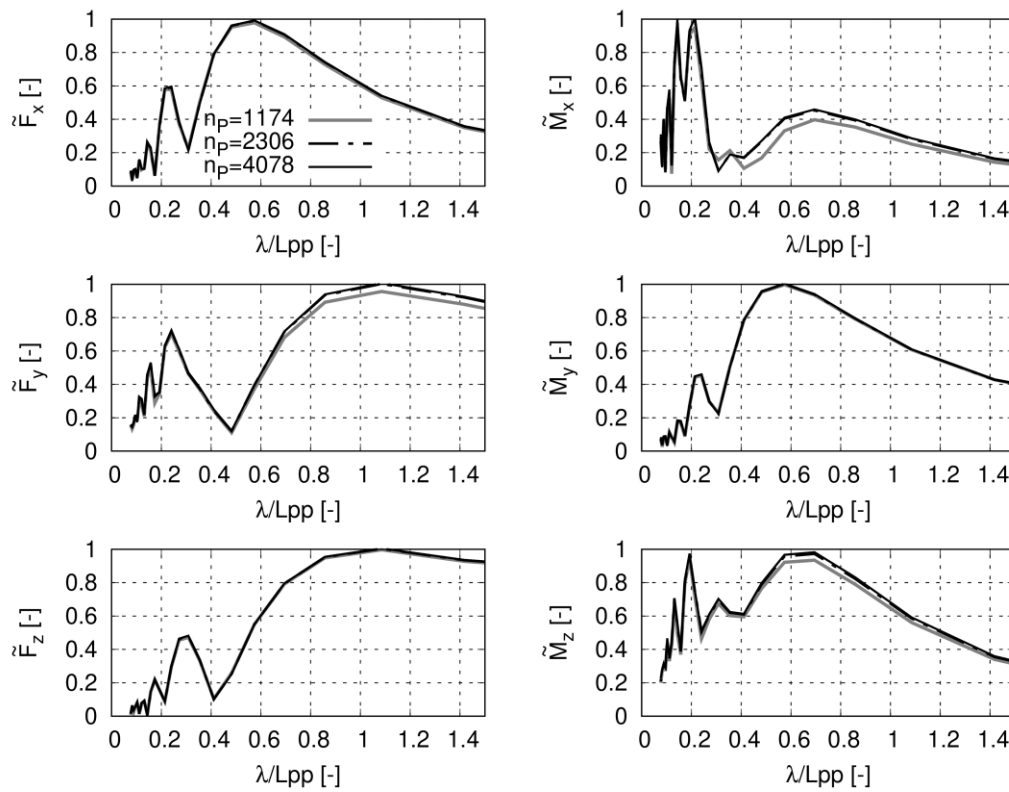


Figure 33: Normalized transfer functions of the diffraction forces and moments for the three different body discretization. n_p designates the number of body panels.

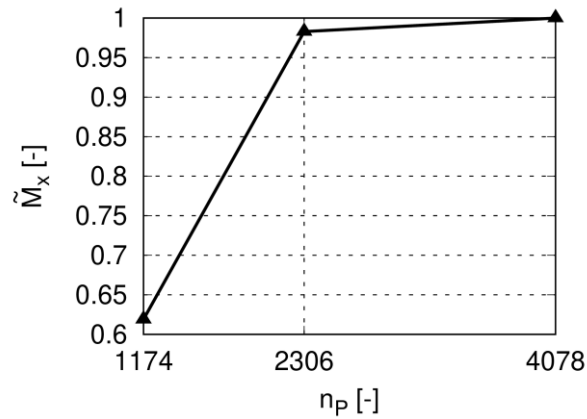


Figure 34: Normalized diffraction roll moments for $\lambda/L_{pp} = 0.58$ plotted against the number of body panels n_p .

In the following validation steps, the number of body panels was kept constant with 2306 panels, but the size of the free surface panels in the inner free surface grid was varied. The length of a free surface panel was designated l_p . Thus, the number of free surface panels per wave length follows from the relation λ/l_p . Similar to the previous validation of the number of body panels, the hydrodynamic added mass, hydrodynamic damping and the diffraction forces based on different free surface panels dimensions were compared. Figure 35 compares transfer functions of the normalized hydrodynamic added mass for $\lambda/l_p = 9; 19; 24$. Except for the roll-induced hydrodynamic added mass, only small differences were found. For the roll-induced hydrodynamic added mass, the biggest differences occurred for the lowest wave encounter frequency of $0.04 rad/s$. Figure 36 plots normalized hydrodynamic added masses for $om_e = 0.04 rad/s$ against λ/l_p . With a free surface panel length according to $\lambda/l_p = 9$, the roll-induced hydrodynamic added mass was underestimated by approximately 22.5%. With a panel length according to $\lambda/l_p = 19$, the deviation reduced to approximately 4.5%. With 22 panels per wave length ($\lambda/l_p = 22$), the error reduced to approximately 0.5%.

Figure 37 compares normalized transfer functions of hydrodynamic damping for $\lambda/l_p = 9; 19; 24$. Generally, differences due to different free surface discretizations were small. The biggest differences were found for the surge induced hydrodynamic damping, $\tilde{\mathbf{B}}_{11}$, at $om_e \approx 0.75$. Figure 38 plots $\tilde{\mathbf{B}}_{11}$ for $om_e \approx 0.75$ against the relation of the wave length to the free surface panel length, λ/l_p . With nine free surface panels per wave length ($\lambda/l_p = 9$), the $\tilde{\mathbf{B}}_{11}$ was underestimated by approximately 4.25%. With nineteen free surface panels per wave length, the error reduced to less than 1%.

4.1 Time and Spatial Discretisation Study

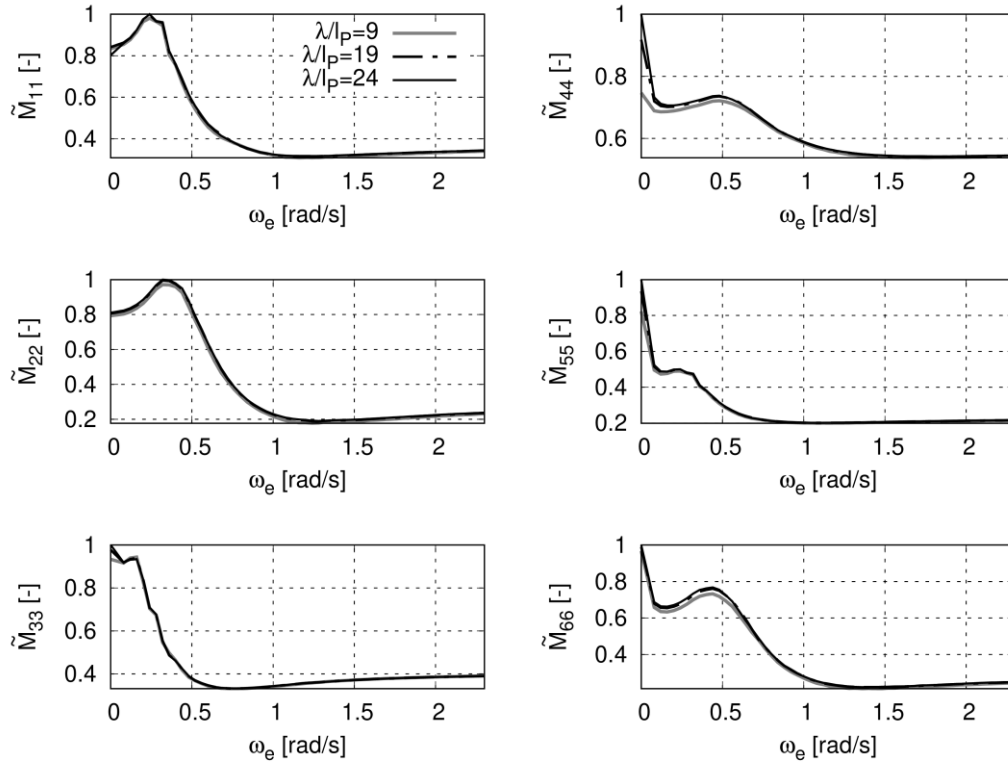


Figure 35: Normalized transfer functions of the hydrodynamic added mass resulting from the three different free surface discretization, $\lambda/l_p = 9; 19; 24$

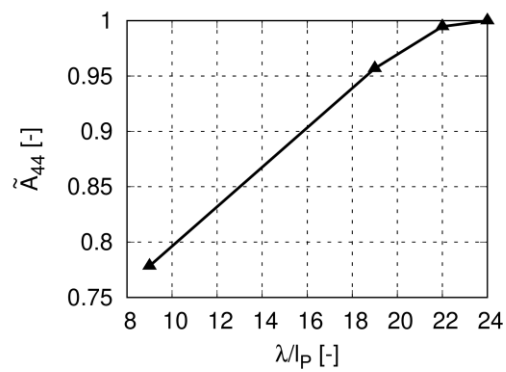


Figure 36: Normalized hydrodynamic added roll mass for $\omega_e = 0.04 \text{ rad/s}$ plotted against λ/l_p .

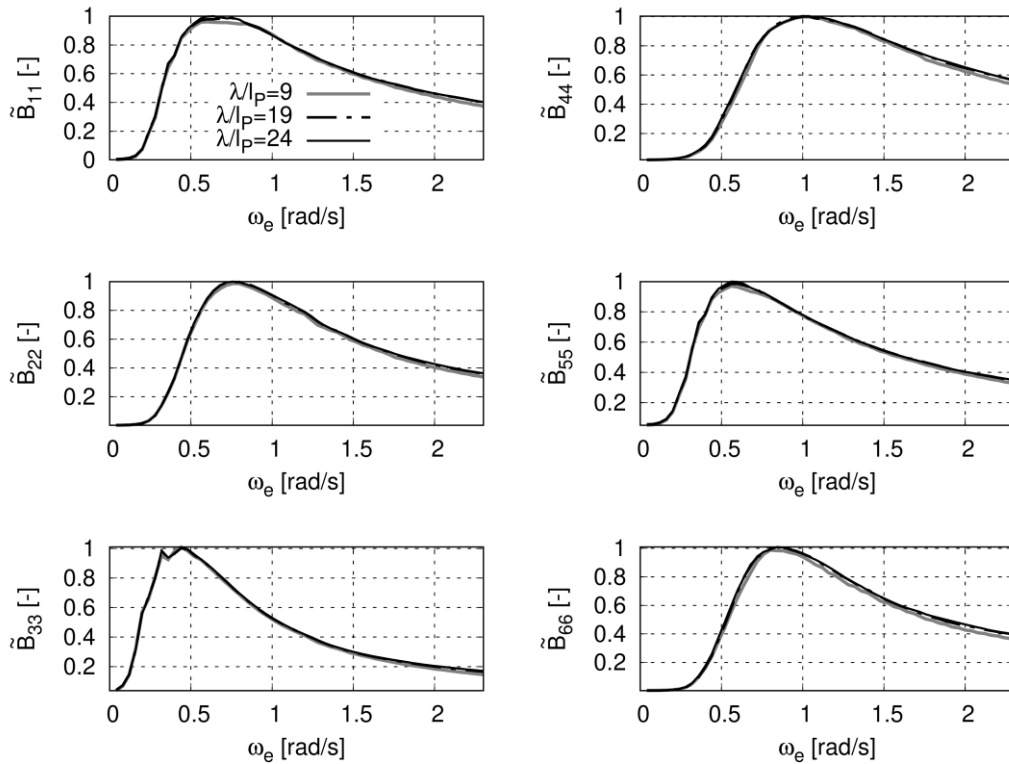


Figure 37: Normalized transfer functions of hydrodynamic damping resulting from the three different free surface discretization, $\lambda/l_p = 9; 19; 24$

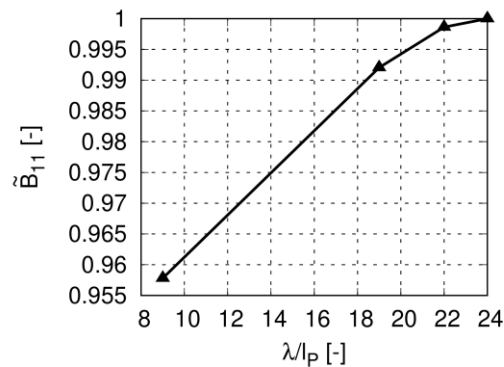


Figure 38: Normalized hydrodynamic surge damping for $\omega_e = 0.64 rad/s$ plotted against λ/l_p .

Figure 39 plots transfer functions of the normalized diffraction force amplitudes against λ/L_{PP} for free surface panel lengths according to $\lambda/l_p = 9; 19; 24$. Significant differences could only be found for the yaw moment with the highest deviations for $\lambda/L_{PP} = 0.58$. For this wave scenario, Figure 40 plots the normalized diffraction yaw moment against the number of free surface panels per wave length, λ/l_p . With the biggest free surface panels

4.1 Time and Spatial Discretisation Study

($\lambda/l_p = 9$), the diffraction yaw moment was underestimated by approximately 9%. Decreasing the panel length to $\lambda/l_p = 19$ reduced the error to approximately 1%.

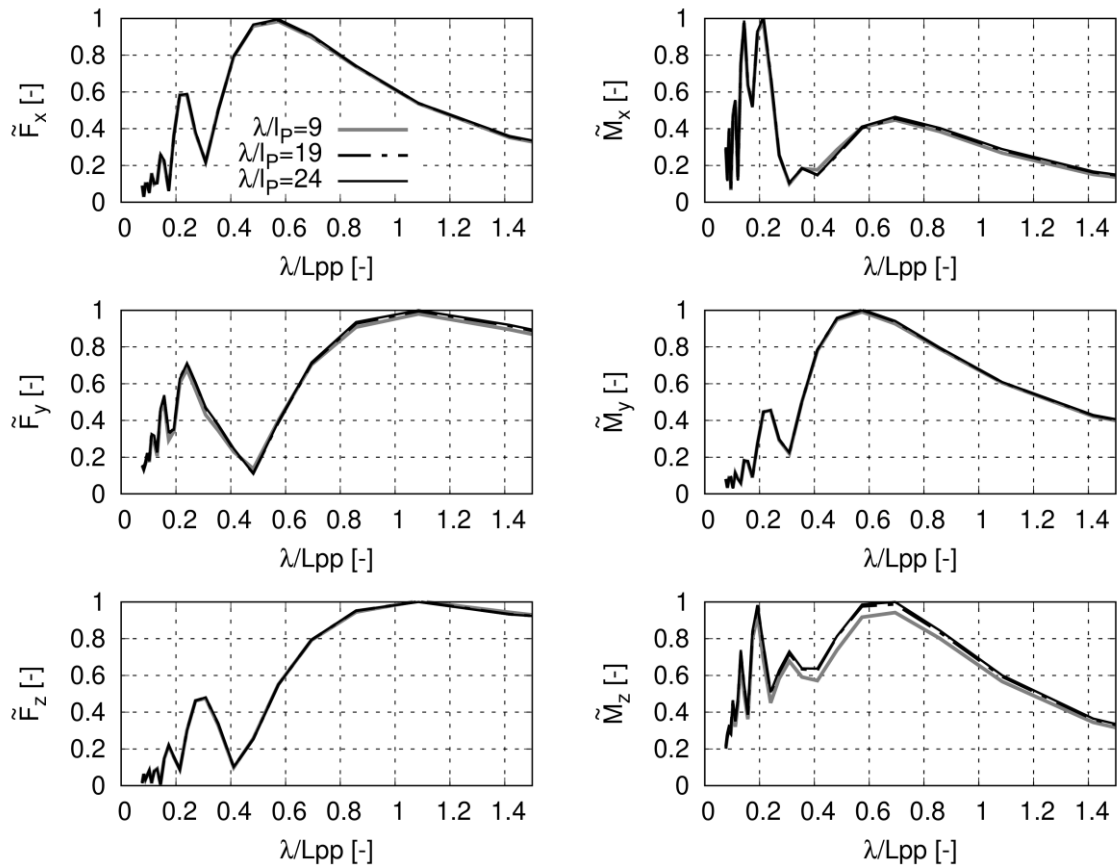


Figure 39: Normalized transfer functions of the diffraction forces and moments resulting from three different free surface discretization, $\lambda/l_p = 9; 19; 24$.

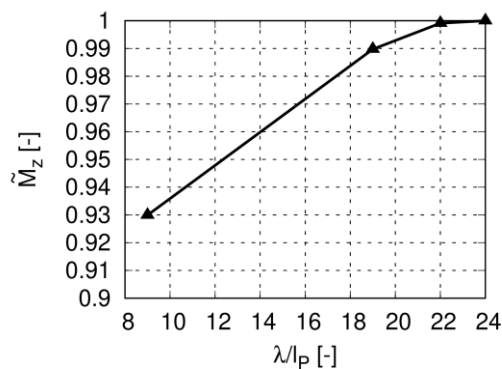


Figure 40: Normalized diffraction yaw moments for $\lambda/L_{pp} = 0.58$ from three different free surface discretization, $\lambda/l_p = 9; 19; 24$.

The grid study showed that at most degrees of freedom, the frequency domain hydrodynamic coefficients and the diffraction forces and moments depend only minimally on the body discretization and free surface discretization. An exception was the roll induced hydrodynamic added mass and damping as well as the longitudinal diffraction force and diffraction yaw moment. It was concluded that 2306 body panels at the time averaged wetted hull surface are a sufficiently discretize the hull and that 19 free surface panels per wave length sufficiently discretize the free surface.

4.1.2 Time Domain Hydrodynamic Forces and Rigid Body Motions

The time domain solver integrated Froude-Krylov and hydrostatic forces and moments over the instantaneous wetted hull surface. The pressure integration near the free surface was improved by modifying panels intersected by the free surface, see section 2.5. However, the pressure integration still depended on the discretization of the ship's hull. Therefore, the combined Froude-Krylov and hydrostatic forces and moments obtained on all three body grids in Table 9 were compared. To eliminate the influence of the time discretization, ship motions were suppressed in all degree of freedom. In total, 28 waves between $7.7 \geq \lambda/L_{pp} \geq 0.08$ were analyzed. To cause a strong variation of the wetted hull surface a constant wave steepness of $h = 0.07$ was applied. Although these waves were steep, Froude-Krylov and restoring forces and moments obtained on all three grids converged to the same values in longer waves. Only in shorter waves differences were found. The largest deviations occurred for the vertical combined Froude-Krylov and hydrostatic force for $\lambda/L_{pp} = 0.110$. Figure 41 plots normalized (respect to maximum amplitude at the fine grid) time histories of calculated combined Froude-Krylov and hydrostatic forces and moments for $\lambda/L_{pp} = 0.110$. The left side plots from top to bottom the longitudinal, transvers and vertical force. The right side the roll, pitch and yaw moments. Figure 42 compares the normalized maximum negative vertical force amplitude (normalized with the result of the fine grid). With the coarse grid (1836 panels at the total hull), the maximum negative amplitude was overestimated by approximately 16.25% compared to the result of the fine grid with 6794 panels. Increasing the number of body panels to 3880 panels reduced the error to approximately 1.9%. This result shows that 3880 panels at the complete hull (time domain body grid) are sufficient to discretize the body surface.

4.1 Time and Spatial Discretisation Study

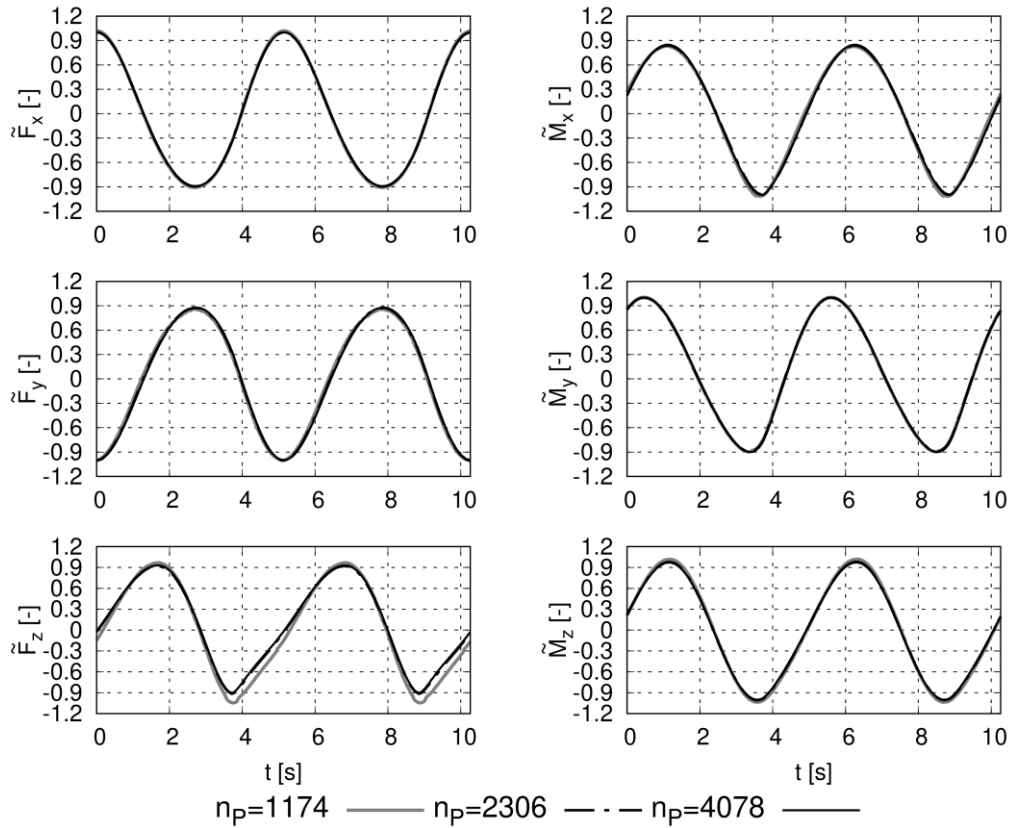


Figure 41: Time histories of combined normalized Froude-Krylov and hydrostatic forces and moments for the fixed ship at $\lambda/L_{pp} = 0.110$.

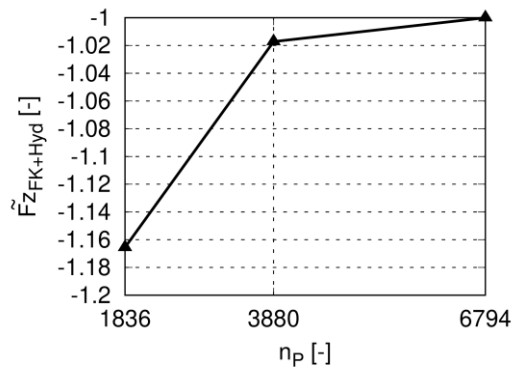


Figure 42: Normalized minimum combined Froude-Krylov and hydrostatic forces vertical forces for $\lambda/L_{pp} = 0.110$ plotted against the number of body panels n_p .

As the nonlinear equation of rigid body motions was solved using the implicit Euler method, it was necessary to investigate the time discretization in addition to spatial discretization. Specifically, the influence of different time steps on the solution of ship

motions was analysed. To ensure large ship motions in all degree of freedom, simulations at a wave encounter angle of $\mu = 120$ degree were performed applying a wave length to ship length ratio of $\lambda/L_{pp} = 0.984$. To avoid green water (water on deck) the wave steepness was reduced to $h = 0.03$. Simulations were performed with three different time steps of $\Delta t = 0.2, 0.075$ and 0.025 seconds. Exemplary Figure 43 plots the ship motions resulting from all three time steps. It can be seen that amplitudes of all motions, except roll, do not change significantly due to different time steps. Only the phase angle of the surge motion changes slightly. To enable a more detailed view on the change of each motions due to different time steps, Table 10 lists first harmonic response amplitudes of each degree-of-freedom. Table 10 lists also the largest percentage deviations from responses obtained with the smallest time step ($\Delta t = 0.025s$), which in this case occurred for roll motions. The roll amplitude increased about 6.7% when the time step was reduced from 0.2 to 0.075s. Reducing the time step again to $\Delta t = 0.025s$ increased the roll amplitude by only about 2.8% compared to roll amplitude using a time step of 0.075s. Figure 44 plots the first harmonic amplitude of the roll angle against the time step. As it was assumed for the implicit Euler method, the plot indicates a linear relation between the roll angle amplitude and the time step. Based on a linear extrapolation the time step independent first harmonic roll angle amplitude was 0.0391rad and consequently approximately 1.2% higher than the result based on $\Delta t = 0.025s$. For all further simulation a time step of 0.025s or less was applied.

4.1 Time and Spatial Discretisation Study

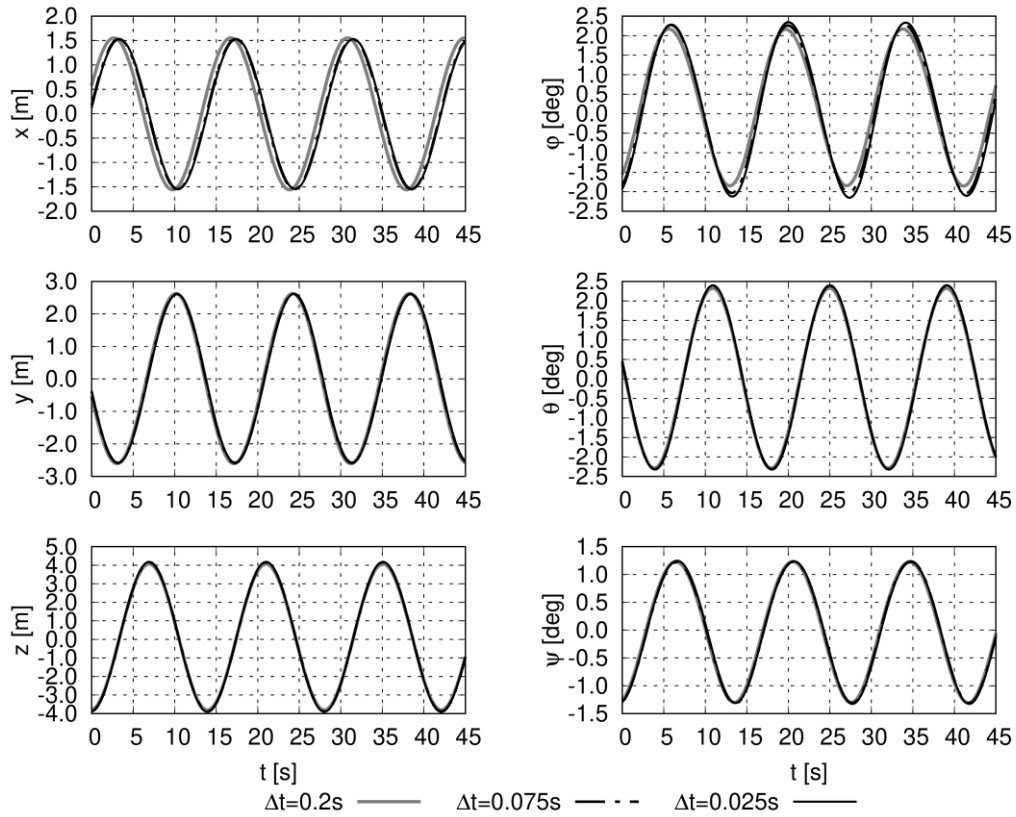


Figure 43: Time histories of ship motions at $\lambda/L_{pp} = 0.984$ obtained from a time step of 0.2s, 0.075s and 0.025s

Table 10: First harmonic responses of each degree-of-freedom from simulations obtained from the time step study.

Δt [s]	Surge [m]	Sway [m]	Heave [m]	Roll [rad]	Pitch [rad]	Yaw [rad]	Deviation [%]
0.2	1.5581	2.6150	3.9356	0.03499	0.04024	0.02208	10.3
0.075	1.5388	2.5981	4.0184	0.03750	0.04106	0.02219	2.93
0.025	1.5364	2.5945	4.0353	0.03860	0.04118	0.02228	-

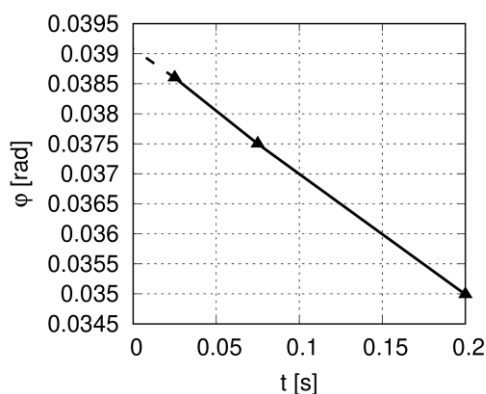


Figure 44: First harmonic amplitude of the roll motion against the time step.

4.2 Verification of the Convolution Integral to Compute Radiation Forces

In this section the application of convolution integrals to describe radiation forces is verified. For the present method the impulse response function \mathbf{k} (see equation (22)) was computed based on Fourier transformed transfer functions of the hydrodynamic damping or hydrodynamic added mass according to equation (27) and (28). Consequently, an equivalent time domain solution exists for every frequency domain solution. To verify that the time domain solution based on convolution integrals can compute equivalent results to the frequency domain solution, the linear equation of rigid body motions instead of the nonlinear equation of rigid body motions was applied. Furthermore, the nonlinear combined Froude-Krylov and hydrostatic forces were replaced by their linear representation and the waterline force was not considered. For the verification procedure, the heave and pitch motions of the Cruise ship, the VLCC tanker and the Containership A were compared. First, results for zero forward speed were compared. At zero forward speed, the stationary velocity potential is zero and does not contribute. Thus, zero forward speed is the simplest scenario. Afterwards, comparisons for medium forward speed according to a Froude Number of $Fn \approx 0.15$ and at higher forward speed according to a Froude Number of $Fn = 0.218$ were performed. All time domain simulations were performed for a unified wave amplitude of one meter.

Figure 45 shows exemplary the normalized transfer function of the hydrodynamic damping (left) and hydrodynamic added mass (right) for the Containership A at zero speed.

“ \mathbf{B}_{33} ” denotes the hydrodynamic damping in vertical direction due to a vertical motion (heave) and “ \mathbf{B}_{55} ” denotes the hydrodynamic damping of the pitch motion due to a pitch motion. Accordingly, “ \mathbf{M}_{33} ” denotes the hydrodynamic added mass in vertical direction due to a heave motion and “ M_{55} ” the hydrodynamic added mass of the pitch motion due to a pitch motion. The transfer functions were normalized with their maximum amplitudes. The black coloured part of each line designates that this part of the transfer function was integrated numerically to achieve the impulse response function and the grey coloured part was integrated analytically, see equation (27) and (28). Hydrodynamic damping at zero frequency is zero and it converges also zero at infinite frequency. However, at forward speed, hydrodynamic damping at infinite frequency is not necessary zero, see equation (205). The hydrodynamic added mass reached its maximum near zero frequency and has also a significant magnitude at high frequencies or even infinite frequency. This behaviour can lead to significant computational errors when the hydrodynamic added mass was used to calculate the impulse response functions and only a numerical integration of equation (24) would be performed. The accuracy of the numerical integration depends significantly on the upper integration limit. For ships, an integration limit higher than 10 rad/s is necessary to achieve accurate results. However, usually, such high angular frequencies cannot be computed with a boundary element method based on Rankine sources because the necessary free surface refinements increase the computational effort strongly. In the present method, the integration was split into a numerical integration up to a frequency of approximately 2rad/s (in the present case) and into an analytical integration that integrated the missing components up to infinite frequency, see equation (28). This technique enables to use the hydrodynamic added mass for the computation of the impulse response function without reducing the accuracy or increasing the numerical effort strongly.

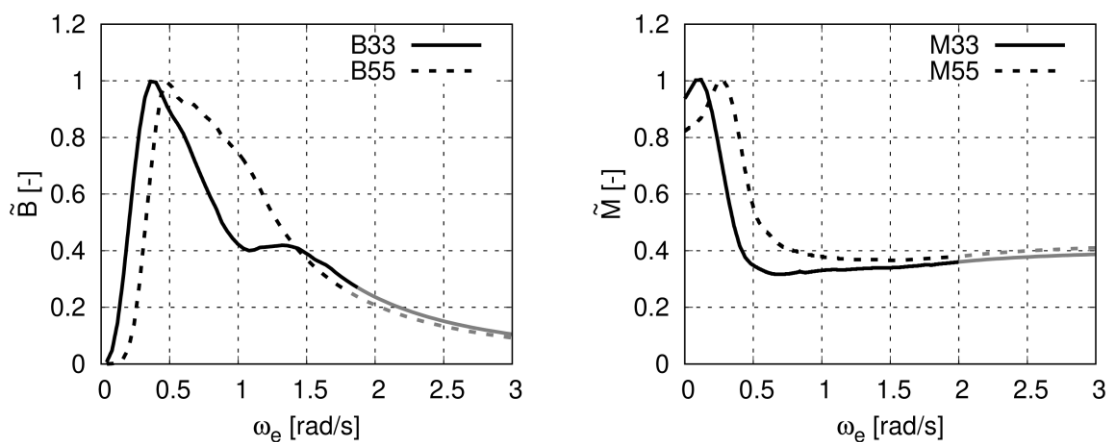


Figure 45: Normalized hydrodynamic heave (B_{33}) and pitch (B_{55}) damping (left) and normalized hydrodynamic heave (A_{33}) and pitch (A_{55}) added mass (right)

Figure 46 compares the corresponding impulse response function. On the left plot of Figure 46, " $K_{33} D$ " denotes that this impulse response function was computed by integrating the transfer function of the hydrodynamic damping " B_{33} " and " $K_{33} M$ " denotes that this impulse response function was computed by integrating the hydrodynamic added mass " M_{33} ". On the same principle, the impulse response functions " $K_{55} D$ " and " $K_{55} M$ " on the right plot of Figure 46 were computed. The impulse response functions " $K_{33} D$ " and " $K_{33} M$ " were normalized with the maximum amplitude of " $K_{33} D$ " and the transfer function " $K_{55} D$ " and " $K_{55} M$ " were normalized with the maximum amplitude of " $K_{55} D$ ". All four impulse response functions characterize the general behaviour of a causal, damped system. At negative times, the impulse response functions are zero; and for past impulses generated a long time ago, they converge to zero.

It can be seen that the impulse response functions that were computed based on hydrodynamic damping, " $K_{33} D$ " and " $K_{55} D$ ", differ slightly from the impulse response functions based on the hydrodynamic added mass, " $K_{33} M$ " and " $K_{55} M$ ". For the heave impulse response functions, " $K_{33} D$ " and " $K_{33} M$ ", the maximum amplitude at $t = 0s$ are almost identical, however, small differences appeared at the minimum amplitude at $t \approx 5s$. For the pitch impulse response function, " $K_{55} D$ " and " $K_{55} M$ ", the maximum amplitude at $t = 0s$ differed slightly but the minimum amplitude at $t \approx 2.5s$ was similar.

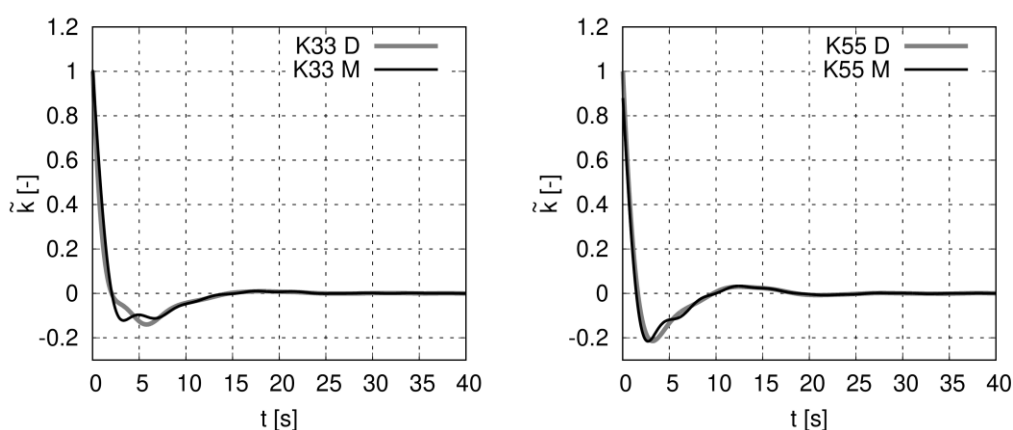


Figure 46: Normalized heave impulse response functions (left) and pitch impulse response functions (right)

Figure 47 compares the transfer functions of the heave (left plot) and pitch motions (right plot) of the Containership A at zero forward speed computed with the impulse response functions based on hydrodynamic damping and hydrodynamic added mass with

the result of a frequency domain method. The motions are plotted against the relation of the wave length to the ship length, λ/L_{pp} . Heave motions were normalized with the wave amplitude, ζ^1 , as follows

$$\tilde{z} = \frac{z}{\zeta^1} \quad (212)$$

The pitch motion was normalized with the wave amplitude and wave number, k , as follows

$$\tilde{\theta} = \frac{\theta}{\zeta^1 k} \quad (213)$$

“linear M” denotes results that were computed with impulse response functions based on the hydrodynamic added mass and “linear B” denotes results that were computed with impulse response functions based on hydrodynamic damping. Recall that the intention of these comparisons was to identify if the time domain solutions of “linear M” and “linear B” were equivalent to the frequency domain solution “linear frq.”. For that reason, “linear M” and “linear B” were computed fully linear by using linear Froude-Krylov and hydrostatic forces, neglecting the waterline force and using the linear equation of motion.

It can be seen that the results of “linear D” are almost identical to the frequency domain results “linear frq.”. Small differences can only be seen at the pitch motions in longer waves. For the heave motion, results of “linear M” differ stronger. In waves of medium length, $0.4 \leq \lambda/L_{pp} \leq 0.8$, “linear A” overestimates the heave motion compared to “linear frq.” and in long waves of $\lambda/L_{pp} \geq 0.8$ it underestimates the heave motion. The pitch motion of “linear M” and “linear D” are almost identical.

Figure 48 and Figure 49 compare the transfer functions of heave and pitch motions of the VLCC tanker and cruise vessel for zero forward speed computed with “linear D”, “linear M” and “linear frq.”, respectively. The results of the heave motions of the VLCC tanker in Figure 48 (left plot) show a good agreement of “linear D” and “linear M” compared to “linear frq.” in short and in long waves. In waves of medium length $0.6 \leq \lambda/L_{pp} \leq 1.0$, “linear D” and “linear M” underestimates the heave motions compared to “linear frq.”, whereas the deviation of “linear A” is slightly larger. For the pitch motions of the VLCC tanker (right plot in Figure 49) “linear D” and “linear frq.” are almost identical. “linear M”

underestimated the frequency domain results “linear freq.” slightly in long waves. The result of the cruise vessel in Figure 49 indicates a good agreement. For the heave motion, only “linear D” overestimated the motion amplitudes slightly compared to “linear freq.” and for the pitch motions, both methods, “linear D” and “linear A” overestimated the motion amplitudes in long waves slightly.

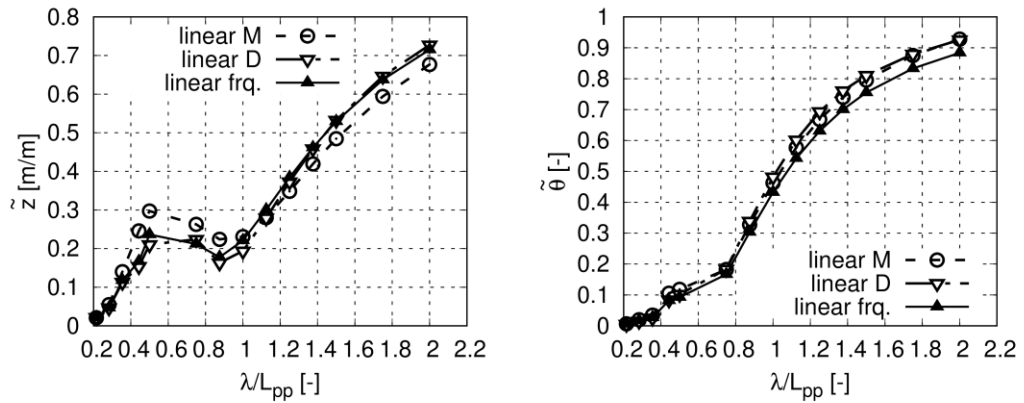


Figure 47: Transfer functions of heave (left) and pitch (right) motions of the containership A in head waves computed with the linear time domain solver with impulse response functions based on hydrodynamic damping “linear D”, based on the hydrodynamic added mass “linear M” and using the frequency domain solver “linear freq.”.

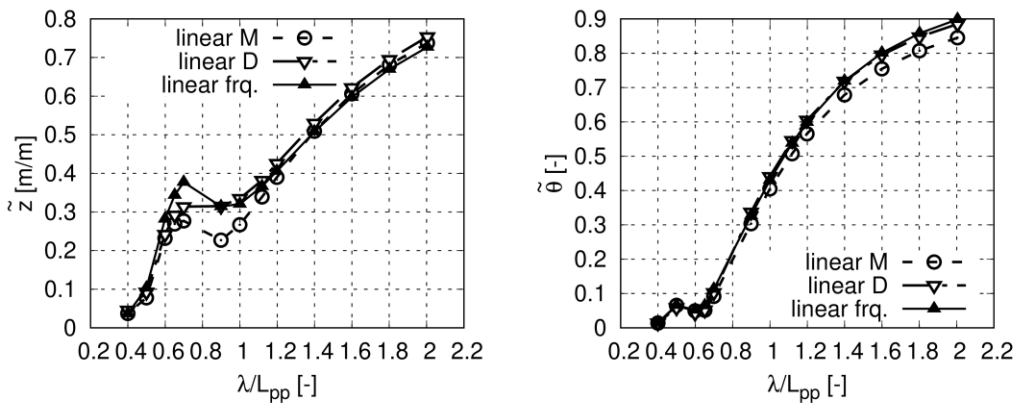


Figure 48: Transfer functions of heave (left) and pitch (right) motions of the VLCC tanker in head waves computed with the linear time domain solver with impulse response functions based on hydrodynamic damping “linear D”, based on the hydrodynamic added mass “linear M” and using the frequency domain solver.

4.2 Verification of the Convolution Integral to Compute Radiation Forces

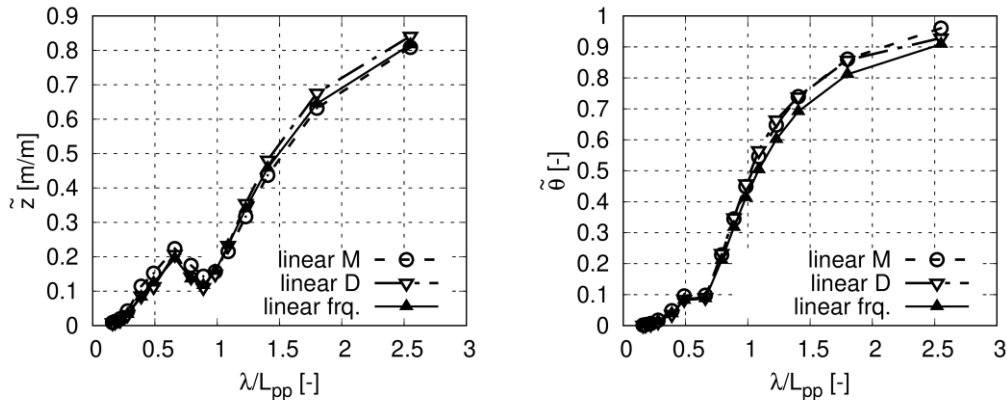


Figure 49: Transfer functions of heave (left) and pitch (right) motions of the cruise vessel in head waves computed with the linear time domain solver with impulse response functions based on hydrodynamic damping “linear D”, based on the hydrodynamic added mass “linear M” and using the frequency domain solver.

For medium forward speed Figure 51, Figure 52 and Figure 52 plot the transfer function of the heave and pitch motion of the containership A, VLCC tanker and cruise vessel, respectively. Figure 50 plots the results of the Containership A at a constant forward speed corresponding to a Froude Number of $Fn = 0.139$, Figure 51 the results of the VLCC tanker at a Froude Number of $Fn = 0.142$ and Figure 52 the results of the cruise vessel at a Froude Number of $Fn = 0.166$. For the results of the containership A (Figure 50) “linear D” and “linear M” differ only minimally for the prediction of the transfer function of the heave motion. At pitch motions, both methods show almost identical results. Compared to “linear freq.”, both methods slightly underestimated the heave and pitch motions. For the heave and pitch transfer functions of the VLCC tanker, Figure 52 shows larger differences. “linear D” and “linear M” underestimate the result compared to “linear freq.” for both motions. For the heave motions, a pronounced response amplitude can be seen for $\lambda/L_{pp} \approx 1.4$ (small resonant oscillation). The frequency domain method seems to be less damped and consequently predicts larger heave motions. Figure 52 plots the transfer function of the heave and pitch motions of the cruise vessel. In general, all methods agree well with small deviations at longer waves.

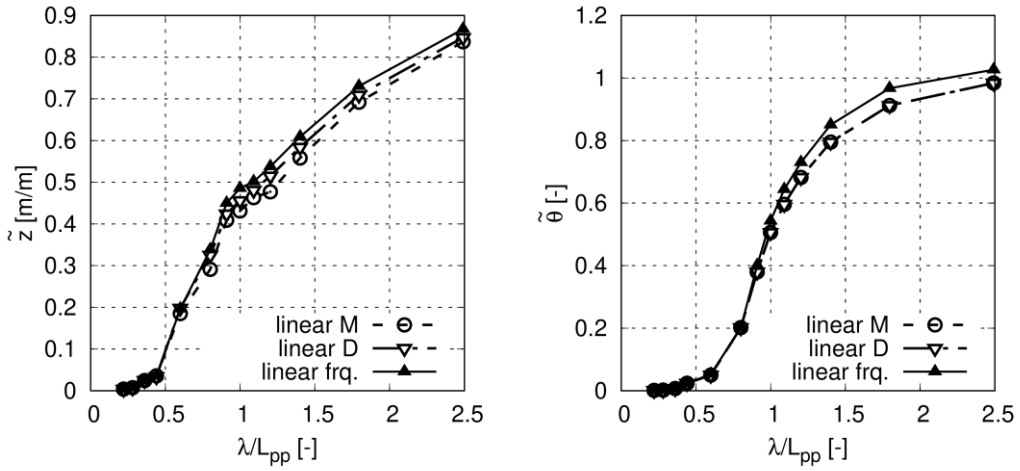


Figure 50: Transfer functions of heave (left) and pitch (right) motions of the containership A in head waves with a forward speed according to $F_n = 0.139$. “linear D” and “linear M” designates linear time domain simulations with impulse response functions based on hydrodynamic damping and hydrodynamic added mass “linear M”. “linear freq.” designates results from the linear frequency domain solver.

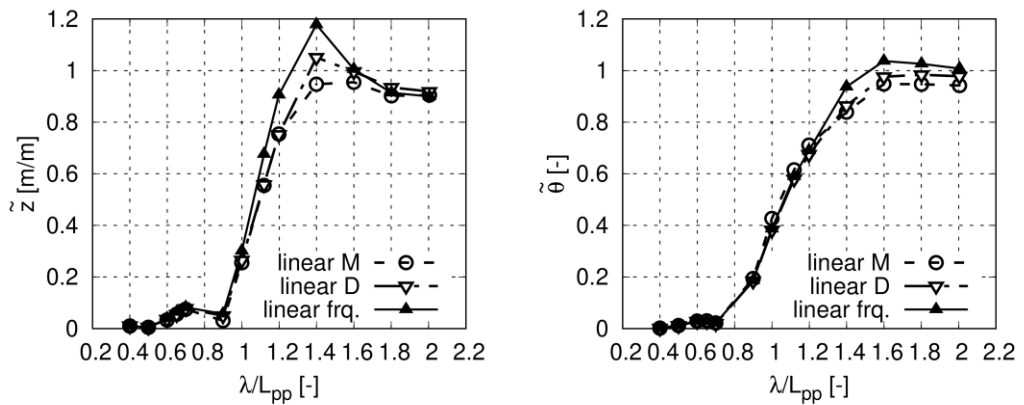


Figure 51: Transfer functions of heave (left) and pitch (right) motions of the VLCC tanker in head waves with a forward speed according to $F_n = 0.142$. “linear D” and “linear M” designates linear time domain simulations with impulse response functions based on hydrodynamic damping and hydrodynamic added mass “linear M”. “linear freq.” designates results from the linear frequency domain solver.

4.2 Verification of the Convolution Integral to Compute Radiation Forces

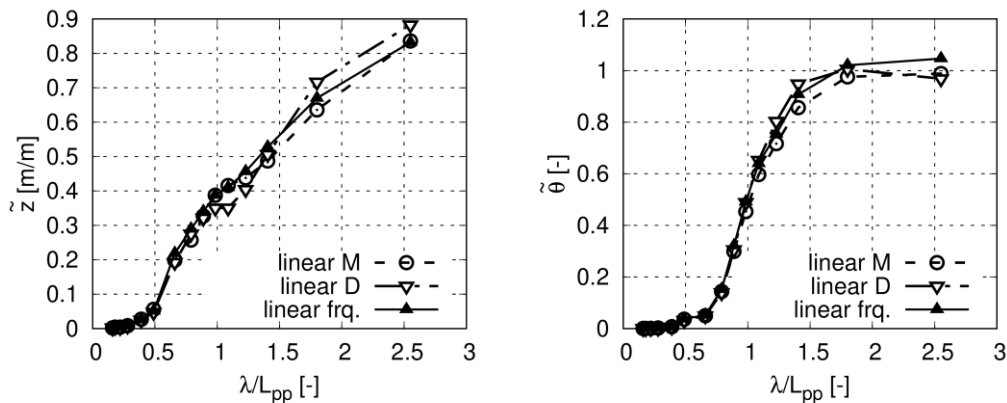


Figure 52: Transfer functions of heave (left) and pitch (right) motions of the cruise vessel in head waves with a forward speed according to $Fn = 0.166$. "linear D" and "linear M" designates linear time domain simulations with impulse response functions based on hydrodynamic damping and hydrodynamic added mass "linear M". "linear freq." designates results from the linear frequency domain solver.

Figure 53 plots the transfer function of the heave and pitch motions of the Containership A for a higher forward speed corresponding to $Fn = 0.218$. The heave and pitch motions of "linear M" agree favorable to the frequency domain results "linear freq.". However, the linear time domain simulations computed with impulse response functions based on hydrodynamic damping, "linear D", underestimated the ship motions strongly, especially the pitch motion in long waves.

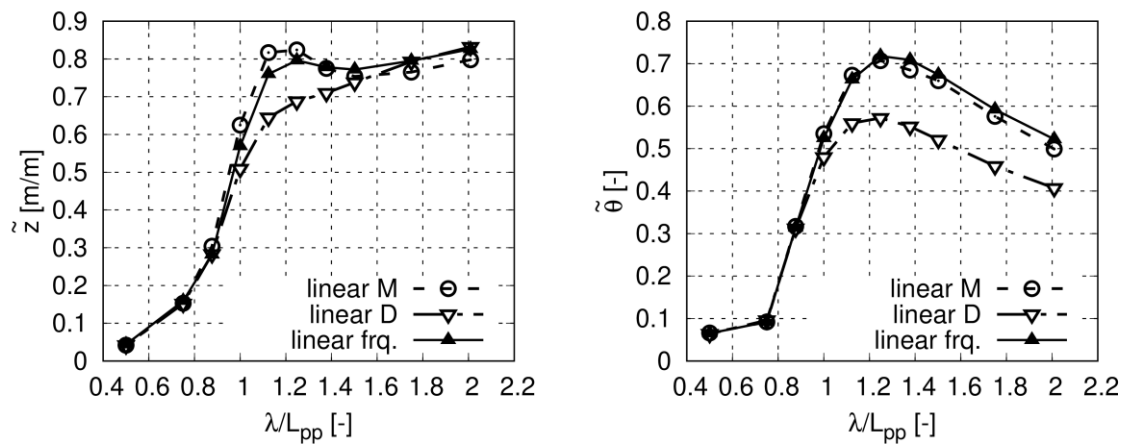


Figure 53: : Transfer functions of heave (left) and pitch (right) motions of the containership A in head waves with a forward speed according to $Fn = 0.218$. "linear D" and "linear M" designates linear time domain simulations with impulse response functions based on hydrodynamic damping and hydrodynamic added mass "linear M". "linear freq." designates results from the linear frequency domain solver.

The previous results showed that the linear time domain simulations, “linear D” and “linear M” gave comparable results to the frequency domain solver “linear freq.” at zero and medium forward speeds. In most of these cases, results from damping based impulse response functions, “linear D,” agreed better to the frequency domain solution than the results from added mass based impulse response functions, “linear M”. However, at higher forward speed (Figure 53), “linear D” was strongly overdamped, whereas results of “linear M” were almost identical to the frequency domain results “linear freq.”. For the Containership A at zero speed, Figure 46 compares the damping based impulse response functions with the added mass based impulse response functions of the heave and pitch motion and both methods computed comparable impulse response functions. The left plot in Figure 54 shows normalized hydrodynamic damping and hydrodynamic added mass (both normalized with its maximum amplitude) of the pitch motion of the containership A at $Fn = 0.218$. The right side of Figure 54 compares the corresponding normalized impulse response functions, both normalized with the maximum amplitude of the hydrodynamic added mass based impulse response function “ $\mathbf{K}_{55} M$ ”. The impulse response function based on hydrodynamic damping and on hydrodynamic added mass differ significantly. The maximum amplitude of the hydrodynamic damping based impulse response function “ $\mathbf{K}_{55} D$ ” at $t = 0s$ is approximately 2.2 times larger than the hydrodynamic added mass based impulse response function “ $\mathbf{K}_{55} M$ ”. Furthermore, the maximum negative amplitude of “ $\mathbf{K}_{55} D$ ” is approximately three times smaller than the maximum negative amplitude of “ $\mathbf{K}_{55} M$ ”. This results in a strongly overdamped system and a strongly reduced response amplitude of results based on “ $\mathbf{K}_{55} D$ ”.

To investigate this behavior, Figure 54 shows the normalized hydrodynamic damping transfer function $\tilde{\mathbf{B}}_{55}$ (pitch damping due to pitch motion) and the normalized hydrodynamic added mass transfer function $\tilde{\mathbf{A}}_{55}$. A possible reason for the wrongly computed damping based impulse response function is the discontinuity (strong peak) of the damping transfer function near $\omega_e = 0.25$ rad/s. These discontinuities may result from the radiation condition in the frequency-domain pre-computations. To fulfill the radiation condition at the free surface, the free surface sources were shifted in long waves, see section 2.4. Damping depends strongly on the boundary condition on the free surface and therefore, might be much more influenced by the source shift than the added mass. Discontinuities in the damping transfer function were also discussed by other authors. For instance, Fonseca and Soares (1998) discuss the influence of discontinuities in damping coefficients and the resulting inaccuracies; they concluded that a spline fit of the damping coefficients reduces oscillations of the impulse response function.

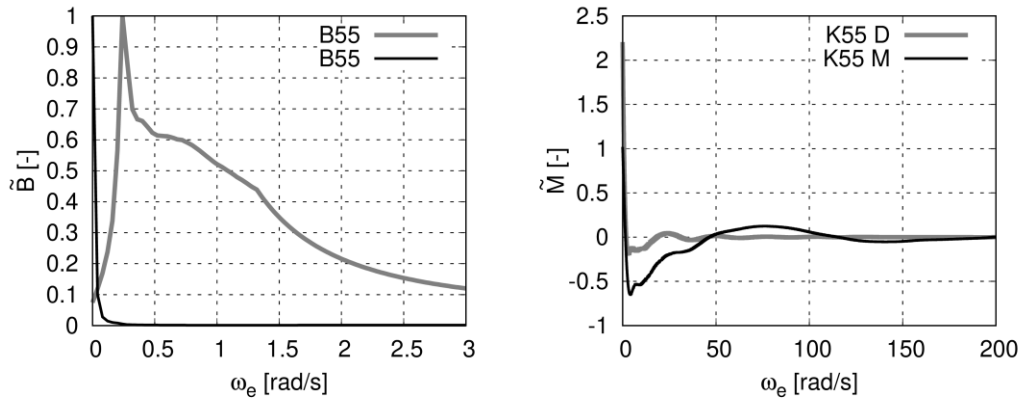


Figure 54: Normalized hydrodynamic damping $B_{55}(\omega_e)$ and normalized hydrodynamic added mass $M_{55}(\omega_e)$ of the pitch motion of containership A at $Fn = 0.218$ (left) and the impulse response function calculated using B_{55} and M_{55} (right).

4.3 Validation of Wave-Induced Forces

The weakly nonlinear hydroelastic solver computes nonlinear hydrodynamic forces and moments and considers the strongly coupled kinematic response of a rigid body and the linear elastic response of the ship hull. For the validation of this new numerical method, it is important to first validate the results of nonlinear hydrodynamic forces and moments without the influence of ship motions and deformations. This was realized by computing wave induced forces at the fixed hull (without radiation forces). Afterwards the effect of ship motions with its radiation forces was investigated by allowing the ship to move and later elasticity of the hull was considered, see section 4.5.

For the validation of wave-induced hydrodynamic forces and moments, results from the new numerical method for the Containership A and VLCC tanker in head waves were compared to numerical results from a Reynolds-Averaged Navier Stokes Equations (RANSE) solver, taken from Sigmund and el Moctar (2018). All comparisons were made for model scale.

The wave induced forces and moments computed with the CFD solver comprises the forces and moments due to the stationary forward speed of the ship and the oscillating wave induced forces. The new numerical solver coupled the fully nonlinear stationary flow problem with the oscillatory flow problem in waves. However, the total hydrodynamic forces and moments in time domain did not include forces due to forward speed. Therefore, to compare time histories from the new numerical method to time histories

from the CFD solver, forces due to forward speed were subtracted from the total hydrodynamic force obtained from the CFD solver.

Wave induced hydrodynamic forces and moments depend on the relation between the wave length, λ , and ship length, L_{pp} . To get a detailed insight of the characteristics of the wave induced forces and moments, comparisons of time histories obtained in a long wave, in a wave with a length close to the ship's length, and in a short wave were performed. Furthermore, the time histories of each single force and moment component, namely combined Froude-Krylov and hydrostatic forces and moments, diffraction forces and moments, radiation forces and moments and the waterline forces and moments were plotted to investigate the contribution of each component. Afterwards, the first, second, third and fourth harmonic response amplitude of the wave induced forces and moments for a wider range of wave length to ship length ratios ($0.5 \leq \lambda/L \leq 2.7$) were computed by applying a Fourier transformation.

The first harmonic amplitude dominantly causes the rigid body motions. The higher order harmonic amplitudes of the wave induced forces are important for the elastic response because they can cause higher order springing. Additionally to the harmonic amplitudes of wave induced forces, the time average of the wave induced force is important for the calculation of the speed loss of ships in waves. Riesner et al. (2018b) investigated the speed loss of the DTC container ship, the VLCC tanker and the cruise vessel due to the wave added resistance. It was shown that with increasing wave height the attainable ship speed reduces significantly until the ship nearly stops in very large waves. For the prediction of wave induces sectional load, it is important to consider the correct forward speed. Wave induced sectional loads depend strongly on forward speed due to a changing wave encounter frequency. This affect the occurrence of linear and higher order springing significantly. For that reason, the time average of the wave induced longitudinal force (wave added resistance) were compared as well. The associated normalized wave drift force, here known as the wave added resistance coefficient, $C_{AW}(\omega_e)$, was expressed as follows:

$$C_{AW}(\omega_e) = \frac{R_{AW}(\omega_e)L_{pp}}{\rho g B^2 (\zeta^1)^2} \quad (214)$$

where R_{AW} is the wave added resistance, g the gravity constant, ρ is the fluid density, and ζ^1 is the wave amplitude.

4.3.1 Weakly-Nonlinear Hydrodynamic Force at a Fixed Ship

The investigation of wave induced forces and moments at a fixed containership is a fictitious scenario because normally a ship is freely floating. However, comparisons of the wave induced forces and moments at a fixed hull are a good procedure to evaluate the hydrodynamic response without any influence from the ship motion.

For the validation of the nonlinear wave induced forces at the fixed Containership A, the ship was advancing with a constant forward speed corresponding to a Froude number of $Fn = 0.139$. To observe nonlinearities due to the changing wetted surface, large wave amplitudes were considered. For regular head waves of length corresponding to $\lambda/L_{PP} = 2.5$ and an amplitude of $\zeta^1 = 6.365m$ (full scale), Figure 55, Figure 56 and Figure 57 plot the time histories of the longitudinal force, vertical force and the pitch moment, respectively. In each figure, the upper graph plots the time histories of the nonlinear Froude-Krylov force or moment (FK+Hyd); the center graph the time histories of the diffraction force or moment (Dif) and its nonlinear waterline contribution (WL). The lower graph compares the total hydrodynamic force obtained from the new numerical method (nonlinear) and the force from the CFD method (CFD). The radiation forces and moments are zero for the fixed ship and thus not plotted. Furthermore, the time average of the forces and moments were subtracted from the time histories.

For the longitudinal force in Figure 55, the amplitude of the combined Froude-Krylov and hydrostatic force (FK+Hyd) is about six times higher than the amplitude of the diffraction force (Dif), and the phase shift is about 180deg. Furthermore, the diffraction force describes a harmonic oscillation (only linear diffraction pressure acted on the non-moving ship hull), but the nonlinear FK+Hyd force is non-harmonic, indicated by the longer time span between a positive peak and a negative peak than the corresponding time span between a negative and a positive peak.

The force component caused by the diffraction pressure acting on the non-average wetted surface plus its coupling effects with the Froude-Krylov pressure (WL) is three times smaller than the diffraction force, and its main period equals half of the wave encounter period (second order effect). However, its time average value of $-8.99N$ is negative, and its magnitude is almost twice as large as the magnitude of the time average FK+Hyd force of $-4.77N$. Consequently, although the waterline force did not strongly influence the amplitude of the total hydrodynamic force, it needed to be considered for the calculation of drift forces.

The sum of all forces is the total hydrodynamic force (nonlinear) plotted in the lower graph in Figure 55. The phase shift between FK+Hyd and Dif caused the amplitude of the total hydrodynamic force to be slightly smaller than the amplitude of the FK+Hyd force. The total nonlinear hydrodynamic force of the new numerical method agrees favourably to the force obtained from the CFD method. Their first harmonic amplitudes are nearly equal (from nonlinear 211.3N; from the CFD method 219.34N). However, their time average forces differ (from nonlinear -13.76N; from the CFD method -19.70N).

The vertical hydrodynamic forces behave similar, see Figure 56. The combined Froude-Krylov and hydrostatic force is the main contributor to the total hydrodynamic forces and its amplitude is approximately 3.5 times larger than the amplitude of the diffraction force and approximately 30 times larger than the amplitude of the waterline force. The agreement between the new numerical method (nonlinear) and the CFD results (CFD) is favourable. The first harmonic amplitude computed with the new numerical method was 2255.5N and the CFD result was 2167.2N.

Figure 57 plots the wave induced pitch moments. The combined Froude-Krylov and hydrostatic moment is approximately 4.75 times larger than the diffraction induced pitch moment and 14 times larger than the waterline induced pitch moment. However, the amplitude of the waterline induced pitch moment is still significant and shows that the waterline force might contribute to higher order springing vibrations. The result of the new numerical method and from CFD agreed well. The new numerical method computed a first harmonic amplitude of the pitch moment of 2217.85N and the CFD solver a first harmonic amplitude of 2201.4N.

4.3 Validation of Wave-Induced Forces

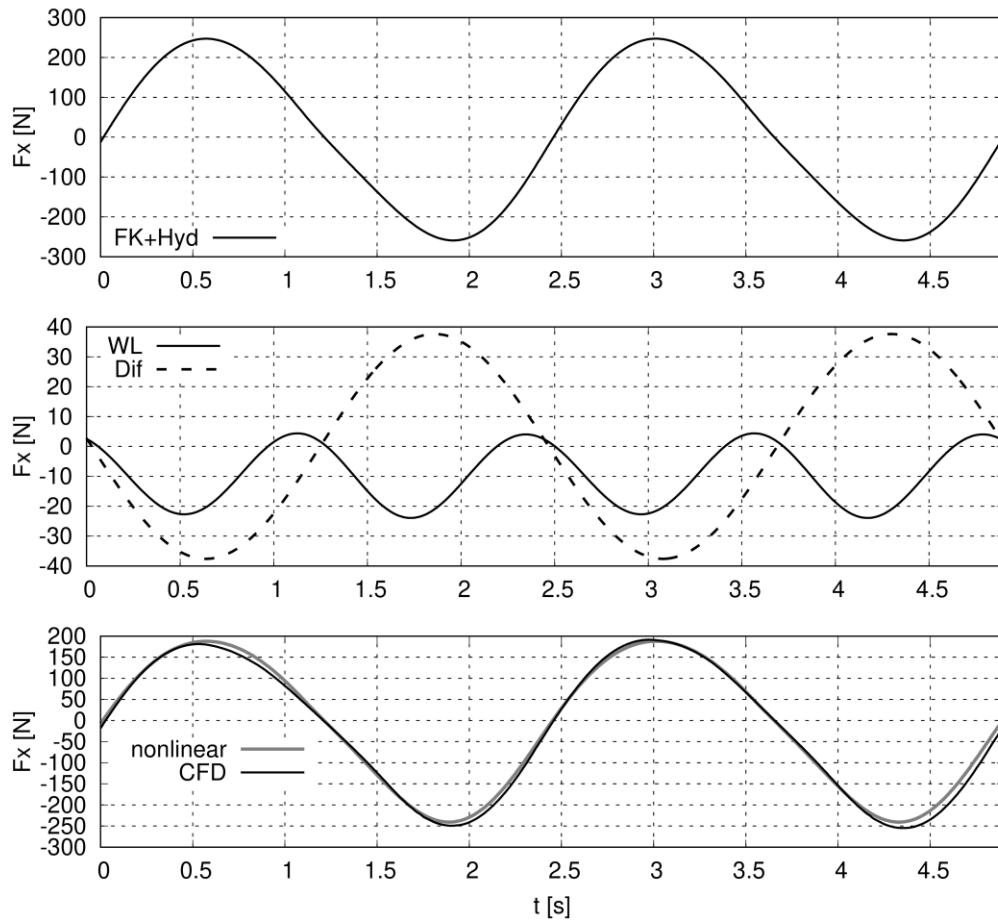


Figure 55: Time histories of longitudinal forces for the fixed Containership A ($F_n = 0.139$) in head waves of $\lambda/L = 2.50$ and a wave steepness $h = 0.011$. "FK+Hyd" denotes the combined Froude-Krylov and hydrostatic forces, "WL" denotes nonlinear waterline forces, "Dif" denotes diffraction forces and "nonlinear" denotes the total hydrodynamic force compared to the CFD result.

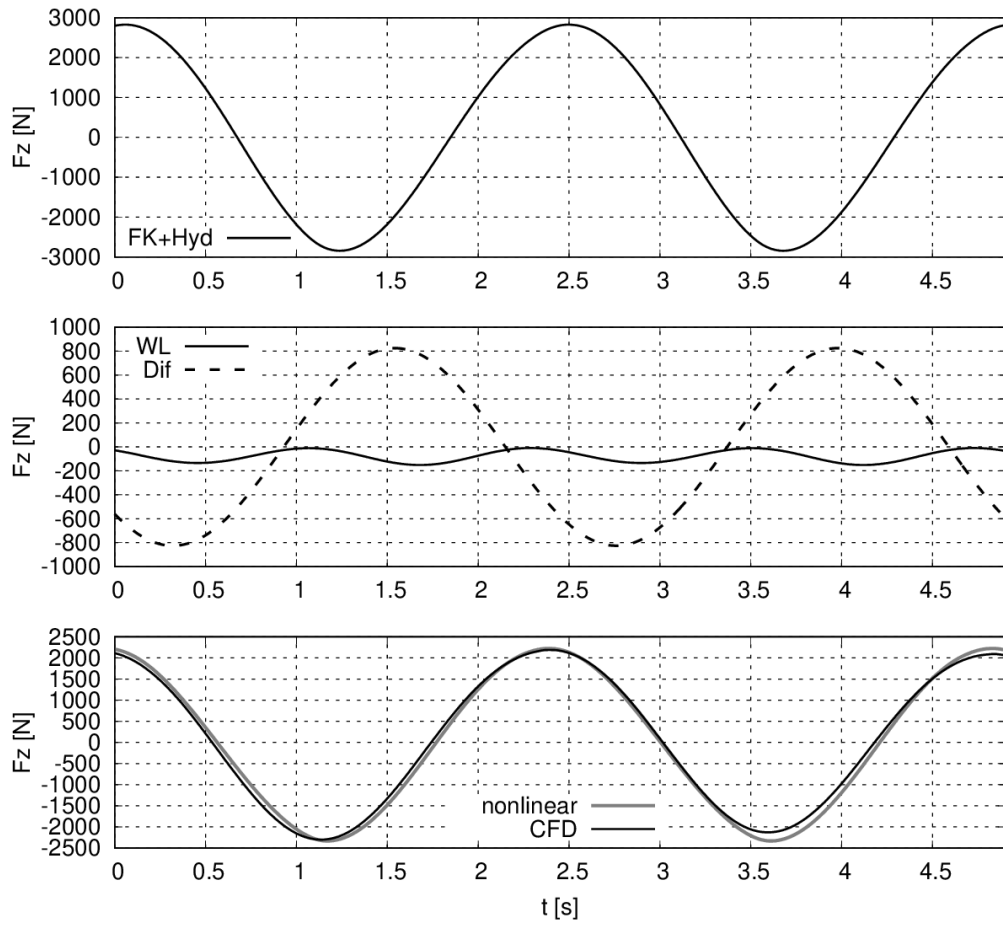


Figure 56: Time histories of vertical forces for the fixed Containership A ($F_n = 0.139$) in head waves of $\lambda/L = 2.50$ and a wave steepness $h = 0.011$. “FK+Hyd” denotes the combined Froude-Krylov and hydrostatic forces, “WL” denotes nonlinear waterline forces, “Dif” denotes diffraction forces and “nonlinear” denotes the total hydrodynamic force compared to the CFD result.

4.3 Validation of Wave-Induced Forces

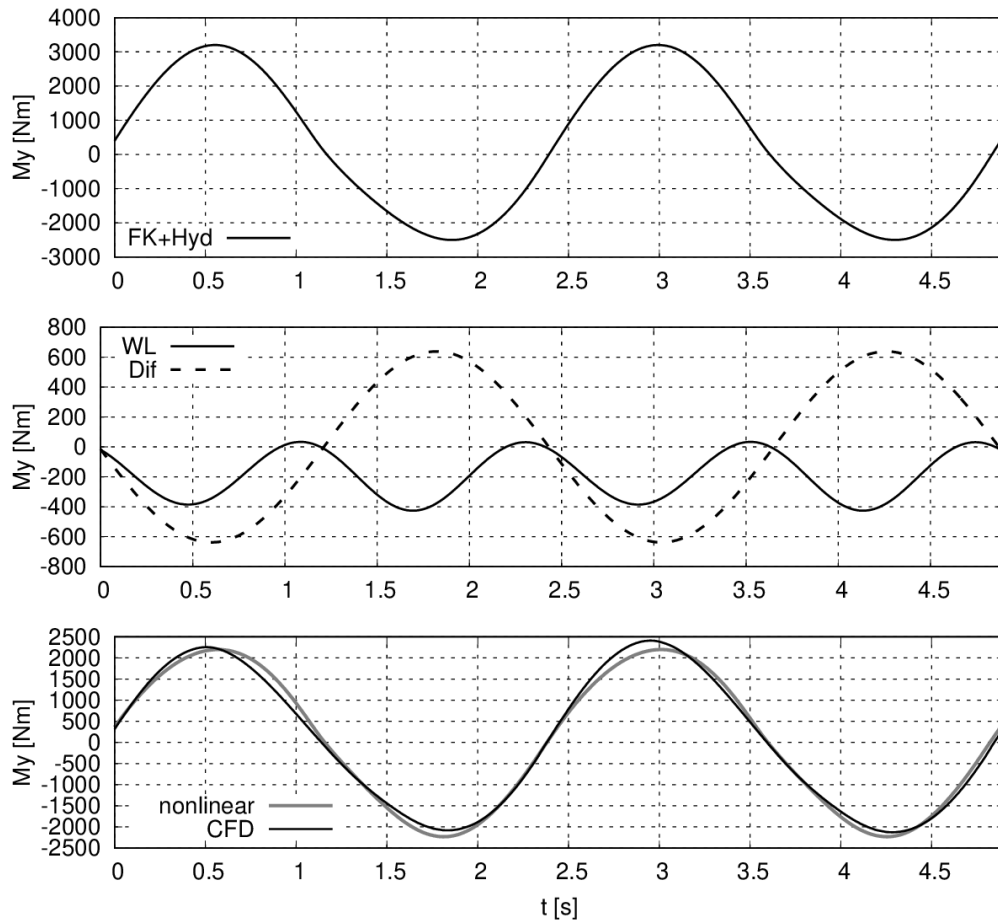


Figure 57: Time histories of pitch moments for the fixed Containership A ($F_n = 0.139$) in head waves of $\lambda/L = 2.50$ and a wave steepness $h = 0.011$. “FK+Hyd” denotes combined Froude-Krylov and hydrostatic moment, “WL” denotes nonlinear waterline moment, “Dif” denotes diffraction moment and “nonlinear” denotes the total hydrodynamic moment compared to the CFD result.

For the fixed Containership A in regular head waves of length corresponding to $\lambda/L = 1.09$ and an amplitude of $\zeta = 5.60\text{m}$ (full scale) Figure 58, Figure 59 and Figure 60 plot time histories of the wave induced longitudinal forces, vertical forces and pitch moments, respectively. Similar to the time histories plots in waves of $\lambda/L = 2.50$, the longitudinal combined Froude-Krylov and hydrostatic force (FK+Hyd) is again non-harmonic. However, in this case the time span between a positive and a negative peak is shorter than the time span between a negative and a positive peak. The difference between the first order harmonic amplitude of the combined longitudinal Froude-Krylov and hydrostatic force and the longitudinal diffraction force is smaller than for the case of $\lambda/L = 2.50$ (The amplitude of the FK+Hyd force is about twice as large). The time average of the FK+Hyd force is -3.33N . The first order harmonic amplitude of the longitudinal nonlinear water line force is still small compared to the FK+Hyd and Dif amplitudes. However, its time average of

-8.96N is the largest contribution to the total drift force. The time history of the longitudinal total hydrodynamic force (nonlinear) compared favourably to the time history from the CFD method (CFD). The first order harmonic amplitude of the new numerical method is 166.23N; from the CFD method, 177.41N. Furthermore, the time average agreed favorably. The new numerical method computed a time average of -12.30N; the CFD solver computed a time average of -14.78N.

A similar trend was found for the wave induced vertical force plotted in Figure 59. The combined Froude-Krylov and hydrostatic force showed a non-harmonic behaviour and its amplitude is larger compared to the amplitude of the waterline force. However, the diffraction force amplitude is only slightly smaller and contributes significantly to the total hydrodynamic force. The agreement between the total hydrodynamic force (nonlinear) and the CFD result (CFD) is slightly less good as for the previous comparisons. The computed first harmonic amplitude of the vertical wave-induced force was 333.6N compared to the CFD result of 391.0N. The result of the new numerical method indicated higher order oscillation. More details of the higher order harmonic amplitudes are discussed in the end of this section.

Figure 60 compares the wave induced pitch moments. The total hydrodynamic moment of the new numerical method (first harmonic amplitude of 1792.0N) compares well to the CFD results (first harmonic amplitude of 1908.3N) and again, the amplitude of the wave induced waterline moment is relatively high. The amplitude of the wave induced waterline moment is approximately 5.5 times smaller than the amplitude of the Froude-Krylov moment.

4.3 Validation of Wave-Induced Forces

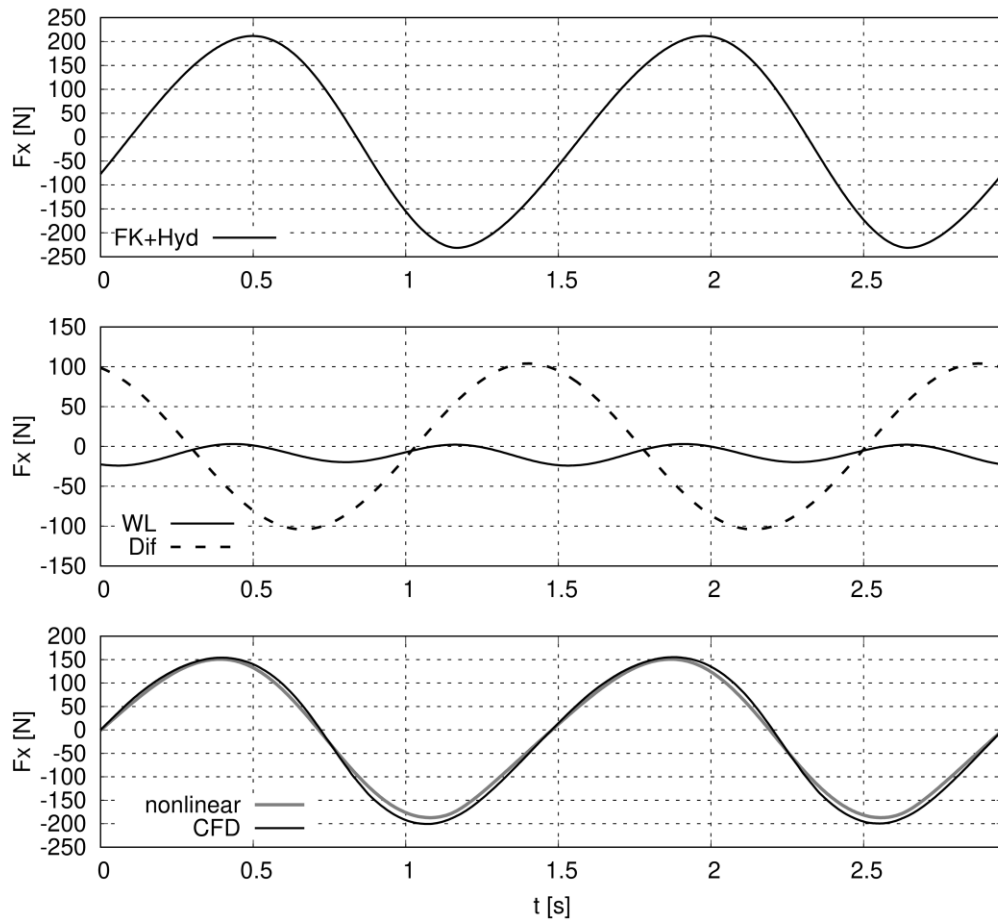


Figure 58: Time histories of longitudinal forces for the fixed Containership A ($F_n = 0.139$) in head waves of $\lambda/L = 1.09$ and a wave steepness $h = 0.023$. “FK+Hyd” denotes combined Froude-Krylov and hydrostatic forces, “WL” denotes nonlinear waterline forces, “Dif” denotes diffraction forces and “nonlinear” denotes the total hydrodynamic force compared to CFD results.

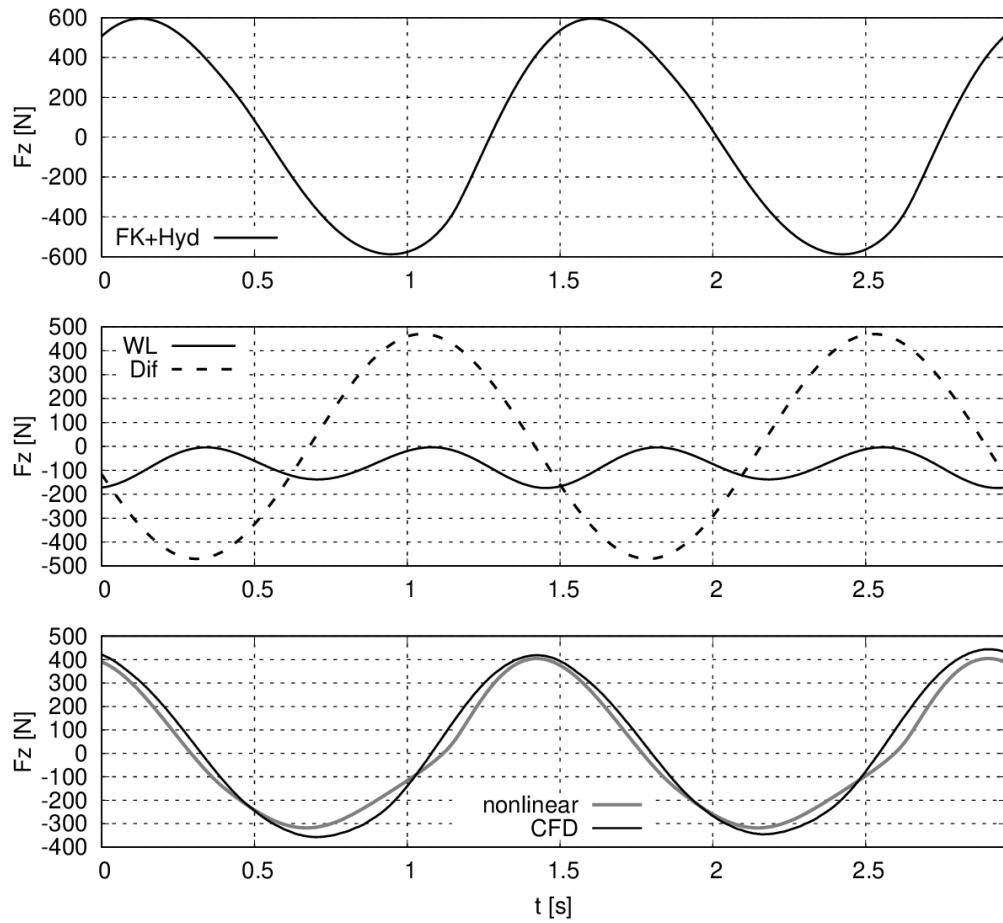


Figure 59: Time histories of vertical forces for the fixed Containership A ($F_n = 0.139$) in head waves of $\lambda/L = 1.09$ and a wave steepness $h = 0.023$. “FK+Hyd” denotes combined Froude-Krylov and hydrostatic forces, “WL” denotes nonlinear waterline forces, “Dif” denotes diffraction forces and “nonlinear” denotes the total hydrodynamic force compared to the CFD result.

4.3 Validation of Wave-Induced Forces

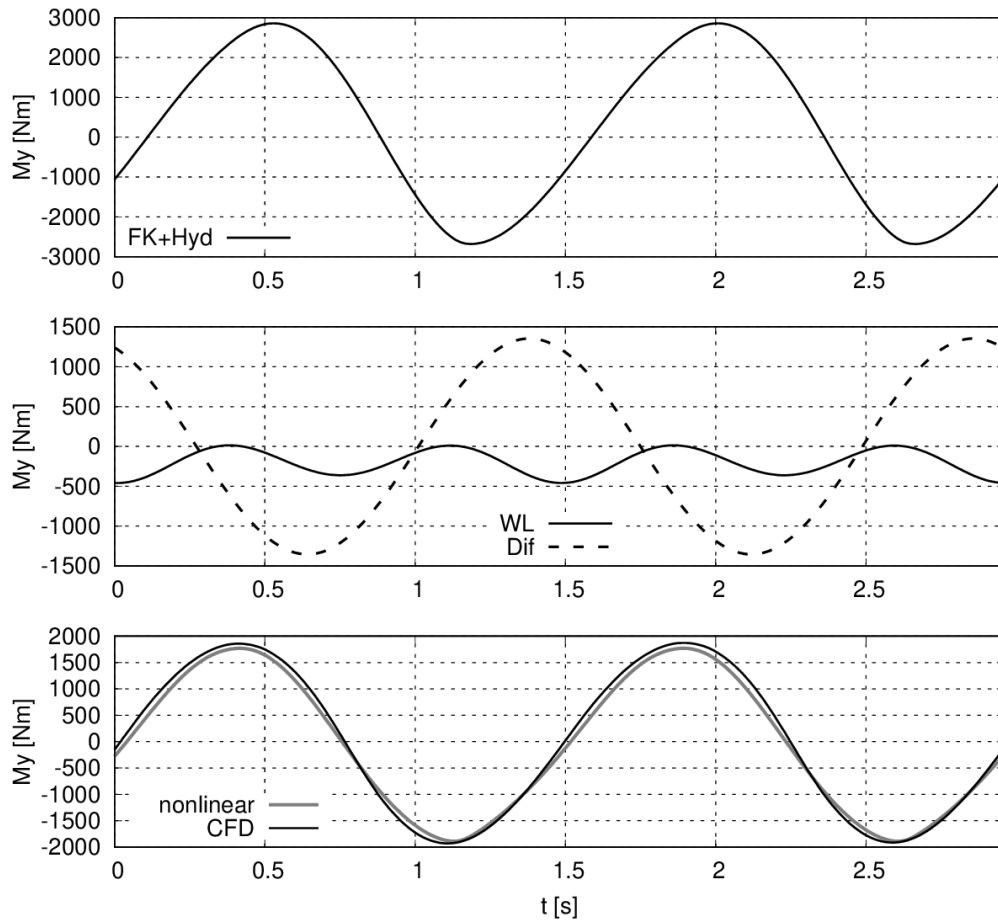


Figure 60: Time histories of wave induced pitch moments for the fixed containership A ($F_n = 0.139$) in head waves of $\lambda/L = 1.09$ and a wave steepness $h = 0.023$. “FK+Hyd” denotes the combined Froude-Krylov and hydrostatic moment, “WL” denotes nonlinear waterline moment, “Dif” denotes diffraction moment and “nonlinear” denotes the total hydrodynamic moment compared to the CFD result.

For the fixed Containership A in regular head waves of length corresponding to $\lambda/L = 0.60$ and a wave amplitude of $\zeta = 3.775\text{m}$ (full scale), Figure 61, Figure 62 and Figure 63 plot the wave induced longitudinal force, vertical force and pitch moment, respectively. Figure 61 indicates that the characteristic of the longitudinal force did not change significant compared to the results of the previously discussed waves. The amplitude of the combined Froude-Krylov and hydrostatic force dominated the total hydrodynamic force and is approximately four times larger than the amplitude of the diffraction force. The amplitude of the waterline force was approximately half of the amplitude of the diffraction force. However, its time average was the largest contribution. The time average of the Froude-Krylov force was -1.20N ; the time average of the water line force, -4.41N .

The total hydrodynamic force computed with the new numerical method (nonlinear) showed small differences to the results of the CFD solver (CFD), especially at the maximum negative amplitude. However, the first harmonic amplitudes of 41.02N from the new numerical method (nonlinear) and of 38.17N from the CFD method (CFD) were still similar and their time averages values of -5.69N from the new numerical method and -6.40N from the CFD method (CFD) correlate more closely than for the case of $\lambda/L = 2.50$.

Figure 62 plots the wave induced vertical forces. In contrast to the longitudinal force, the amplitude of the diffraction force was similar to the amplitude of the combined Froude-Krylov and hydrostatic force. However, the amplitude of the waterline force was small. Comparing the total hydrodynamic force of the new numerical method (a first harmonic amplitude of 263.1N) with the CFD result (a first harmonic amplitude of 303.6N) some differences can be seen. This is different for the wave induced pitch moment plotted in Figure 63. The total hydrodynamic pitch moment from the new numerical method (a harmonic amplitude of 227.0N) and the CFD solver (a first harmonic amplitude of 167.4N) showed clear differences at maximum negative peaks. The maximum negative peak appears when a wave trough was located at the stern of the ship. In this situation the flat hull bottom above the propeller emerged and the wetted surface changed strongly. The combined Froude-Krylov and hydrostatic moment considers this effect, because the pressure was integrated over the instantaneous wetted surface. However, the diffraction force was linear and thus could not consider the effect of the changing wetted surface. The effect of the changing wetted surface on diffraction forces was considered by the waterline integral, as discussed in section 2.2.2.4, using the method of Boese (1970). This method is based on the assumption that the hull normal vector near the time average waterline does not change. This assumption is acceptable for most parts of the waterline and if the motion of the waterline relative to the ship hull is moderate. However, for the current scenario, the ship was fixed and thus could not follow the slope of the wave. Furthermore, the investigated wave amplitude was relatively large. Both effects caused the wetted surface at the stern to change strongly. The assumption that the hull normal vector is constant in the region of the changing wetted surface is not correct anymore. And causes the differences between the results of the new numerical method and the CFD solver. This effect was not observable at the previous discussed results of longer waves because the amplitude of the diffraction moment and thus also the amplitude of the waterline moment was significantly smaller compared to the amplitudes of the combined Froude-Krylov and hydrostatic moment. The effect existed there as well but its influence on the total hydrodynamic force was significantly smaller.

4.3 Validation of Wave-Induced Forces

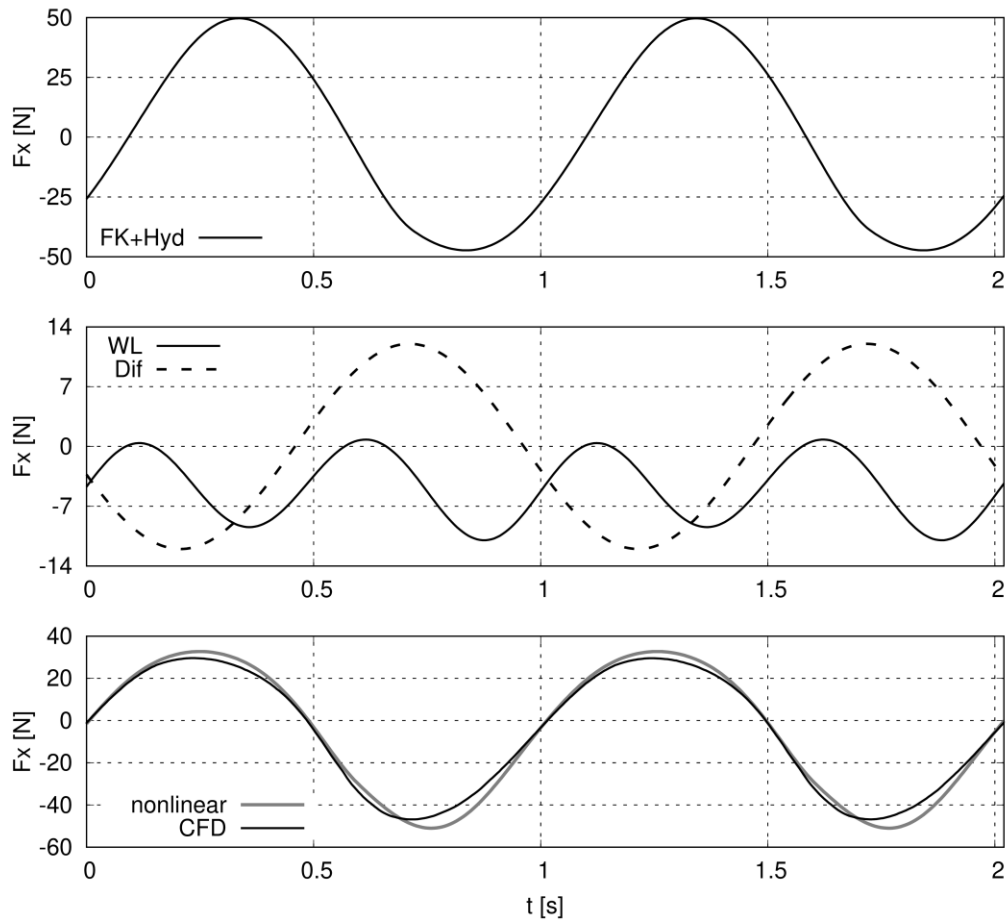


Figure 61: Time histories of longitudinal forces for the fixed Containership A ($F_n=0.139$) in head waves of $\lambda/L_{pp} = 0, 6$ and a wave steepness $h = 0.028$. "FK+Hyd" denotes combined Froude-Krylov and hydrostatic forces, "WL" denotes nonlinear waterline forces, "Dif" denotes diffraction forces and "nonlinear" denotes the total hydrodynamic force compared to the CFD result.

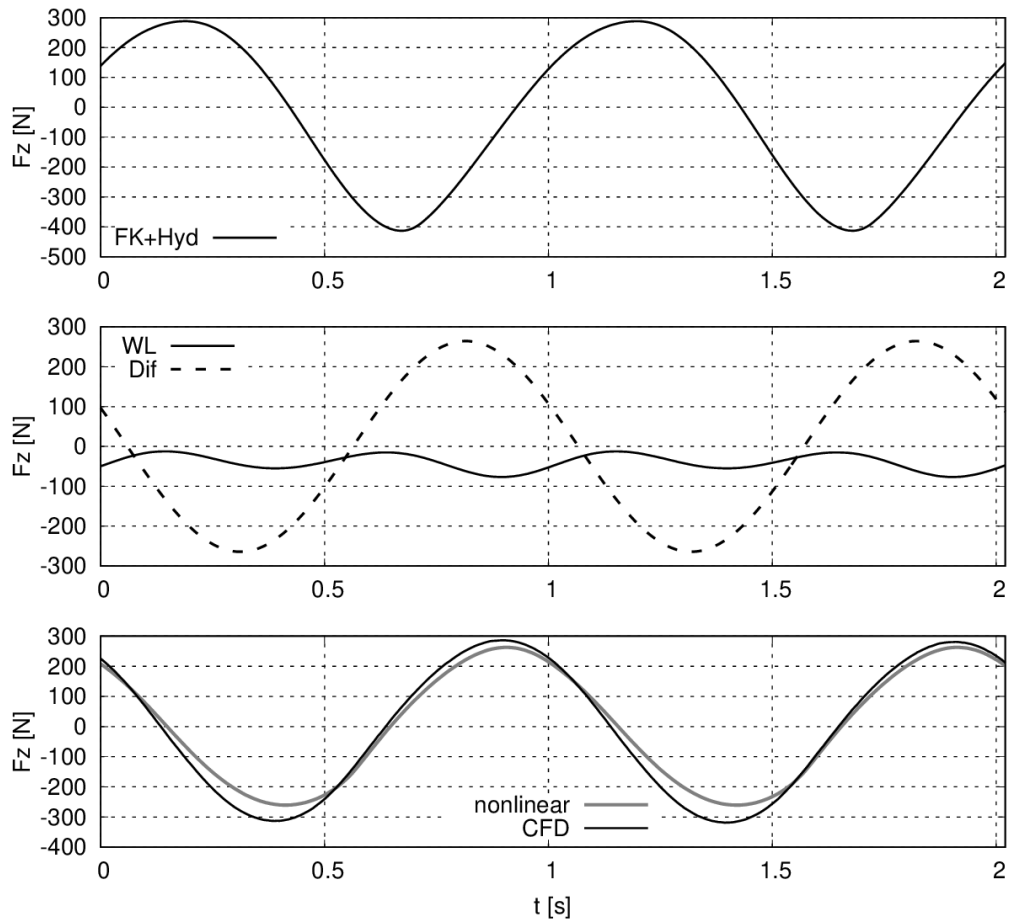


Figure 62: Time histories of vertical forces for the fixed Containership A ($F_n=0.139$) in head waves of $\lambda/L = 0.6$ and a wave steepness $h = 0.028$. “FK+Hyd” denotes the combined Froude-Krylov and hydrostatic force, “WL” denotes the nonlinear waterline force, “Dif” denotes the diffraction force and “nonlinear” denotes the total hydrodynamic force compared to the CFD result.

4.3 Validation of Wave-Induced Forces

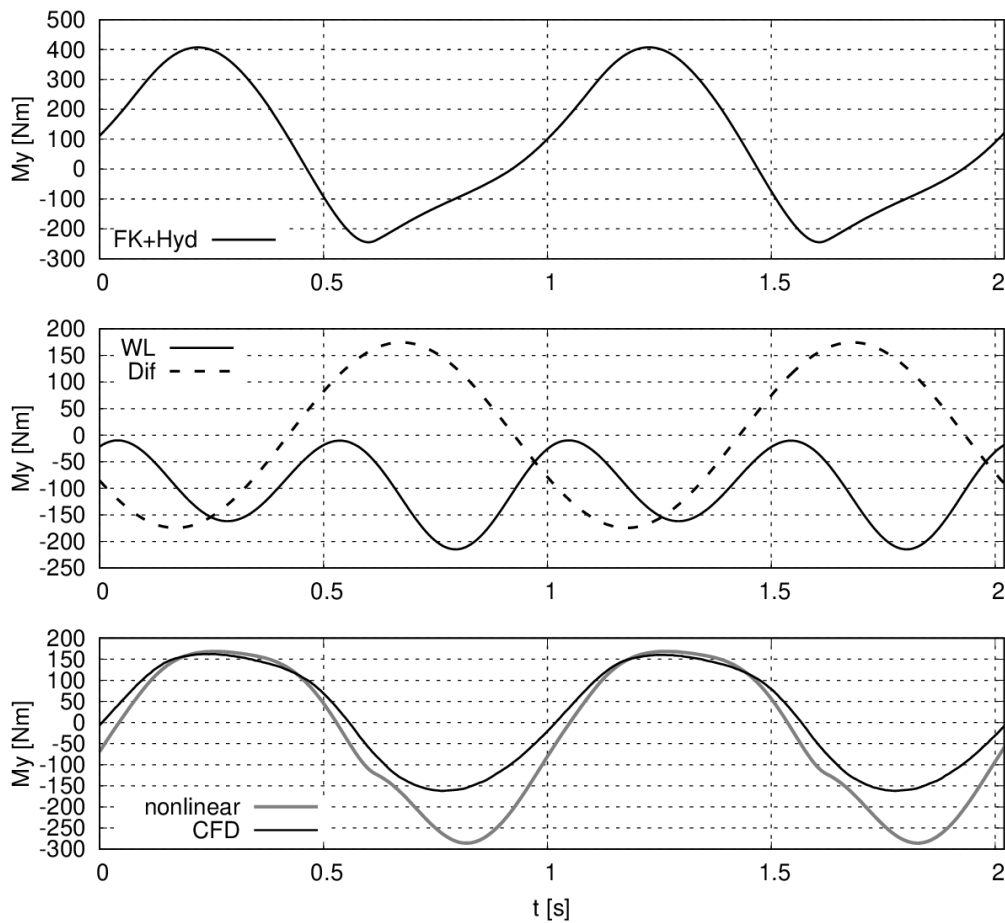


Figure 63: Time histories of the pitch moment for the fixed containership A ($F_n = 0.139$) in head waves of $\lambda/L = 0.6$ and a wave steepness $h = 0.028$. “FK+Hyd” denotes combined Froude-Krylov and hydrostatic moments, “WL” denotes nonlinear waterline moments, “Dif” denotes diffraction moments and “nonlinear” denotes the total hydrodynamic moment compared to the CFD result.

The comparisons of the three wave scenarios discussed above showed a favourable agreement between the results from the new numerical method and the CFD-Solver. The new numerical method was capable to account for the most dominant nonlinear effects. Only the pitch moment for the wave corresponding to $\lambda/L = 0.60$ showed stronger deviations that could be associated to the changing wetted surface at the stern. However, it is assumed that this effect is less pronounced when the ship is free to move and thus follow the free surface elevation. To compare results of the new numerical method and the CFD solver for a wider range of wave length to ship length scenarios, Figure 64, Figure 65, Figure 66 plot first, second, third and fourth harmonic amplitudes of the longitudinal force, vertical force and pitch moment against λ/L_{pp} . The harmonic amplitudes were obtained by applying a Fourier transformation of every time series. In these figures, the upper left graph plots comparative first harmonic amplitudes; the upper right graph plots

second harmonic amplitude; the lower left graph plots third harmonic amplitudes and the lower right graph plots fourth harmonic amplitudes. Table 11 lists the wave properties, namely the wave angular frequency ω , wave encounter frequency ω_e , wave length to ship length ratio λ/L_{pp} , the wave amplitude ζ^1 and the wave steepness h of the investigated waves.

Table 11: Wave length ratio, wave amplitude, and wave steepness for the considered cases.

ω [rad/s]	ω_e [rad/s]	λ/L_{pp} [-]	ζ^1 [m]	h [-]
0.264	0.323	2.50	5.902	0.011
0.311	0.392	1.80	5.902	0.016
0.352	0.456	1.40	5.902	0.02
0.380	0.502	1.20	4.074	0.019
0.399	0.533	1.09	4.481	0.023
0.417	0.564	1.00	4.710	0.027
0.437	0.597	0.91	3.800	0.024
0.466	0.649	0.80	3.972	0.028
0.538	0.782	0.60	3.004	0.028

The first harmonic amplitudes of the longitudinal force (Figure 64) showed a good agreement between the new numerical method (denoted as “nonlinear”) and the CFD solver (CFD). The first harmonic amplitudes increased with increasing wave length until it reached its maxima at $\lambda/L_{pp} = 1.40$ (CFD) and $\lambda/L_{pp} = 1.80$ (nonlinear). For some wave scenarios larger deviations were found, e.g. the first harmonic amplitude computed with the new numerical method (nonlinear) for $\lambda/L = 1.20$ is about 23 percent lower than the CFD result. However, the overall trend is favourably captured. A similar characteristic was found for the second harmonic amplitudes of the longitudinal force. For some wave scenarios results of the new numerical method and the CFD solver differed clearly, e.g. $\lambda/L_{pp} = 1.20$, however, the overall agreement is good. Focusing on the third and fourth harmonic amplitudes of the longitudinal force it is more difficult to find a clear overall trend. Especially for the third harmonic amplitudes, the CFD results oscillated significantly. The corresponding results of the new numerical method indicated an overall trend with an increasing third order amplitude for increasing wave length. The results of the new numerical method and the CFD solver differed clearly, however, the third harmonic amplitudes of both methods are of similar magnitude. Furthermore, third harmonic amplitudes are relatively small compared to first harmonic amplitude (approximately 50 times smaller) and influence the total ship response only minimally. For the fourth harmonic amplitude, result of the new numerical method and the CFD solver showed a similar overall trend, however, the new numerical method underestimated the fourth

4.3 Validation of Wave-Induced Forces

harmonic amplitude especially in long waves. However, the fourth harmonic amplitudes were approximately 100 times smaller than the first harmonic amplitudes and not relevant for the total longitudinal force.

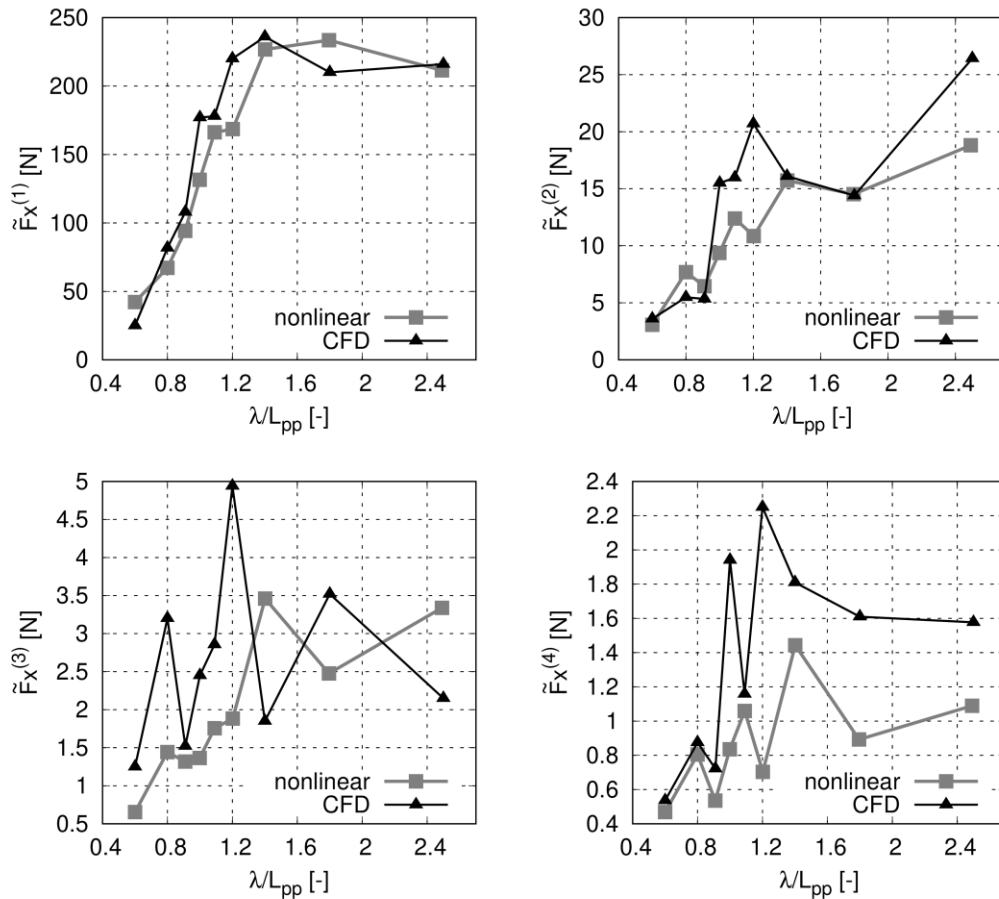


Figure 64: First, second, third and fourth harmonic amplitudes of the longitudinal force of the Containership A in head waves with a forward speed according to $F_n = 0.139$.

Figure 65 compares the first, second, third and fourth harmonic amplitude of the vertical wave-induced force. The agreement of the first harmonic amplitudes is good. Higher deviations could only be found for $\lambda/L_{pp} = 1.20$ and $\lambda/L = 1.80$. The second harmonic amplitudes agree less favourable. Especially in waves corresponding to $\lambda/L_{pp} \approx 1.0$ and $\lambda/L_{pp} \geq 1.8$ the new numerical method underestimated second harmonic amplitudes. This effect can be most likely explained by the changing wetted surface at the flat bottom near the stern. As demonstrated before, due to the large wave amplitude of 5.9 meter, a large area of the hull was periodically immersed and emerged near the stern. This affects especially the vertical force and pitch moment. As aforementioned, the

combined Froude-Krylov and hydrostatic force considers the change of the wetted surface because they were integrated over the instantaneous wetted surface. However, diffraction forces were based on linear potential theory and did not consider the changing wetted surface. The effect of the changing wetted surface on radiation and diffraction forces was considered by the waterline integral. As already mentioned, the waterline integral cannot consider such strong variations of the wetted surface and causes most likely the deviations between the new numerical method and the CFD solver. The third harmonic amplitudes oscillated stronger than the first and second harmonic amplitudes and results from the new numerical method and from CFD differed for some wave scenarios. However, the overall agreement was favourable. Regarding the fourth harmonic amplitudes of the vertical wave induced force, the new numerical method overestimates the amplitudes compared to the CFD solver, except for $\lambda/L_{pp} = 1.8$. However, in principle fourth and third harmonic amplitudes were small compared to first harmonic amplitudes and influenced the total hydrodynamic force only minimally.

4.3 Validation of Wave-Induced Forces

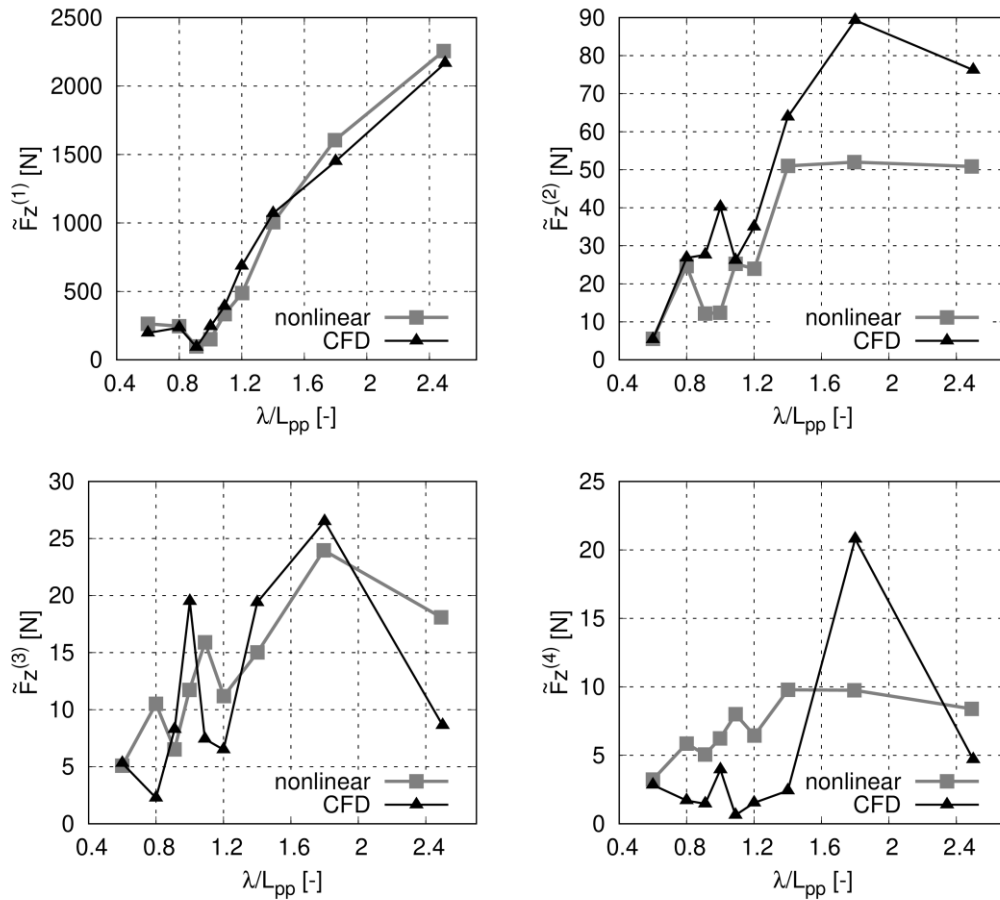


Figure 65: First, second, third and fourth harmonic amplitudes of the vertical force of the Containership A in head waves with a forward speed according to $Fn = 0.139$.

The first, second, third and fourth harmonic amplitudes of the pitch moment are plotted in Figure 66. The first harmonic amplitudes showed a similar characteristic as the first harmonic amplitudes of the longitudinal force. For some wave scenarios results of the new numerical method and the CFD solver differed slightly, e.g. $\lambda/L_{pp} = 1.0; 1.2; 1.8$. However, the overall agreement was good. For the second harmonic amplitudes the agreement between both numerical methods was less favourable. The new numerical method predicted a similar trend of the second harmonic amplitudes, however, underestimated the results especially in long waves. As aforementioned, this effect was mainly caused by the strongly changing wetted surface at the ship's stern. The third and fourth harmonic amplitudes, again, showed stronger oscillations. For the third harmonic amplitudes, results of the new numerical method and CFD solver were of similar magnitude even the results for some waves deviated. For the fourth harmonic amplitudes,

both numerical methods showed a similar trend, however, the new numerical method overestimated the response.

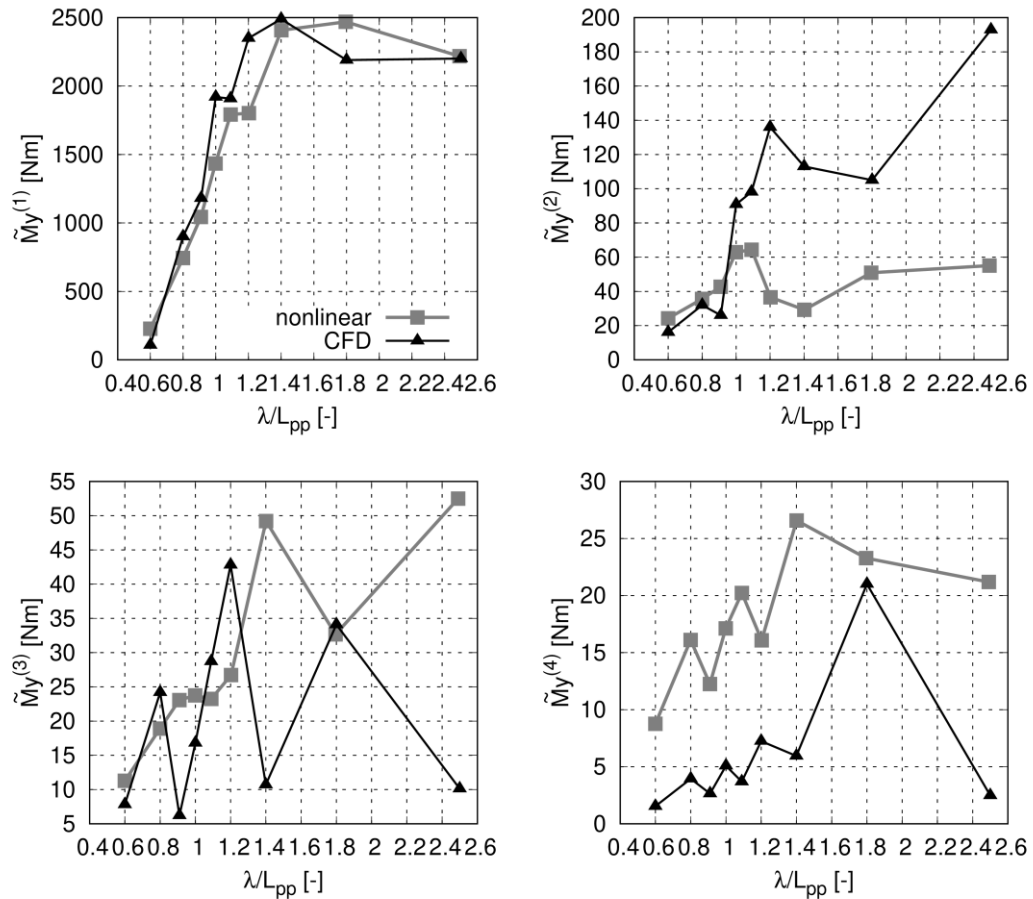


Figure 66: First, second, third and fourth harmonic amplitudes of the pitch moment of the Containership A in head waves with a forward speed according to $Fn = 0.139$.

4.3.2 Weakly-Nonlinear Hydrodynamic Forces at a Moving Ship

Wave induced forces and moments on the freely floating ship are of practical matter for the ship design. For the freely moving containership A at a constant forward speed according to $Fn = 0.139$, Table 12 lists the investigated wave properties, namely the wave angular frequency ω , wave encounter frequency ω_e , the wave length to ship length ratio λ/L_{PP} , the wave amplitude ζ^1 and the wave steepness h .

4.3 Validation of Wave-Induced Forces

Table 12: Wave length ratio, wave amplitude, and wave steepness for the considered cases

ω [rad/s]	ω_e [rad/s]	λ/L [-]	ζ^1 [m]	h [-]
0.264	0.322	2.50	5.902	0.011
0.311	0.392	1.80	5.902	0.016
0.352	0.456	1.40	5.902	0.02
0.380	0.502	1.20	4.074	0.019
0.399	0.533	1.09	4.481	0.023
0.417	0.564	1.00	4.710	0.027
0.437	0.598	0.91	3.800	0.024
0.466	0.649	0.80	3.972	0.028
0.538	0.782	0.60	3.004	0.028
0.628	0.960	0.44	4.551	0.058
0.694	1.010	0.36	3.119	0.049
0.787	1.309	0.28	2.287	0.048

The present validation study focus on wave-induced forces and moment in head waves. Results of the new numerical method were compared to CFD result. In the CFD simulations, only the heave and pitch motion were free and the surge motion was suppressed. For that reason, the surge motion was also suppressed during the simulations with the new numerical method. Forward speed corresponding to $Fn = 0.139$ was applied.

Figure 67 to Figure 69 plot the time histories of the longitudinal force, vertical force and the pitch motion, respectively, for a regular head wave of $\lambda/L_{PP} = 2.5$. In each figure, the upper graph plots the time histories of the nonlinear combined Froude-Krylov and hydrostatic force (FK+Hyd); the center graph the time histories of the diffraction force (Dif), the radiation force (Rad) and their nonlinear waterline contribution (WL). The lower graph compares the total hydrodynamic force obtained from the new numerical method (nonlinear) and the force from the CFD method (CFD).

For the longitudinal forces, the FK+Hyd force oscillates almost harmonically about its time average of -3.02N . With a first harmonic amplitude of 198N and a second harmonic amplitude of only 1.26N . The first harmonic amplitude of the diffraction force (30.71N) and the first harmonic amplitude of the radiation force (40.83N) were smaller than the first harmonic amplitude of the combined Froude-Krylov and hydrostatic force. However, they oscillate clearly non-harmonically. The radiations and diffraction force are based on the solution of a linear frequency domain computation. During the linear frequency domain computation, the radiation and diffraction pressure oscillates harmonically. However, in Figure 67 it can be seen that the radiation and diffraction force in time domain behaves non-harmonically. This effect results from the assumption that the diffraction

induced pressure oscillates harmonically on the body surface. Due to ship motions, this can generate a non-harmonic oscillation of the diffraction force in the inertial coordinate system. The same effect occurs at the radiation forces. The convolution integrals were computed based on the integration of the radiation pressure over the hull surface and thus are defined in the body coordinate system and were transferred into the inertial coordinate system for solving the nonlinear rigid body motion equation. Furthermore, the ship motions act as an input signal in the convolution integral and scale linearly the result of the convolution integral. Consequently, a non-harmonic ship motion initiates a non-harmonic radiation force. This phenomenon causes the diffraction and radiation force to be non-harmonic which can also be seen from high second harmonic amplitudes of 11.65N for the diffraction force and 16.38N for the radiation force and time average values of 7.82N for the radiation force and -6.73 N for the diffraction force. The first harmonic amplitude of the waterline force was small (0.646N). However, the second harmonic (5.82N) and the third harmonic (0.921N) amplitudes were considerably larger, demonstrating that the coupled waterline force (WL) accounted for higher order effects of the radiation and diffraction force due to the changing wetted surface. Although the time average of the waterline force (-1.47N) contributed to total wave added resistance, its contribution was the smallest of all other force components. The total result of the new numerical method (nonlinear) compared favorably to comparable CFD computation (CFD), whereas the associated time average force (-3.40N) differed somewhat from the time average CFD force (-2.75N). However, relative to their first harmonic amplitudes, the difference was less than one percent.

The comparisons between the new numerical method (nonlinear) and the CFD solver (CFD) for the vertical wave induced force was similarly good as for the longitudinal force. Focusing on each force component, the vertical radiation force had the highest amplitude, followed by the diffraction force, the nonlinear combined Froude-Krylov and hydrostatic force and the waterline force. Radiation and diffraction forces had a phase shift of approximately 180deg. The new numerical method computed an almost identical total hydrodynamic force compared to the CFD solver with a first harmonic amplitude of 308.0N computed with the new numerical method and 302.3N computed with the CFD solver.

The total wave induced pitch moment computed with the new numerical method and the CFD solver (Figure 69) showed a strong nonlinear behaviour and slightly higher deviations between both methods. The first harmonic amplitude from the new numerical method was 267.5N and from the CFD solver 298.5N. For the current scenario, radiation and diffraction forces contribute significantly to the total hydrodynamic force. Recall that the effect of the changing wetted surface on radiation and diffraction forces were

4.3 Validation of Wave-Induced Forces

considered by the waterline force. The waterline force can capture only moderate changes of the wetted surface, which may cause the deviation between the new numerical method (nonlinear) and the CFD solver (CFD).

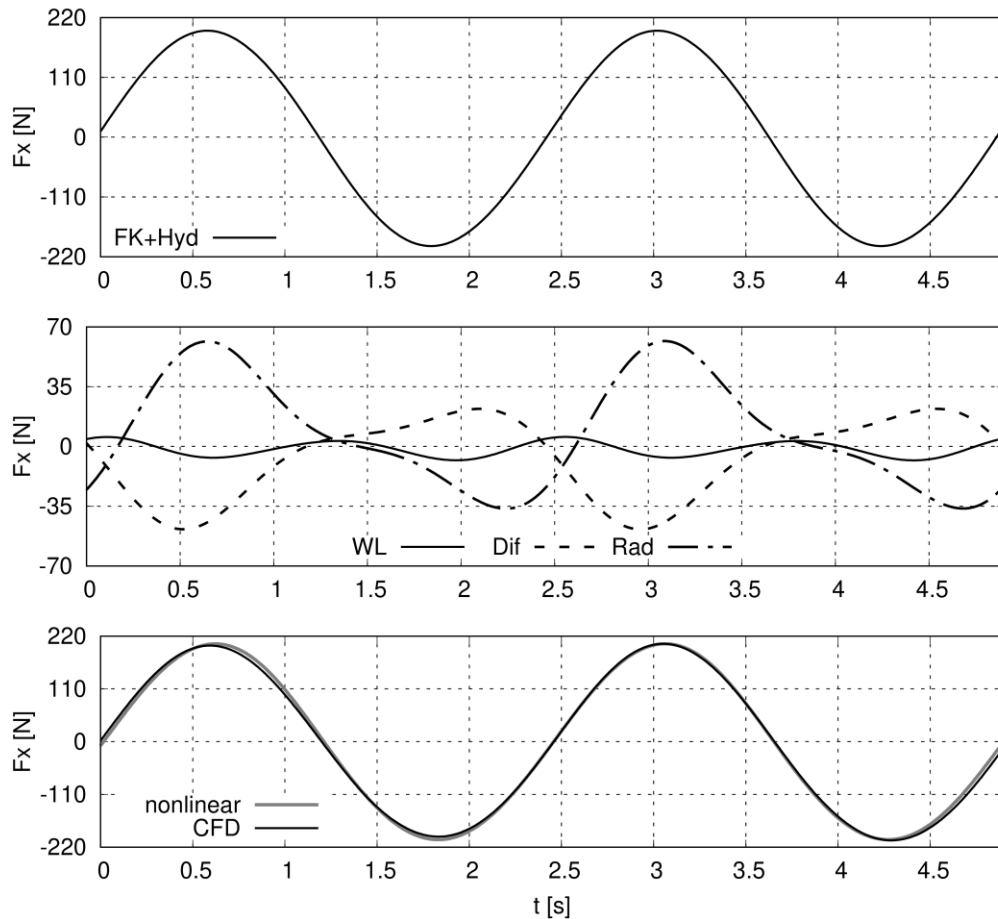


Figure 67: Time histories of the longitudinal forces for the freely floating Containership A ($F_n=0.139$) in head waves of $\lambda/L = 2.5$ and a wave steepness $\bar{h} = 0.011$. "FK+Hyd" denotes the combined Froude-Krylov and hydrostatic force, "WL" denotes nonlinear waterline forces, "Dif" denotes diffraction forces, "Rad" denotes the radiation force and "nonlinear" denotes the total hydrodynamic force.

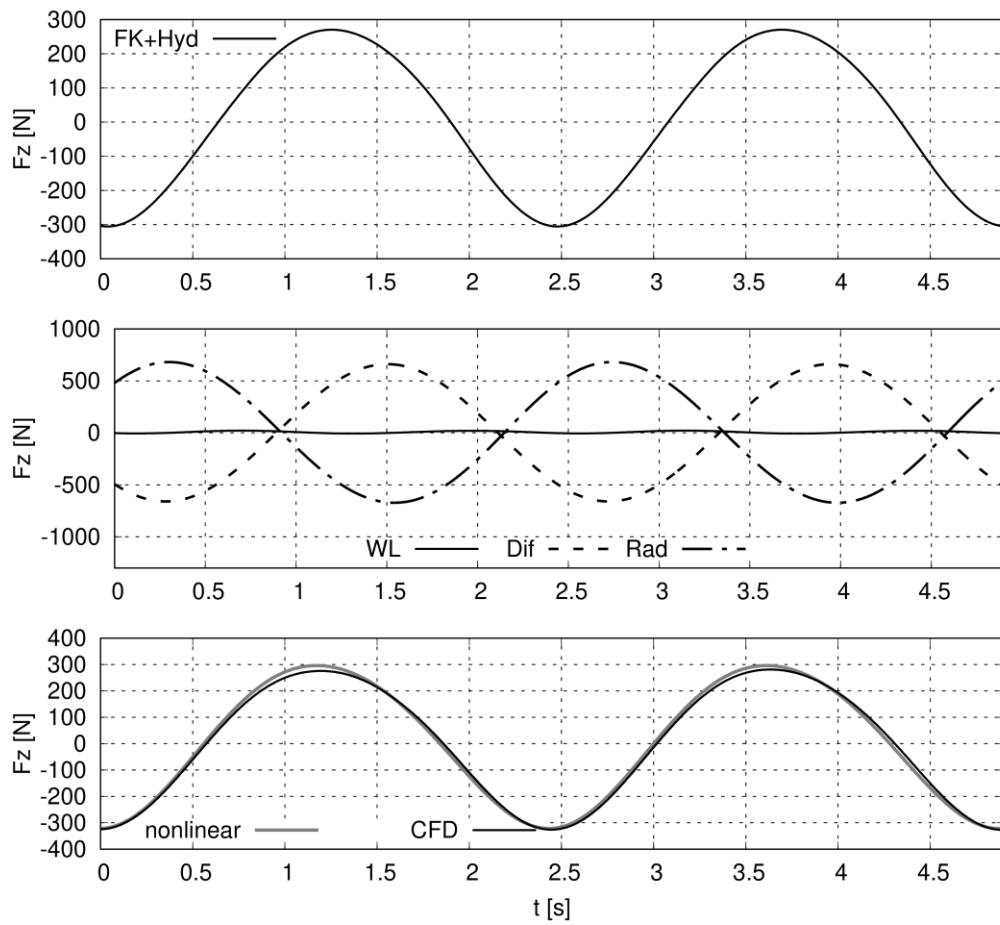


Figure 68: Time histories of the vertical forces for the freely floating Containership A ($F_n=0.139$) in head waves of $\lambda/L = 2.5$ and a wave steepness $h = 0.011$. "FK+Hyd" denotes the combined Froude-Krylov and hydrostatic force, "WL" denotes nonlinear waterline forces, "Dif" denotes diffraction forces, "Rad" denotes the radiation force and "nonlinear" denotes the total hydrodynamic force.

4.3 Validation of Wave-Induced Forces

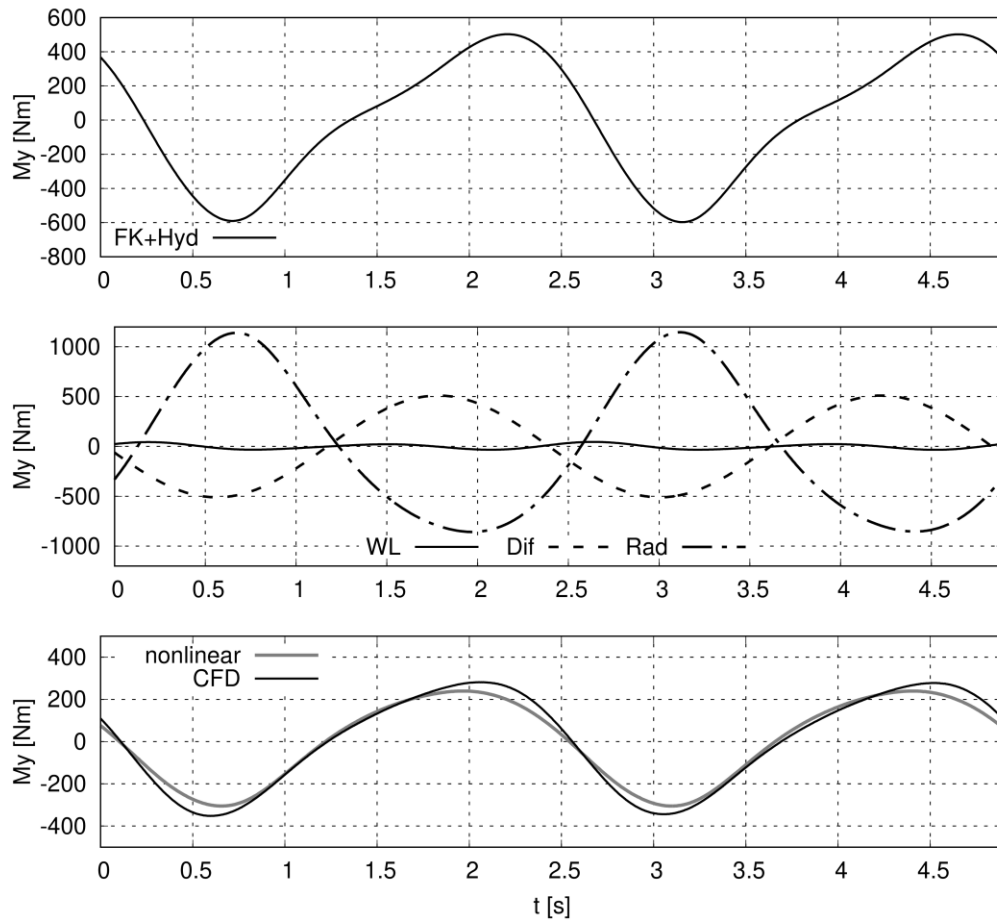


Figure 69: Time histories of the pitch moment for the freely floating Containership A ($F_n=0.139$) in head waves of $\lambda/L = 2.5$ and a wave steepness $h = 0.011$. “FK+Hyd” denotes the combined Froude-Krylov and hydrostatic moment, “WL” denotes nonlinear waterline moment, “Dif” denotes diffraction moment, “Rad” denotes the radiation moment and “nonlinear” denotes the total hydrodynamic moment.

With decreasing wave length, the behaviour of each hydrodynamic force or moment component, namely nonlinear combined Froude-Krylov and hydrostatic, radiation, diffraction and waterline forces and moments, did not change significantly. However, it could be observed that the amplitude of the waterline integral increased relative to the amplitudes of the remaining forces. Thus, the influence of the waterline force increased with decreasing wave length. Because the principal behaviour of the force and moment components did not change significantly, only the total hydrodynamic force computed with the new numerical method (nonlinear) and the CFD solver (CFD) are plotted for the wave of medium length $\lambda/L_{PP} = 1.09$ and the short wave $\lambda/L_{PP} = 0.6$. Comparisons of harmonic amplitudes are discussed later, see Figure 72, Figure 73 and Figure 74. Figure 70 compares the longitudinal force (top), the vertical force (center) and the pitch moment

(bottom) computed with the new numerical method (nonlinear) and the CFD solver (CFD) for a regular wave of $\lambda/L_{PP} = 1.09$. Both methods computed similar result with a favourable agreement for the pitch moment, some small deviations for the longitudinal force and slightly larger deviations for the vertical force. For the maximum amplitudes of the longitudinal and vertical force, the new numerical method underestimated the forces. The wave amplitude was relatively high, 4.481m in full scale, caused the ship to move strongly. As a consequence, wave breaking might be occurred in the CFD simulations and could have reduced the maximum amplitude of the wave induced forces.

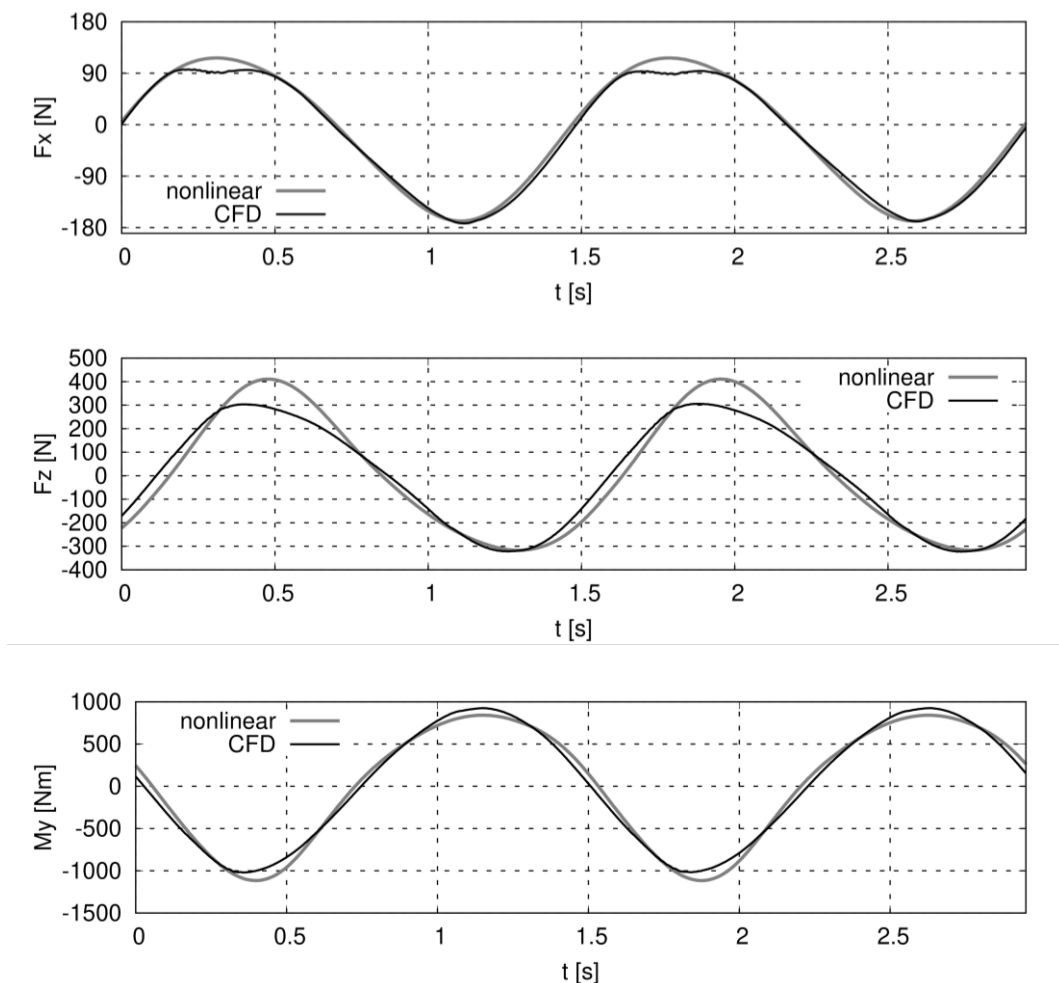


Figure 70: Time histories of the longitudinal force (top), vertical forces (center) and pitch moment (bottom) for the freely floating Containership A ($F_n=0.139$) in head waves of $\lambda/L_{PP} = 1.09$ and a wave steepness $h = 0.023$. “nonlinear” denotes results of the new numerical method and “CFD” denotes results from the CFD solver.

Figure 71 compares the longitudinal force (top), the vertical force (center) and the pitch moment (bottom) computed with the new numerical method (nonlinear) and the CFD solver (CFD) for a regular wave of $\lambda/L = 0.6$. Small deviations between the new numerical

4.3 Validation of Wave-Induced Forces

method and the CFD solver can be seen for every force and moment component, however, considering that the wave amplitude is relatively high (3m in full scale) the agreement between both methods is favourable.

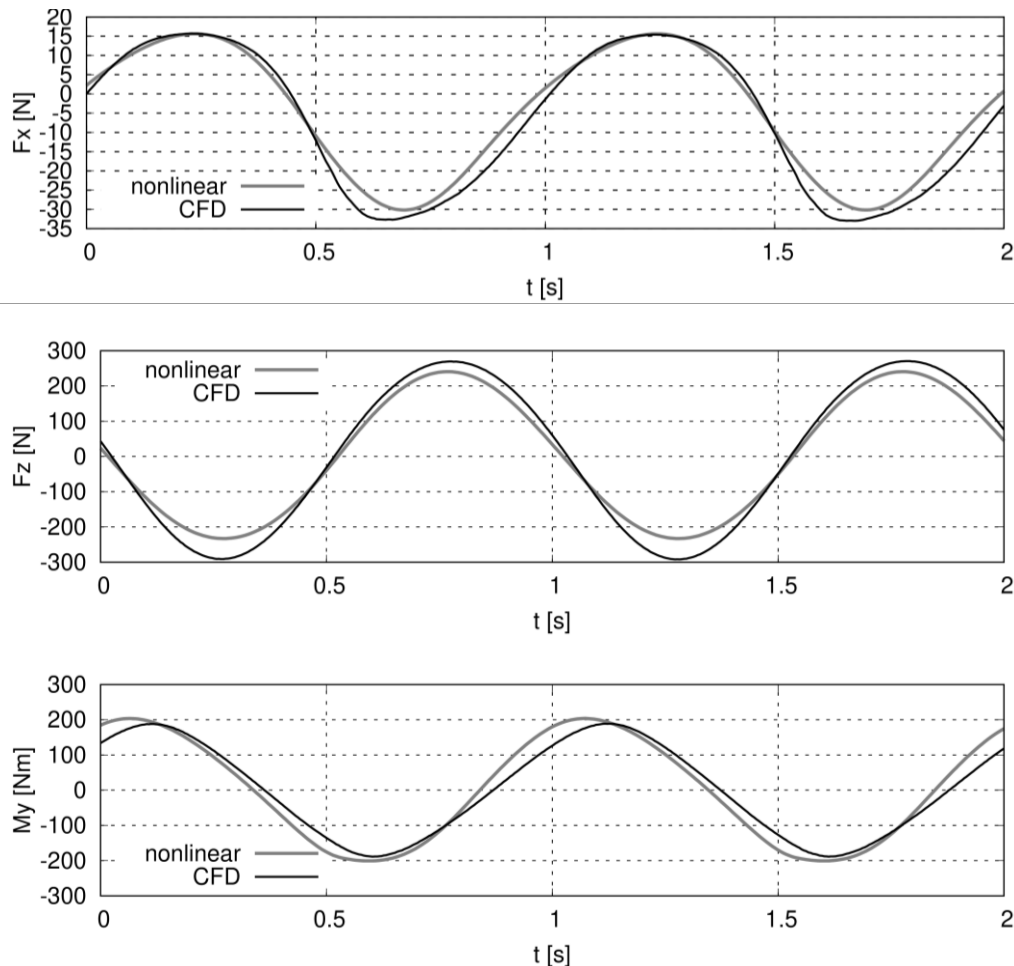


Figure 71: Time histories of the longitudinal force (top), vertical forces (center) and pitch moment (bottom) for the freely floating Containership A ($F_n=0.139$) in head waves of $\lambda/L_{PP} = 0.6$ and a wave steepness $h = 0.0289$. “nonlinear” denotes results of the new numerical method and “CFD” denotes results from the CFD solver.

The comparisons of the wave induced forces and moments of the freely moving ship in three different wave scenarios of a long wave, a wave with medium length and a short wave showed a favourable agreement between the results from the new numerical method and the CFD-Solver. Compared to the results of the fixed container ship, the agreement of the wave induced forces at the moving ship were even better. As aforementioned, when the container ship was fixed, a strongly changing wetted surface at the ship stern caused deviations between both numerical methods. When the ship is free to move, it follows the wave elevation resulting in a less strongly changing wetted surface.

As a result, the waterline force, that covers the effect of the changing wetted surface on the radiation and diffraction force, considered the changing wetted surface more accurately.

Figure 72 to Figure 74 compare the first, second, third and fourth harmonic amplitudes of the longitudinal and vertical wave induced force and the wave induced pitch moment for all waves listed in Table 12 against λ/L_{PP} . The response amplitudes were obtained by applying a Fourier transformation of every time series. The upper left graph plots comparative first harmonic amplitudes; the upper right graph plots second harmonic amplitude; the lower left graph plots third harmonic amplitudes and the lower right graph plots fourth harmonic amplitudes.

Figure 72 plots the response amplitudes of the longitudinal force, Figure 73 the response amplitudes of the vertical force and Figure 74 plots the response amplitudes of the pitch moment. The first harmonic amplitudes of the forces and moment computed with the new numerical method agreed favorable to the CFD results. First harmonic amplitudes of the longitudinal and vertical force as well as the pitch moment were almost identical. Small deviations were only found for the first harmonic amplitudes of the vertical force for waves of $0.6 \leq \lambda/L \leq 1.2$. For the second harmonic amplitude of the longitudinal and vertical force both numerical methods agreed favorably, predicting almost identical maximum response amplitudes at $\lambda/L = 1.0$. Furthermore, also the overall trend agreed well, with some deviations at the longest waves. For the second harmonic amplitudes of the pitch moment, both numerical methods predicted similar moment amplitudes in short and long waves. In waves of medium length according to $0.9 \leq \lambda/L_{PP} \leq 1.4$, the new numerical method computed the maximum response amplitude, however, the CFD solver did not confirm this behavior. Third harmonic amplitudes of the vertical force and pitch moment agreed well. The new numerical solver predicted the maximum response amplitude at $\lambda/L_{PP} \approx 1.0$, which was also confirmed by the CFD solver. However, third harmonic amplitudes of the longitudinal force differed. The CFD solver predicted a large maximum response amplitude at $\lambda/L_{PP} = 1.0$, with a third harmonic amplitude of approximately 10N. The new numerical method predicted the maximum third harmonic amplitude at the same wave length, however, with a maximum amplitude of approximately 2.2N. The same effect could be found for the fourth harmonic amplitude of the longitudinal force. The new numerical method used the transom condition (see chapter 2.4.1), that forces the lower edge of the transom to be a trailing edge and consequently generates a dry transom. For modern container ships at a certain forward speed, the transom is usually dry. However, the current ship speed of $Fn = 0.132$ might not be high enough to keep the transom dry when the ship is moving in waves of

high amplitude (at $\lambda/L = 1.0$ the wave amplitude was 4.71m). As a consequence, the transom was slightly immersed and emerged during the CFD simulations. This effect influences the total response of the longitudinal force only minimally, however, it can have an effect on higher order components of the force and could cause the differences between the new numerical method and the CFD solver for the third and fourth harmonic amplitudes.

The agreement for the fourth harmonic amplitude of the vertical force and the pitch moment was good. Both numerical methods predicted an almost equal maximum fourth harmonic amplitude of the vertical force at $\lambda/L_{PP} = 1.0$ and similar results in longer and shorter waves. Respect the fourth harmonic amplitude of the pitch moment, the new numerical method predicted a similar trend, however, overestimated the amplitudes.

It was shown in the previous validation study of the longitudinal and vertical wave-induced force and the wave-induced pitch moments of the fixed and freely moving containership in head waves that the new numerical method predicted the wave induced forces and moments with a favorable agreement to numerical results obtained with a field method based on solving the Reynolds-averaged Navier–Stokes equations. Often, boundary element method based on potential theory are capable of predicting first harmonic amplitudes of wave-induced forces and moments with a satisfying accuracy for engineering purpose. However, often these methods are not capable to predict higher order effects reliable. The present validation study showed that the new numerical method is able to predict first harmonic amplitudes as well as second, third and fourth harmonic amplitudes of the post-Panamax Containership A at a forward speed in large head waves with a favorable agreement to results of a CFD solver.

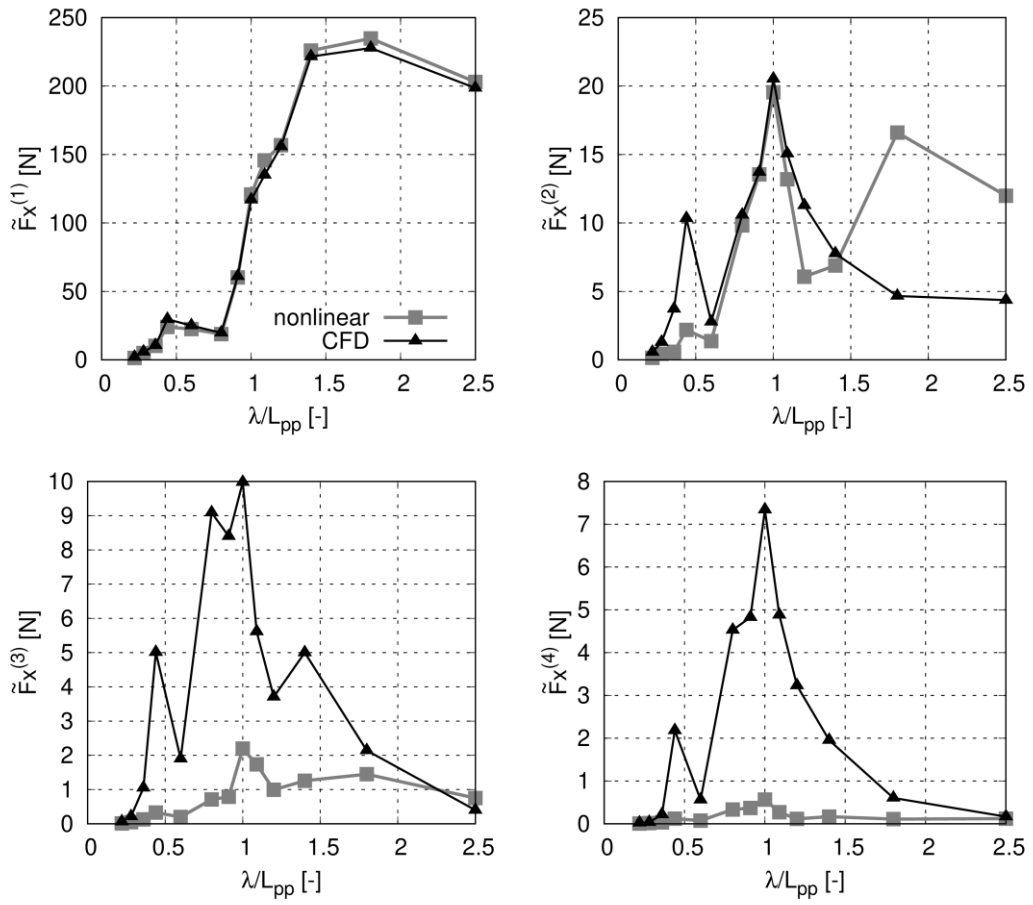


Figure 72: First, second, third and fourth harmonic amplitudes of the longitudinal force of the Containership A in head waves with a forward speed according to $Fn = 0.139$.

4.3 Validation of Wave-Induced Forces

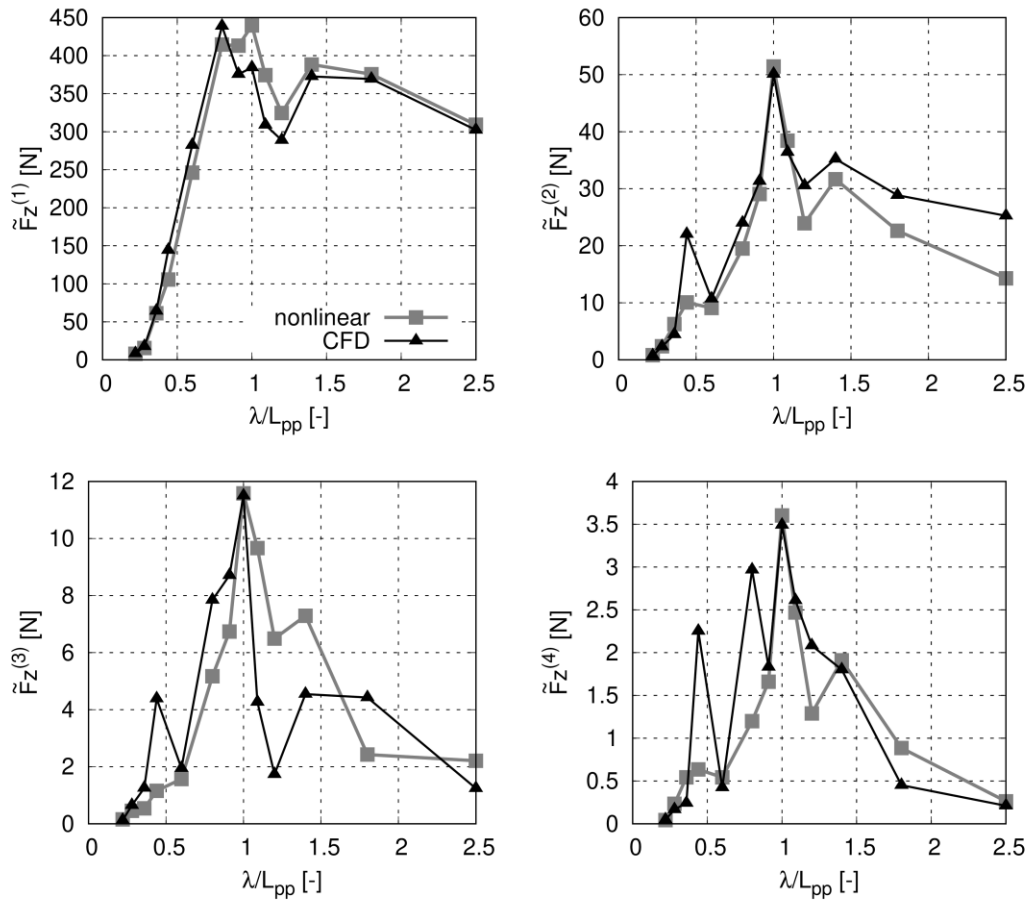


Figure 73: First, second, third and fourth harmonic amplitudes of the vertical force of the Containership A in head waves with a forward speed according to $Fn = 0.139$.

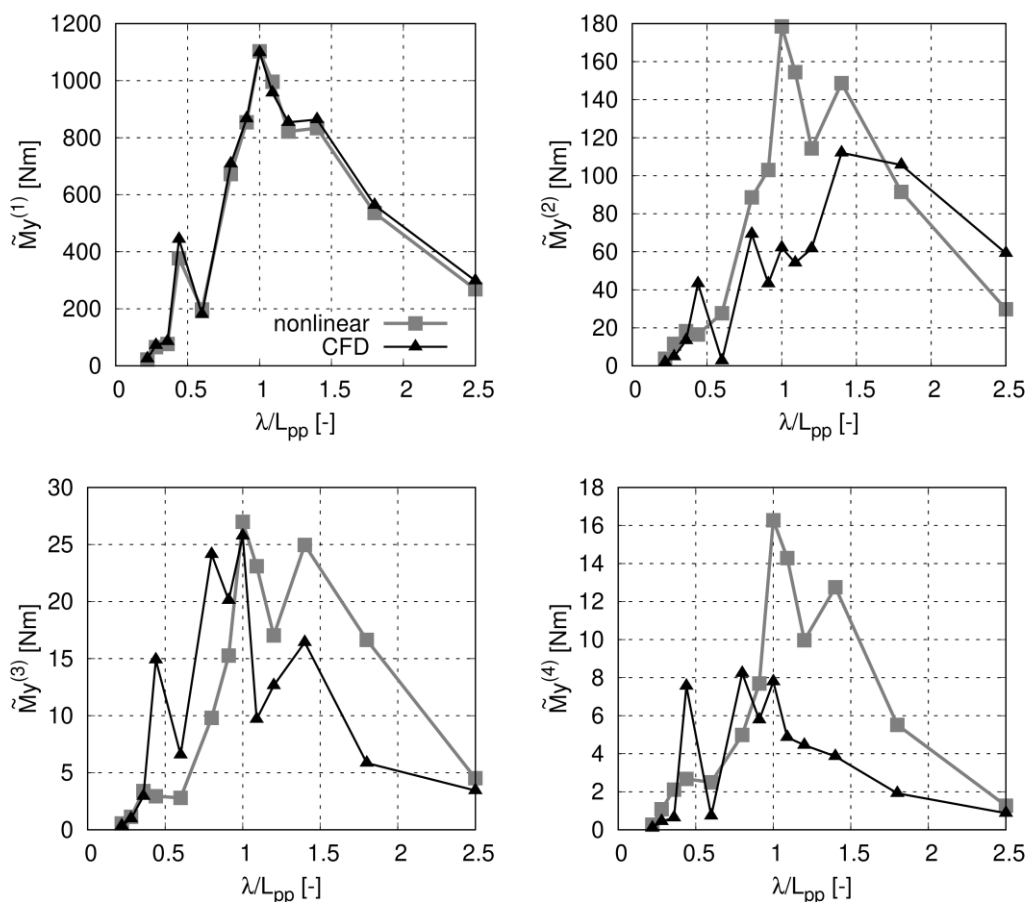


Figure 74: First, second, third and fourth harmonic amplitudes of the pitch moment of the Containership A in head waves with a forward speed according to $Fn = 0.139$.

Figure 75 compares the first harmonic amplitudes of non-dimensional heave (left) and pitch motions (right). The amplitudes were normalized according to equation (212) and (213). Figure 75 plots results of the new numerical method (nonlinear), a RANS based CFD method (CFD), a frequency domain solver (linear frq.) and experimental result (EXP). The frequency domain method applies a unified wave amplitude. The experiments were performed at MARINTEK and the experimental results were available from the international project “SHOPERA”. Furthermore, a description of the model test can be found in el Moctar et al. (2016), Papanikolaou et al. (2016) or Sprenger and Fathi (2015). For the heave motion the agreement between the new numerical method (nonlinear), the CFD solver (CFD) and the experiments was good. Small differences can be seen for $0.5 \leq \lambda/L_{pp} \leq 0.8$. Result from the frequency domain solver agree slightly less favourable. For waves according to $\lambda/L_{pp} \geq 0.8$, the frequency domain method overestimates the heave

amplitudes. The first harmonic amplitudes of the pitch motions from all three numerical methods and the experiments were almost identical.

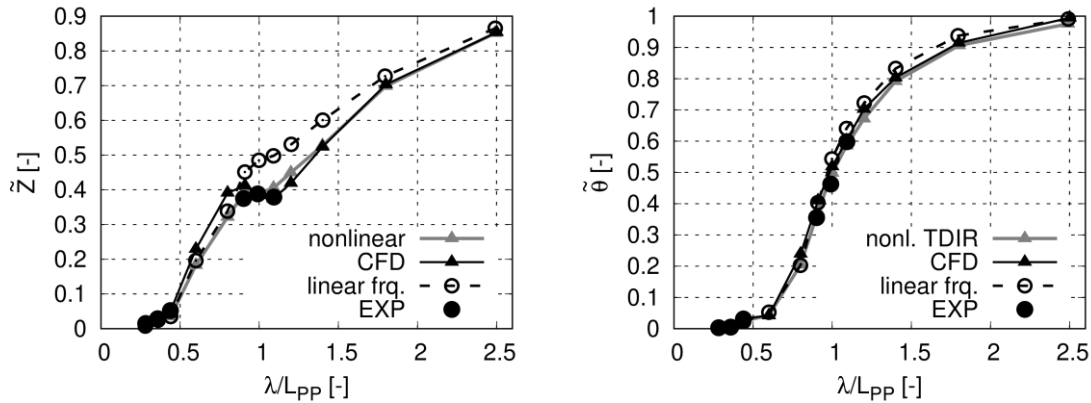


Figure 75: First harmonic amplitudes of the heave motion (left) and the pitch motion (right) for the Containership A at a forward speed of $Fn = 0.139$ in head waves.

According to Journee (2001) and Kashiwagi (1995, 2009), wave bow interactions are important for an accurate calculation of wave induced phenomena that depend on higher order effects such as springing induced vibrations or the wave added resistance. Wave bow interactions depend on the relative motions of a ship’s bow and the free surface resulting mainly from coupled heave and pitch motions and the incident waves. To investigate this relationship, Figure 76 plots phase angles between incident waves and heave (left) and pitch (right) motions, respectively, again against wave length to ship length ratio, λ/L_{PP} , obtained from the new numerical method (nonlinear), from the CFD method (CFD) and from the linear frequency domain method (linear frq.). The incident wave elevation was calculated with respect to the ship’s center of gravity. A positive heave motion was defined as a vertical upward motion and a positive pitch motion was defined to be bow down. A negative phase angle means that the motion follows the wave. Figure 76 shows that in long waves heave was in phase with the incident wave ($\varphi \approx 0$) and that the phase angle increases with decreasing wave length. The phase angle between incident wave and pitch shows that in long waves the phase angle converged towards -90deg and decreases with decreasing wave length. Overall, the results of the new numerical method (nonlinear) agreed favourably with CFD results. Only for the heave phase angle in waves of $0.8 \leq \lambda/L_{PP} \leq 0.9$ small differences are noticeable. The frequency domain method seemed to underestimate the heave and pitch phase angles in short waves.

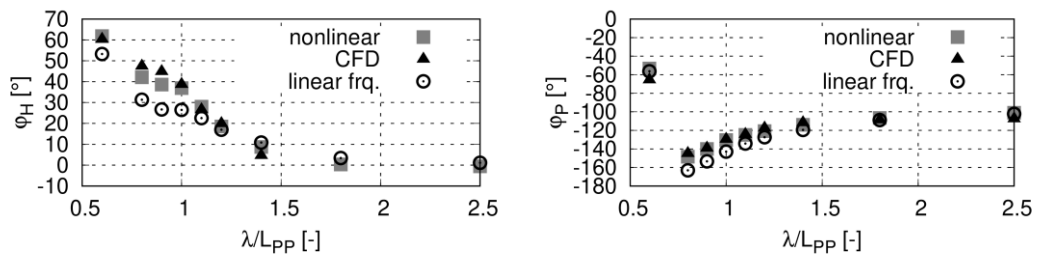


Figure 76: Phase angle between the incident wave and heave (left) and pitch (right) motion of the Containership A at a forward speed of $F_n = 0.139$ in head waves.

4.3.3 Wave Added Resistance of a Fixed and Moving Ship

It was already discussed in the introduction that speed loss in waves needs to be considered when computing springing induced vibrations. Riesner et al. (2018b) investigated the speed loss of the post-Panamax Containership A in irregular waves. They showed that the container ship is able to reach service speed only in relatively small seastats. With increasing significant wave height, the maximum reachable ship speed decreases significant. At a significant wave height of 3m, the ship could reach only 93% of the design speed. At a significant wave height of 4.5m the ship was only able to reach 85% of the design speed. The reduction of the ship speed changes the wave encounter frequencies and thus influences the relation between the wave encounter frequency and the natural frequency of the elastic hull girder. In principle, speed loss in waves is caused by multiple hydrodynamic effects, e.g. wave added resistance, propulsion characteristics in waves, additional aerodynamic resistance due to high wind speed. However, it was shown by Sigmund and el Moctar (2017) that the main contribution to the speed loss of cargo ships in waves is caused by the increase of the total resistance due to the wave added resistance. The longitudinal wave induced force at the fixed and freely moving post-Panamax Containership A was investigated in section 4.3.1 and 4.3.2 and the new numerical method showed a good agreement of computed force amplitudes as well as time average longitudinal forces compared with result of the CFD solver and experimental data. In this chapter the wave added resistance of the post-Panamax containership and the VLCC tanker will be investigated for a wider range of wave frequencies and results of the new numerical method will be validated against results obtained from a CFD solver that is based on the solution of the Reynolds-averaged Navier–Stokes equations and results from model tests. The CFD results for the containership and tanker were taken from Sigmund and el Moctar (2018a). The model test results of the containership were carried out at MARINTEK within the framework of the EU funded project SHOPERA (el Moctar et

al. (2016), Papanikolaou et al. (2015), Sprenger et al. (2017)). The model test results for the VLCC tanker were taken from Sadat-Hosseini et al. (2013). To validate results of the wave added resistance from the new numerical method, quadratic transfer functions of the wave added resistance were computed according to equation (214). The application of the quadratic transfer function of the wave added resistance is based on the assumption that the wave added resistance can be related to the square of the wave amplitude. In principle, this assumption is only valid for small wave amplitudes. Furthermore, a quadratic transfer function of the wave added resistance should be determined based on numerical simulations or experiments that were performed with a constant wave steepness. For the present study the wave steepness varied and was relatively high for some of the investigated scenarios. Nevertheless, the quadratic transfer functions of the wave added resistance is used to compare the results of the present study because it gives an extensive overview of the wave added resistance for a wide range of wave frequencies.

Figure 77 plots comparative quadratic transfer functions of the wave added resistance of the fixed post-Panamax container ship in head waves with wave parameters according to Table 11. “nonlinear” denotes results of the new numerical method, “linear freq.” denotes results of a frequency domain solver and “CFD” denotes results of the CFD solver. To get a better insight into results in short waves, results are plotted against $(L_{PP}/\lambda)^{0.5}$. Additionally, the second x axis plots the corresponding ratio of λ/L_{PP} .

It can be seen that both boundary element methods underestimated the wave added resistance over the total range of investigated waves. Usually, seakeeping methods based on potential theory underestimate the wave added resistance of freely moving ships in short waves, see e.g. Lyu and el Moctar (2017). Ship motions decrease with decreasing wave length and radiation forces became almost zero in very short waves, see also the heave and pitch motions of the container ship plotted in Figure 75. A ship in very short waves is comparable to the scenario of the fixed ship in waves. Sigmund and el Moctar (2018a) showed that viscous effects contribute significantly to the wave added resistance of freely moving ships in short waves. It might be possible that a similar effect causes some of the difference between the boundary element methods and the CFD solver for the fixed containership. Furthermore, it was already discussed in section 4.3.1 and 4.3.2 that the changing wetted surface affects the wave induced forces of the fixed container ship even stronger compared to the freely moving ship. From Figure 77 it can be seen that the changing wetted surface significantly affects the wave added resistance of the fixed container ship. The results of the new numerical method (nonlinear) agree markedly better to the CFD results (CFD) than the results of the linear frequency domain solver

(linear freq.), recalling that the main differences between these two boundary element methods is that the new numerical method considered the changing wetted surface more precisely. However, it can be seen that results of the new numerical method and the CFD solver still differ, especially in long and short waves.

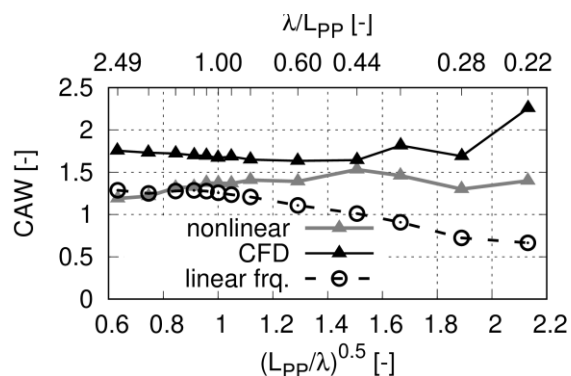


Figure 77: Quadratic transfer function of the wave added resistance for the fixed Containership A at a forward speed of $Fn = 0.139$.

Figure 78 compares the quadratic transfer function of the wave added resistance of the freely moving container ship in regular head waves. The parameters of the investigated waves are listed in Table 12. Figure 78 compares results of the new numerical method (nonlinear) with results obtained with the linear frequency domain method (linear freq.), the CFD solver (CFD) and model test results (EXP) performed at MARINTEK, see e.g. el Moctar et al. (2016). The agreement of the wave added resistance in long waves ($\lambda/L \leq 1.2$) was favourable for all four method. In shorter waves, CFD and EXP agreed well, whereas the new numerical method and the linear frequency domain solver underestimated the result. However, the new numerical method showed major improvements and underestimated the wave added resistance in short waves almost 50% less than the linear frequency domain solver.

4.3 Validation of Wave-Induced Forces

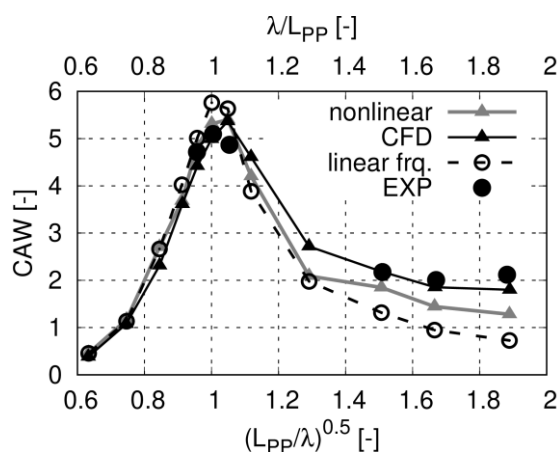


Figure 78: Quadratic transfer function of the wave added resistance for the free Containership A at a forward speed of $Fn = 0.139$

Additional to the investigation of the wave added resistance of the post-Panamax Containership A, the wave added resistance of the VLCC tanker was analysed and a validation study was performed by comparing result from the new numerical method, the a CFD solver, the linear frequency domain method and model test results (when available). In principle, the validation study of the wave added resistance of the VLCC tanker followed the same procedure as for the post-Panamax containership. First, time series of the wave induced longitudinal force at the fixed VLCC tanker computed with the new numerical method and the CFD solver were compared. Second, the quadratic transfer function of the wave added resistance of the fixed tanker computed with the new numerical method was compared to results obtained from the CFD solver and the linear frequency domain method. In principal, the general behavior of the time series of the longitudinal wave induced forces at the fixed tanker did not differ significantly from the corresponding result for the already discussed Containership A. For that reason, the time histories of the wave induced longitudinal forces at the fixed tanker are not presented and discussed. However, these results can be found in the Appendix.

Figure 79 compares the quadratic transfer functions of the wave added resistance of the fixed VLCC tanker in regular head waves with λ/L_{PP} ratios between 0.4 and 2.0 and a wave amplitude of 3.0m. Similar to the results of the Containership A, the wave added resistance of the tanker was underestimated by the new numerical method (nonlinear) and the linear frequency domain method (linear freq.) in long waves. In short waves, results of the new numerical method and the CFD solver were almost identical, whereas the linear frequency domain method underestimated the result.

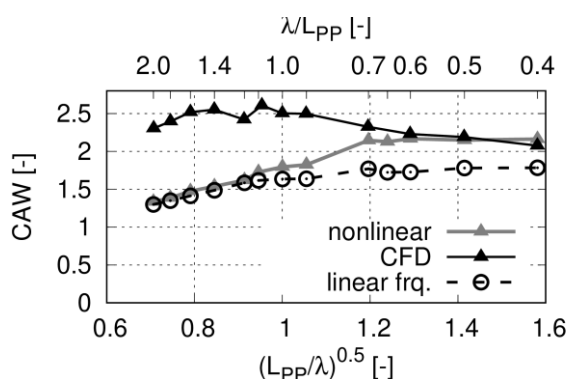


Figure 79: Quadratic transfer function of the wave added resistance for the fixed VLCC tanker at a forward speed of ($F_n = 0.142$).

As aforementioned, when the ship is free to move the relative motion of the ship bow and the incident wave is crucial for an accurate computation of wave induced forces. To investigate this behaviour, Figure 80 plots the normalized first harmonic amplitudes (normalized according equations (212) and (213)) of the heave motion (left) and pitch motion (right) for the freely moving tanker (surge motion was suppressed) in regular head waves for λ/L_{pp} ratios between 0.4 and 2.0 and a wave amplitude of 3m. “nonlinear” denotes the results of the new numerical method, “linear freq.” results of the linear frequency domain solver, “CFD” results of the CFD solver that were taken from Sigmund and el Moctar (2018a) and “EXP” denotes model test results that were taken from Sadat-Hosseini et al. (2013). A constant wave amplitude of 3m resulted in an increasing wave steepness when the wave length decreased. This effected the computed first harmonic motion amplitudes. For waves of $0.9 \leq \lambda/L \leq 1.3$ the new numerical method underestimated the first harmonic heave amplitudes. Due to the relatively high wave amplitude, the deck immersed during the computation of that wave scenarios. This can cause intensive wave breaking. However, breaking waves cannot be considered with the new numerical method. This most likely caused the difference between the new numerical method and the CFD and EXP results of the heave motion. The linear frequency domain method (linear freq.) did not underestimate the heave motion, possibly because it is based on the flow solution with a unified wave amplitude. Consequently, the wave amplitude is significantly smaller. Furthermore, the linear frequency domain solver integrates the wave induced pressure only over the time averaged wetted surface, thus the deck cannot immerse. Results of the pitch motion from the new numerical method (nonlinear) correlated favourable to the model test results (EXP). The linear frequency domain solver and the CFD solver slightly overestimated the pitch motion in long waves.

4.3 Validation of Wave-Induced Forces

Figure 81 plots the phase angles between the incident wave and the tanker's heave motion (left) and pitch motion (right). These phase angles behaved similarly to those for the Containership A in section 4.3.2. Generally, the new numerical method (nonlinear) agreed favorably to results of the CFD solver (CFD) and the model test results (EXP). Some small deviations can be seen for waves $0.9 \leq \lambda/L \leq 1.2$. However, for almost every wave scenario, the new numerical method predicted the phase angles more closely the results of the CFD solver and the model test results than the linear frequency domain solver.

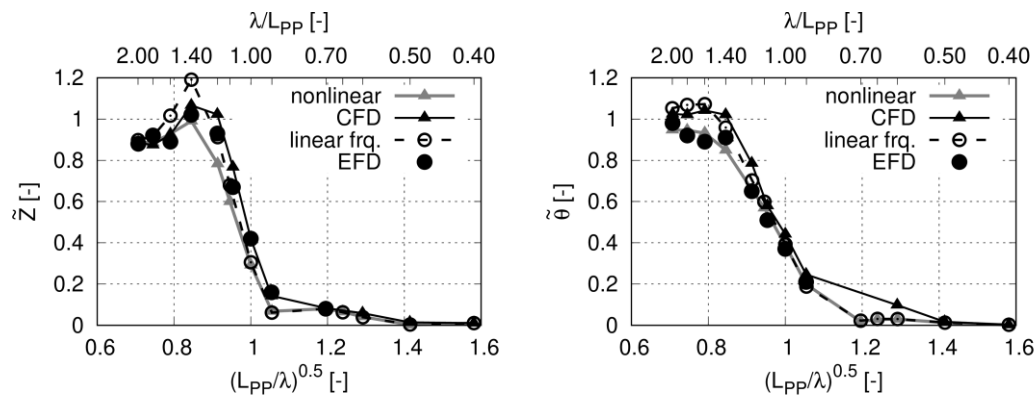


Figure 80: Normalized first harmonic amplitudes of the heave (left) and pitch motion (right) for the VLCC tanker with a forward speed according to $F_n = 0.142$ in head waves.

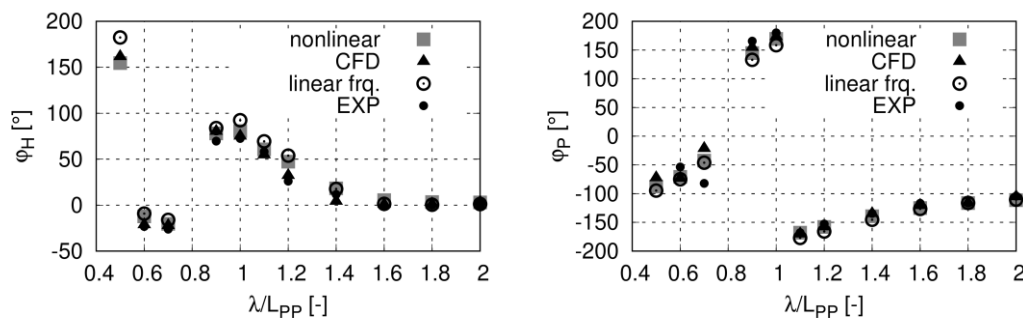


Figure 81: Phase angle between incident wave and heave (left) and pitch (right) motion of the VLCC tanker at a forward speed of $F_n = 0.142$ in head waves.

Also for the VLCC tanker moving freely in heave and pitch, first, time series of the longitudinal wave induced force for a long wave, a wave of medium length and a short wave computed with the new numerical method were compared to results of the CFD solver. However, the principle behavior of that times series did not differ significantly to the results of the previously investigated post-Panamax Containership A. For that reason, the time series of the longitudinal force at the tanker are not included in the present discussion. However, the results can be found in the Appendix.

Figure 82 compares the quadratic transfer function of the wave added resistance computed with the new numerical method (nonlinear), a linear frequency domain method (linear frq.), a CFD solver (CFD) and results from model tests (EXP). It can be seen that results of the new numerical method correlated favourably with results from the CFD solver and model tests. The new numerical method predicted the maximum response at $\lambda/L_{PP} \approx 1.2$ precisely and showed a significant improvement compared to results from the linear frequency domain solver. As aforementioned, relatively high waves forced the ship to move strongly for waves of $0.9 \leq \lambda/L_{PP} \leq 1.4$, causing a strongly changing wetted surface at the bow. First, the linear frequency domain method cannot account for the effect of a strongly changing wetted surface accurately. A further reason of the difference between the linear frequency domain solver and the new numerical method might be the effect of different wave steepnesses on the quadratic transfer function of the wave added resistance. It was shown by e.g. Sigmund and el Moctar (2018a), that the wave steepness can affect the transfer function of the wave added resistance.

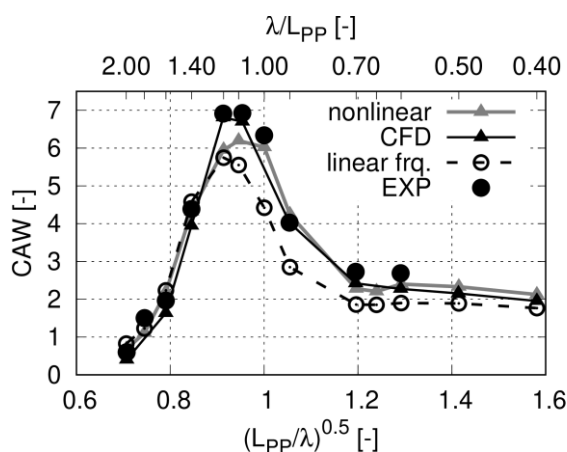


Figure 82: Quadratic transfer function of the wave added resistance for the moving VLCC tanker at a forward speed of $Fn = 0.142$.

4.3.3.1 Estimation of the frictional wave added resistance

Usually, it is assumed that the wave added resistance is caused by pressure variations at the ship hull. However, Sigmund and el Moctar (2018a) showed that also shear forces due to the fluid viscosity play a significant role in short waves of $\lambda/L \leq 0.5$, and that it vanishes in longer waves when the ship is free to heave and pitch.

So far, the new numerical method based on potential theory neglected viscous effects. However, to remedy this defect, a simplified exponential equation that accounted for

4.3 Validation of Wave-Induced Forces

frictional effects on the wave added resistance in head waves was developed. Often, the wave added resistance is expressed as a non-dimensional quadratic transfer function and the associated wave added resistance coefficient, $C_{AW}(\omega_e)$, is expressed according to equation (214). In the following, the total wave added resistance was calculated as the sum of the wave induced pressure added resistance and the friction wave added resistance

$$C_{AW,Tot} = C_{AW} \left(1 + \bar{f}_{fric} \right) \quad (215)$$

$C_{AW,Tot}$ is the normalized total wave added resistance, C_{AW} the normalized pressure induced wave added resistance and \bar{f}_{fric} is the relative friction wave added resistance.

$$\bar{f}_{fric} = \frac{C_{fric}}{C_{AW}}, \quad (216)$$

Where C_{fric} is the normalized friction wave added resistance.

It was assumed that the relationship between the pressure and friction wave added resistance does not depend on the ship speed. The following exponential function was found to adequately represent \bar{f}_{fric} depending on the following parameters: wave length to ship length ratio λ/L and ship's block coefficient c_B :

$$\bar{f}_{fric} = \frac{c_1}{c_B^{c_2}} e^{c_3 c_B \frac{\lambda}{L}} \quad (217)$$

where c_1 , c_2 , and c_3 are assumed to be ship independent constants. c_1 , c_2 , and c_3 were determined based on a regression analysis of CFD data from Sigmund and el Moctar (2018a) based on a least square fit. First, the CFD results of Sigmund and el Moctar (2018a) were applied to compute \bar{f}_{fric} for the containership A and the VLCC tanker. Figure 83 plots the corresponding results, where "VLCC_{CFD}" designates CFD results of the VLCC tanker and "Containership A_{CFD}" results of the Containership A. Applying the regression method on the CFD results identified the coefficients as $c_1 = 0.4$, $c_2 = 1.67$ and $c_3 = -5.8$ which results in the following mathematical expression of the relative friction wave added resistance:

$$\bar{f}_{fric} = \frac{0.4}{c_B^{1.67}} e^{-5.8c_B \frac{\lambda}{L}} \quad (218)$$

For the post-Panamax Containership A and the VLCC tanker, Figure 83 compares the relative friction wave added resistance, \bar{f}_{fric} , obtained from the empirical function (218) with results from the CFD method (taken from Sigmund and el Moctar (2018a)). Index emp designates values from equation (218); index CFD, values from the CFD method. It is seen that the frictional contribution to the total added resistance was higher for the containership than for the tanker. This behavior was well captured by the mathematic formulation.

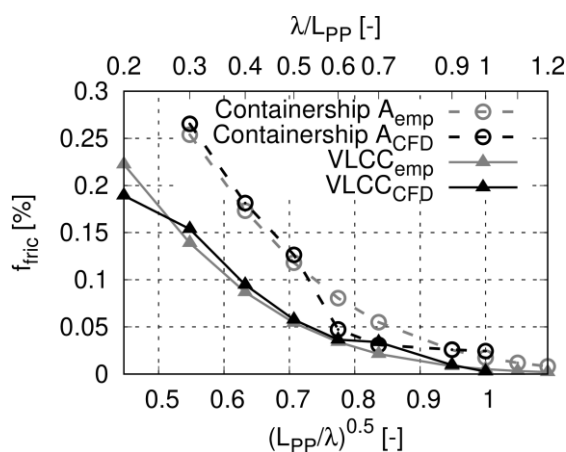


Figure 83: Percentage frictional wave added resistance for the Containership ($F_n = 0.139$) and the VLCC tanker ($F_n = 0.142$)

Figure 84 plot comparative values of the quadratic transfer functions of the wave added resistance, obtained from the new numerical method (nonlinear), from the new numerical method including friction effects (nonlinear + fric), from the CFD method (CFD), from the linear frequency domain method (linear frq.), and from model test measurements (EXP). For the results of the Containership A (left plot of Figure 84) it is seen that the additional friction force component yields a better agreement between the new numerical method and CFD predictions as well as measurement based (EXP) predictions. For the tanker, differences were smaller. Furthermore, in short waves, the new numerical method slightly overestimated the wave added resistance compared to CFD predictions, even without considering the friction force contribution. Nevertheless, including the friction component improved the predictions compared to measurement based (EXP) predictions.

4.4 Validation of Rigid Body Ship Motions in Steep Oblique Waves

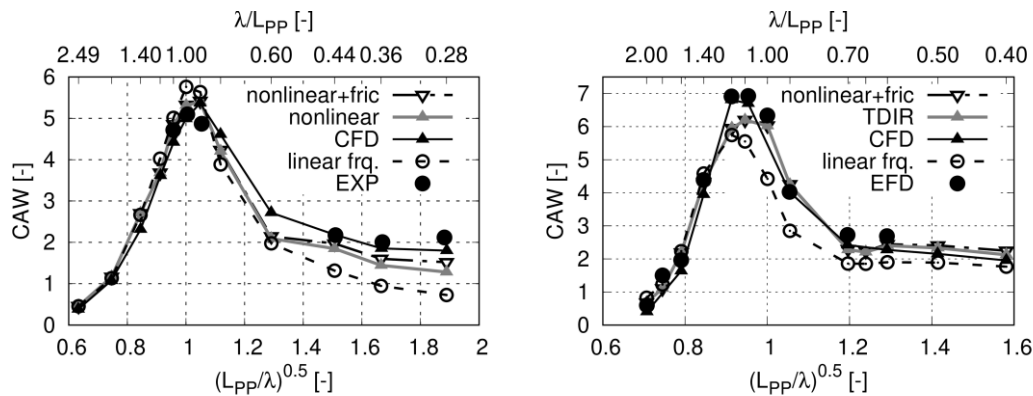


Figure 84: Quadratic transfer function of the wave added resistance including friction effects for the post-Panamax Containership A (left) at $Fn = 0.139$ and the VLCC tanker (right) at $Fn = 0.142$.

The wave length strongly influenced the friction wave added resistance component, especially in shorter waves. Furthermore, ship motions were mitigated in shorter waves. From that perspective, it seemed reasonable to relate the friction wave added resistance also to the relative ship motions (heave and pitch). If wave added resistance were to be calculated for the fixed ship, a significant frictional component should result also in long waves and perhaps explain why the predictions with the new numerical method of the wave added resistance for the freely moving ship in long waves agreed so favorably to the CFD predictions, but differed for the fixed ship. To clarify whether friction wave added resistance is relevant also in long waves when the ship is fixed, additional CFD computations would be necessary.

4.4 Validation of Rigid Body Ship Motions in Steep Oblique Waves

The previous validation study focused on periodic wave-induced forces and the wave added resistance on the fixed and on the moving hull with a good agreement to RANS based CFD computations and experimental results. Furthermore, the new numerical method showed significant improvements compared to a linear frequency domain solver. In a next validation study, results of ship motions of the Containership A advancing with a forward speed according to $Fn = 0.0523$ in steep oblique waves are compared to model test results. The ship is allowed to perform rigid body motions in all six degree of freedom. Furthermore, high wave amplitudes were analyzed to force large ship responses. Of great importance were the rigid body rotation (roll, pitch and yaw) because they exceeded the limit of 5deg strongly, which was defined as the limit for the use of a linear equation of

rigid body motions. Thus, strong kinematic coupling between the body rotations became important and the use of a nonlinear equation of rigid body motions became mandatory.

To minimize the influence of time average drift motions on degrees of freedom that were not subject to restoring forces, i.e., in surge, sway, and yaw, a mooring system based of soft springs positioned the model during the experiment, see Figure 85. The numerical time domain simulations of the new numerical method accounted for similar mooring forces. Linear springs provided restoring forces in surge and sway; a torsional spring, in yaw.

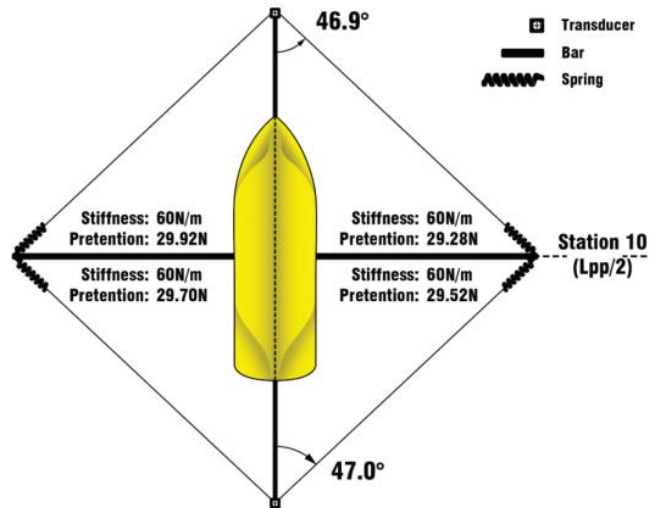


Figure 85: Spring based mooring system used in model tests (el Moctar et al. (2016))

4.4.1 Viscous Roll Damping

Numerical simulations based on potential theory cannot consider viscous effects and consequently could underestimate hydrodynamic damping. Especially for roll motions in oblique waves, viscous damping effects may influence the roll amplitudes. Therefore, viscous roll damping effects were considered according to a linear roll damping approach, see. Equation (38). The associated damping coefficient ζ_d was computed from model test results. Roll damping characteristics of the subject Containership A were investigated experimentally during the international project “SHOPERA”, Sprenger and Fathi (2015). An evaluation of the model test results pointed out that the relation, ζ_d , of the effective

4.4 Validation of Rigid Body Ship Motions in Steep Oblique Waves

damping coefficient and the critical damping coefficient, is almost constant with respect to the roll amplitude. For that reason, a linear viscous damping regression function was a good representation. Similar was found out by Liu and Papanikolaou (2014). Table 13 shows measured critical roll damping coefficients for roll amplitudes of 4.81, 3.54, 1.5 and 0.2 degrees. $\zeta_d = 0.020$ represented the average of all measured damping coefficients and, thus, was chosen for the simulations with the new numerical method.

Table 13: Critical roll damping coefficient against roll amplitude of the Containership A at zero speed.

Roll amplitude	ζ_d
4.81°	0.0212
3.54°	0.0204
1.50°	0.0192
0.20°	0.0195

Figure 86 compares time histories of the roll decay test obtained from experimental data (EXP) and with the new numerical method (nonlinear). The initial roll amplitude for these tests was 5.0 degree. Although measured and computed roll amplitudes differed only slightly. It is seen that measured amplitudes are marginally smaller at the beginning and at the end of the test and marginally bigger at mid time. This indicates that damping during the model test changed slightly due to changing roll amplitude and angular velocity. However, overall the linear viscous damping approach agree well and caused only minimal differences between measurements and numerical results (maximum differences between EXP and TDIR are less than 5%).

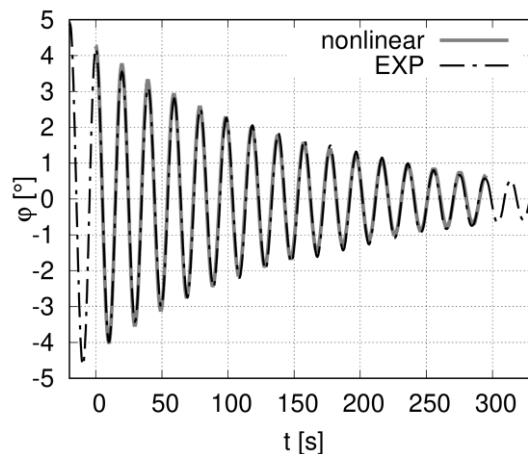


Figure 86: Roll decay tests from model test (Sprenger and Fathi (2015)) and nonlinear numerical simulation.

4.4.2 Rigid Body Motions

Direct comparisons of ship motions between time domain calculations with the new numerical method and experimental results were performed. The time domain simulations followed the experimental conditions. In order to validate the weakly-nonlinear numerical method, wave conditions that caused complex ship motions were chosen (i.e. large ship motions considering coupling between different degrees of freedom). In principle, large ship motions occur when the wave length is close to the ship length. For that reason, the following case listed in Table 14 was selected from the experiments

Table 14: Wave conditions.

λ/L_{pp}	$\zeta^1[m]$	$h[-]$	$Fn[-]$	$\mu[^\circ]$
1.09	4.01	0.023	0.052	30

Figure 87 plots the corresponding time histories. The left side plots longitudinal, transvers and vertical translations (from top to bottom) and the right side plots the roll, pitch and yaw motion. From the model test results the surge motion showed a large amplitude (more than 40m in full scale) oscillation with a period of 60s which is far away from the wave encounter period. This dominant low frequency surge oscillation was most likely influenced by the characteristic of the spring system's restoring force that positioned the model to the carriage. However, if the harmonic amplitude response due to the specific wave encounter frequency is captured using a Fourier transformation, a first harmonic surge amplitude of 2.04m from the model test was obtained. A harmonic oscillation based on the obtained surge amplitude and wave encounter frequency was included in Figure 87 to represent model tests results for the surge motion. As it can be seen from the comparisons the surge motion amplitude from the model test (2.04m) and the numerical simulation (1.93m) matched well. As seen in Figure 87, the other motion components agree favorably to measurements. Although sway and roll amplitudes from model tests showed interferences and vary between 1.29 and 2.05 degrees, their average values compare favourably to numerical results. A similar behavior can be seen for sway and yaw. The best agreement is seen to have occurred for heave and pitch.

4.4 Validation of Rigid Body Ship Motions in Steep Oblique Waves

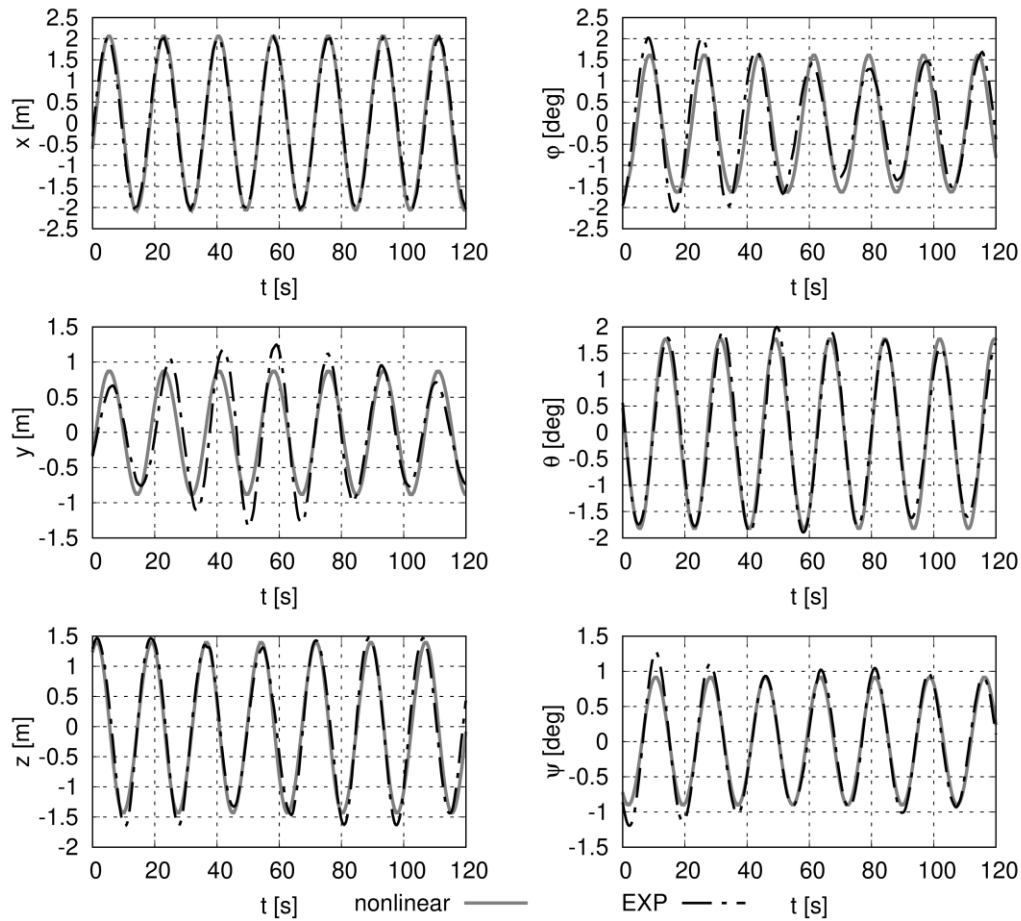


Figure 87: Time histories of computed and measured rigid body motions of the Containership A at $F_n = 0.0523$ in 4.02m amplitude waves of $\lambda/L_{pp} = 1.09$ (wave steepness $h = 0.023$) at wave encounter angle of 30deg.

In the previous comparison the numerical method showed a good agreement for almost all degrees of freedom. The comparisons of time histories are a good procedure to validate numerical results to model test. However, it allows only the comparisons of a limited number of wave conditions. To compare the numerical result and model test result in a wider range of wave conditions and wave encounter angles, comparative normalized first harmonic amplitudes of the ship motions comprised results obtained from time domain simulations with the new numerical method (denoted “nonlinear”), the linear frequency domain boundary element method (denoted “linear frq.”) and model tests (denoted “EXP”) on waves with wave encounter angles of 30 and 60 degrees for the ship at a forward speed corresponding to $F_n = 0.0523$. The model tests were conducted in waves of different steepness. Computations with the linear frequency domain method considered roll damping with a damping factor of 2% of the critical damping (the same as for the nonlinear time domain simulations). Table 15 lists the wave frequencies ω , the

wave length to ship length ratios λ/L_{pp} and the wave steepnesses h investigated during the model tests.

Table 15: Wave particulars investigated during model tests.

ω [rad/s]	λ/L [-]	h [-]
0.400	1.095	0.0289
0.419	0.984	0.0369
0.628	0.440	0.0760
0.785	0.281	0.0707
0.898	0.216	0.0602

Figure 88 plots normalized surge (\tilde{x}), sway (\tilde{y}), heave (\tilde{z}), roll ($\tilde{\varphi}$), pitch ($\tilde{\theta}$), and yaw ($\tilde{\psi}$) amplitudes against wave length to ship length ratio, λ/L_{pp} , at the wave encounter angle of 60 degrees. The heave and pitch motion were normalized according to equation (212) and (213). The surge and sway motion were normalized as

$$\tilde{x} = \frac{x}{\zeta^1} \quad (219)$$

$$\tilde{y} = \frac{y}{\zeta^1} \quad (220)$$

And the roll and yaw motions were normalized as

$$\tilde{\varphi} = \frac{\varphi}{k \zeta^1} \quad (221)$$

$$\tilde{\psi} = \frac{\psi}{k \zeta^1} \quad (222)$$

Generally, all computed motion amplitudes (nonlinear and linear frq.) compare favorably to model test measurements (EFD). Deviations occurred in shorter waves for sway and heave motions, where model tests were conducted in very steep waves. The nonlinear behaviour of steep waves (non-sinusoidal) as well as wave breaking at the ship hull may play an increasing role. However, such nonlinearities were not considered in the new numerical method.

4.4 Validation of Rigid Body Ship Motions in Steep Oblique Waves

In long waves, the linear frequency domain method (linear frq.) overestimated the roll and underestimated the yaw motions. In both cases the new numerical method (nonlinear) was closer to model test results.

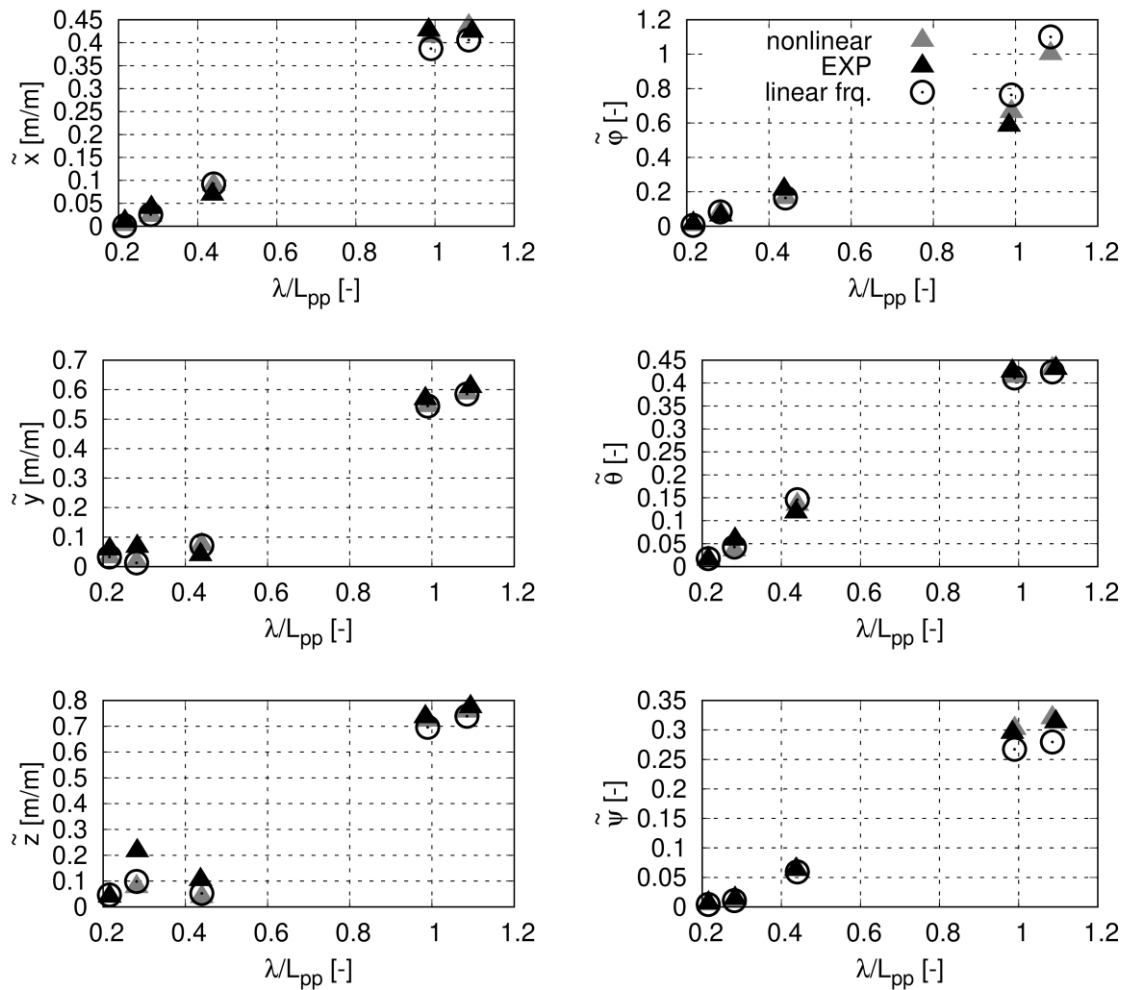


Figure 88: Comparisons of normalized first harmonic motions amplitudes computed with the new numerical method (nonlinear), a linear frequency domain method (linear frq.) and model test results (EXP) for the Containership A at $Fn = 0.0523$ and wave heading of 60deg.

Figure 89 plots similarly normalized first harmonic amplitudes of the ship motions at a wave encounter angle of 30 degrees. It can be seen that, in general, the agreement between computed amplitudes of the new numerical method (nonlinear), the linear frequency domain method (linear frq.) and model test measurements (EXP) is good, with almost identical results for sway and pitch motions. Surge and heave amplitudes differ sometimes, especially in short waves (high wave steepness) and yaw amplitudes differ by

small amounts in long waves. Roll motions agree well for shorter waves, with increasing deviations in longer waves. Comparing results from the linear frequency domain method with the experiment deviations occurred especially for roll and yaw motions in long waves. In both cases better results were conducted using the new numerical method.

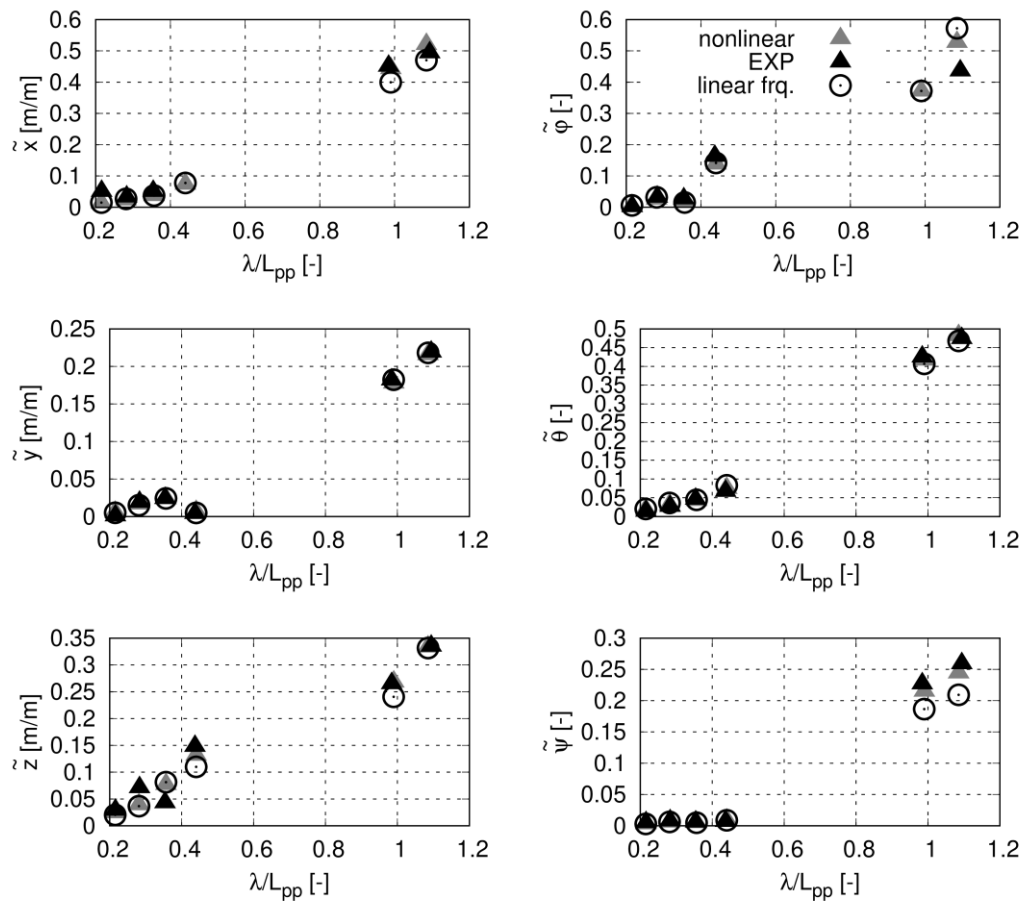


Figure 89: Comparisons of normalized first harmonic motions amplitudes computed with the new numerical method (nonlinear), a linear frequency domain method (linear freq.) and model test results (EXP) for the Containership A at $Fn = 0.0523$ and wave heading of 30deg.

4.5 Validation of the Hydroelastic Reponse in Waves

Content of this section was already published in Riesner and el Moctar (2021a, 2021b).

As described in chapter 2, the hydroelastic response in waves was obtained by superposing the rigid body response with the elastic body response. The weakly-nonlinear boundary element method obtained the hydrodynamic pressure at the moving and elastic vibrating hull. The nonlinear rigid body motion equations, see equation (70) were solved to compute the rigid body motions and the linear elastic deformation equations (see equation (135)) were solved to obtain the elastic deformation of the ship hull. Within the previous validation studies, it was shown that the new numerical method computed wave induced forces and moments at the fixed and moving ship with a favorable agreement to a CFD solver and that the nonlinear rigid body motions solver accurately predicts rigid body motions in head waves and steep oblique waves. In this section, the numerical method to compute elastic vibrations of the floating hull in waves is validated. All computations were performed for the post-Panamax Containership B, see section 3.4.

4.5.1 Grid Study for the Finite Beam Element Method

Wet natural modes were computed by solving the eigen vectors of the characteristic system equation of the undamped wetted hull according to equation (134). The first six natural modes describe low frequency oscillations. These oscillations are usually called rigid body motions, although they can include slightly bending. As discussed in chapter 2, these rigid body motions were computed with the nonlinear rigid body motions solver. The response in all other modes were solved by the linear elastic body motion solver.

For the post-Panamax containership B, Table 16 describes the elastic natural modes from mode 7 to mode 12 obtained by solving the eigenvectors of equation (134).

Table 16: Elastic natural modes of the subjected containership B

Mode	Description
7	One-node torsion-horizontal-bending
8	Two-node torsion-horizontal-bending
9	Two-node vertical bending
10	Three-node torsion-horizontal-bending
11	Four-node torsion-horizontal-bending
12	Three-node vertical bending

Figure 90 plots nodal displacements for the wet natural modes 7 to 12 of the containership B with full scale structural properties advancing at a constant 15kn forward speed ($Fn = 0.135$). The upper left plot shows two-node vertical bending (mode 9), the upper right plot shows three-node vertical bending (mode 12). “z” designates the vertical

translation of a point at the hull and rot-y stands for the rotation of a cross section around the y-axis. For clarity, rotations were multiplied with 20.0. The lower left plot Figure 90 shows coupled one-node torsion-horizontal-bending (mode 7) the lower center plot shows coupled two-node torsion-horizontal-bending (mode 8) and the lower right plots shows coupled three-node torsion-horizontal-bending (mode 10). Solid dots denote displacements related to torsion; open circles denote displacements related to horizontal bending. Translation “y” represents the horizontal translation, and rotation “rot-z” stands for the rotation about the vertical z-axis. Rotation “ χ ” designates the twist angle about the longitudinal x-axis (torsion), and “ ϑ ” indicates the variation of the twist angle. The nodal displacements in Figure 90 were normalized, such that the modal mass matrix became unity, i.e., $\bar{\mathbf{M}}_{jj} = \vec{\underline{u}}_j^T (\mathbf{M} + \mathbf{m}(\infty)) \vec{\underline{u}}_j = 1.0$. However, for clarity, “ ϑ ” was multiplied by 50.0. The upper left and right plot indicate the principle behavior of a bending beam. The largest vertical translations occur at the stern and the bow of the ship. The two-node vertical bending mode induces the maximum vertical bending moment near amidships ($x \approx 167\text{m}$) and the three-node vertical bending mode induces the maximum vertical bending moment approximately at 1/4 and 3/4 of the ship length. The lower left plot (mode 7) indicates that the rotation “rot-z” is almost constant for the one-node torsion-horizontal bending mode, which indicated that this mode contributed only slightly towards horizontal bending and mostly towards torsion. The lower center graph shows that the coupled two-node torsion-horizontal-bending contributed towards the torsional moment and the horizontal bending moment. However, as the variation of the twist angle is almost zero at amidships ($x \approx 167\text{m}$), the torsional moment amidships turned out to be small. The lower right plot shows the coupled three node-torsion and three-node horizontal bending modes. The introduced horizontal bending moment amidships is small, however, the introduced torsional moment is relatively large.

4.5 Validation of the Hydroelastic Reponse in Waves

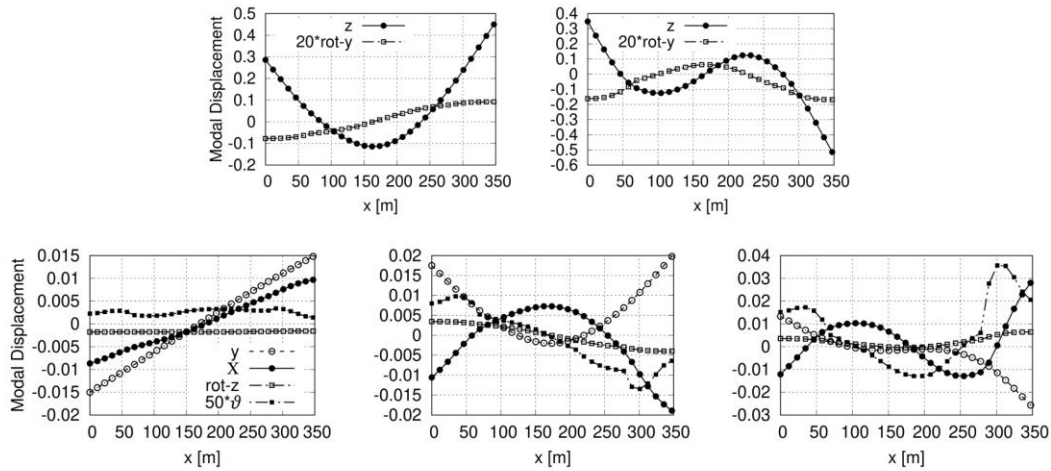


Figure 90: Natural modes of two-node vertical bending (top left), three-node vertical bending (top right), coupled one-node torsion-horizontal-bending (lower left), two-node torsion-horizontal-bending (lower center), and three-node torsion-horizontal-bending (lower right).

The left plot of Figure 91 shows the corresponding impulse response functions of the two-node vertical bending mode (VB2), three-node vertical bending mode (VB3) and four-node vertical bending mode (VB4) and the right plot shows the impulse response functions of the coupled one-node (TB1), two-node (TB2) and three-node (TB3) torsional-horizontal-bending mode. All impulse response functions characterize the general behaviour of a causal, damped system. At negative times, the impulse functions are zero; and for past impulses generated a long time ago, they converge to zero.

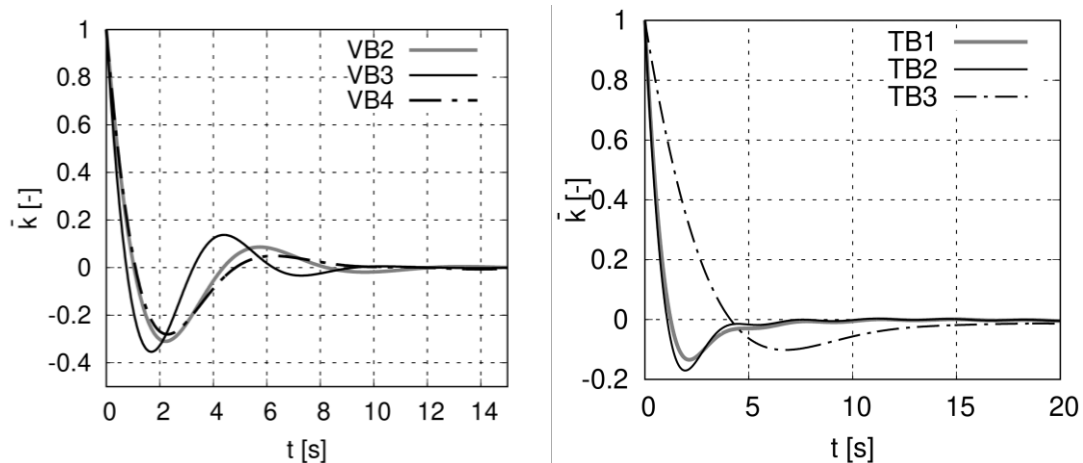


Figure 91: Normalized impulse response function for two-node, three-node and four-node vertical bending (left) and one-, two- and three-node coupled torsional-horizontal-bending modes (right).

To verify the numerical error during hydroelastic simulations and to assess the error associated with the number of beam elements, a discretisation study was performed. The following two important effects were investigated:

- the influence of the number of beam elements on the structural behaviour of the hull
- the influence of the number of beam elements on wave-induced forces

The element shape functions that were used to describe the deformation of one beam element (see equations (98), (99), (104) and (116)) are approximations for the deformation of a hull segment with constant cross section properties. To approximate the structural behaviour of the total ship with varying cross section properties, the hull is discretised by a certain number of beam element. Thus, the number of applied beam elements influences the structural behaviour of the ship during the hydroelasticity simulation. As aforementioned in section 2.3 (see Figure 7), a longitudinal, vertical and horizontal forces per unit length and a torsional moment per unit length were applied on each beam element. These loads per unit length represent the wave and motion-induced hydrodynamic loads and resulted from the procedure of mapping the hydrodynamic pressure computed at the hull surface on the finite beam element, see equation (122). The load per unit length was simplified by applying a constant load over each element. As a consequence, the number of beam elements also affects the change of fluid induced loads along the hull. To verify the effect of the number of beam elements on the structural behaviour of the ship structure and on fluid induced loads for the hydroelastic solver, a two-step discretisation study was performed. It was assumed that fluid induced loads are more strongly influenced by the number of beam elements than the structural behaviour of the ship. Consequently, an accurate representation of the fluid induced loads requires more beam elements than an accurate representation of the structural behaviour. For that reason, the minimum number of beam elements that are necessary to describe the structural behaviour of the ship was evaluated in the first step of the discretisation study. In the second step, the minimum number of beam elements to represent fluid induced forces accurately were evaluated.

The effect of the number of beam elements on the structural behaviour was evaluated by investigating the change of dry natural frequencies due to an increasing number of beam elements. For the grid study the realistic full-scale structural and mass properties given in section 3.4.2 were used.

4.5 Validation of the Hydroelastic Reponse in Waves

To verify the effect of varying the number of beam elements on the dry natural frequencies, each of the six ship hull segments were discretized with one, two and three beam elements, thereby idealizing the complete hull with a total of six, twelve and eighteen elements, respectively. Table 17 compares the dry natural frequencies obtained from this three different discretization. The variable Δ stands for the percentage change after refining the discretization. The natural frequencies are given in rad/s because later, the natural frequencies were related to the wave encounter frequency which is typically given in rad/s . Increasing the number of elements from six to twelve reduced the dry natural frequency of mode 10, i.e., the coupled three-node torsion-horizontal-bending mode by 1.892%. Increasing the number of elements to 18 changed the natural frequencies only minimally (0.1744%) and it was concluded that 18 elements were sufficed to discretizes the hull structure. Table 17 includes also comparative dry natural frequencies obtained from 3D finite element computations (3D FEM) of Bureau Veritas (results can be found in Maron and Kapsenberg (2014)). As seen, the agreement of the numerical beam element results with the 3D finite element computations were favourable. An exception was the natural frequency of mode 12, the three-node vertical bending mode. Here, the prediction of the new numerical method exceeded the comparative frequency obtained with the 3D finite element solver.

Table 17: Comparative dry natural frequencies of the Containership B.

Mode	3D FEM	6 Elements	12 Elements		18 Elements	
	ω [rad/s]	ω [rad/s]	ω [rad/s]	Δ [%]	ω [rad/s]	Δ [%]
7	2.32	2.2261	2.2324	0.281	2.2337	0.0802
8	3.52	3.7021	3.6581	-1.182	3.6518	-0.1744
9	4.21	4.1833	4.1821	-0.027	4.1846	0.056
10	6.22	6.5345	6.4107	-1.892	6.3931	-0.277
11	8.55	9.1182	9.2017	0.916	9.1766	-0.27
12	8.67	9.8998	9.8803	-0.194	9.8841	0.0369

To verify the effect of the number of beam elements on hydrodynamic loads, wet natural frequencies computed with an increasing number of elements were compared in the second step of the discretisation study. The number of beam elements were further increased; specifically, three, four and five elements per hull segment were applied, resulting in a total number of 18, 24 and 30 beam elements for the entire hull. The only difference between the computation of dry and wet natural frequencies is that in case of wet natural frequencies hydrodynamic loads act on the hull surface. Recall that 18 elements sufficed to discretizes the structure and to compute natural frequencies of the dry hull. Consequently, during the discretisation study of wet natural frequencies with 18,

24 and 30 beam elements, the differences between the natural frequencies were mainly due to hydrodynamic effects.

To compute wet natural frequencies, numerical decay tests in time domain were performed. This necessitated performing pre-computations for every discretization. Thus, the hull was discretised with 18, 24 and 30 beam elements to obtain, first, the corresponding transfer functions of hydrodynamic damping as a function of encounter frequency and then the impulse response function for each mode. According to equation (71), the displacement vector for every degree of freedom, $\vec{u}(t)$, was determined by multiplying the mode shape, \vec{u}_j , with the response factor, v_j . Setting $v_j(0) = 0.001$ for every natural mode initiated the decaying oscillation.

Table 18 lists comparative computed wet natural frequencies, ω , for zero forward speed. Table 18 includes also the percentage change, Δ , of the natural frequency relative to the natural frequency determined from the previous refinement. As seen, increasing the number of beam elements that idealized the hull from 18 to 24 elements affected the wet natural frequencies only marginally. The maximum change of 0.1763% was found for the three-node vertical bending vibration (mode 10). The further refinement of 30 elements hardly changed the wet natural frequencies. With a relative change of 0.0841%, the maximum difference was found for the three-node vertical bending vibration. Based on these results, it can be concluded that idealizing the hull with 30 beam elements sufficed to accurately compute the structural and hydrodynamic behavior of this ship. Figure 92 plots exemplary the time history of the normalized decaying vibration of the one-node torsion-horizontal-bending mode (Mode 7) and two-node torsion-horizontal-bending mode (Mode 8).

Table 18: Comparative wet natural frequencies of the Containership B with real full-scale properties.

Mode	18 Elements	24 Elements		30 Elements	
	ω [rad/s]	ω [rad/s]	Δ [%]	ω [rad/s]	Δ [%]
7	2.156	2.153	0.1283	2.151	0.0809
8	3.490	3.478	0.061	3.476	0.0387
9	3.355	3.357	-0.0283	3.357	-0.0144
10	6.156	6.146	0.1764	6.140	0.0841
11	8.935	8.916	0.1564	8.916	0.0568
12	7.835	7.838	0.0312	7.838	0.0

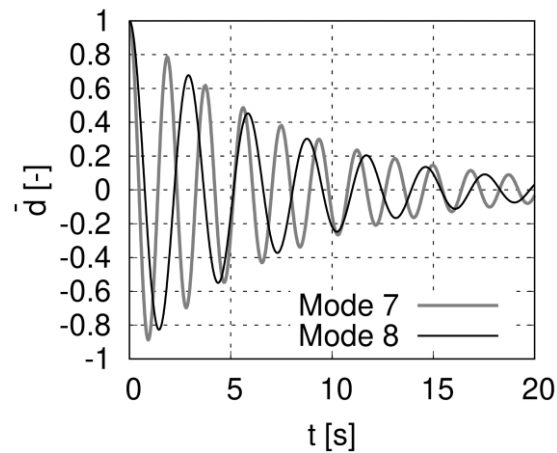


Figure 92: Normalized decaying vibration of the one-node torsion-horizontal-bending mode (Mode 7) and two-node torsion-horizontal-bending mode (Mode 8).

4.5.2 Validation of Wave Induced Sectional Loads

Recall that the new numerical method coupled torsional and bending phenomena. To validate this new method, numerically computed sectional loads were compared with appropriate model test measurements; that is, the experimental test setup had to account for such a coupling effect. Several experimental studies regarding torsional moments of ships in waves have been performed, and often a backbone modelled the structural stiffness of the ship's hull. Generally, a backbone model is suitable to investigate vertical bending vibrations of a ship with port-starboard symmetry. However, its capability to model torsional and horizontal bending properties is limited. Recall that the shear center of a large containership may be located far below the keel; as seen in section 3.4.2, it is located more than 12m under the keel for the analysed Containership B. Consequently, horizontal bending and torsion were strongly coupled. Simple backbone cross sections, such as H-profiles or rectangular profiles, cannot be used to model such phenomena, because their shear center coincides with the neutral bending axis and, therefore, coupling effects then not exist. In some cases, U-profiles have been used to shift the shear center downwards. Although such backbone models do account for some coupling effects between torsion and bending, in general, the cross section of the backbone is too small compared with the cross section of a real ship. Furthermore, the backbone is usually mounted inside the hull and often not at keel height. Consequently, the shear center of such test setups is higher than it should be. Indeed, it is often located near the keel line and in some cases even above the keel line. Therefore, a backbone model setup usually does not model properties of the full-scale ship correctly. Even such model test results do

not represent the structural behaviour of ships realistically, they can still be used to validate the new numerical method. After the validation study, numerical computations of springing induced sectional loads for the same container ship with realistic full-scale hull structural properties were performed.

For the validation study, numerical predictions with the new numerical method were compared with experimental measurements for the post-Panamax Containership B introduced in section 3.4.

Experimental results of the subject containership were available from the EU-funded project ExtremeSeas. The model tests were performed at the Canal de Experiencias Hidrodinámicas de El Pardo (CEHIPAR) (Maron and Kapsenbeerg (2014)). For the validation, midship torsional moment and the vertical and horizontal midship bending moment for the ship advancing at constant forward speed. Table 19 lists numerically computed natural frequencies and comparative values from model tests performed at CEHIPAR (Maron and Kapsenbeerg (2014)). Recall that for the validation study, the model was equipped with a backbone. The dry natural frequencies compared favourably; however, some deviations occurred. Dry natural frequencies of mode 7 (one-node torsion-horizontal-bending) differed only by about 3%, whereas dry natural frequency of mode 8 (two-node torsion-horizontal-bending) differed by about 12%. Due to the open cross section of the U-beam, warping effects of the cross section become important. During model tests, links connected the backbone to the hull. This connection could have influenced the stiffness and the warping characteristic of the beam. Furthermore, the backbone extended from about 44m ahead of the ship's aft perpendicular to about 5m aft of its forward perpendicular. Although the beam's stiffness and the mounting mechanism at its ends were important for the vibration behaviour, it was impossible to consider such effects in the numerical beam element model. These effects were most likely responsible for the deviations of the dry natural frequencies. Maron and Kapsenbeerg (2014) did not provide wet natural frequencies. However, time series of performed vertical bending hammering tests for zero forward speed were available from the research project ExtremeSeas. A more detailed investigation of the hammering tests is given in section 4.5.2.1.

Comparing numerically computed wet natural frequencies with experimental results show a good agreement. Furthermore, it can be seen that the wet natural frequencies of the two-node and three-node vertical bending mode are considerably lower as the dry natural frequencies. This effect results from the hydrodynamic pressure acting on the vibrating hull (radiation pressure). As discussed in section 2.2.2.1 , the radiation forces can

4.5 Validation of the Hydroelastic Reponse in Waves

be split into components resulting from a hydrodynamic added mass, hydrodynamic damping and restoring. Hydrodynamic damping does not strongly affect the natural frequencies, however, the hydrodynamic added mass and restoring does. Hydrostatic restoring is often smaller than structural restoring (structural stiffness), the hydrodynamic added mass is often of similar magnitude than the structural mass. The hydrodynamic added mass of torsion is usually smaller than the structural inertial moment but the hydrodynamic added mass of vertical bending vibrations is often larger than the structural inertial terms. As a result, the wet natural frequencies of vertical bending modes are considerably lower than the corresponding dry natural frequency but the wet natural frequencies of torsional modes are only slightly lower than the corresponding dry natural frequencies. For coupled torsional-horizontal bending modes it can be concluded that the wet natural frequencies of modes that are dominated by torsion are only slightly smaller than the corresponding dry natural frequencies. For modes that are dominated by horizontal bending, slightly higher differences between wet and dry natural frequencies are expected. The results of the new numerical method (Table 19) showed this behaviour. The wet natural frequency of mode 7 (coupled one-node torsion-horizontal-bending) is only slightly lower than the dry natural frequency (this mode is dominated by torsion). Mode 8 (coupled two-node torsion-horizontal-bending) has slightly more horizontal bending, which can also be seen from a slightly stronger reduced wet natural frequency.

Table 19: Comparative dry and wet natural frequencies of the Containership B with backbone structural properties.

Mode	Experiment (DRY)	Hammering Test (WET)	Simulation (DRY)	Simulation (WET)
	ω [rad/s]	ω [rad/s]	ω [rad/s]	ω [rad/s]
7	1.885	-	1.942	1.848
8	3.58	-	3.158	3.004
9	4.335	3.38	4.107	3.369
10	5.404	-	5.900	5.630
11	8.17	-	9.012	8.661
12	9.613	8.00	10.11	8.170

The new numerical method comprises further developments that affect the hydroelastic response of the ship significantly and improves the prediction of cross section loads in many aspects, such as considering the fully nonlinear stationary forward speed solution, integrating the Froude-Krylov and hydrostatic pressure over the instantaneous wetted surface, a new finite beam element approach to account for coupling effects of torsion and bending, et cetera. The new numerical method was developed to predict the hydroelastic response of ships in oblique wave. This scenario is complex because all of the

new developed methods interact and contribute to the total response of the elastic hull. To investigate and validate the contribution of each new method more independently, the hydroelastic response for a wave encounter angle of 180deg, 150deg and 120deg was analyzed. A wave encounter angle of 180deg is the simplest of these three scenarios because the elastic hull is exited symmetrically. During the present validation study, longitudinal compression and elongation was not investigated, thus a wave encounter angle of 180deg causes only a vertical bending response. This scenario is used to verify the effect of forward speed and the changing wetted surface on sectional loads of the elastic ship and on springing-induced vibrations.

A wave encounter angle of 150deg introduced strong elastic deformations due to torsion, vertical bending and horizontal bending and includes most likely the strongest coupling effects between all degrees of freedom. A wave encounter angle of 120deg initiates only a moderate vertical bending response, however, a strong torsion and horizontal bending response. Consequently, this scenario initiates the strongest coupled torsion-horizontal-bending response of all three scenarios. The validation study in section 4.5.2.1, 4.5.2.2 and 4.5.2.3 were performed with the model equipped with the backbone, see section 3.4.1.

4.5.2.1 Response in Waves at 180deg Encounter Angle

For a wave encounter angle of 180deg the midship vertical bending oscillations of the 333m long post-Panamax Containership B advancing at constant forward speeds of 15 ($F_n = 0.135$) and 22kn ($F_n = 0.198$) in regular head waves were investigated.

As aforementioned, a time series record of the experimental hammering test of the wet vertical bending decaying response at zero speed was available. Based on this record, the wet natural frequencies of the two-node and three-node bending modes were computed using a curve fitting algorithm. The following curve fit was superposed on the linear oscillatory decay response of the two single oscillations denoted by the indices 1 and 2:

$$f(t) = a_0 + a_1 e^{\{-\delta_1 \omega_1 t\}} \cos\left(\omega_1 \sqrt{1 - \delta_1^2} + \varphi_1\right) + a_2 e^{\{-\delta_2 \omega_2 t\}} \cos\left(\omega_2 \sqrt{1 - \delta_2^2} + \varphi_2\right) \quad (223)$$

4.5 Validation of the Hydroelastic Reponse in Waves

Here, a_0 is the mean value, and a_n , δ_n , ω_n , and φ_n are the amplitude, damping ratio, undamped natural frequency, and phase angle, respectively. The damped natural frequency was computed from $\omega_{d,n} = \omega_n \sqrt{1 - \delta_n^2}$. The least square method was used to determine a curve fit of the decaying model test results. The mean value was $a_0 = 8.515e^{-3}$. The other corresponding parameters are listed in Table 20.

Table 20: Curve fitting results of the experimental decay tests

n	$a_n[-]$	$\delta_n[-]$	$\omega_{d,n}[rad/s]$	$\varphi_n [rad]$
1	1.0	0.0419	3.38	-0.818
2	0.09952	0.02608	8.00	-2.987

Index 1 represents the two-node and index 2 the three-node vertical bending mode. With a damping ratio of $\delta_1 = 0.0419$, the model tests were overdamped for the two-node bending vibration. The full-scale damping ratio is normally about 2% of critical damping; for some ships, it is even less (e.g., Orlowitz and Brandt (2014), Storhaug (2014), Storhaug et al. (2017)). Total damping for containerhips comprises hydrodynamic damping and structural damping. Although the welded steel structure of cargo ships is weakly damped, cargo in contact with the structure is excited and, therefore, slightly increases structural damping.

In the model tests, the aluminium backbone provided the structural behaviour of the ship. Bolts connected the backbone to the wooden hull. The combination of materials and fitted screws may have increased the model's structural damping. Furthermore, model tests were based on Froude scaling, which overpredicted viscous effects, and this could have led to higher damping ratios. In addition, the model was equipped with bilge keels, which may have further increased damping. The decay tests were performed at zero speed. Consequently, it is assumed that damping could be higher at forward speed (Orlowitz and Brandt, 2014). Figure 93 compares time records of the midship vertical bending moment obtained from model test measurements (EXP), from fitting curve, equation (223), to these measurements (curve fit), and from numerical computations (nonlinear) from the new numerical method. These bending moments were normalized against the maximum amplitude that was measured at the beginning of the decay test.

The numerical damping rate was adapted to the model test results by applying a critical damping rate of $\delta_j = 0.037$ according to equation (126). The hydrodynamic potential damping was small and a constant damping coefficient of $\delta_j = 0.037$ for every mode was sufficient to achieve a similar total damping ratio in the numerical decay test as it was found from the model tests.

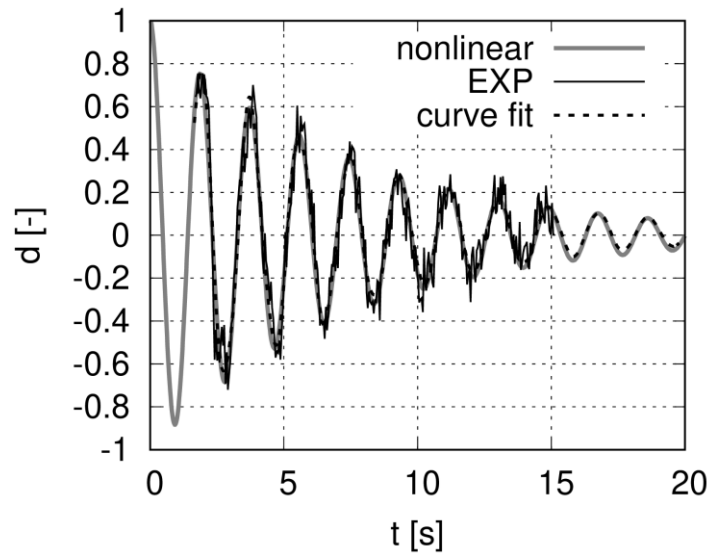


Figure 93: Comparative decaying normalized vertical midship bending moments obtained from model tests (EXP Decay), from a fitted curve based on these model tests (curve fit), and from time domain simulations with the new numerical method (nonlinear)

A second, faster numerical computation to determine the wet natural frequencies was applied by directly solving the system's characteristic equations (134) considering the estimated hydrodynamic added mass and restoring matrices, \tilde{m} and \tilde{k} . Recall that these estimated matrices were computed previously without knowing the real mode shapes. Furthermore, the high frequency free surface boundary condition was applied.

Nevertheless, natural frequencies obtained from time domain simulations and from solving the system's characteristic motion equations (134) compared favorably to model test measurements. Table 21 compares the numerical results for zero speed, 15kn and 22kn of forward speed with the experimental data (only zero speed data was available).

Table 21: Wet natural frequencies of the two and three-node vertical bending vibration for the ship at forward speeds of 0, 15, and 22kn

Forward Speed	0kn		15kn		22kn	
	Two-node [rad/s]	Three-node [rad/s]	Two-node [rad/s]	Three-node [rad/s]	Two-node [rad/s]	Three-node [rad/s]
EXP	3.38	8.00	-	-	-	-
nonlinear (time domain)	3.37	8.17	3.32	7.92	3.20	7.85
Characteristic system equation	3.20	7.79	3.30	7.82	3.13	7.57

The results of wet natural frequencies from the new numerical time domain method indicate, that the wet natural frequencies decreases with increasing forward speed. A more detailed investigation of this phenomenon is performed in section 5.2.1.

In the following, the vertical bending moments of the Containership B in head waves are discussed for 15kn and 22kn of forward speed.

Vertical Bending Moments at 15kn Forward Speed

In principle, large excitation forces occurred when the ship length to wave length ratio is unfavourable, especially when the wave length is similar to the ship length. This situation causes large ship motions and hull girder vibrations and, consequently, result in relatively large changes of the wetted surface and intensified nonlinear effects. Regarding the excitation of vertical bending, similar effects occur when the wave length is close to one-half or one-third of the ship length. However, in such situations the excitation forces are smaller. Resonant vibrations, in principle, appear when the frequency of the excitation force is similar to the wet natural frequency of the hull structure. Therefore, linear springing happens only in short waves. However, higher order springing may develop in longer waves, too. For the subject containership, for example, third order springing occurred at an encounter frequency near 1.0 rad/s. Thus, short and longer waves were examined in the validation study. For a wave encounter angle of 180deg and a forward speed of 15kn, twelve different waves scenarios were considered. Table 22 lists the corresponding five parameters, namely, wave frequency ω , wave encounter frequency ω_e , wave length to ship length ratio λ/L_{pp} , wave amplitude ζ^1 , and wave steepness h .

Table 22: Wave parameters of the 12 waves considered for the ship speed of 15kn and a wave encounter angle of 180deg.

Case	ω [rad/s]	ω_e [rad/s]	λ/L_{pp} [-]	ζ_W [m]	h [-]
1	0.422	0.562	1.041	4.0	0.0231
2	0.439	0.590	0.961	1.5	0.00937
3	0.448	0.605	0.924	4.0	0.0260
4	0.507	0.709	0.721	4.0	0.0333
5	0.522	0.736	0.680	1.5	0.0133
6	0.539	0.767	0.637	4.0	0.0377
7	0.580	0.844	0.551	1.5	0.0164
8	0.631	0.945	0.464	2.5	0.0323
9	0.651	0.985	0.437	4.0	0.0550
10	0.661	1.000	0.424	2.5	0.0354
11	0.887	1.507	0.235	1.0	0.0256
12	1.40	2.950	0.0941	0.425	0.0271

During the simulations, the ship was free to move in all six degree of freedom. A mooring system consisting of soft springs prevented the ship from carrying out low-frequency oscillations and the small spring stiffness ensured that the natural frequency of the mooring system was well below the wave encounter frequencies.

Figure 94 compares computed normalized first harmonic amplitudes of the heave and pitch motions to model test measurements. The heave and pitch motion were normalized according to equation (212) and (213). Numerical results are denoted by “nonlinear” and experimental results by “EXP”. The general agreement was favourable and only small differences are seen to have occurred in medium length waves.

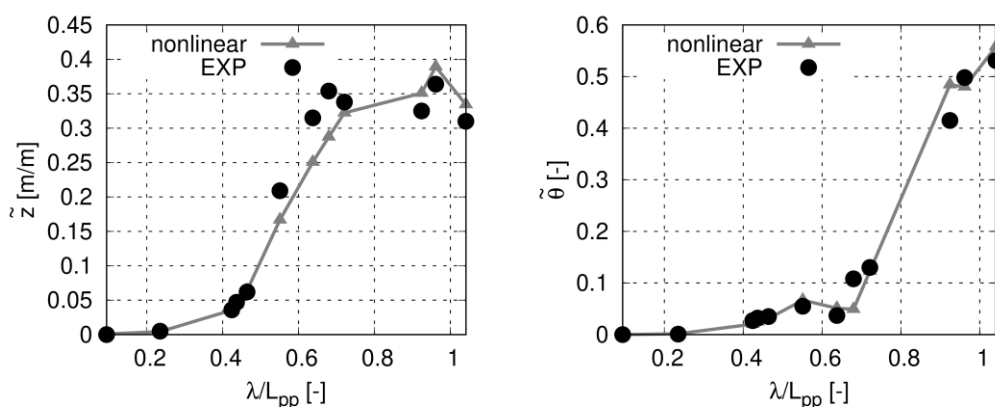


Figure 94: Comparative normalized first harmonic amplitudes of the heave (left) and pitch (right) motions for a wave encounter angle of 180deg and a forward speed of 15 kn.

Figure 95 (left) plots time histories of the computed normalized two-node and three-node modal hydrodynamic vertical bending force, \tilde{F} , for the wave case 1, normalized against their first harmonic amplitude. Here, the grey line identifies two-note bending forces; the black line, three-node bending forces. Figure 95 (right) plots time histories of the computed midship vertical bending moment, \tilde{M}_y , divided by the wave amplitude, and the comparable model test measurements. Here, the black line marks measured bending moments; the grey line, computed bending moments. The index “BB” indicates that the modal was equipped with a backbone. The wave encounter frequency was 0.562rad/s, and the corresponding wave length was close to the ship length. The relatively high wave amplitude of 4.0m led to large amplitude ship motions and hull girder deflections. This caused greater changes of the wetted surface at the ship’s bow and transom, and the associated nonlinearities affected the time histories of the excitation forces as seen by the irregular peaks and troughs. Nonlinearities in the hydrodynamic force of the three-node bending mode were even stronger than in the two-node bending mode. However, the

4.5 Validation of the Hydroelastic Reponse in Waves

midship vertical bending moment was dominated by two-node bending. Therefore, the influence of the three-node vertical bending mode on the vertical bending moment was small, as seen in the time histories of \tilde{M}_y (Figure 95, right). Computed and measured vertical bending moments compared favourably. Both time histories showed the influence of higher order effects, especially at their maximum negative amplitudes.

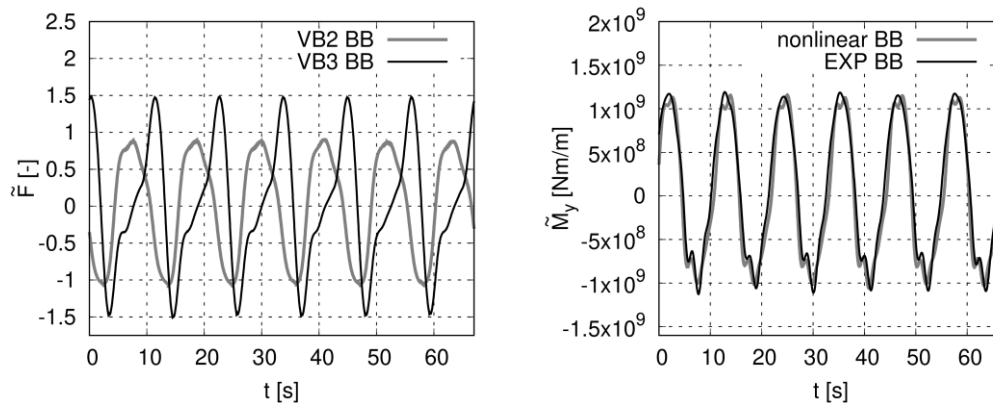


Figure 95: Normalized two-node and three-node modal hydrodynamic vertical bending forces (left) and the vertical bending moments (right) for the wave of case 1 with $\omega_e = 0.562\text{rad/s}$ and 4.0m wave amplitude ($h = 0.0231$) for a wave encounter angle of 180deg and a forward speed of 15kn.

Figure 96 plots the corresponding results for wave case 2, where the wave encounter frequency of 0.590rad/s was nearly the same as for case 1, but where the wave amplitude was reduced to 1.5m. As assumed, nonlinearities were now reduced, which caused the modal hydrodynamic forces, \tilde{F} , and the bending moments, \tilde{M}_y , to behave nearly harmonically. This response was confirmed by the favourable agreement of the computed vertical bending moments to comparable model test measurements. The computations for the ship subject to waves of different wave amplitudes but of similar wave frequency indicated that the new numerical method was capable to accurately account for the influence of the changing wetted surface.

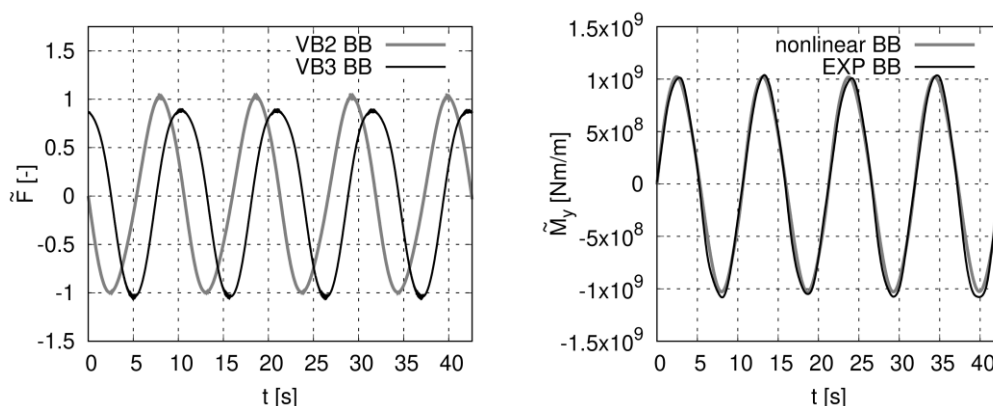


Figure 96: Normalized two-node and three-node modal hydrodynamic vertical bending forces (left) and the vertical bending moments (right) for the wave of case 2 with $\omega_e = 0.590\text{rad/s}$ and 1.5m wave amplitude ($h = 0.00937$) for a wave encounter angle of 180deg and a forward speed of 15kn.

Figure 97 and Figure 98 compare time histories of the modal hydrodynamic vertical bending forces (left) and vertical bending moments (right) for two cases where the wave encounter frequency was close to one-third of the natural frequency of the vertical two-node bending mode but where the wave amplitude differed. Figure 97 shows results for wave case 9 (encounter frequency = 0.985rad/s) and an amplitude of 4.0m; Figure 98, for wave case 10 (encounter frequency = 1.00rad/s) and an amplitude of 2.5m. The modal hydrodynamic forces were again normalized against each first harmonic response amplitude, and the corresponding bending moments were divided by the wave amplitude.

The wave encounter frequencies of these two waves were almost identical. In Figure 97 it can be seen that the modal hydrodynamic forces were strongly affected by higher order effects. These high frequency oscillations arose from the elastic deflection of the ship's hull girder. Froude-Krylov and hydrostatic forces were integrated over the instantiations wetted surface, considering rigid body motions and elastic deflections and a waterline integral that accounted for geometrical nonlinearities of radiation and diffraction forces. Consequently, the effect of high frequency elastic vibrations was noticeable in the time histories of hydrodynamic forces and bending moments (two-way coupling algorithm). However, when comparing the corresponding numerical result of the vertical bending moment with model test results, the numerical and experimental results matched only over certain time intervals. Response maxima agreed well; however, although higher order oscillations showed a similar tendency, they were not congruently aligned. The corresponding first, second, third, and fourth harmonic response amplitudes of computed bending moments turned out to be 2.05e8, 1.71e8, 2.91e8, and 8.90e7Nm/m, respectively, and the corresponding model tests obtained 1.92e8, 1.30e8, 2.65e8, and

4.5 Validation of the Hydroelastic Reponse in Waves

4.89e7Nm/m, respectively. This indicated that the first three harmonic amplitudes were dominant. Presumably, small differences of phase angles and amplitudes significantly changed these time histories. Magnitudes of computed and measured harmonic amplitudes differed slightly. However, the dominant third harmonic amplitude caused by third order springing was similar.

Figure 98 compares the corresponding results for a similar wave frequency, but for a smaller wave amplitude (2.5m). In principle, it is assumed that the first harmonic amplitude of the vertical bending moment is proportional to the wave amplitude and, consequently, the normalized responses should not change significantly. However, this assumption is not necessarily true for higher order effects due to the changing wetted surface. The time histories of two-node and three-node modal hydrodynamic forces plotted in Figure 98 indicate that higher order components were greatly reduced relative to first order effects. The same is seen in the time histories of the vertical bending moment. Visually, numerical and experimental results correlated well. Computed first, second, third, and fourth harmonic amplitudes of 2.14e8, 8.06e7, 6.10e7, and 7.24e6Nm/m, respectively, compared favourably to the corresponding model test measurements of 2.02e8, 6.04e7, 1.09e8, and 1.12e7Nm/m, respectively. As expected, the normalized first harmonic amplitudes of the bending moment obtained for these two wave cases of different amplitude were nearly identical. However, higher order normalized harmonic amplitudes decreased. Specifically, computed and measured second normalized harmonic amplitudes of the bending moment were reduced by a factor of about 0.5; the third and fourth harmonic amplitudes, by an even smaller factor.

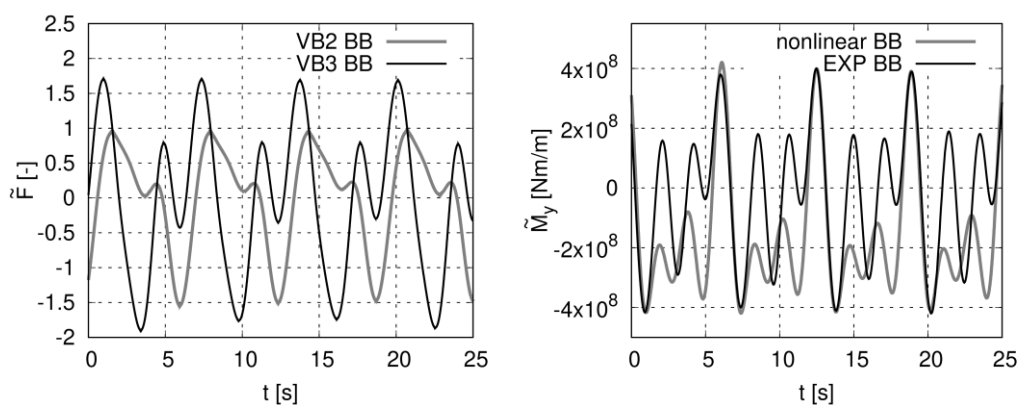


Figure 97: Normalized two-node and three-node modal hydrodynamic vertical bending forces (left) and the vertical bending moments (right) for the wave of case 9 with $\omega_e = 0.985 \text{ rad/s}$ and 4.0m wave amplitude ($h = 0.055$) for a wave encounter angle of 180deg and a forward speed of 15kn.

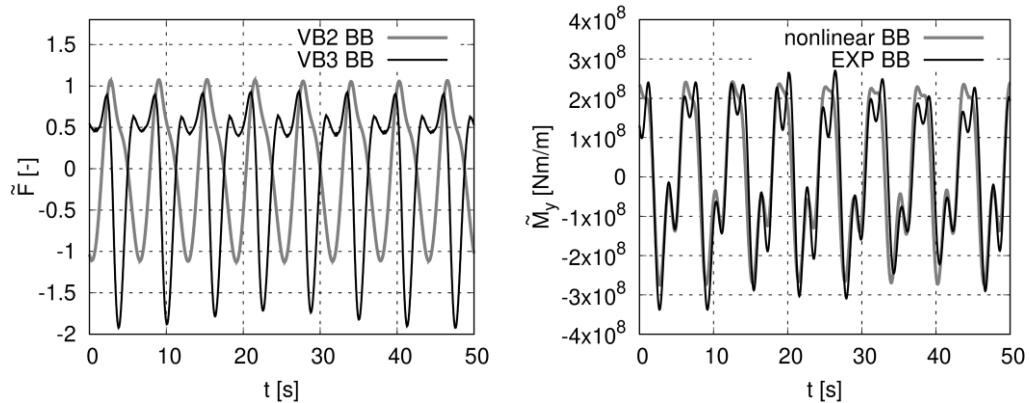


Figure 98: Normalized two-node and three-node modal hydrodynamic vertical bending forces (left) and the vertical bending moments (right) for the wave of case 10 with $\omega_e = 1.00\text{rad/s}$ and 2.5m wave amplitude ($h = 0.0354$) for a wave encounter angle of 180deg and a forward speed of 15kn.

The above results showed that the vertical bending moment was sometimes strongly affected by higher order effects. In long waves, these effects were small, and they occurred largely in higher amplitude waves in conjunction with the associated changing wetted surface. In shorter waves, these nonlinear effects caused resonant vertical two-node bending vibrations (accompanied by third-order springing). The new numerical method adequately captured nonlinear effects caused by the changing wetted surface. However, when resonant vibrations developed, computed and measured time histories sometimes differed. Nevertheless, the response amplitudes of higher order springing depend strongly on the natural frequency of the hull girder and, consequently, small differences of the natural frequency led to large differences of the associated response amplitudes. Small discrepancies between computed and measured natural frequencies at forward speed most likely caused the associated harmonic response amplitudes of elastic resonant vibrations to differ, thereby demonstrating the importance of considering a number of different waves at frequencies in the neighbourhood of structural resonance.

Figure 99 compares first, second, third, and fourth harmonic amplitudes of computed (nonlinear BB) and measured (EXP BB) vertical bending moments for all wave cases listed in Table 22, obtained from discrete Fourier transformations of the time histories divided by the associated wave amplitude. Thus, $\tilde{M}_y^{(1)}$ represents the first harmonic amplitude of vertical bending moment, and $\tilde{M}_y^{(2)}$, $\tilde{M}_y^{(3)}$, and $\tilde{M}_y^{(4)}$ are the corresponding second, third and fourth harmonic amplitudes. In general, the first harmonic amplitudes (top left graph of Figure 99) agree well. In long waves, the new numerical method slightly overestimated the experimental results, whereas in medium length waves, the agreement was fair. In the shortest wave of $\omega_e \approx 3.0\text{rad/s}$, computed and experimental results differed most. In

this case, the wave encounter frequency was marginally below the natural frequency of two-node vertical bending, see Table 21. Consequently, linear springing effects were assumed to be increased. However, experimental results did not show such effects. As discussed above, this might have been caused by small differences of the computed and measured natural frequencies. However, further experiments would have been necessary to clarify this issue.

The second harmonic amplitudes (right top graph in Figure 99) did not behave as consistently. The harmonic amplitudes sometimes varied strongly with wave encounter frequency. One cause may have been the unequal wave steepness and/or wave amplitude. Recall that changing the wave amplitude altered the higher order response amplitudes significantly. To explore this phenomenon, the wave steepness should have been varied systematically. For many cases, computations generally compared favourably to measurements, but in some cases, differences were noticeable. Second order springing effects were expected at a wave encounter frequency of about 1.5rad/s. However, neither numerical nor experimental results showed such phenomena. Larger second order harmonic amplitudes were obtained from the numerical calculations and from model tests in longer waves of, e.g., $\omega m_e \approx 1.0 \text{ rad/s}$. For this wave encounter frequency, the presence of third order springing effects were already discussed, see Figure 97 and Figure 98. Possibly, the third order springing vibration interacted with second order effects. In even longer waves, second order effects still existed, and these were most likely caused by the changing wetted surface.

Third order harmonic amplitudes of vertical bending moments characterized computed and measured third order springing responses at $\omega m_e \approx 1.0 \text{ rad/s}$ (bottom left plot of Figure 99). The corresponding third order harmonic amplitude was approximately 3.0e8Nm/m and consequently higher than the first order response of that wave frequency and nearly 30% of the overall maximum first harmonic response. However, the vibration frequency of third order springing is three times the wave encounter frequency, what at least indicates the fatigue aging effect of this vibration. In longer waves, a third order harmonic amplitude of 1.0e8Nm/m was measured during model test, which was approximately 10% of the maximum first order response. In this frequency range, computations slightly underestimated the measured response. Recall that higher order responses changed strongly when the wave frequency differed only slightly. Measurements of additional wave frequencies would have had to be considered to clarify this difference.

Similar is true for the fourth harmonic amplitudes (bottom right graph in Figure 99). The number of model tests performed at wave encounter frequencies in the range of fourth order springing was small. Numerical and experimental results suggested that fourth order springing occurred at encounter frequencies of $0.60 \leq \omega_e \leq 0.75 \text{ rad/s}$. However, due to the wet natural frequency of the two-node vertical bending vibration (3.279 rad/s), fourth order springing was assumed to occur in slightly shorter waves at $\omega_e \approx 0.80 \text{ rad/s}$. In very short waves, a fourth order contribution to the vertical bending moment was not found. Consequently, the corresponding plot focused on wave encounter frequencies of $0.5 \leq \omega_e \leq 1.6 \text{ rad/s}$. The computed maximum fourth harmonic amplitude was approximately $4.2 \times 10^8 \text{ Nm/m}$ and thus even larger than the maximum third harmonic amplitude.

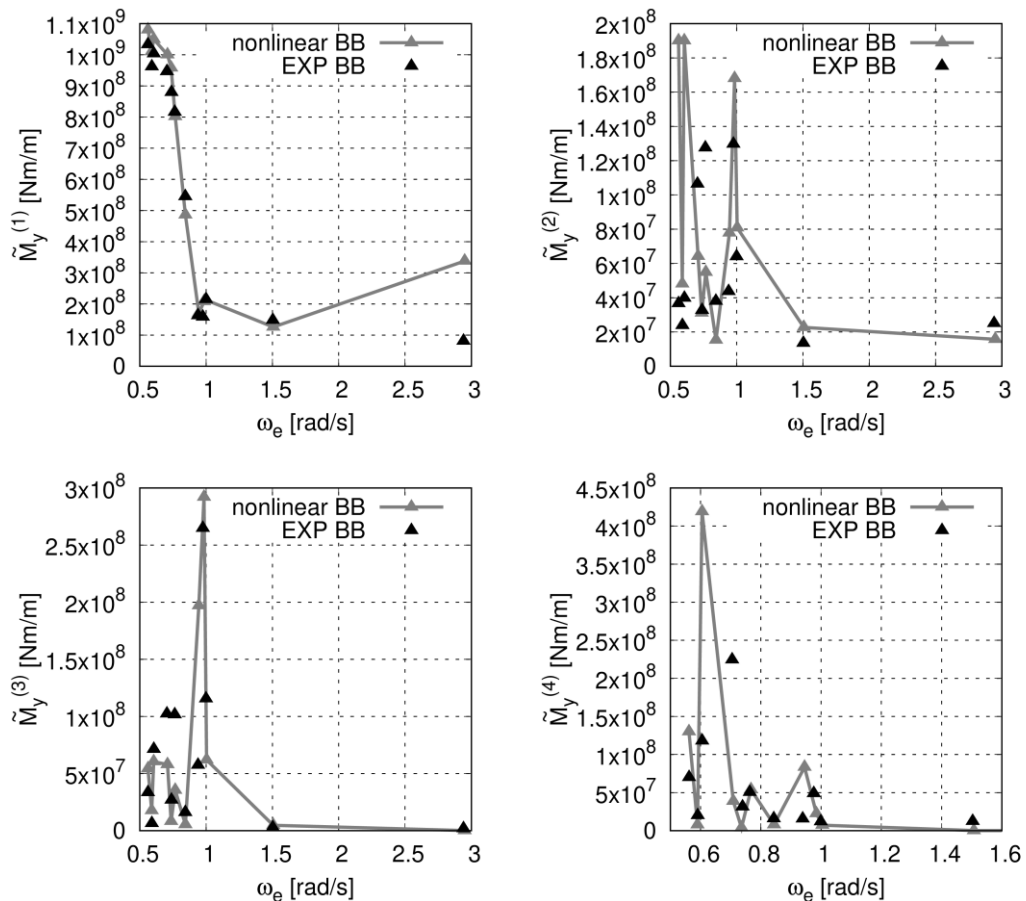


Figure 99: Normalized first ($\tilde{M}_y^{(1)}$), second ($\tilde{M}_y^{(2)}$), third ($\tilde{M}_y^{(3)}$), and fourth ($\tilde{M}_y^{(4)}$) harmonic amplitudes of the vertical bending moment vs. the encounter frequency for a wave encounter angle of 180° and a forward speed of 15 kn .

4.5 Validation of the Hydroelastic Reponse in Waves

For a forward speed of 15kn the new numerical method was able to compute the vertical bending moments of the subjected containership accurately compared to model test results. Direct comparisons of time histories showed differences between the numerical method and model test results in one case. However, the corresponding harmonic amplitudes showed a good agreement. The comparative normalized first, second, third, and fourth harmonic amplitudes of the vertical bending moment showed that the new numerical method was able to predict higher order springing-induced vibrations of the midship vertical bending moment in head waves.

Vertical Bending Moments at 22kn Forward Speed

For a forward speed of 22kn another eight wave scenarios were investigated. Table 23 lists the corresponding wave parameters for each case, comprising wave frequency ω , wave encounter frequency ω_e , wave length to ship length ratio λ/L_{pp} , wave amplitude ζ^1 , and wave steepness h .

Table 23: Wave parameters of the investigated waves scenarios considered for the ship at 22kn.

Case	ω [rad/s]	ω_e [rad/s]	λ/L_{pp} [-]	ζ_W [m]	h [-]
13	0.403	0.590	1.140	1.5	0.00790
14	0.436	0.655	0.974	1.5	0.00925
15	0.476	0.737	0.817	1.5	0.0110
16	0.525	0.843	0.672	1.5	0.0134
17	0.587	0.984	0.537	1.5	0.0167
18	0.667	1.180	0.416	1.5	0.0217
19	0.778	1.476	0.306	1.5	0.0295
20	1.215	2.918	0.125	0.410	0.0196

Figure 100 compares the normalized first harmonic amplitudes of computed (nonlinear) heave and pitch motion, normalized according equations (212) and (213), with the corresponding model tested results (EXP). The new numerical method computed heave amplitudes slightly underestimated compared to the measured values, whereas the pitch amplitudes were almost identical to measured values.

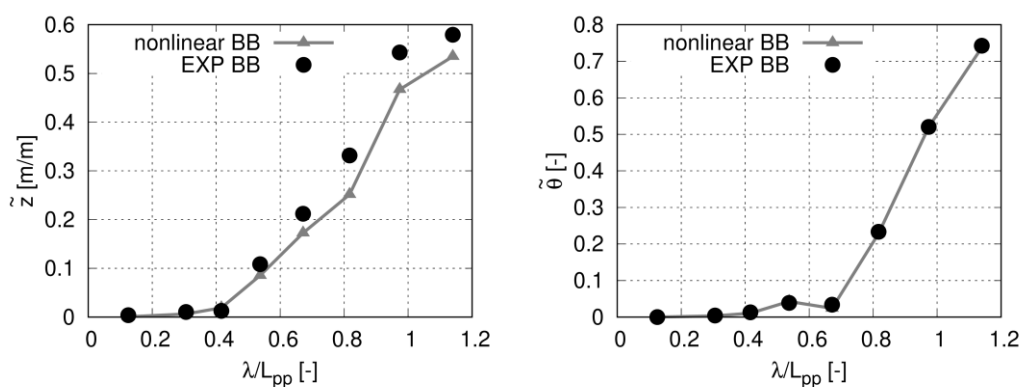


Figure 100: Comparative normalized first harmonic amplitudes of the heave (left) and pitch (right) motions for a wave encounter angle of 180deg and a forward speed of 22 kn.

The increased forward speed changed the wave encounter frequency. Consequently, resonant springing vibrations occurred in longer waves compared to those at a forward speed of 15kn. Figure 101 plots time histories of computed and measured vertical bending

moments for case 17 (left) and case 19 (right) divided by the wave amplitude. For case 17, the encounter wave frequency of 0.984 rad/s was close to one-third of the natural two-node vertical bending frequency. Visually, the computed time history agreed well with experimental results. This was confirmed by comparing the harmonic response amplitudes. First, second, third, and fourth harmonic amplitudes of the computed bending moment were 4.37e8, 2.22e7, 4.13e7, and 1.12e5Nm/m, respectively; the corresponding model test results, 4.49e8, 3.36e7, 6.99e7, and 5.62e6Nm/m, respectively. Thus, the first harmonic amplitude was almost identical, but the higher order amplitudes differed. However, the higher order amplitudes were small compared to the first harmonic amplitudes and hardly affected the total bending moment. Nevertheless, computed and measured third harmonic amplitudes exceeded the second harmonic amplitudes, indicating that at least a small amount of third order springing was present.

For case 19, the encounter frequency of 1.476rad/s was about one-half of the natural hull girder bending frequency. Time histories of computed and measured bending moments showed the influence of second order springing. Numerical and model test results were not fully aligned. Additional low and high frequency oscillations influenced the second and third harmonic amplitudes. The associated amplitude spectra of computed (nonlinear) and measured (EXP) vertical bending moments, plotted in Figure 102, indicate the occurrence of the first harmonic response amplitude at a frequency of 1.48rad/s and the second order springing response at a frequency of 2.95rad/s. In addition, the model test spectrum shows that further oscillations occurred at frequencies below 0.50rad/s. These oscillations could have been caused by the spring based mooring system of the model or related equipment. Another oscillation at 3.315rad/s of the model test spectrum was most likely attributable to the natural two-node bending frequency.

Comparing computed first, second, third, and fourth harmonic response amplitudes of 6.38e7, 2.31e8, 4.52e6, and 1.28e6Nm/m with amplitudes from model test measurements of 9.74e7, 1.50e8, 5.06e6, and 6.37e5Nm/m showed that the first harmonic response from model test exceeded the computed value, whereas the reverse was the case for the second harmonic response, that is, the computed second harmonic response exceeded the measured value. This was reasonable because the computed natural two-node vertical bending frequency was slightly lower than the natural two-node vertical bending frequency of the model. Consequently, the frequency of the second harmonic excitation force was closer to the natural frequency of two-node vertical bending and caused a larger resonant vibration.

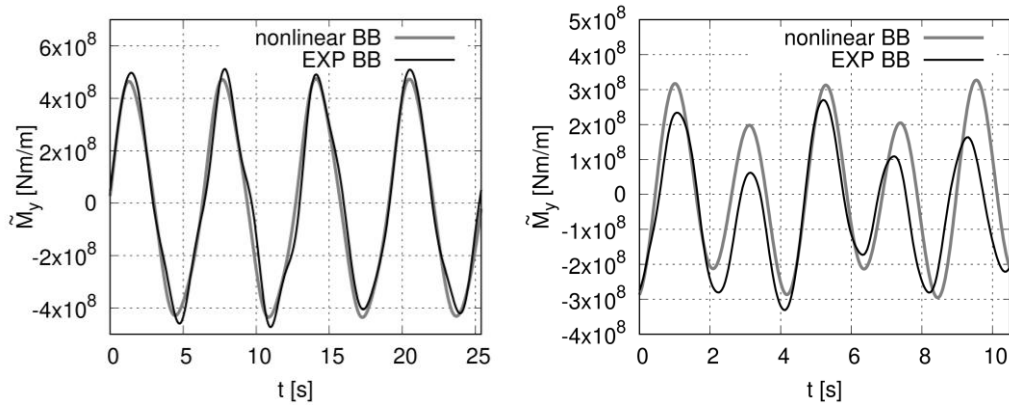


Figure 101: Normalized midship vertical bending moments for wave case 17 (left) with $\omega_e = 0.984\text{rad/s}$ and a wave steepness $h = 0.0167$ and for wave case 19 (right) with $\omega_e = 1.476\text{rad/s}$ and a wave steepness $h = 0.0295$

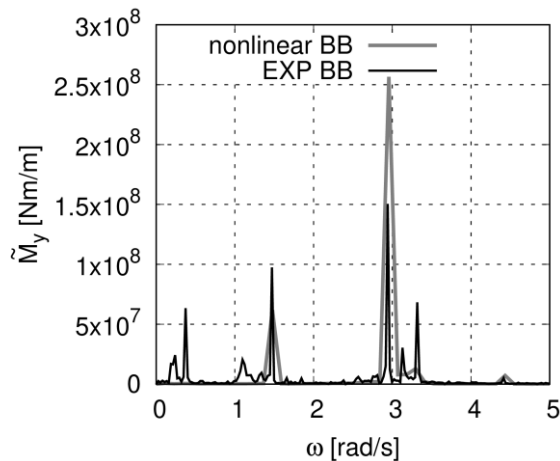


Figure 102: Amplitude spectra of vertical bending moment for wave case 19 with $\omega_e = 1.476\text{rad/s}$, a wave amplitude of 1.5m and a wave steepness $h = 0.0295$

Figure 103 plots computed (nonlinear) and measured (EXP) first (top left), second (top right), third (bottom left), and fourth (bottom right) harmonic amplitudes of the vertical bending moments versus wave encounter frequency for all cases listed in Table 23. Computed first harmonic amplitudes compared favourably to comparable model test measurements although, in long waves (cases 13, 14, and 15), they slightly underestimated measured amplitudes. Except for case 19, the second harmonic amplitudes agreed also favourably with measured amplitudes. Although previously discussed (Figure 101, right), this case again demonstrated that deviations between computed and measured second order springing amplitudes were due to their slightly different natural frequencies of the

vertical two-node bending mode. The computed third order harmonic amplitudes compared somewhat less favourably with measured amplitudes than the first and second order harmonic amplitudes. For case 17, at wave encounter frequency around unity, computed and measured third order springing occurred; however, the measured amplitude exceeded the computed amplitude. This was so also for cases 14 and 15. Although unable to justify this difference, it was already demonstrated for the ship at 15kn, that a small change of the wave encounter frequency strongly effected higher order response amplitudes. For the ship at 22kn, computed third order harmonic amplitudes increased again in long waves (cases 13 and 14). Additional model test measurements in long waves would have been required to resolve this discrepancy. The same holds true for the fourth order harmonic amplitudes. Fourth order springing was assumed to occur at a wave encounter frequency around 0.82rad/s. However, model tests yielded fourth order springing at wave encounter frequencies of 0.655 and 0.737rad/s (cases 14 and 15), but not at the frequency of 0.843rad/s (case 16). The numerical results did not show fourth order springing for any of the investigated waves for 22kn.

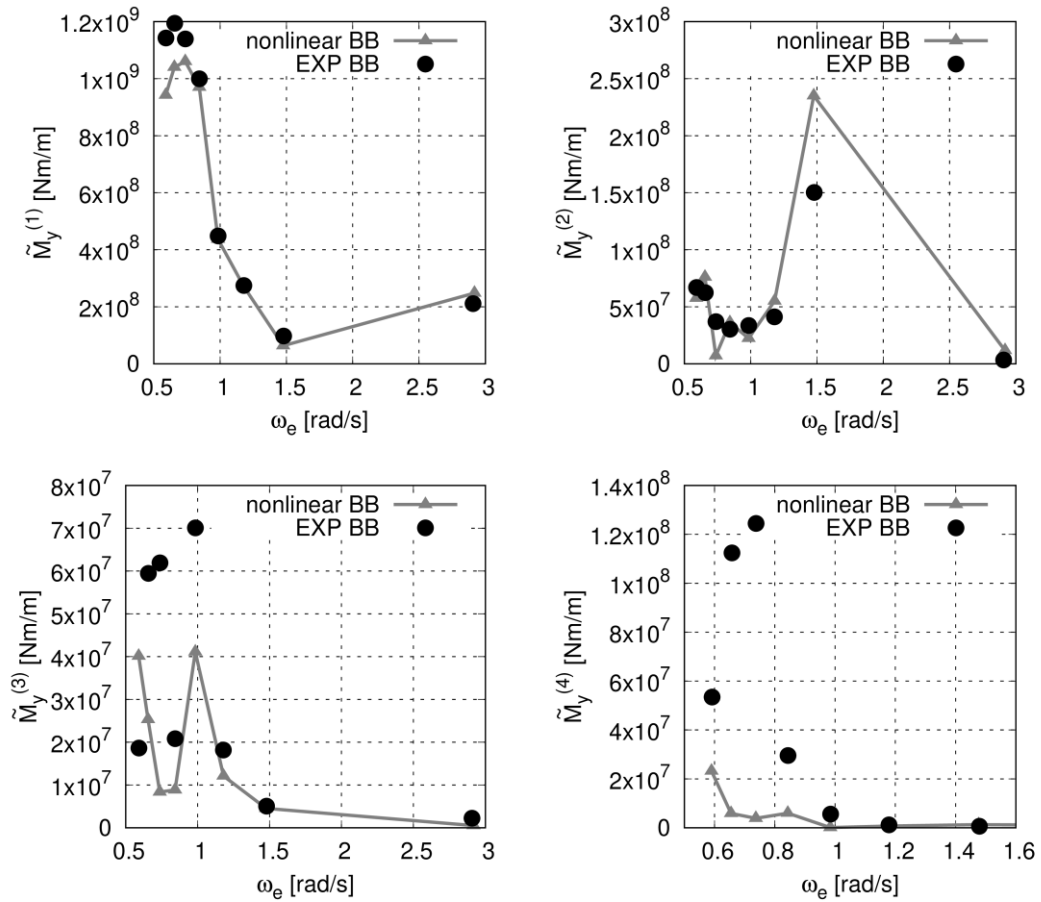


Figure 103: Normalized first ($\tilde{M}_y^{(1)}$), second ($\tilde{M}_y^{(2)}$), third ($\tilde{M}_y^{(3)}$), and fourth ($\tilde{M}_y^{(4)}$) harmonic amplitudes of vertical bending moment vs. the encounter frequency for a wave encounter angle of 180deg and a forward speed of 22kn.

4.5.2.2 Response in Waves at 150deg Heading

An experimental hammering test to measure the wet natural vertical bending frequencies was available and was also used to determine the damping ratio of the vertical bending vibration during the model test in waves of 180deg heading, see section 4.5.2.1. However, the damping two-node vertical bending mode ($\delta = 0.0419$) was significantly higher than usual for experiments in model scale or at full scale. For that reason, a more realistic damping was applied for the numerical computations in oblique waves. Damping depends on many parameters; among these are loading condition, vibration modes, and the associated hull natural frequencies. For the vertical bending vibrations of containerships, Storhaug et al. (2017) estimated damping between 1.5 and 2.5% of critical damping. Generally, the coupled torsion-bending modes are more strongly damped. Full-

4.5 Validation of the Hydroelastic Reponse in Waves

scale measurements of Storhaug and Kahl (2015) and Storhaug and Kahl (2016) showed that damping for such vibrations may be as high as 5% or more of critical damping. Generally, model tests of elastic ship vibrations underestimate damping effects (ISSC (2018)). For the hydroelastic response in waves of 150deg and 120deg, 2.0% of critical damping for the vertical bending modes and 4.0% of critical damping for the coupled torsion-bending modes were assumed.

For a wave heading of 150deg, time series of measured values were available for four different regular wave cases with a forward speed of 15kn. Table 24 lists the corresponding wave parameters, namely, wave frequency ω , wave encounter frequency ω_e , wave length to ship length ratio λ/L_{pp} , wave amplitude ζ_W , and wave steepness h .

Table 24: Wave parameters of the investigated waves scenarios at a wave encounter angle of 150deg and a ship forward speed of 22kn.

Case	ω [rad/s]	ω_e [rad/s]	λ/L_{pp} [-]	ζ_W [m]	h [-]
1	0.507	0.682	0.721	4.0	0.0333
2	0.537	0.733	0.643	4.0	0.0374
3	0.563	0.778	0.585	4.0	0.0411
4	0.967	1.603	0.198	1.0	0.0303

Recall that wave induced forces and thus springing-induced resonant vibrations are significantly affected by rigid body ship motions, first, numerically computed rigid body motions were compared to the model test results. During the numerical simulations and during model tests, the ship was moored with a system of soft springs to avoid drift motions. It turned out that during model tests this spring system was too soft for the investigated wave scenarios and the ship's forward speed. The measured translations in the longitudinal and transverse directions increased continuously and did not reach an equilibrium position. Using a mooring system of soft springs often causes small errors during experiments because the tank length is limited. Therefore, measurements of motions and forces have to be stopped before reaching the equilibrium of wave induced drift forces and time-averaged spring forces. However, only the time series of surge, sway, and yaw motion were affected by drift. The sectional loads were not affected and showed an unambiguous oscillatory behavior. However, in some scenarios, the time-averaged yaw angle reached 5deg. Generally, this changed the wave heading angle and might have had a small effect on ship motions and wave induced sectional loads.

In the following, "nonlinear BB" denotes numerical result for the Containership B equipped with a backbone, and "EXP BB" stands for the corresponding results of the measurements. Figure 104 compares first harmonic amplitudes of the normalized heave

\tilde{z} (left), roll $\tilde{\varphi}$ (center), and pitch motion $\tilde{\theta}$ (right) normalized according to equation (212), (221) and (213). First harmonic amplitudes of surge, sway, and, yaw motions could not be computed using an FFT. In principle, rigid body motions are only slightly affected by viscous effects. An exception is the roll motion, which is affected by viscous damping, especially in waves at encounter frequencies near the ship's natural roll frequency. For the present computations a linear roll damping approach to account for the effect of viscous damping was used (see equation (38)) and a damping rate 1.5 percent of critical damping was applied. However, the effect of viscous damping on roll was assumed to be small because the natural roll frequency of the ship was about 0.25rad/s, that is, it was significantly lower than the wave encounter frequencies. Normalized heave motions compared favorably. In shorter waves, heave amplitudes were almost identical. In longer waves, a small deviation was found. A similar trend was found for the pitch motion. However, for the roll motion, larger deviations occurred. One reason might have been the changing wave heading angle caused by a time-averaged yaw angle during model tests. Furthermore, tests were performed in relatively large waves of 4m amplitude. Consequently, the wave height was significant for an oblique waves scenario and might have induced wave breaking at the ship's bow. This effect could not be captured by the potential flow solver.

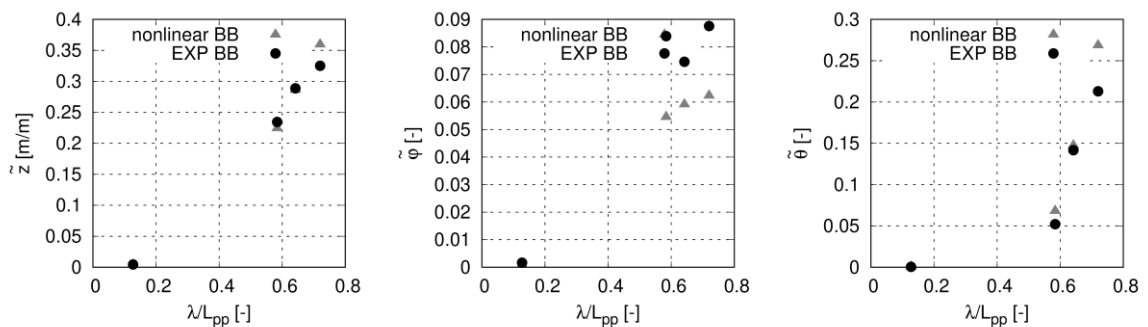


Figure 104: Comparative first harmonic amplitudes of heave (left), roll (centre), and pitch (right) for the ship, equipped with a backbone, in regular waves at 150deg heading at 15kn of forward speed.

Plots in Figure 105 shows midship torsional moment, \tilde{M}_x , vertical bending, \tilde{M}_y , and horizontal bending moment, \tilde{M}_z , respectively, and the associated amplitude spectra for wave case 1. All results were normalized with the wave amplitude. In general, computed and measured first harmonic amplitudes of the torsional moment agreed favorably. The computed torsional moment showed a slight third order springing occurring at the encounter frequency, ω_e , of about 2rad/s. Furthermore, the numerical and measured time series indicate that small second order harmonic response occurred at $\omega_e \approx 1.4$ rad/s. This frequency did not correspond to a natural frequency of the elastic hull. However, it was

already shown in section 4.5.2.1 that a second harmonic response may result from the effect of the changing wetted surface. Additionally, the measured time series indicate significant high frequency vibrations at encounter frequencies between 4.0 and 6.1rad/s. These frequencies seemed not to be in the range of wet natural frequencies of the hull and were not assumed to be generated by the changing wetted surface. An explanation for these vibrations was not found. Computed and measured first and third harmonic amplitudes of the vertical bending moment compared favorably. The second, fourth and fifth harmonic amplitudes were underestimated by the numerical method, however, the second and fifth harmonic amplitudes were small and did not affect the total response significantly. The frequency of the fifth harmonic amplitude was close to the natural frequency of the two-node vertical bending and probably indicated the occurrence of fifth order springing. Comparative horizontal bending moments also agreed favorably. The frequency of the third harmonic amplitude was close to the natural frequency of the coupled one-node torsional-horizontal-bending mode. Numerical and measured results confirmed the occurrence of a small third order springing response. However, the coupled one-node torsional-horizontal-bending mode generally induced a large torsional moment and only a small horizontal bending moment, see Figure 90. Consequently, the third order springing response was small.

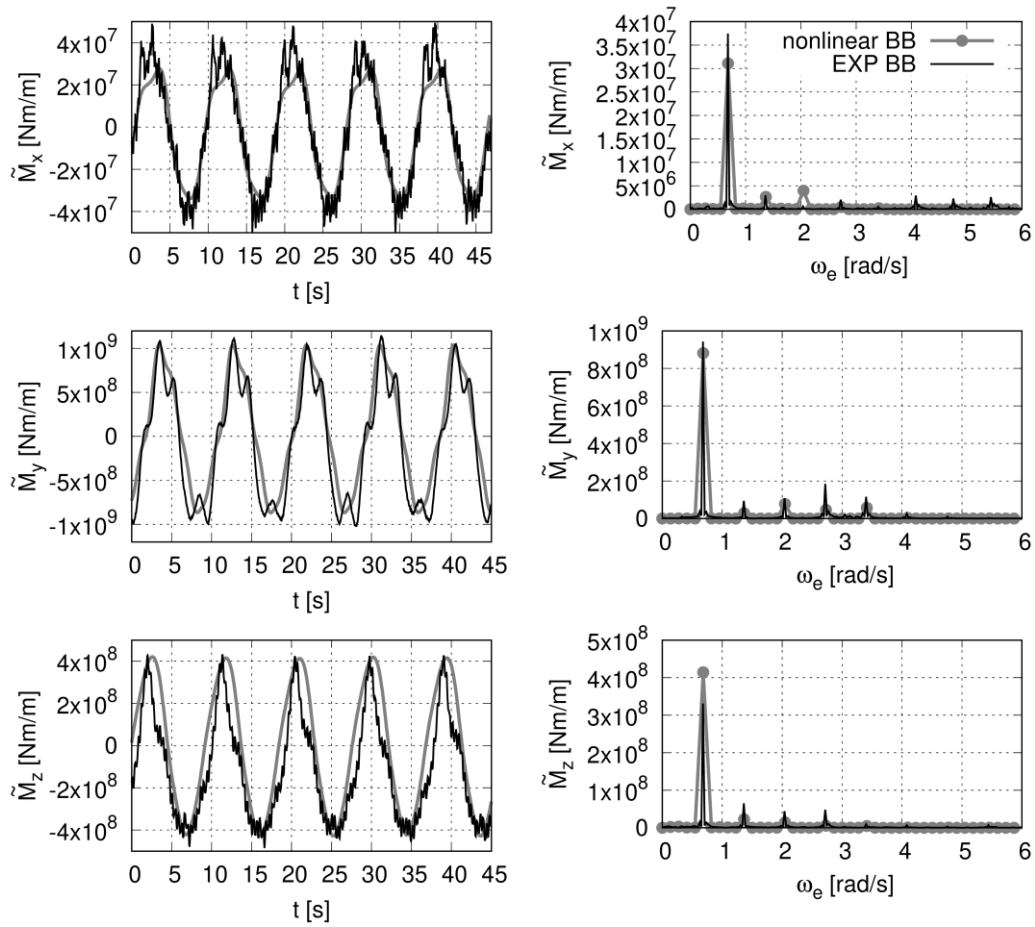


Figure 105: Comparative time series (left) and amplitude spectra (right) of the torsional moment (top), vertical bending (mid) and horizontal bending moment (bottom) for the ship, equipped with a backbone, in waves of case 1 ($h = 0.0333$) at 150deg heading.

Figure 106 plots comparative sectional loads for wave case 2. Computed and measured first harmonic amplitudes of the torsional moment agreed well; however, the measured results showed significant high frequency vibrations with a frequency of approximately 7.5rad/s, especially at the maximum peaks. However, the corresponding amplitude spectrum does not clearly indicate an associated harmonic amplitude for this vibration. The numerical results showed a second harmonic response occurring at $\omega_e \approx 1.5rad/s$. Similar to wave case 1, the second harmonic amplitude most likely resulted from the effect of the changing wetted surface. Computed and measured first harmonic amplitudes of the vertical bending moment agreed favorably. Differences can be seen to have occurred at the fourth harmonic amplitude. The frequency of the fourth harmonic amplitude was approximately 0.35rad/s less than the natural frequency of the two-node vertical bending mode. The numerical computation showed only a small fourth order response; however, during the experiments, the model seemed to be excited in a wider frequency range,

4.5 Validation of the Hydroelastic Reponse in Waves

thereby extending the range of vibration frequencies close to the natural frequency of the two-node vertical bending mode. This caused the amplitude to increase, clearly seen in the time series. Computed and measured horizontal bending moments agreed favorably. Both computed and measured results indicated the occurrence of the similar first harmonic amplitude and small higher order responses.

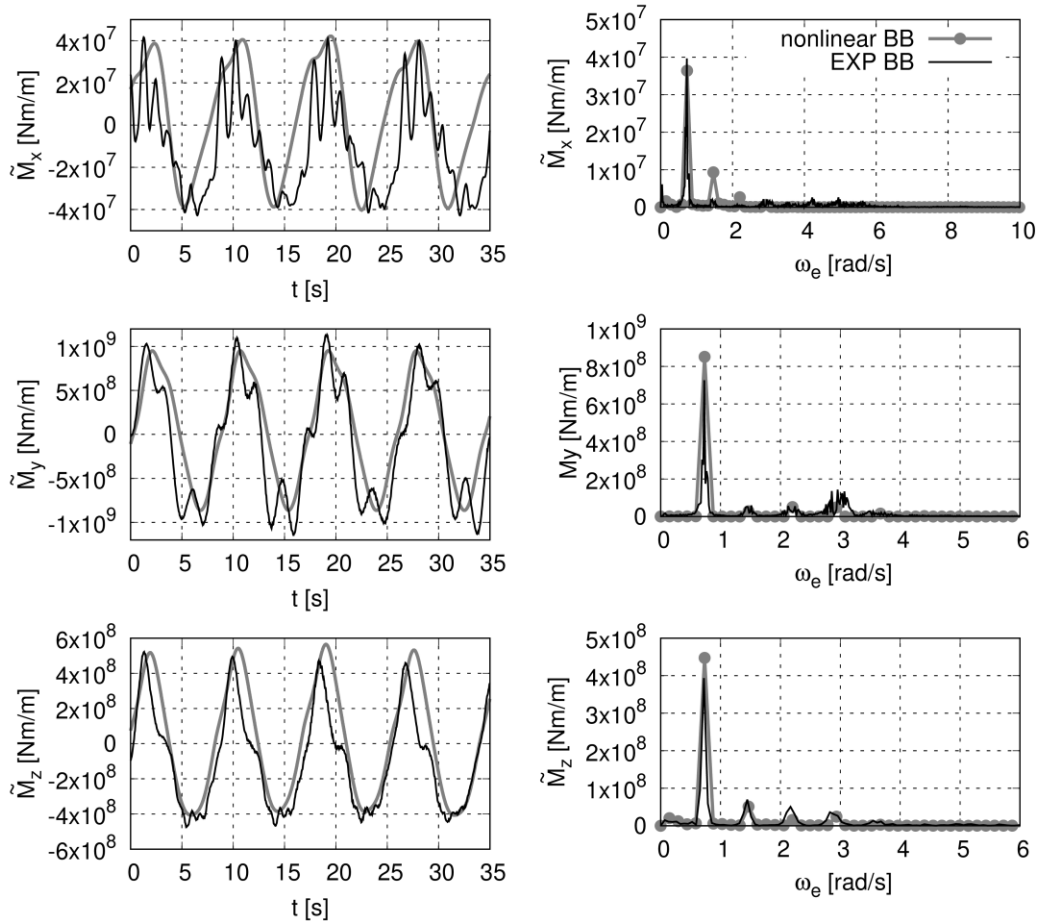


Figure 106: Competitive time series (left) and amplitude spectra (right) of the midship torsional moment (top), vertical bending moment (mid) and horizontal bending moment (bottom) for the ship, equipped with a backbone, in waves of case 2 ($h = 0.0374$) at 150deg heading at 15kn of forward speed.

Figure 107 plots the results for wave case 3. Computed and measured torsional moments show a favorable agreement of the first harmonic amplitude. The numerical simulation slightly overestimated the second harmonic amplitude. Furthermore, a small third and fourth harmonic response is visible. For the vertical bending moment, the first and second harmonic amplitudes were almost identical. However, the numerical simulation underestimated the third and fourth harmonic amplitudes. The fourth harmonic amplitude indicated significant fourth order springing, which can also be seen

clearly in the measured time series. The numerical simulation showed fourth order springing, too; however, it was less dominant. Higher order springing depends strongly on the hull's natural frequency and the associated structural and hydrodynamic damping. Small differences of these parameters between numerical simulation and experiments could have changed the response amplitude significantly. These differences, most likely, were responsible for the deviating results. The first and second harmonic amplitude of the computed and measured horizontal bending moment agreed favorably. The third harmonic amplitude differed, and the numerical simulation seemed to underestimate the response. It is uncertain whether the measurements showed third order springing or whether the response was initiated by the changing wetted surface. The natural frequency of the one-node torsional-horizontal-bending mode was about 0.5rad/s lower than the frequency of the third harmonic response. Consequently, it was assumed that third order springing did not occur.

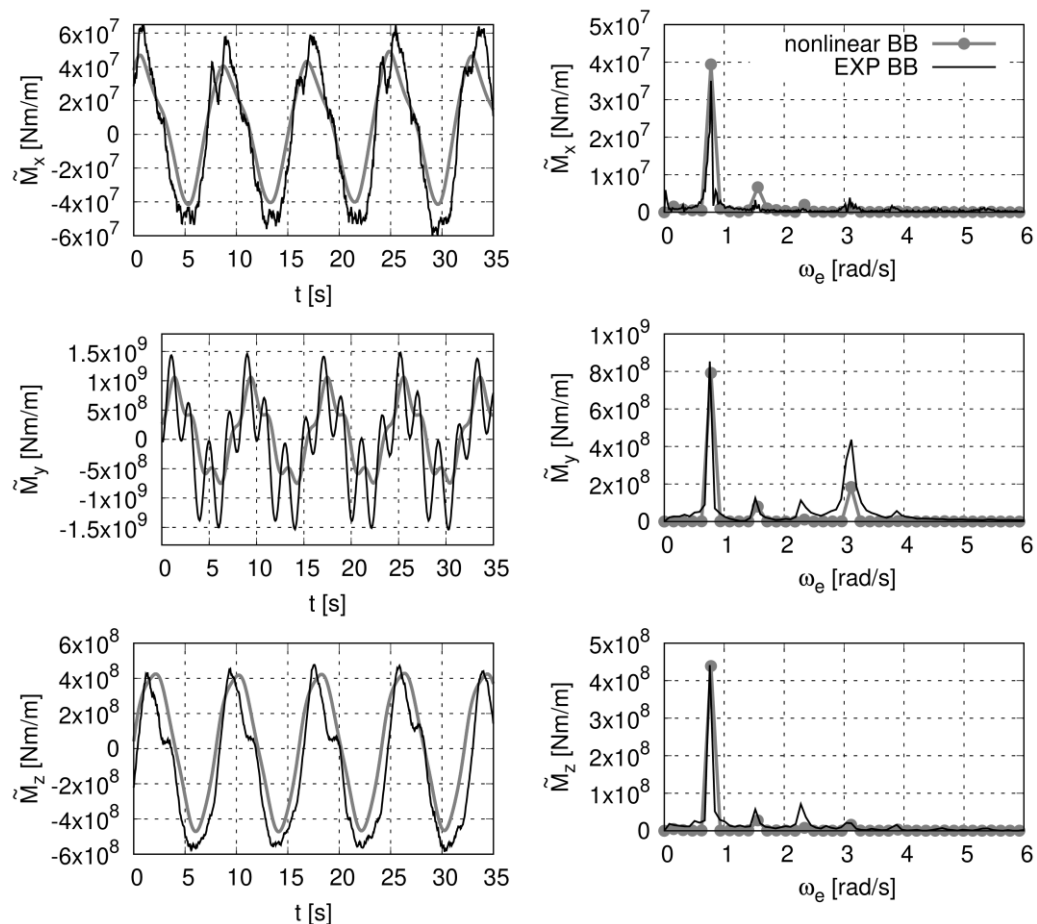


Figure 107: Comparative time series (left) and amplitude spectra (right) of the torsional moment (top), vertical bending moment (mid) and horizontal bending moment (bottom) for the ship, equipped with a backbone, in waves of case 3 ($h = 0.0411$) at 150deg heading.

Figure 108 plots the results for wave case 4. The wave encounter frequency of 1.603rad/s was relatively high, and the time series of the measurements seemed to be more influenced by low and high frequency vibrations. Visually comparing computed and measured torsional moments indicate a favorable agreement. Higher order vibrations were not found; however, the measurements showed low frequency vibrations. Computed and measured vertical bending moments showed a significant second order springing-induced vibration of almost identical second harmonic amplitude. However, the time series are not fully congruent, which resulted from an underestimation of the computed first harmonic amplitude and additional low frequency vibrations from the measurements. Comparing horizontal bending moments time series was difficult because the measurements seemed to be more strongly affected by low frequency vibrations. However, the amplitude spectrum indicates that the numerical simulations overestimated the first harmonic amplitude. In contrast, the second order springing-induced response agrees well. However, the source of the low frequency vibrations could not be identified, and they could have affected also the first and second order harmonic responses. In general, wave case 4 showed that comparisons of scenarios with higher wave encounter frequencies became more difficult because the response amplitudes were reduced, but the solution seemed to be more affected by additional vibrations.

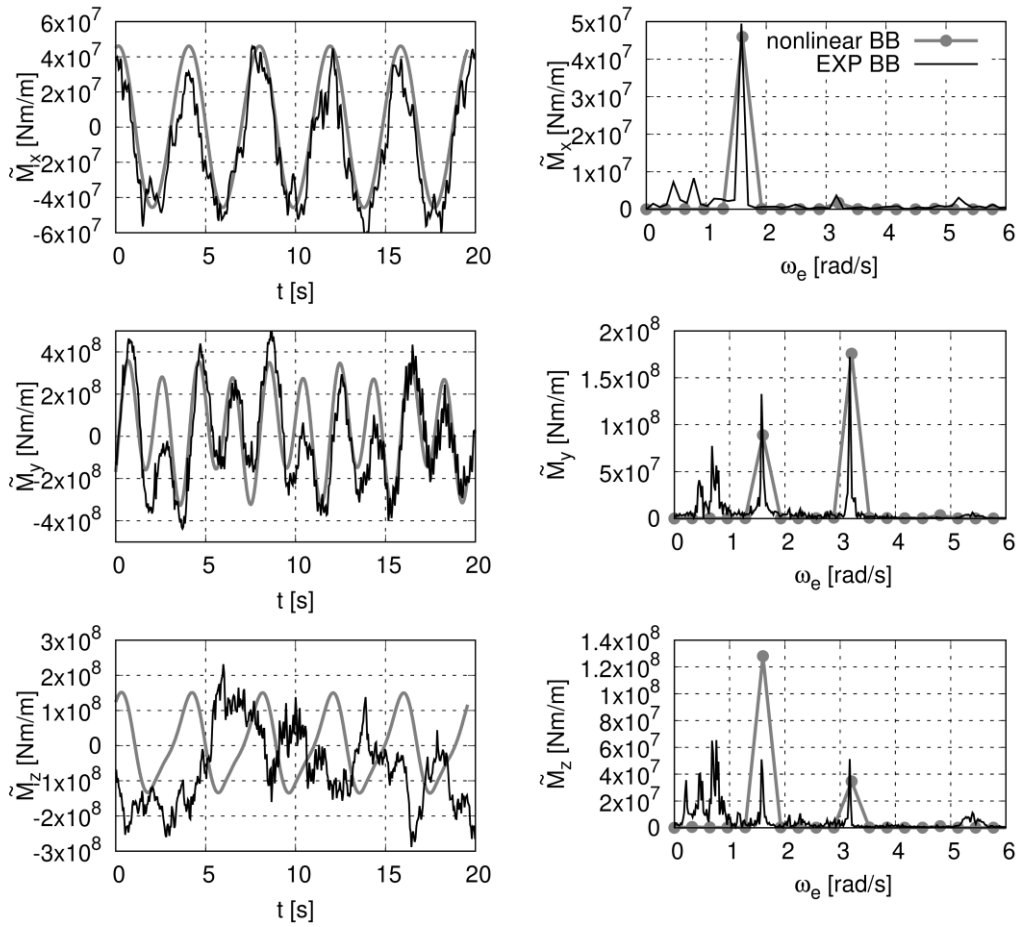


Figure 108: Comparative time series (left) and amplitude spectra (right) of the torsional moment (top), vertical bending moment (mid) and horizontal bending moment (bottom) for the ship, equipped with a backbone, in waves of case 4 ($h = 0.0303$) at 150deg heading.

4.5.2.3 Response in Waves at 120deg Heading

For a wave heading angle of 120deg, sectional loads for three different wave scenarios were compared. Table 25 lists the corresponding wave parameters.

Table 25: Comparative first harmonic amplitudes of heave (left), roll (center), and pitch (right) for the ship, equipped with a backbone, in regular waves at 120deg heading at 15kn of forward speed.

Case	ω [rad/s]	ω_e [rad/s]	λ/L_{pp} [-]	ζ_W [m]	h [-]
1	0.64	0.801	0.469	4.0	0.0532
2	0.83	1.100	0.279	1.525	0.0341
3	1.11	1.595	0.156	0.8	0.0320

4.5 Validation of the Hydroelastic Reponse in Waves

Figure 109 compares first harmonic amplitudes of computed and measured ship motions. Surge, sway, and yaw motion amplitudes were not compared, because measured results showed strong drift motions. In the following, “nonlinear BB” denotes numerical result for the subject containership with backbone stiffness and “EXP BB” the corresponding measured results. Figure 109 plots first harmonic amplitudes of heave, roll, and pitch for the subjected wave scenarios. Computed and measured heave motions compared favorably. Roll and pitch motions showed small deviations. These deviations were most likely caused by the soft spring system used during model test and the corresponding change of the wave heading angle due to a time-averaged yaw angle.

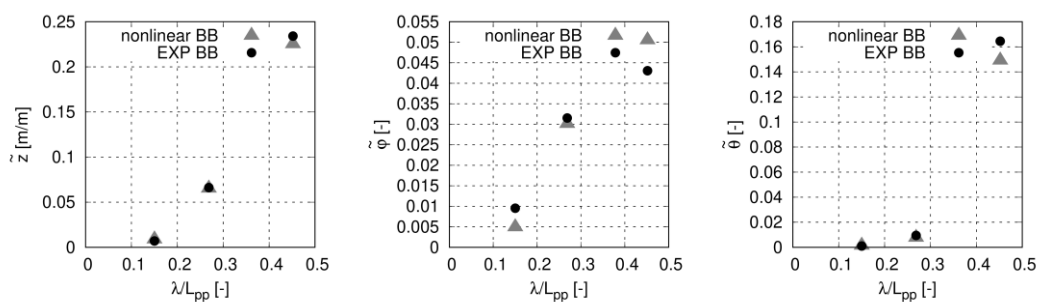


Figure 109: Comparative first harmonic amplitudes of heave (left), roll (centre), and pitch (right) for the ship, equipped with a backbone, in regular waves at 120deg heading and 15kn of forward speed

Figure 110 compares time series of the computed and measured torsional moment as well as vertical and horizontal bending moments for wave case 1 and the corresponding amplitude spectra obtained via a Fourier transformation. The results were divided by the wave amplitude. The time series indicate that the wave encounter frequency during model tests was slightly different than the computed and predefined wave encounter frequency. Such effects occurred more often for the wave encounter frequency of 120deg and were caused by continuous surge and sway drift motions. Furthermore, measurements indicated high frequency vibrations occurring especially at the peaks. Recall that the wave amplitude of 4m was significantly high for a wave heading angle of 120deg. Consequently, the high frequency vibrations might have been caused by strong wave impacts and associated breaking waves. Computed and measured first harmonic amplitudes of the torsional moment agreed well. Furthermore, the numerical computations indicate the occurrence of a second harmonic amplitude and the measurements a fourth harmonic amplitude. The first harmonic amplitude of the vertical bending moment agreed well. Furthermore, the measured vertical bending moment indicated fourth order springing. The computed fourth order springing amplitude was significantly larger than the measured amplitude. Furthermore, it can be seen that the frequency of the measured fourth

harmonic amplitude was higher than the computed response. This was caused by the small differences of the natural frequencies and of the wave encounter frequency and caused, most likely, the deviations of computed and measured fourth harmonic amplitudes. Generally, computed and measured horizontal bending moments agreed well. However, the corresponding amplitude spectrum indicates that the numerical computations overpredicted the first and second harmonic amplitude and underpredicted the third and fourth harmonic amplitude.

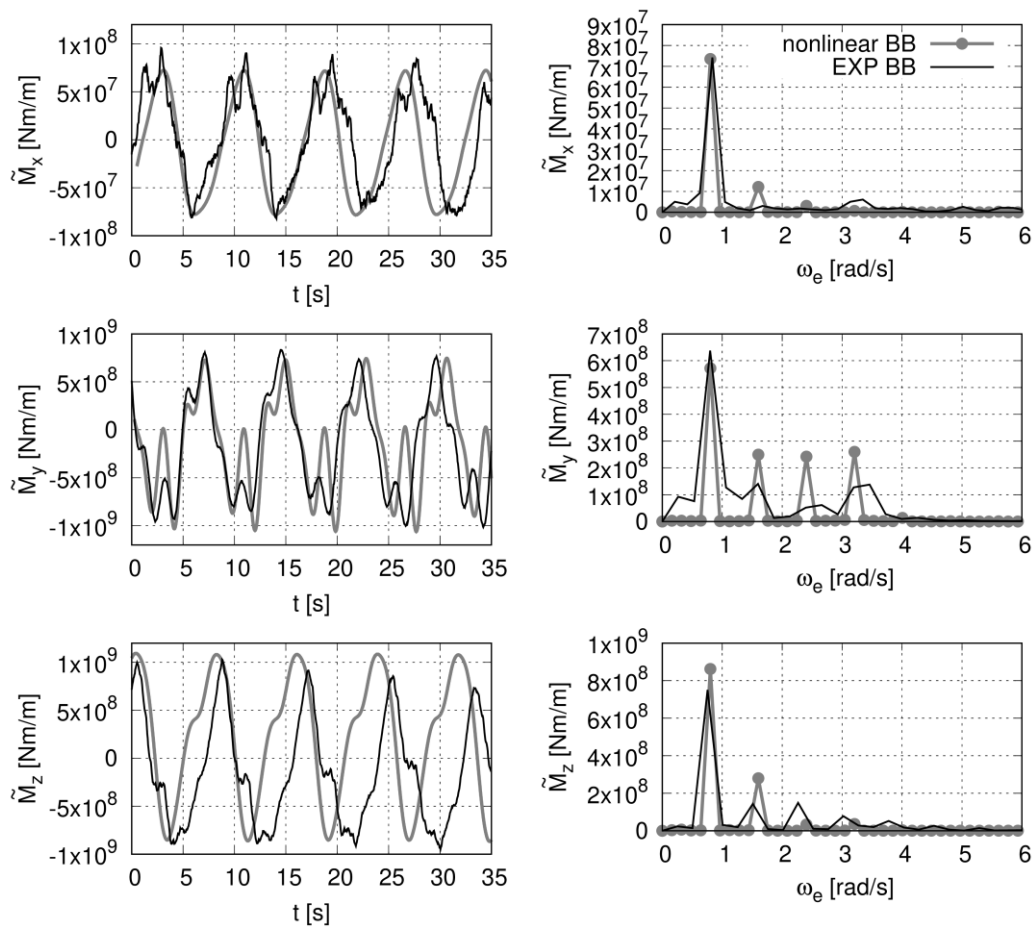


Figure 110: Comparative time series (left) and amplitude spectra (right) of the torsional moment (top), vertical bending moment (mid) and horizontal bending moment (bottom) for the ship, equipped with a backbone, in waves of case 1 ($h = 0.0532$) at 120deg heading at 15kn of forward.

Figure 111 compare computed and measured results for wave case 2. Again, the wave encounter frequencies differed slightly. Visually, the torsional moments agree well. The associated amplitude spectra show that the first harmonic amplitude was slightly underestimated by the numerical computations. The computed and measured vertical bending moments indicate strong third order springing. However, the measured third

4.5 Validation of the Hydroelastic Reponse in Waves

harmonic amplitude was higher. Furthermore, it can be seen that the frequency of measured third order springing was lower than the computed frequency. This was caused by the effect of different wave encounter frequencies and was most likely the main reason for the different third harmonic amplitudes. Furthermore, different damping could have influenced higher order vibrations. The measured horizontal bending moment shows second order springing occurring at the maxima in the time series. However, numerical simulations obtained only minimal second order springing.

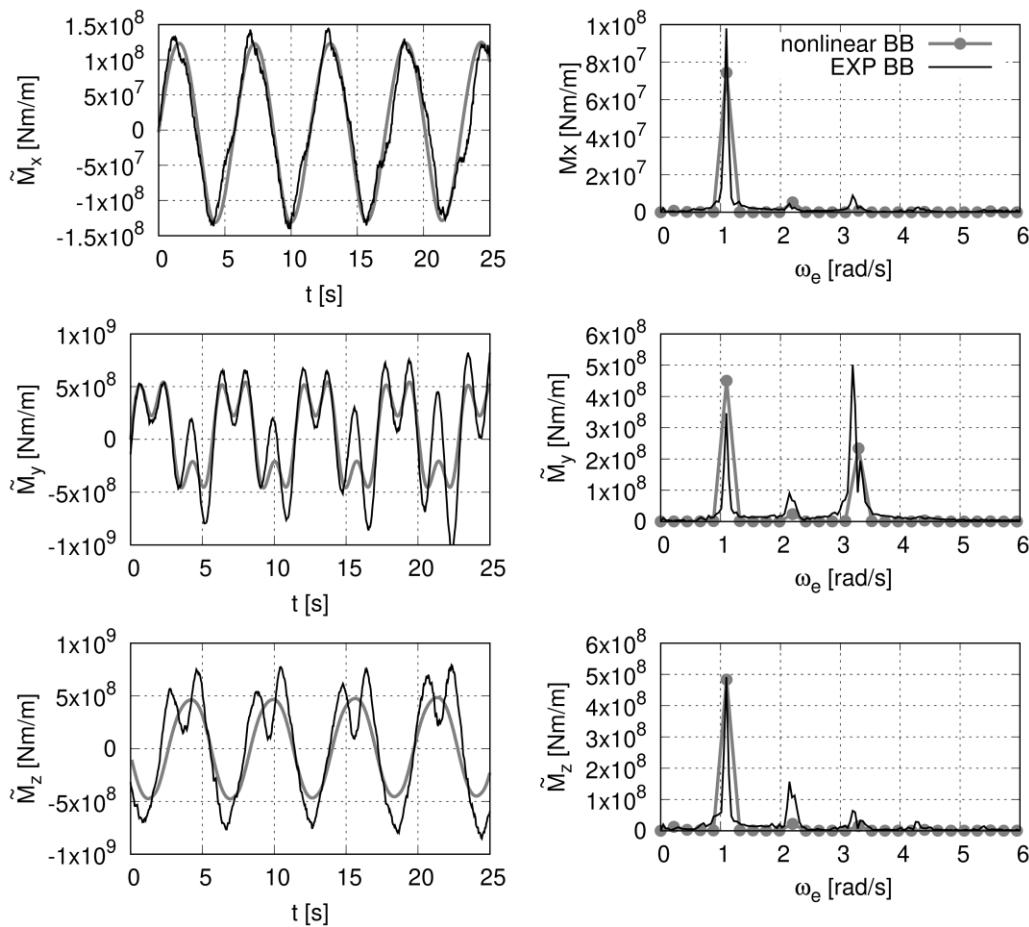


Figure 111: Comparative time series (left) and amplitude spectra (right) of the torsional moment (top), vertical bending moment (mid) and horizontal bending moment (bottom) for the Containership B, equipped with a backbone, in waves of case 2 ($h = 0.0341$) at 120deg heading and 15kn of forward speed.

Figure 112 compares computed and measured results for wave case 3. The wave encounter frequency of $\omega_e \approx 1.6 \text{ rad/s}$ was relatively high. In general, computed and measured results did not agree as well as they did for the previous wave scenarios. The measured torsional moment showed strong higher order vibrations. The associated amplitude spectrum indicates that the numerical prediction overestimated the first

harmonic amplitude and underestimated the second harmonic amplitude. However, measured higher order components were dominated by high frequency vibrations with an encounter frequency of $\omega_e > 5.0 \text{ rad/s}$. These vibrations did not correlate clearly with natural frequencies of the elastic hull, and could not be explained. The vertical bending moment showed strong second order springing. The numerical predictions underestimated the second order springing vibration. This was most likely caused by small differences of the natural frequency of the two-node vertical bending vibration, by small differences of the wave encounter frequency and by damping effects. Computed and measured horizontal bending moments did not show a similar trend. First and second harmonic amplitudes were similar; however, measurements were affected by low frequency vibrations at $\omega_e \approx 0.15 \text{ rad/s}$ and high frequency vibrations at $\omega_e \approx 5.1 \text{ rad/s}$.

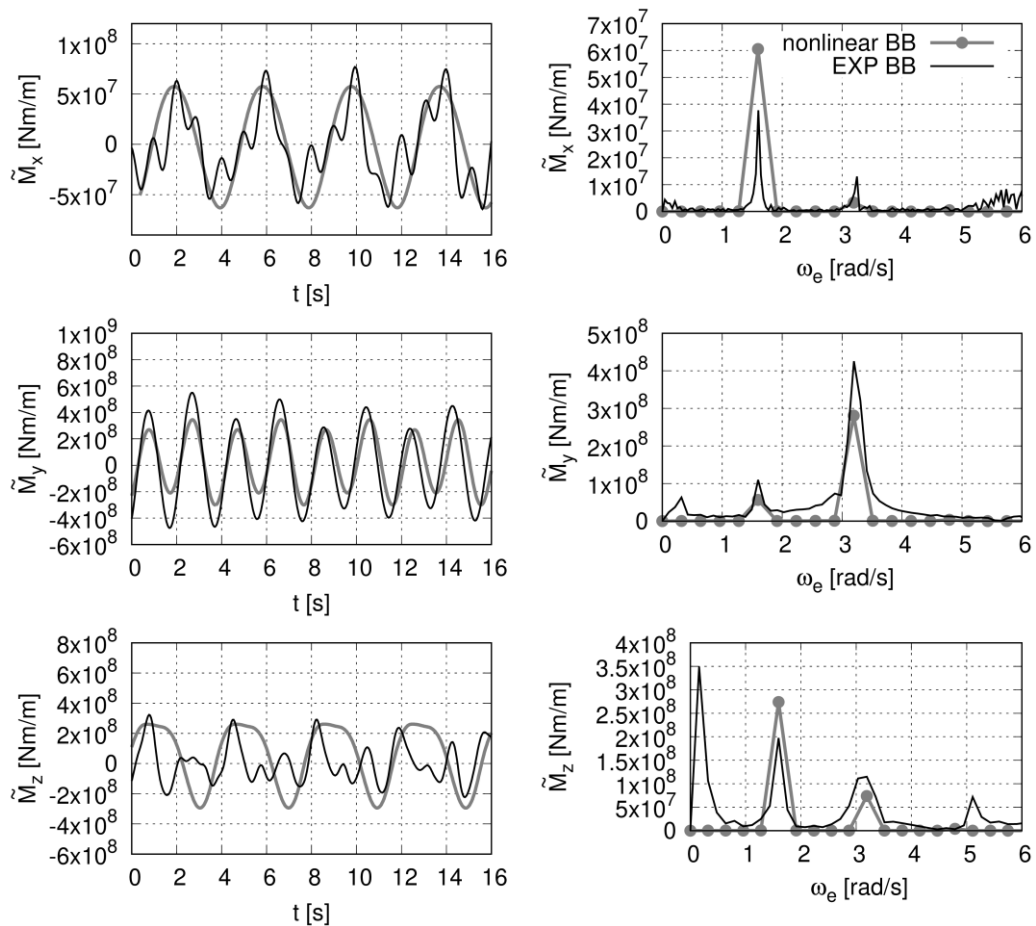


Figure 112: Comparative time series (left) and amplitude spectra (right) of the torsional moment (top), vertical bending moment (mid) and horizontal bending moment (bottom) for the ship, equipped with a backbone, in waves of case 3 ($h = 0.0320$) at 120deg heading and 15kn of forward speed.

4.6 Computational Performance

For all numerical simulations with the new numerical method, a wave ramp increased the wave amplitude in the beginning of the simulation. This wave ramp was applied over the first three wave encounter periods. Afterwards, the full wave amplitude was reached. For numerical computations of rigid body motions, usually, the simulation converged, at least, after ten wave encounter periods and oscillations with constant amplitudes occurred. The following four wave encounter periods were applied for the computations of harmonic amplitudes and time averaged values using a Fourier transformation.

For wave scenarios that induced resonant elastic vibrations (springing), sometimes more wave encounter periods had to be simulated. Exemplary Figure 113 shows a time series of the normalized vertical bending moment (normalized with its maximum amplitude) of the Containership B in head waves with a wave encounter frequency of 3.25rad/s (linear springing) at 22kn of forward speed. The full vertical bending moment developed after approximately 20 wave encounter periods.

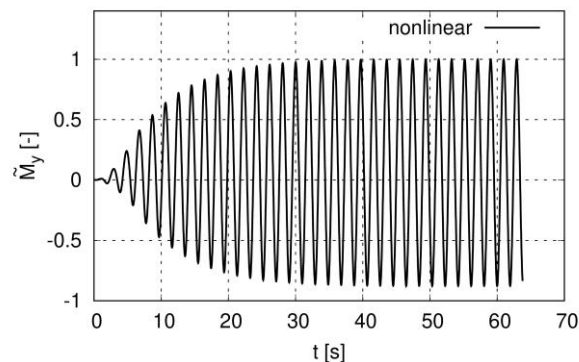


Figure 113: Time series of the normalized vertical bending moment of the Containership B in head waves with a wave encounter frequency of 3.25rad/s and a forward speed of 22kn.

For the simulations, a time step of 0.025s was applied. For simulations of the elastic ship in waves the computational performance was about 20 time steps per second (using one core of a standard personal computer). When elasticity was disabled and only rigid body motions were solved, approximately 40 time steps per second were solved. When the ship was fixed, convolution integrals for each waterline panel and the complete hull forces and moments need not to be solved. In that case, the computational performance increased up to 70 time steps per second.

5 Results

The validation study showed that rigid body motions and elastic vibrations may be affected by the wave steepness and are thus not proportional to the wave amplitude. Similar was also found out e.g. by Fonseca and Guedes Soares (2004) investigated experimentally the nonlinear effects on vertical motions and loads of a containership in regular head waves. They found out that the normalized first and second harmonic heave and pitch amplitudes differ clearly due to wave steepness. Furthermore, the validation study also showed that forward speed had an effect on the wet natural frequencies of the elastic vibration modes and consequently affect the sectional loads. Section 5.1 analyses the effect of the wave steepness on normalized rigid body motions (normalized with the wave amplitude) of the Containership A in oblique waves and section 5.2 investigates the effect of the wave steepness and forward speed on normalized sectional loads of the containership B in head waves.

The validation of sectional loads was performed for the Containership B equipped with a backbone to simulate the structural properties. It was already discussed that a backbone cannot simulate the structural properties of a ship realistically because of the incorrect location of the shear center. In section 5.3, sectional load for the Containership B with realistic full scale structural properties (see section 3.4.2) in oblique waves with wave encounter angles of 150 and 120deg are discussed and compared to results obtained from the backbone model. Furthermore, the influence of the wave steepness on normalized sectional loads is investigated.

5.1 Influence of the Wave Steepness on Ship Motions in Oblique Waves

The influence of the wave steepness on ship motions was investigated numerically by performing systematic computations in increasingly steep waves of $h = 0.01$, 0.02 , and 0.03 . The Containership A was advancing at 16kn ($Fn = 0.139$) of forward speed in waves

of 30deg encounter angle. To compare the results of different wave steepnesses conveniently, ship motions were normalized according to equations (212), (213),(219), (220), (221) and (222).

Figure 114 plots the normalized time histories of all six rigid body motions for a wave according to $\lambda/L_{pp} = 0.633$. On the left side, surge, sway and heave are plotted (from top to bottom) and on the right side, roll pitch and yaw motions are plotted. Symbols “nonlinear-0.01”, “nonlinear-0.02”, and” nonlinear-0.03” identify results from the new numerical method in waves of steepness $h = 0.01, 0.02,$ and $0.03,$ respectively. It can be seen that the increasing wave steepness reduces the normalized surge, roll, pitch and heave motions. Furthermore, nonlinear effects became more dominant with increasing wave steepness. Especially the surge, heave and pitch motions were affected. Figure 115 compares the amplitude spectra of the surge motions for a wave steepness of 0.01 and 0.03. For a wave steepness of 0.01, the normalized first harmonic amplitude of the surge motion reduced strongly with increasing wave steepness and the second harmonic amplitude increased slightly with increasing wave steepness.

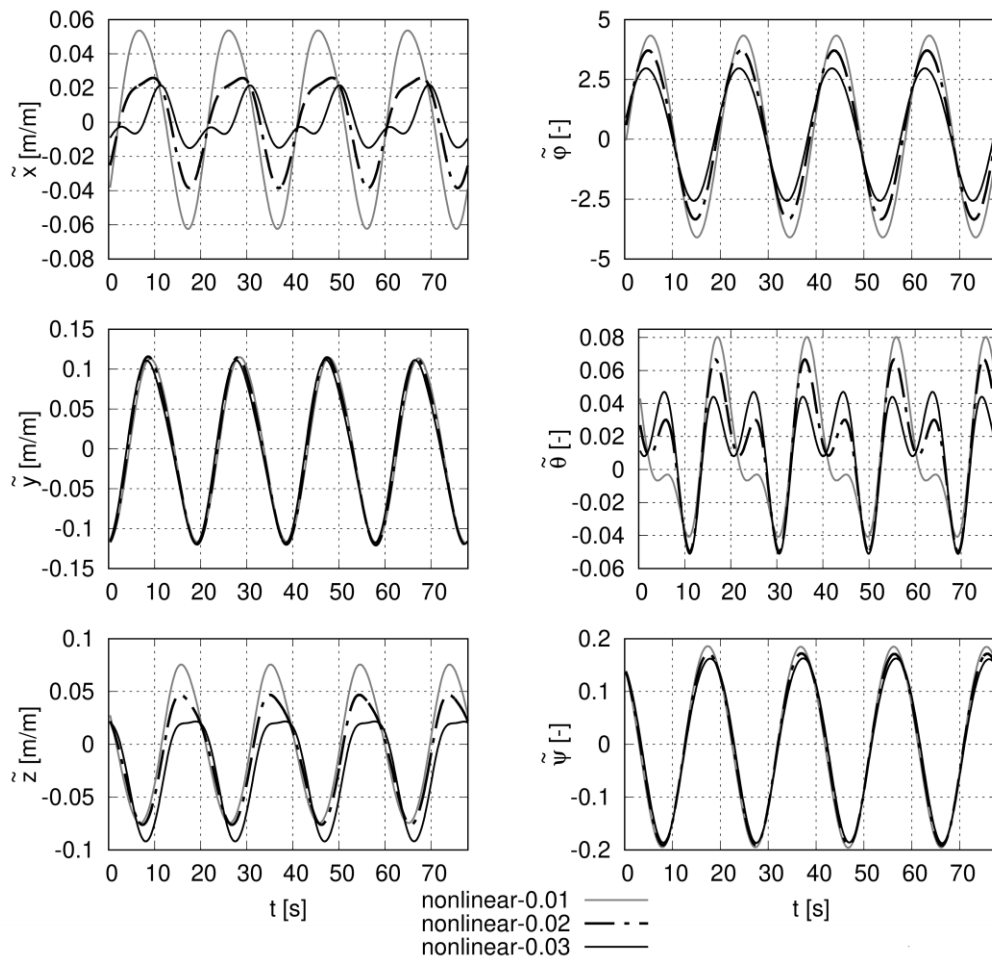


Figure 114: Time histories of rigid body motions for the Containership A at $Fn = 0.139$ in waves of $\lambda/L_{pp} = 0.633$ and at wave encounter angle of 30deg for wave steepness $h = 0.01$, $h = 0.02$, $h = 0.03$.

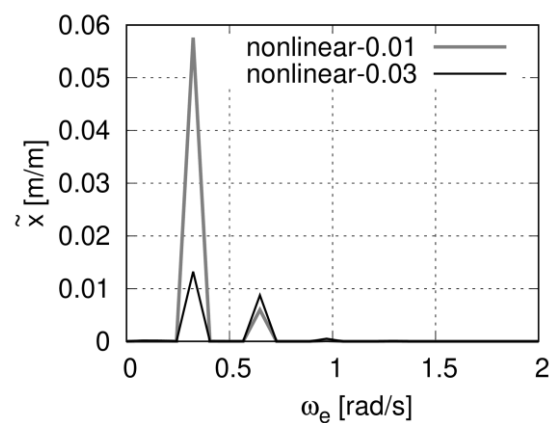


Figure 115: Comparative normalized amplitude spectra of the surge motion for the Containership A at $Fn = 0.139$ in waves of $\lambda/L_{pp} = 0.633$ and at wave encounter angle of 30deg for wave steepness $h = 0.01$ and $h = 0.03$.

To get a better understanding of the effect of the wave steepness on a wider range of ratios of λ/L_{pp} , Figure 116 plots normalized first harmonic amplitudes of surge (\tilde{x}), sway (\tilde{y}), heave (\tilde{z}), roll ($\tilde{\varphi}$), pitch ($\tilde{\theta}$), and yaw ($\tilde{\psi}$) amplitudes against wave length to ship length ratio, λ/L_{pp} , for a wave encounter angle of 30 degrees. Symbols “nonlinear-0.01”, “nonlinear-0.02”, and “nonlinear-0.03” identify results from the new numerical method in waves of steepness $h = 0.01, 0.02, \text{ and } 0.03$, respectively. Symbol “linear frq.” represents results from the frequency domain boundary element method. It can be seen that time-domain results from the new numerical method of surge, sway and heave motions in waves with smallest steepness (nonlinear-0.01) are almost identical to the frequency domain results (linear frq.). Normalized roll and pitch amplitudes from nonlinear-0.01 and linear frq. differ slightly. Normalized yaw amplitudes from the new numerical method and the linear frequency domain solver agreed well in short waves. However, in longer waves the deviations are more pronounced. The frequency domain method underestimated the yaw amplitudes, which was also shown for a smaller forward speed of $F_n = 0.0523$ see Figure 89.

Generally, it can be seen that surge, heave, roll and pitch motions were influenced considerably by the wave steepness and that the normalized first harmonic motion amplitudes reduced with increasing wave steepness in all cases. The strongest relative changes were shown for surge, roll and pitch motions at $\lambda/L_{pp} = 0.633$, where the roll natural frequency was close to the wave encounter frequency. The sway amplitude was influenced only for $\lambda/L_{pp} \approx 0.5$. and the yaw amplitudes was nearly not affected by the wave steepness. For all motions, except the yaw motions, the nonlinear time domain solution seemed to converge to the frequency domain solution when the wave steepness is reduced. This behavior was not confirmed for the yaw motion. The wave steepness seemed to have almost no effect on the normalized first harmonic yaw amplitude. However, the result of the nonlinear time domain method and the frequency domain method still differ. The frequency domain method underestimated the response in longer waves, which was also be found in the previous validation study, see Figure 88 and Figure 89. An explanation for the underestimation of the frequency domain solver was not found.

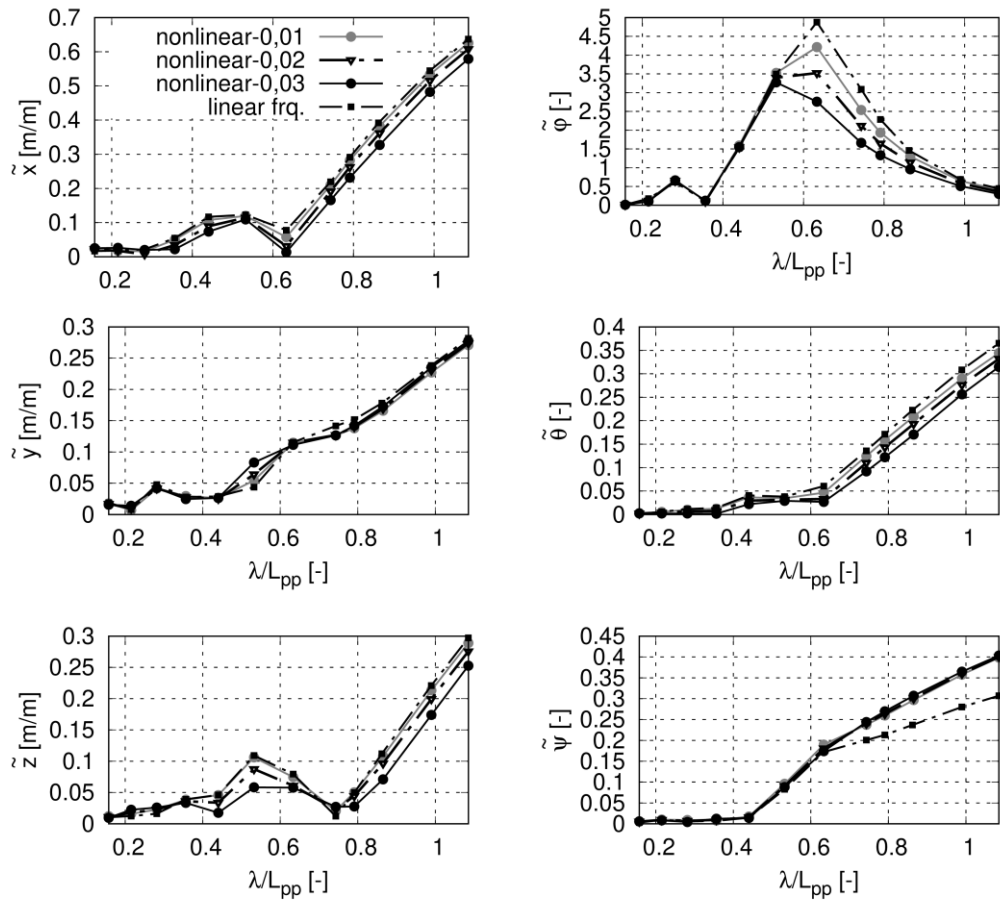


Figure 116: Computed normalized first harmonic amplitudes of surge, sway, heave (top), roll, pitch, and yaw (bottom) for a forward speed according $Fn = 0.139$ and a wave heading of 30deg.

5.2 Forward Speed and Wave Steepness Effects on Sectional Loads in Head Waves

Recall that some of the major novelties of the new numerical method are the consideration of the fully nonlinear stationary forward speed solution and the consideration of geometric nonlinearities due to the changing wetted surface. Forward speed influences the time average position due to dynamic trim and sinkage and the time average wetted surface due to the stationary wave system. As a result, stationary forward speed influences wave-induced forces and consequently wave induced rigid body motions and elastic deformation. In section 4.5.2.1 the vertical bending moment in head waves was

analyzed for two different velocities according to $Fn = 0.1349$ and $Fn = 0.198$. Experimental results of the wet natural frequency of the two-node vertical bending mode (3.38rad/s) was only performed at zero speed. However, Figure 102 showed an amplitude spectrum of the vertical bending moment at forward speed according to $Fn = 0.198$. The amplitude spectrum showed a response amplitude at 3.315rad/s, which was most likely the wet natural two-node vertical bending frequency. Comparing the natural frequency for zero speed with the natural frequency at $Fn = 0.198$ indicates that the natural frequency reduces with increasing forward speed. To investigate this behavior more systematically, the effect of forward speed on the wet natural frequency of vertical bending modes is analyzed in section 5.2.1.

The validation of wave-induced sectional loads in section 4.5.2 was performed in waves of varying wave steepness. The results revealed that the wave steepness may affect normalized sectional loads and higher order vibrations significantly. To investigate the effect of the wave steepness on normalized sectional loads, the wave steepness was varied systematically. The corresponding results are discussed in section 5.2.2. To further analyze the effect of the fully nonlinear stationary forward speed solution on wave-induced sectional loads, the computations were made based on a double body approach and on solving the fully nonlinear stationary forward speed problem.

The numerical simulation in the section 5.2.1. and 5.2.2 were performed for the containership B equipped with the backbone according to section 3.4.1.

5.2.1 Forward Speed Effect on Wet Natural Frequencies

To investigate the effect of different forward speeds on wet natural frequencies, constant ship speeds of 0, 10, 15, 22, and 30kn were analysed. Figure 117 shows the nonlinearly computed free surface elevations of the resulting stationary wave systems determined for the four nonzero ship speeds. (The associated Froude number, Fn , is listed.) The upper diagram refers to the lowest speed of 10kn; the other three diagrams, to the ship speeds of 15, 22, and 30kn, respectively. Table 26 lists the resulting dynamic trim and sinkage and the negative maxima, ζ_{min} , and positive maxima, ζ_{max} , wave elevations computed with the nonlinear stationary forward speed flow solver. Maximum negative wave elevation occurred always near the ship's transom and maximum positive wave elevation always near the ship's bow. Generally, the maximum wave elevation increased with increasing forward speed. An exception was the maximum negative wave elevation at 10kn forward speed, where the maximum negative wave elevation was already relatively large.

Comparative dynamic trim was small for all considered ship speeds; however, sinkage increased strongly with increasing forward speed. The larger free surface elevations near bow and transom and the accompanying greater sinkages led to assume that, at higher ship speeds, hydrodynamic added masses increased and, consequently, natural frequencies decreased.

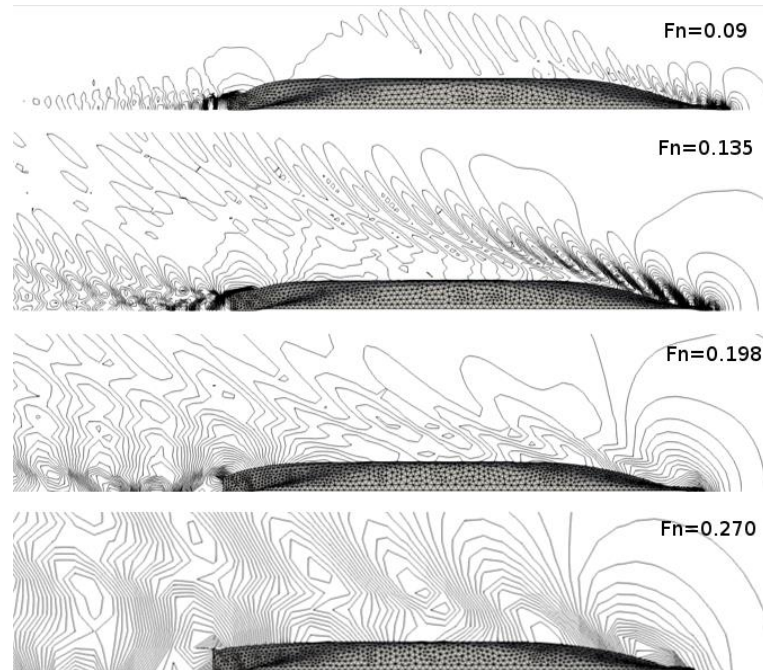


Figure 117: Free surface elevations of the stationary wave systems for the ship at speeds of 10, 15, 22, and 30kn

Table 26: Dynamic trim, sinkage, and maxima of free surface wave elevation at bow and transom for ship speeds of 10, 15, 22, and 30kn

Speed [kn]	F_n [-]	Trim [°]	Sinkage [m]	ζ_{min}^0 [m]	ζ_{max}^0 [m]
0.0	0.000	0.0	0.0	0.0	0.0
10	0.090	0.00228	-0.0546	-0.587	1.024
15	0.135	0.0179	-0.120	-0.513	1.572
22	0.198	0.0572	-0.270	-0.916	1.720
30	0.270	0.104	-0.552	-1.917	3.000

For these five different forward speeds, Figure 118 plots two-node vertical bending wet natural frequencies (left) and three-node vertical bending wet natural frequencies (right). Furthermore, Figure 118 compares results of the time domain solver based on the nonlinear stationary forward speed solution with results based on a double body solution without the stationary wave system and without accounting for dynamic trim and sinkage. The wet natural frequency of combined torsional-horizontal bending modes was not

analysed. Due to the significantly lower hydrodynamic added mass of torsional deflection, it is assumed that the effect of forward speed on torsional natural frequencies is less pronounced.

The natural frequencies were based on a computed time domain decay test. In Figure 118, dashed lines connect the steady double body results (DB); solid lines, the nonlinear (nonlinear) results. It is seen that the double body stationary solution yielded natural frequencies that changed only minimally with ship speed. Especially the two-node bending natural frequencies remained almost constant, whereas the nonlinear forward speed time domain solver obtained significantly reduced frequencies as ship speed increased. This demonstrated the importance of considering the nonlinear stationary forward speed solution when computing resonant vibrations.

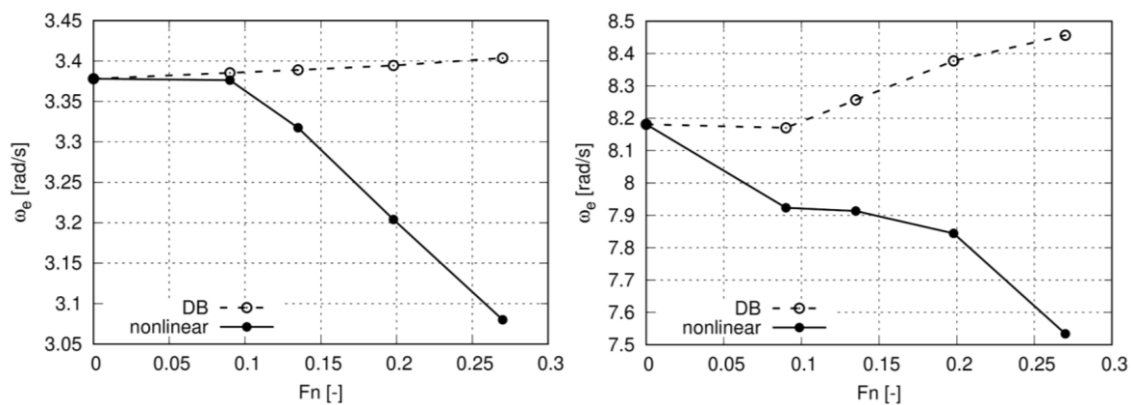


Figure 118: Comparative two-node (left) and three-node (right) vertical bending natural frequencies obtained from the double body (DB) and the nonlinear (nonlinear) forward speed solution method

5.2.2 Effect of Wave Steepness on Sectional Loads

The effect of the wave steepness on sectional loads was investigated for the Containership B advancing at two different forward speeds according to 15kn ($Fn = 0.135$) and 22kn ($Fn = 0.198$) in head waves. The wave steepness was varied according to $h = 0.1$ and 0.2 .

5.2.2.1 Results for 15kn of Forward Speed

Figure 119. compares the resulting normalized midship vertical bending moments of the Containership B at 15kn of forward speed in head waves. The vertical bending moments were normalized with the wave amplitude. Dashed lines identify results

obtained for a wave of steepness 0.01; continuous lines with points, results obtained for a wave of steepness of 0.02. “DB” denotes results based on the forward speed double body solution and “SW” denotes results based on the fully nonlinear stationary forward speed solution. The upper left plot compares first harmonic amplitudes, the upper right second harmonic amplitudes, the lower left plot third harmonic amplitudes and the lower right plot fourth harmonic amplitudes of the normalized midship vertical bending moment.

Resulting normalized first harmonic amplitudes of the vertical bending moment were congruent over a wide range of wave encounter frequencies. However, first harmonic amplitudes depended on wave steepness in long waves at $\omega_e \approx 0.600\text{rad/s}$. For a wave at $\omega_e = 0.567\text{rad/s}$, the normalized first harmonic amplitude in a wave of steepness 0.01 was approximately 10 percent smaller than in a wave of steepness 0.02. The stationary wave system did not significantly affect the first harmonic amplitude in long waves. Linear springing appeared at a wave encounter frequency of $\omega_e \approx 3.35\text{rad/s}$. It can be seen that the wave steepness had no effect on the linear springing response. However, considering the nonlinear stationary wave system, the maximum springing response appeared at a lower wave encounter frequency, and it was significantly smaller.

Second order harmonic amplitudes of the normalized vertical bending moment differed more between both approaches and the wave steepness influenced the second harmonic amplitudes significantly; steeper waves increased the normalized vertical bending moment. At $\omega_e \approx 1.6\text{rad/s}$, computations based on the stationary wave system resulted in significantly higher normalized second order springing-induced vertical bending moments. In long waves, these amplitudes were high as well. It was already discussed that this response resulted from the effect of the changing wetted surface, corresponding to the strong ship response in waves of lengths close to ship length. For a wave steepness of 0.02, the free surface almost reached the deck when the bow encountered a wave crest. The associated pressure distribution seemed to be influenced by the stationary wave system, resulting in smaller second harmonic amplitudes when the double body stationary solution was applied. Third order springing occurred at $\omega_e \approx 1.1\text{rad/s}$, whereby the double body solution yielded a higher springing-induced normalized vertical bending moment amplitude. In long waves, high frequency vibrations were again more pronounced when the nonlinear stationary wave system was solved. The fourth order harmonic amplitudes showed a similar behavior. Fourth order springing appeared at $\omega_e \approx 0.83\text{rad/s}$, and additional vibrations occurred in long waves.

5.2 Forward Speed and Wave Steepness Effects on Sectional Loads in Head Waves

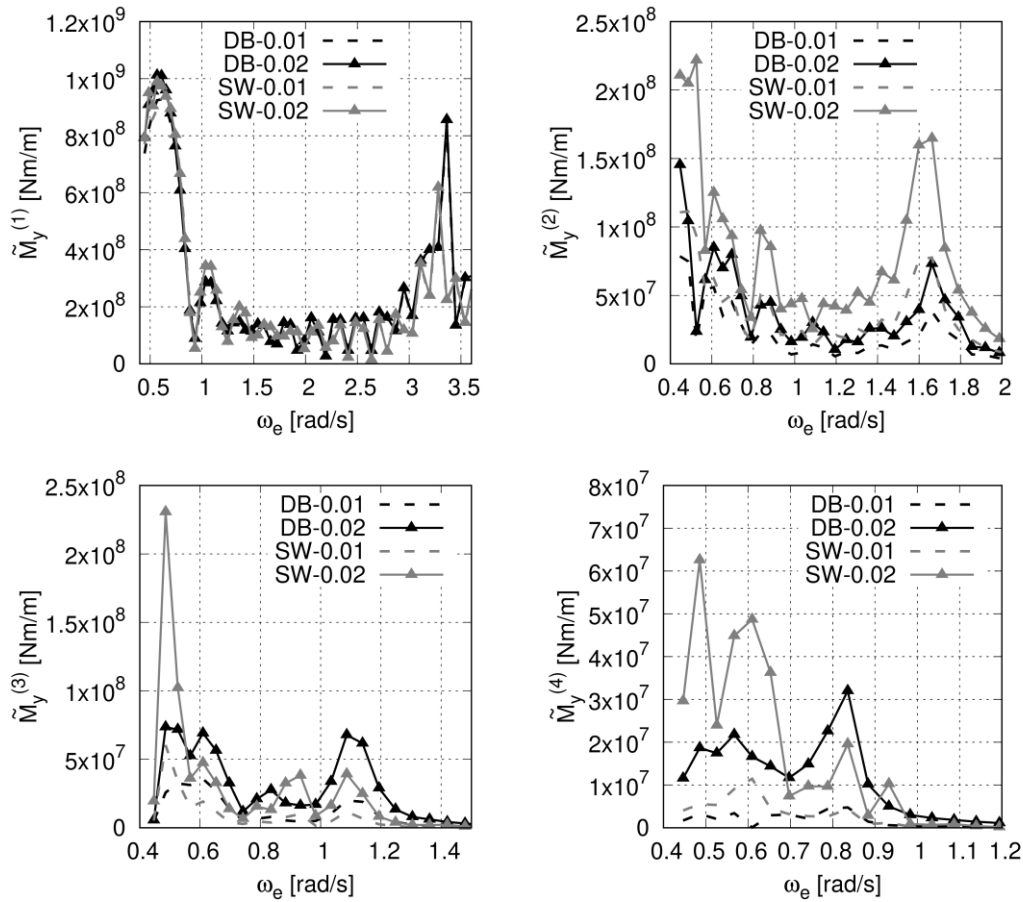


Figure 119: Comparisons of the normalized first ($\tilde{M}_y^{(1)}$), second ($\tilde{M}_y^{(2)}$), third ($\tilde{M}_y^{(3)}$), and fourth ($\tilde{M}_y^{(4)}$) harmonic amplitudes of the vertical bending moment in head waves for a wave steepness of 0.01 and 0.02 at 15kn of forward speed. The stationary forward speed solutions was based on double body free surface boundary condition (DB-0.01 and DB-0.02) and on the fully nonlinear free surface boundary conditions (SW-0.01 and SW-0.02).

It was shown that accounting for the stationary wave system affects higher order wave-induced vertical bending moments and that it has almost no effect on the first harmonic amplitudes of the vertical bending moment. Except for the linear springing vibrations. Figure 120 (left) plots the normalized modal hydrodynamic force of the two-node vertical bending mode against wave encounter frequency, obtained by solving the fully nonlinear stationary wave system and the double body flow. The maximum first harmonic amplitude occurred at $\omega_e \approx 0.6 \text{ rad/s}$, where the wave length was similar to the ship length. With increasing wave encounter frequency, additional local maxima occurred, which might have depended also on the wave length to ship length ratio. The right plot in Figure 120 zooms in the normalized modal hydrodynamic force at encounter frequencies of $3.0 \leq \omega_e \leq 3.6 \text{ rad/s}$, where linear springing occurred. First, it can be seen that the wave-induced hydrodynamic force for linear springing is only about 5 percent of the maximum wave-

induced force, but it induced a significant vertical bending vibration. Second, local maxima and minima are still present even in such short waves. Furthermore, the effect of such local maxima and minima can be seen in the linear springing amplitude of the first harmonic response in Figure 119, demonstrating that the linear springing amplitude can differ significantly due to a small change of the wet natural frequency of the hull. Recall that maxima and minima of the hydrodynamic force varied considerably near the natural frequency. Thus, it was crucial to compute wet natural frequencies accurately. Figure 121, showing plots of the normalized second, third, and fourth harmonic hydrodynamic force amplitudes against wave encounter frequency, illustrates that the RAOs were affected also by local maxima and minima. However, higher harmonic amplitudes of the wave-induced hydrodynamic force were slightly less affected.

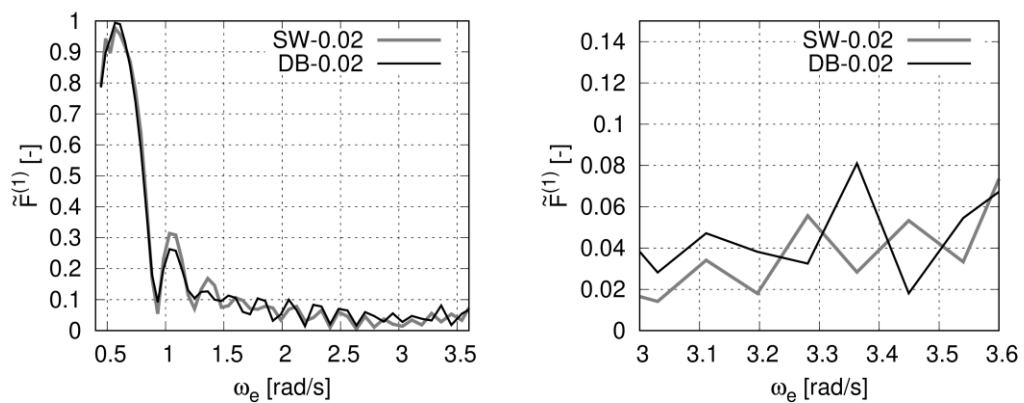


Figure 120: Comparisons of normalized first harmonic amplitudes of the wave-induced modal hydrodynamic force of the two-node vertical bending mode at 15kn of forward speed, considering the fully nonlinear stationary forward speed solution (SW-0.02) and the stationary forward speed solution due to double body free surface boundary condition (DB-0.02)

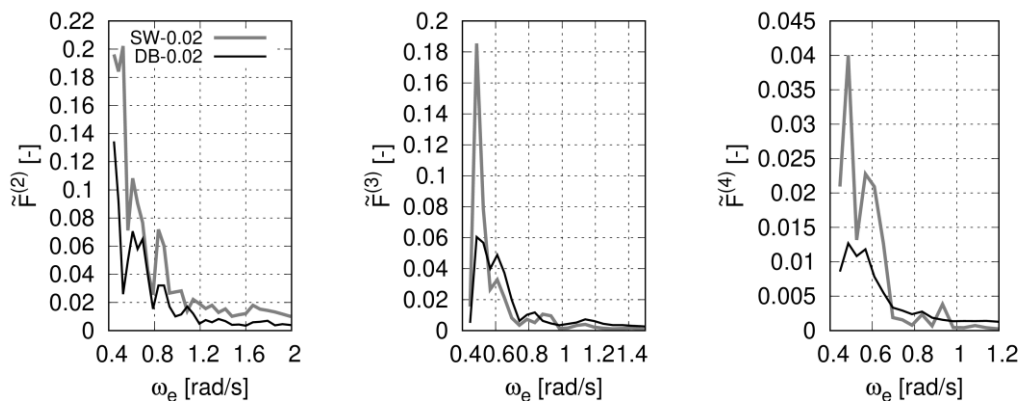


Figure 121: Comparisons of normalized second, third and fourth harmonic amplitudes of the wave-induced modal hydrodynamic force of the two-node vertical bending mode at 15kn of forward speed, considering the fully nonlinear stationary forward speed solution (SW-0.02) and the stationary forward speed solution due to double body free surface boundary condition (DB-0.02)

5.2.2.2 Results for 22kn of Forward Speed

Figure 122 compares first, second, third, and fourth harmonic amplitudes of the midship vertical bending moments, normalized with the wave amplitude, demonstrating the effect of the wave steepness at 22kn forward speed. This figure depicts comparative results obtained by solving the fully nonlinear stationary forward speed case (SW-0.01 and SW-0.02) and results based on the stationary double body solution (DB-0.01 and DB-0.02). Here, SW-0.01 and DB-0.01 denote results for the wave steepness of 0.01; SW-0.02 and DB-0.02, results for the wave steepness of 0.02. Similar to the results at 15kn, first harmonic amplitudes at 22kn depended on wave steepness only in long waves although in steeper waves, the normalized vertical bending moments increased. Furthermore, in long waves, first harmonic amplitudes obtained by solving the fully nonlinear stationary wave system only minimally differed from results based on the stationary double body solution. However, the linear springing response in short waves (at $\omega_e \approx 3.35 \text{ rad/s}$) differed between both methods. Linear springing occurred in slightly longer waves when solving for the nonlinear stationary wave system because the steady wave system reduced the natural frequency.

Figure 123 plots the two-node vertical bending modal wave-induced hydrodynamic force, normalized against the wave amplitude and maximum hydrodynamic force amplitude. For the first harmonic amplitude of the hydrodynamic force it can be seen that,

at $\omega_e \approx 3.5 \text{ rad/s}$, results based on solving the fully nonlinear stationary wave system differed from results based on the stationary double body solution. Most likely this caused the linear springing-induced vertical bending moments to differ.

The higher order harmonic amplitudes of the vertical bending moment plotted in Figure 122 demonstrate that both methods caused second, third, and fourth order springing amplitudes to always increase with increasing wave steepness. Sometimes the springing-induced vertical bending moment differed significantly, depending whether the nonlinear stationary wave system was considered or not.

The corresponding plots of the modal hydrodynamic force presented in Figure 123 show that the differences in the vertical bending moments resulted from the wave-induced hydrodynamic forces. Furthermore, at lower wave encounter frequencies, the nonlinear stationary wave system initiated significant higher order hydrodynamic forces that caused high frequency vibrations of the vertical bending moment. These high frequency vibrations were more dominant when the nonlinear stationary wave system was considered, especially in steeper waves.

Comparing results for the ship at 15kn in Figure 119 with results for the ship at 22kn in Figure 122, it can be concluded that first harmonic amplitudes of the vertical bending moment did not change significantly in long waves, i.e., in waves at $\omega_e \leq 2.0 \text{ rad/s}$. As seen, at higher forward speeds, the first harmonic amplitude of the vertical bending moment increased minimally. However, in shorter waves, the linear springing response was clearly affected by the ship's forward speed. The region of resonant vibrations was wider, and the vibration amplitudes were higher at 22kn forward speed. Furthermore, higher order wave-induced vibrations were significantly larger at higher forward speeds.

5.2 Forward Speed and Wave Steepness Effects on Sectional Loads in Head Waves

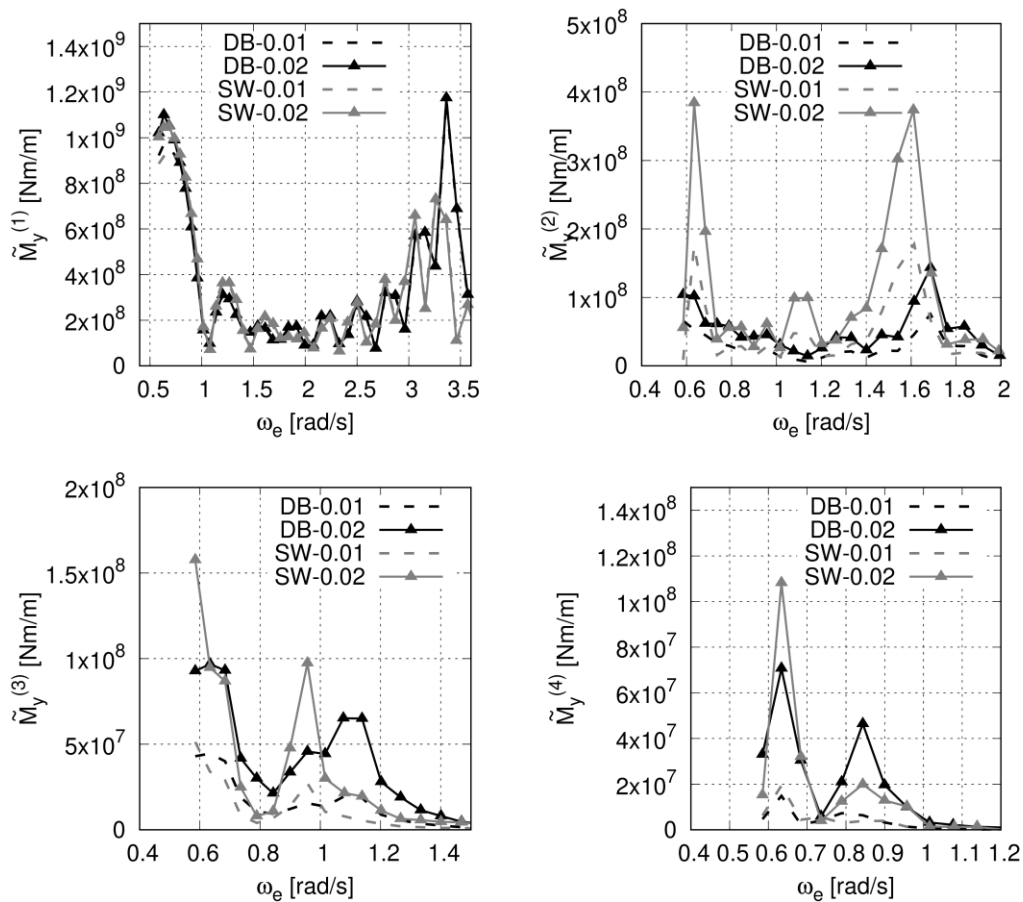


Figure 122: : Comparisons of the normalized first ($\tilde{M}_y^{(1)}$), second ($\tilde{M}_y^{(2)}$), third ($\tilde{M}_y^{(3)}$), and fourth ($\tilde{M}_y^{(4)}$) harmonic amplitudes of the vertical bending moment for head waves with steepness of 0.01 and 0.02 at 22kn of forward speed. The stationary forward speed solutions were based on double body free surface boundary condition (DB-0.01 and DB-0.02) and on the fully nonlinear free surface boundary conditions (SW-0.01 and SW-0.02).

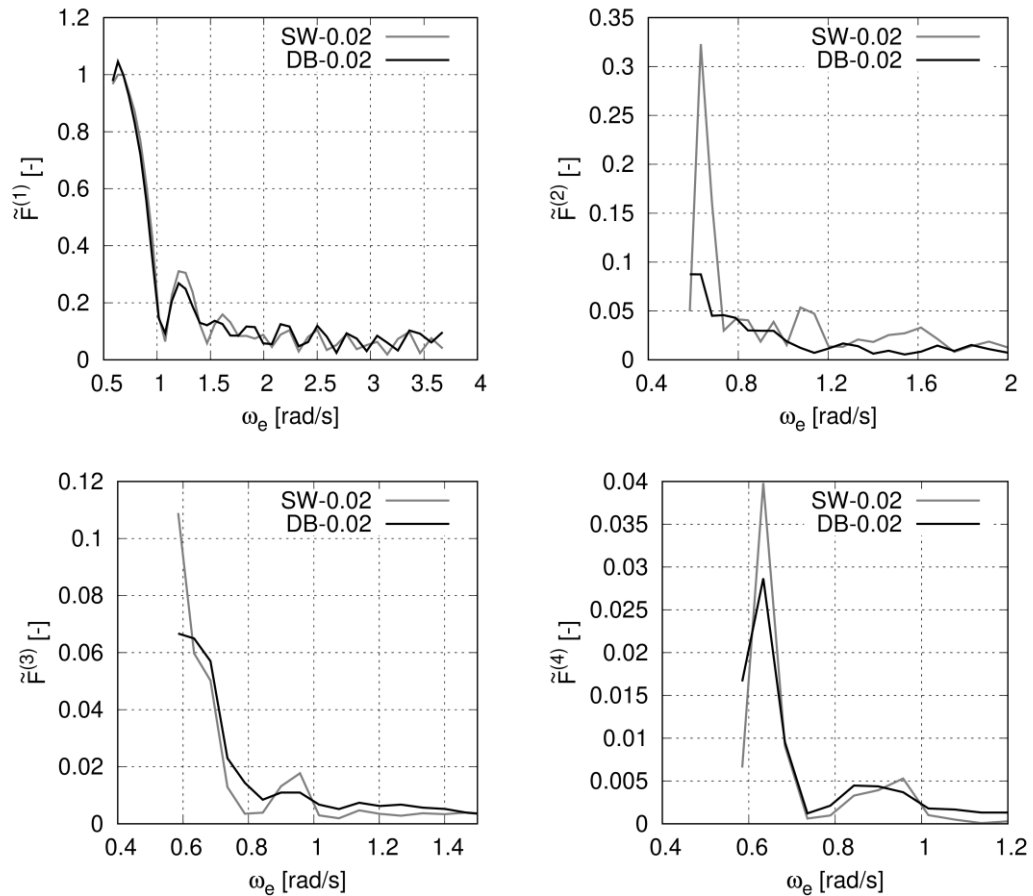


Figure 123: Normalized first, second, third and fourth harmonic amplitudes of the wave-induced modal hydrodynamic force of the two-node vertical bending mode for head waves with a steepness of 0.02 at 22kn of forward speed.

5.3 Hydroelastic Response via Realistic Full-Scale Stiffness Properties

The above elastic computations relied on the cross-sectional properties of a backbone to idealize the hull stiffness of the numerical model and comparative model tests. The validation study demonstrated that the numerical method predicted results that compared favourably to model test measurements of midship torsional moments, midship vertical bending moments and midship horizontal bending moments. However, this standard experimental technique (backbone model) did not correctly idealize stiffness properties of the full-scale ship because the shear center of the backbone was not modeled correctly. To overcome this drawback and, thus, to more accurately investigate also the

hydroelastic behaviour of a full-scale ship, mass and stiffness properties of the subject Containership B were idealised using detailed realistic sectional properties. These properties were already documented above (Section 3.4.2).

Specifically, midship sectional moments for the Containership B at constant 15kn forward speed in oblique waves at heading angles of 150 and 120deg were analysed. Fourier transformations of the simulated time series were performed to compute the first, second, third, and fourth harmonic amplitudes. The wave steepness was systematically varied according $h = 0.01$, 0.02 and 0.03. The simulations were performed with 2% of the critical damping for vertical bending vibrations and 4% of the critical damping for coupled torsional-horizontal-bending vibrations.

The purpose of this study was to demonstrate the effect of using more realistic full-scale ship-related cross sections instead of the backbone to idealize the ship's hull stiffness.

5.3.1 Mid Ship Torsional Moments in Waves at 150deg and 120deg Encounter Angle

Figure 124 and Figure 125 plot the resulting normalized midship torsional moment amplitudes, \tilde{M}_x , normalized against wave amplitude for a wave encounter angle of 150deg and 120deg, respectively. A Fourier transformation of every time series obtained the associated first ($\tilde{M}_x^{(1)}$) , second ($\tilde{M}_x^{(2)}$) , third ($\tilde{M}_x^{(3)}$) , and fourth harmonic ($\tilde{M}_x^{(4)}$) amplitudes. In these figures, the upper left graph plots comparative first harmonic amplitudes; the upper right graph, second harmonic amplitudes; the lower left graph, third harmonic amplitudes; the lower right graph, fourth harmonic amplitudes. Symbols “nonlinear 0.01”, “nonlinear 0.02” and “nonlinear 0.03” identify the numerically computed results obtained for the ship with realistic full-scale stiffness properties in waves with steepnesses of 0.01, 0.02 and 0.03, respectively. Usually, it is assumed that the first harmonic amplitudes do not significantly depend on the structural properties of the ship. Often, the rigid-body behavior of the ship is used to estimate first harmonic amplitudes of the sectional loads. It will be shown that this assumptions in not true, especially for the torsional moment. Therefore, numerical and experimental results of the validation study were included in the plots of first harmonic amplitudes. Recall that the validation study considered the backbone stiffness instead of realistic full-scale stiffness. Symbol “nonlinear BB” identifies numerical results and symbol “EXP BB” experimental results for the ship with backbone properties.

The maximum first harmonic amplitude of the torsional moment for both wave encounter angles occurred at $\omega_e \approx 2.15\text{rad/s}$, indicating linear springing. Furthermore, the first harmonic amplitudes seemed not to depend on the wave steepness. However, results of realistic full-scale stiffness properties and backbone stiffness properties differed, especially for a wave encounter angle of 120deg, see Figure 125. The responses based on the realistic hull idealization were significantly higher than those based on the backbone model. This phenomenon was due to the location of the shear center. For the backbone stiffness model, the shear center was located 1.37m below the keel, whereas for the ship under realistic full-scale stiffness properties the shear center was located 12.23m below the keel. Consequently, computed excitation moments and inertial properties differed strongly and caused significant differences for the torsional moment.

The second harmonic amplitudes were approximately ten times smaller than the first harmonic amplitudes. Second order springing of the one-node torsion-horizontal-bending mode occurred at $\omega_e \approx 1.05\text{rad/s}$. Second order springing of the two-node torsional-horizontal-bending mode was not found. However, it was already discussed that the two-node torsional-horizontal-bending mode initiated only a small torsional moment at the mainframe of the subjected container ship. Third harmonic amplitudes identified a clear third order springing response at $\omega_e \approx 0.72\text{rad/s}$. However, third harmonic amplitudes were relatively small compared to first harmonic amplitudes. The fourth harmonic amplitudes showed an increase of the response in short waves at $\omega_e \approx 0.5\text{rad/s}$, which was associated with fourth order springing. In general, all higher order harmonic amplitudes depended strongly on wave steepness; that is, higher wave steepness resulted in larger amplitudes.

Comparing torsional moments for the different wave encounter angles, the computed maximum torsional moment was about 65% higher at wave heading of 120deg than at a wave heading angle of 150deg.

5.3 Hydroelastic Response via Realistic Full-Scale Stiffness Properties

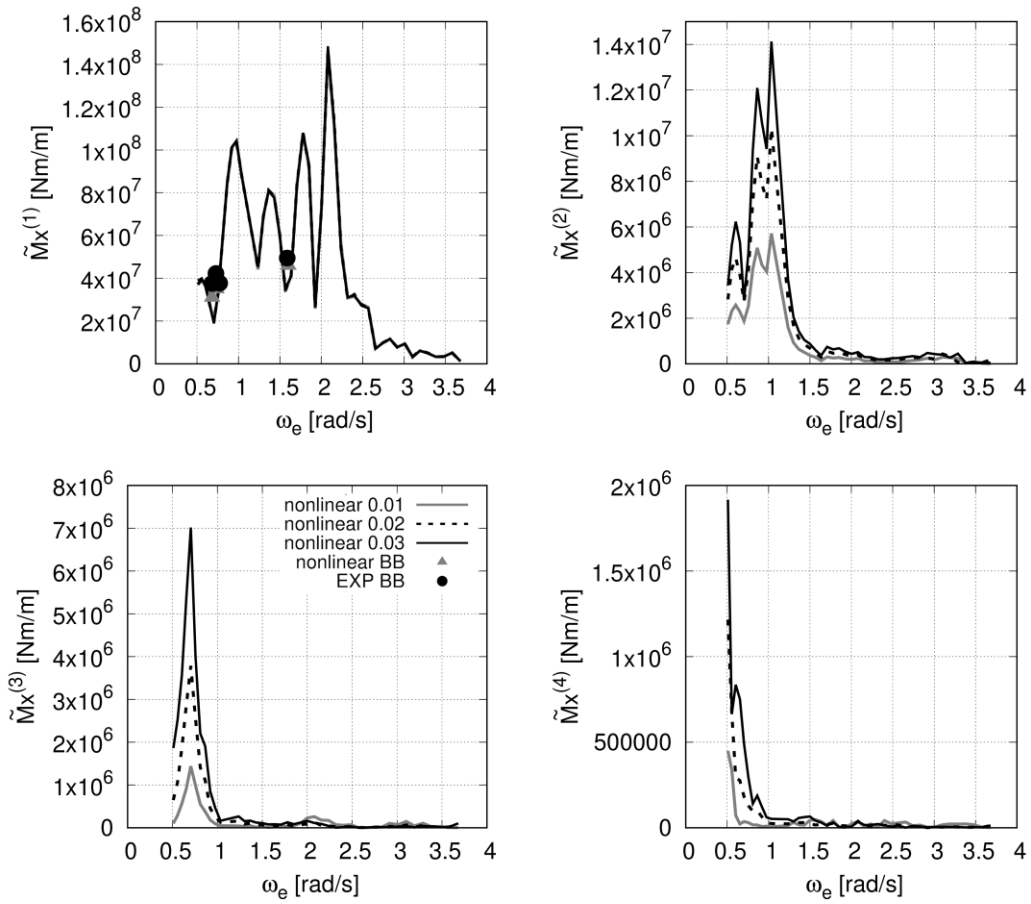


Figure 124: Normalized torsional moments for the Containership B, its hull idealized with realistic full-scale stiffness properties, in regular waves at 150deg encounter angle.

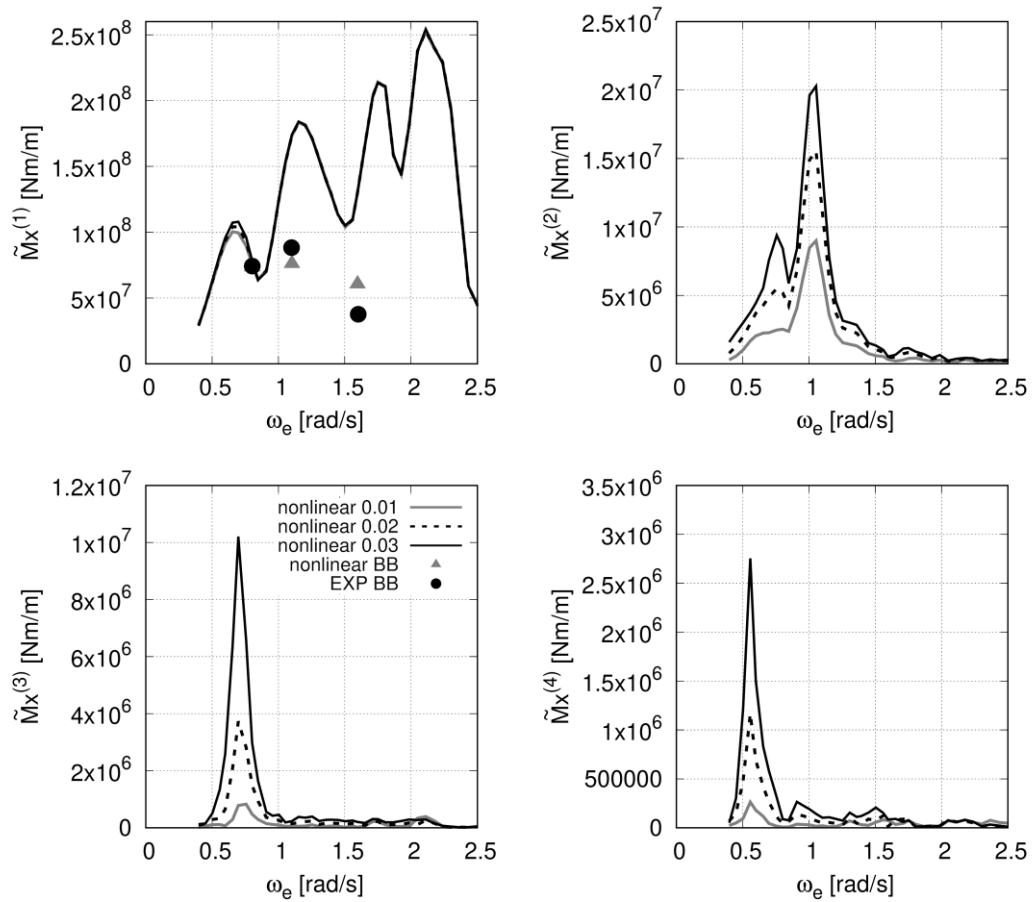


Figure 125: Normalized torsional moments for the Containership B, its hull idealized with realistic full-scale stiffness properties, in regular waves at 120deg heading

5.3.2 Mid Ship Bending Moments in Waves at 150deg and 120deg Encounter Angle

Figure 126 and Figure 127 plot normalized amplitudes of the midship vertical bending moment, \tilde{M}_y , for a wave encounter angle of 150deg and 120deg. Computed first-harmonic amplitudes for a wave encounter angle of 150deg showed a maximum response at $\omega_e = 0.68\text{rad/s}$ and for a wave encounter angle of 120deg at $\omega_e = 0.95\text{ rad/s}$. Furthermore, for a wave encounter angle of 150deg linear springing occurred at $\omega_e \approx 3.35\text{rad/s}$. It was not possible to simulate linear springing for a wave encounter angle of 120deg, because the associated wave length was small, requiring significant refinements of the free surface grid for the computation of diffraction forces. However, vertical bending moments were less critical in waves at 120deg heading compared to those in waves at 150deg heading,

approximately 35% smaller. For both wave encounter angles the first harmonic amplitude depended only slightly on the wave steepness in very long and short waves. However, comparative results computed with realistic full-scale stiffness and backbone stiffness indicated again that also the first harmonic amplitudes depended on the structural properties for some wave cases. However, the differences resulted also from different mass distributions and the corresponding differences of the natural mode shapes.

The second harmonic amplitudes showed two maximum response regions. Second order springing occurred at $\omega_e \approx 1.6\text{rad/s}$, i.e., at one-half of the two-node vertical bending natural frequency. Furthermore, second order harmonic amplitudes occurred in long waves, too. These vibrations were most likely caused by a strongly varying wetted hull surface due to large ship motions and the associated nonlinear effects. A similar behavior was found at third and fourth harmonic amplitudes. Third order springing was identified at $\omega_e \approx 1.1\text{rad/s}$ and additional, large third harmonic amplitudes were found in long waves. However, these third order vibrations were more pronounced for a wave encounter angle of 150deg. Fourth order springing was identified at $\omega_e \approx 0.75\text{rad/s}$ for waves of 150deg and at $\omega_e \approx 0.85$ for waves of 120deg. However, fourth harmonic amplitudes were small compared to first harmonic amplitudes.

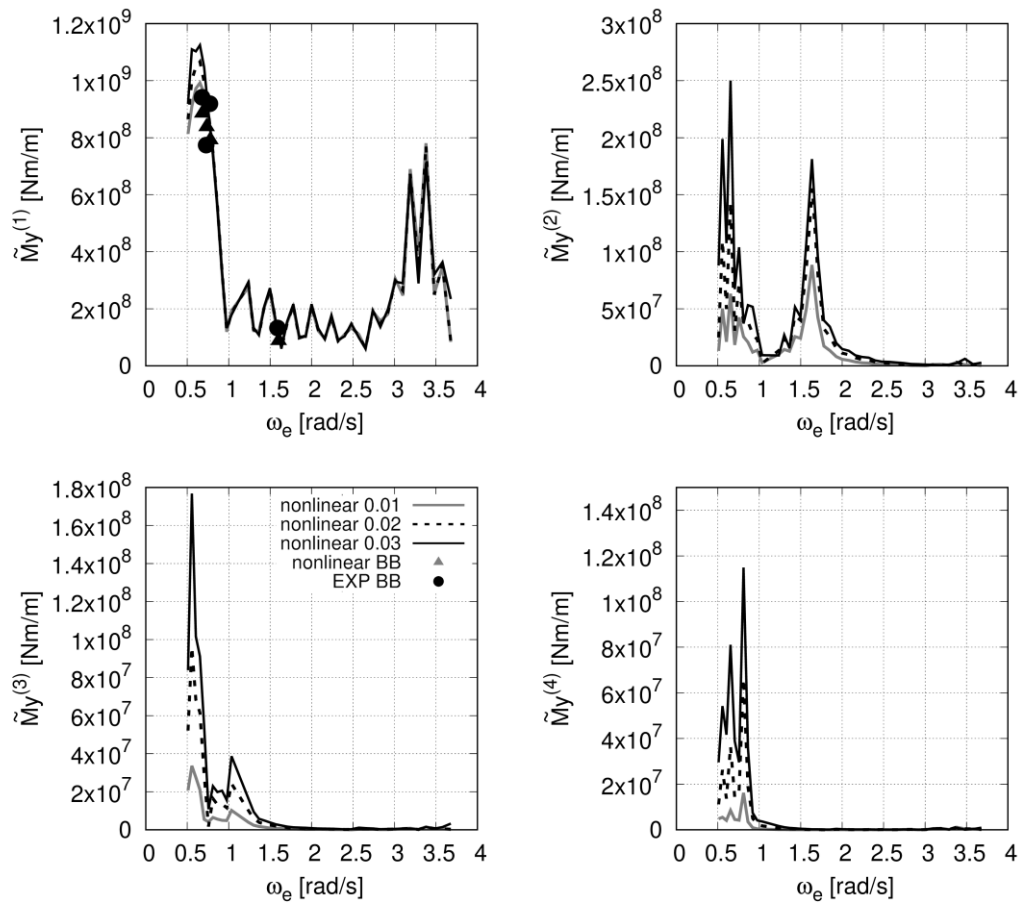


Figure 126: Normalized amplitudes of the vertical the bending moment for the Containership B, its hull idealized with realistic full-scale stiffness properties, in regular waves at 150deg heading

5.3 Hydroelastic Response via Realistic Full-Scale Stiffness Properties

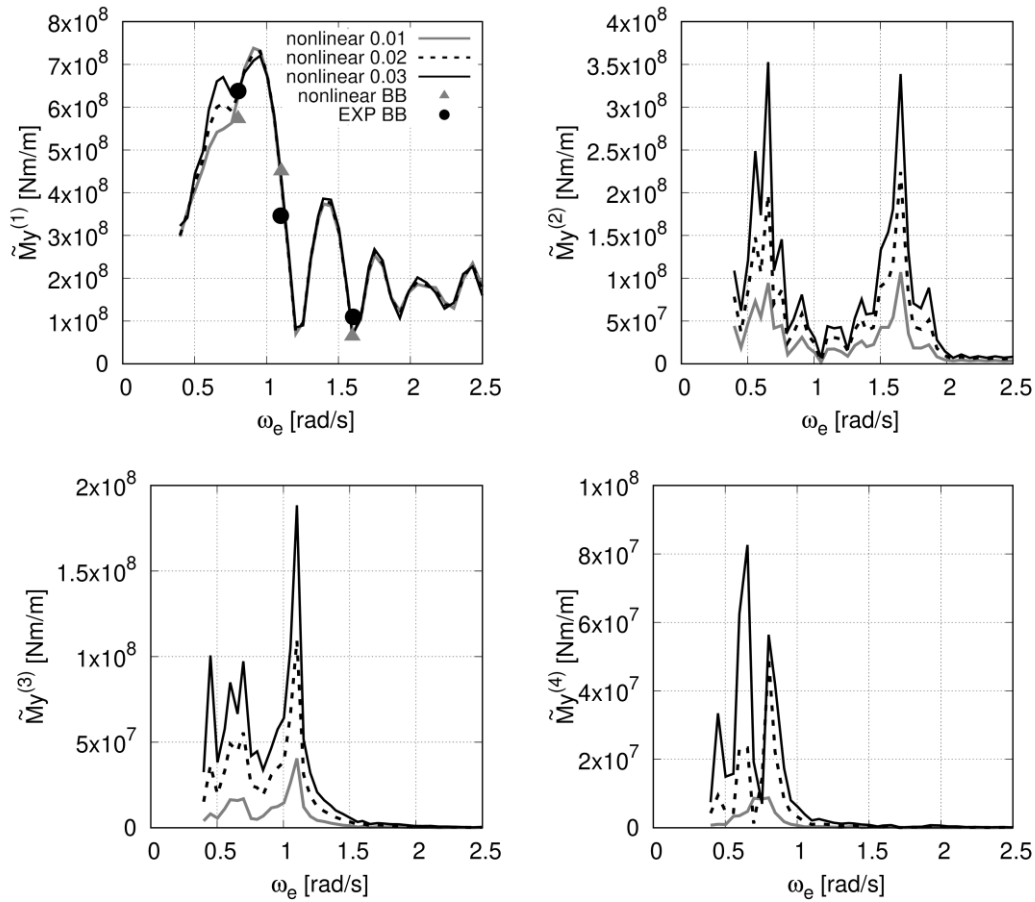


Figure 127: Normalized amplitudes of the vertical bending moment for the Containership B, its hull idealized with realistic full-scale stiffness properties, in regular waves at 120deg heading

Figure 128 and Figure 129 plot normalized amplitudes of midship horizontal bending moment, \tilde{M}_z . The first harmonic amplitudes for a wave encounter angle of 150deg in Figure 128 showed three peaks. The first peak at $\omega_e \approx 0.68$ rad/s was caused by the strong response of the ship in waves with a similar wave length as the ship length. The second peak at $\omega_e = 2.15$ rad/s was identified as linear springing of the one-node torsion-horizontal-bending mode. The third peak was linear springing of the two-node torsion-horizontal-bending mode. Similar to the first harmonic amplitudes, the second harmonic amplitudes showed three peaks, as well. Again, the first peak at $\omega_e \approx 0.68$ rad/s was caused by nonlinear effects due to the changing wetted surface in long waves. The second peak at $\omega_e \approx 1.05$ rad/s identified second order springing of the one-node torsion-horizontal-bending mode, and the third peak at $\omega_e \approx 1.75$ rad/s identified second order springing of the two-node torsion-horizontal-bending mode. The first and second harmonic amplitudes due to waves of 120deg showed a similar trend. However, linear

springing of the two-node torsion-horizontal-bending mode could not be seen because only waves up to a wave encounter frequency of 2.5rad/s were simulated.

For both wave encounter angles, third harmonic amplitudes identified third order springing of the one-node torsion-horizontal-bending mode at $\omega_e \approx 0.7\text{rad/s}$ of the two-node torsion-horizontal-bending mode at $\omega_e \approx 1.1\text{rad/s}$. At fourth harmonic amplitudes, fourth order springing of the one-node torsion-horizontal-bending mode occurred at $\omega_e \approx 0.6\text{rad/s}$, and two-node torsion-horizontal-bending occurred at $\omega_e \approx 0.85\text{rad/s}$. However, fourth harmonic amplitudes were small compared to first harmonic amplitudes. In general, the response amplitudes in waves of 120deg heading were approximately twice as large than in waves of 150deg.

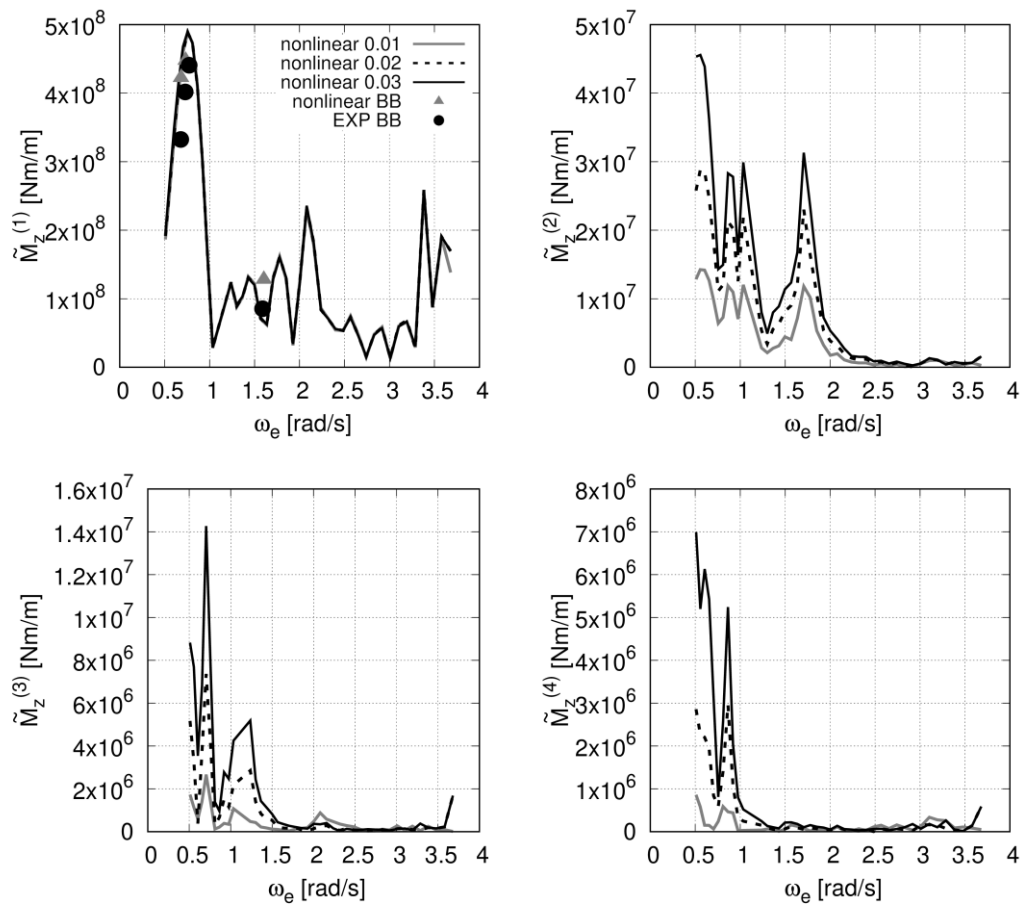


Figure 128: Normalized amplitudes of horizontal bending moments for the Containership B, its hull idealized with realistic full-scale stiffness properties, in regular waves at 150deg heading

5.3 Hydroelastic Response via Realistic Full-Scale Stiffness Properties

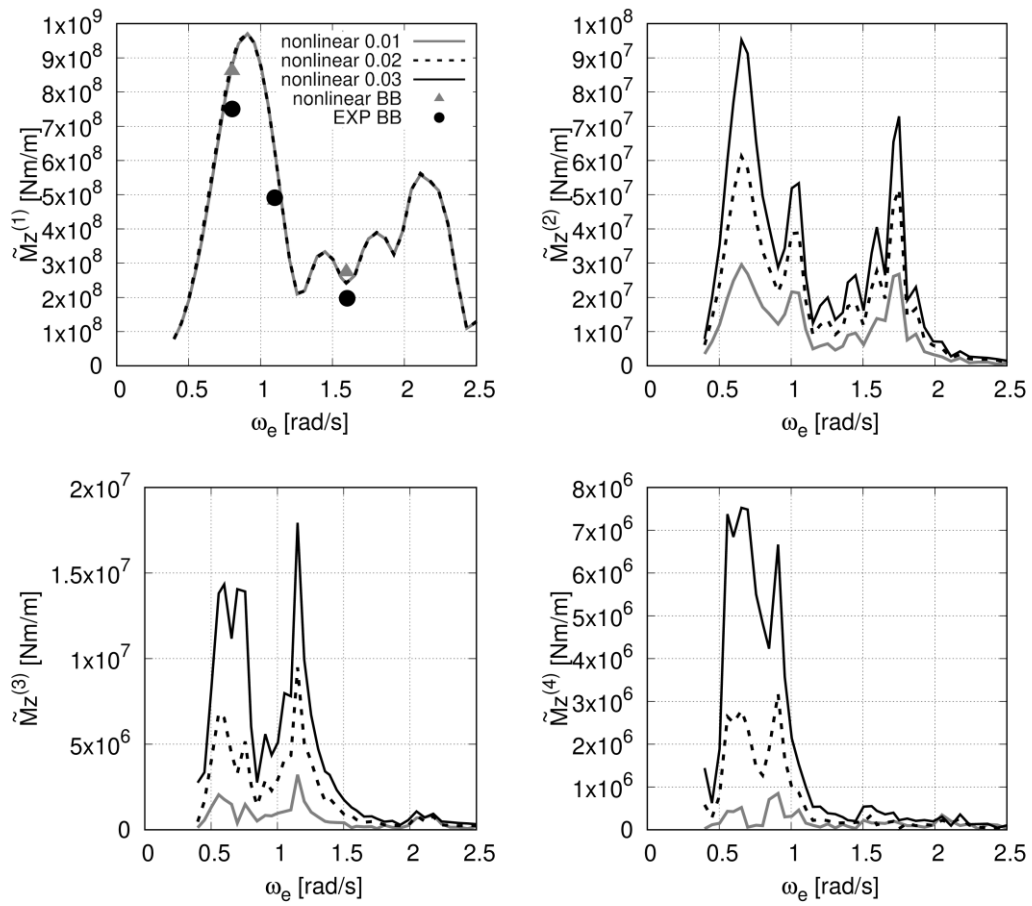


Figure 129: Normalized amplitudes of horizontal bending moment for the containership B, with realistic full-scale stiffness properties, in regular waves at 120deg heading

6 Summary

The present work introduces a new numerical method to compute the hydroelastic response of ships in waves. The new numerical method is capable of computing periodic wave-induced forces and moments, time average wave-induced drift forces, wave-induced rigid body motions and the wave-induced elastic response (torsion as well as vertical and horizontal bending) of ships with special attention to wave-induced resonant vibrations (so-called springing). The new numerical method considers nonlinear effects that are important for the computation of the above-mentioned ship responses and is still numerically efficient. To ensure numerical efficiency, the fluid flow solver of the new numerical method is based on potential theory and a so-called weakly-nonlinear method computes wave-induced hydrodynamic forces and moments in time domain. The most dominant wave-induced nonlinearities are caused by Froude-Krylov forces and moments. Assuming an undisturbed wave, Froude-Krylov and hydrostatic forces and moments are integrated in time domain over the instantaneous wetted hull surface. Radiation and diffraction forces and moments are pre-computed in the frequency domain using a Rankine-source boundary element method and are then transferred into time domain. Radiation forces and moments are computed in time domain using a convolution integral. Diffraction forces and moments result directly from the complex force and moment amplitude of the incident wave diffraction. Consequently, radiation and diffraction forces and moments are integrated over the time average wetted surface. Their nonlinear contribution due to the changing wetted surface is considered by a waterline integral that is computed at every time instance.

Ships forward speed has a significant effect on the hydrodynamic response. For that reason, the stationary velocity potential, the stationary wave system and dynamic trim and sinkage are pre-computed using a fully-nonlinear stationary forward speed solver and coupled with the new weakly-nonlinear hydrodynamic time domain method.

The total hydroelastic response of the ship is split into the rigid body response (rigid body motion) and into the elastic response (elastic deformations). The rigid body motions are computed based on solving nonlinear rigid body motion equations. The elastic response is computed with a finite beam element approach applying the modal superpositioning technique. The new numerical method computes wave-induced torsional moments as well as vertical and horizontal bending moments. A ship structure can be categorised as a thin-walled beam consisting of open and closed cells. For such structures,

torsion induced warping effects of the ships cross section need to be considered. Furthermore, the shear center of ships cross section can be located far below the keel line. For that reason, coupling effects between bending and torsion has to be considered as well. A new beam element approach, specialized for ship structures, was developed to account for these effects. The new beam element accounts for nonuniform torsion-induced twist deformations (restrained warping), vertical and horizontal bending with a linear shear deformation (according to Timoshenko) as well as longitudinal compression. Coupling effects of torsion and bending are considered in the mass and stiffness matrix.

For the computation of the hydroelastic response, the governing equations to describe the structural and hydrodynamic properties of a vibrating ship were coupled. The newly developed weakly-nonlinear hydroelastic solver describes the hydrodynamic properties based on frequency independent coefficient matrixes. This procedure allows to compute vibrations of any frequency, not restricted to the wave encounter frequency. This is particular important for the computation of springing-induced resonant vibrations of higher order because the vibration frequency and the wave encounter frequency differ.

For the use of the modal superposition technique, the wet natural modes of the elastic ship structure need to be pre-computed. In principle, the hydrodynamic properties depend on the vibration frequency and on the mode shape. However, to ensure orthogonality of computed wet natural modes, the coefficient matrixes need to be constant. The present work introduces a new procedure to computed the wet natural modes based on estimated hydrodynamic properties. For the computation of the hydrodynamic properties, the free surface boundary conditions are substituted with a high frequency boundary conditions that is fulfilled analytical. After computing the wet natural modes, the hydrodynamic properties for each mode shape are recomputed with a linear frequency domain boundary element method and transferred into time domain to be applied in the weakly-nonlinear hydroelastic solver. The linear frequency domain boundary element solver couples the fully nonlinear stationary flow with the periodic flow of a moving and elastic vibrating ship. New free surface and body boundary conditions for the elastic vibrating hull were developed.

The new numerical method is systematically evaluated and validated by comparing results of the new method with experimental data and numerical simulations from a field method that solves the Reynolds-averaged Navier-Stokes equations (RANSE). Four different ship types, a VLCC tanker, a 220m long cruise ship, a 355m long post-Panamax containership and a 333m long post-Panamax containership are investigated. The verification and validation study begins with a time and spatial discretisation study of the

frequency domain and time domain solver. Afterwards, the application of the convolution integrals to describe the memory effects of the radiation forces is verified. The validation of the new numerical method proceeds by comparing wave-induced forces and moments on a fixed ship with RANSE based solutions, followed by comparisons of wave-induced forces and moments on a freely moving ship. The comparisons of wave-induced forces and moments comprise direct comparisons of time series as well as comparisons of the first, second, third and fourth harmonic amplitudes computed with Fourier transformations of the time series. Computed periodic wave-induced forces from the new numerical method agreed favourable to RANSE based results. In a few cases deviations of the computation of periodic wave-induced forces were found. These deviations can be associate to the changing wetted surface at the stern of the ship due to large amplitude waves. For such extreme scenarios the waterline integral, that accounted for the effect of the changing wetted surface on radiation and diffraction forces and moments, is not able to capture the changing wetted surface to the full extent. This effect is more pronounced for the fixed ship than for the moving ship. For the moving ship the hull follows the wave elevation which results in a smaller change of the wetted surface.

For the computation of wave-induced rigid body motions and elastic deformations, especially for the computations of springing-induced vibrations, the ships forward speed is an important parameter because it defines the wave encounter frequency and thus influences the wave frequencies which causes resonant vibrations. With increasing wave heights, ships can often not maintain service speed due to an increasing total resistance. The time average longitudinal wave-induced force (called wave added resistance) is one of the major contributors to the increasing total resistance. For that reason, this work focuses also on the computation of the wave added resistance. The new numerical method proves to be capable of computing the wave added resistance of the fixed and moving ship with comparable results to RANSE based simulations and experimental data and shows a clear improvement compared to results of a frequency domain solver. Especially in short waves, where potential flow-based methods usually underestimate the wave added resistance, the new numerical method shows significant improvements. However, the new numerical method still underestimates the waves added resistance in short waves. In short waves, viscous effects on the wave added resistance increase. Such effects cannot be considered by the potential flow based new numerical method. A new empirical correction of the friction induced wave added resistance was developed. The empirical correction is based on RANSE based results. This procedure improves the computation of the wave added resistance in short waves.

After the validation of wave-induced forces and moments, the wave-induced rigid body and elastic response of two container ships is validated against experimental results. It is shown that the new numerical method computes rigid body motions in steep oblique waves with a favourable agreement to the experimental data.

For the validation of the elastic response, mid ship sectional loads of a 333m long post-Panamax containership computed with the new numerical method are compared to model test result. The model is equipped with a backbone that simulates the structural properties. Computed and measured dry and wet natural frequencies showed a good agreement. First, vertical bending moments are compared for a wave encounter angle of 180deg at a forward speed of 15kn and 22kn. Afterwards, torsional moments as well as vertical and horizontal bending moments are compared in waves of 150deg and 120deg encounter angle. The new numerical method shows a favourable agreement to the experimental data and proves to be capable of computing higher order springing up to fourth order springing.

After a successful validation, the new numerical method is applied to investigate the influence of the wave steepness on rigid body motions and elastic sectional loads as well as the effect of forward speed on the two-node and three-node vertical bending natural frequencies as well as mid ship vertical bending moments. It is shown that the wave steepness has a significant effect on the rigid body motions by introducing strong nonlinear effects for a post-Panamax containership in waves of 30deg encountering angle (stern quartering). Normalized first harmonic amplitudes reduce with increasing wave steepness. Normalized higher order harmonic amplitudes increase with increasing wave steepness.

Sectional loads of a post-Panamax containership in head waves are also greatly affected by the wave steepness. To see the effect of the wave steepness, the sectional loads are divided by the wave amplitude. It is shown that the normalized first harmonic response amplitudes of the sectional loads are only minimally affected by the wave steepness in long waves. However, higher order harmonic amplitudes (up to fourth order is investigated) depend strongly on the wave steepness. This is particularly true for resonant vibrations (higher order springing). In every case, higher wave steepness causes higher normalized harmonic amplitudes.

For the investigation of forward speed effects, first computations that are based on a pre-computed stationary double-body simulation and on the fully nonlinear stationary solution including the stationary wave system and dynamic trim and sinkage are compared. Investigation of two-node and three-node vertical bending wet natural

frequencies show that, by considering the fully nonlinear stationary solution, the wet natural frequencies decrease with increasing ship speed due to the increasing hydrodynamic added mass. This behaviour does not exist when the pre-computed double body solution is applied. Furthermore, investigations of the vertical bending moment show significant differences for results based on the stationary double body solution and based on the fully nonlinear stationary solution. For the investigated scenarios, springing-induced vibrations increase with increasing forward speed. The same is true for different wave steepness. Springing induced vibrations increase with increasing wave steepness.

As aforementioned, a backbone simulated the structural properties of the elastic hull. However, a backbone cannot model the structural properties of the ship correctly. The shear center of a realistic ship can be located far below the keel line (approximately 12m for the investigated ship). Equipped with a backbone, the shear center is approximately as high as the keel line. To demonstrate the behaviour of a ship with realistic structural properties and to show that sectional loads depend on structural properties, numerical simulations of the same containership with realistic full-scale stiffness were performed. It is shown that the hull idealization affects higher order harmonic amplitudes and higher order springing. However, it also influences first harmonic amplitudes, especially those of torsional moments and horizontal bending moment. Furthermore, it is shown that with realistic structural properties, torsion and horizontal bending deformations are significantly coupled and pure torsion or pure horizontal bending do not exist. Coupled, linear, and higher order springing effects are found for the one-node and two-node torsion-horizontal-bending vibrations.

6.1 Outlook

The validation study showed stronger deviations of the wave-induced vertical force and the wave induced pitch moment between the new numerical method and a RANSE based solver for a few scenarios. It was examined that these differences occur from the effect of the changing wetted hull surface due to radiation and diffraction forces near the ship stern. As described, geometrical nonlinearities of radiation and diffraction forces are considered using a waterline integral, see section 2.2.2.4. The waterline integral estimates the changing wetted surface due to radiated and diffracted waves based on the instantaneous pressure at the time average waterline. The left side of Figure 130 illustrates this approach for a stern section of a ship. \overline{WL} is the time average free surface, d is the wave elevation due to radiated and diffracted waves and \vec{n} is the hull normal vector. As describes in

section 2.2.2.4, d is computed from the radiation and diffraction pressure at the time average waterline. The force due to the changing wetted surface is estimated assuming a linear pressure distribution $p(z)$ and that the hull normal vector below and above the time average waterline does not change. This assumption is only sufficient for moderate changes of the hull wetted surface. However, in extreme scenarios, as simulated during the validation study, the wetted hull surface changed strongly and the waterline integral was not able to account for this effect in every extend. To overcome this drawback, the correct hull shape should be considered as it is illustrated on the right side of Figure 130.

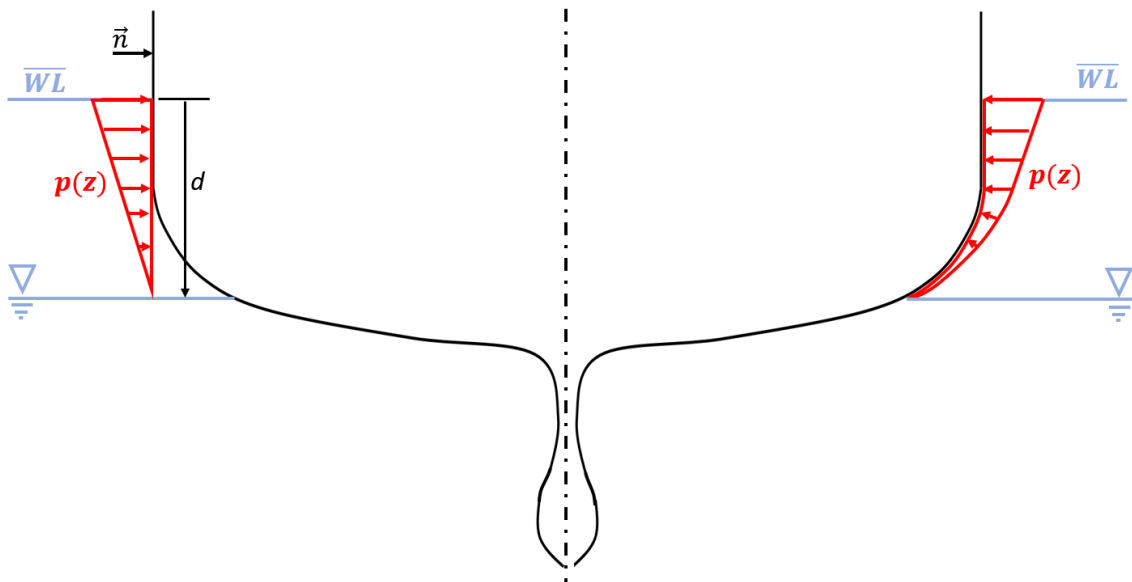


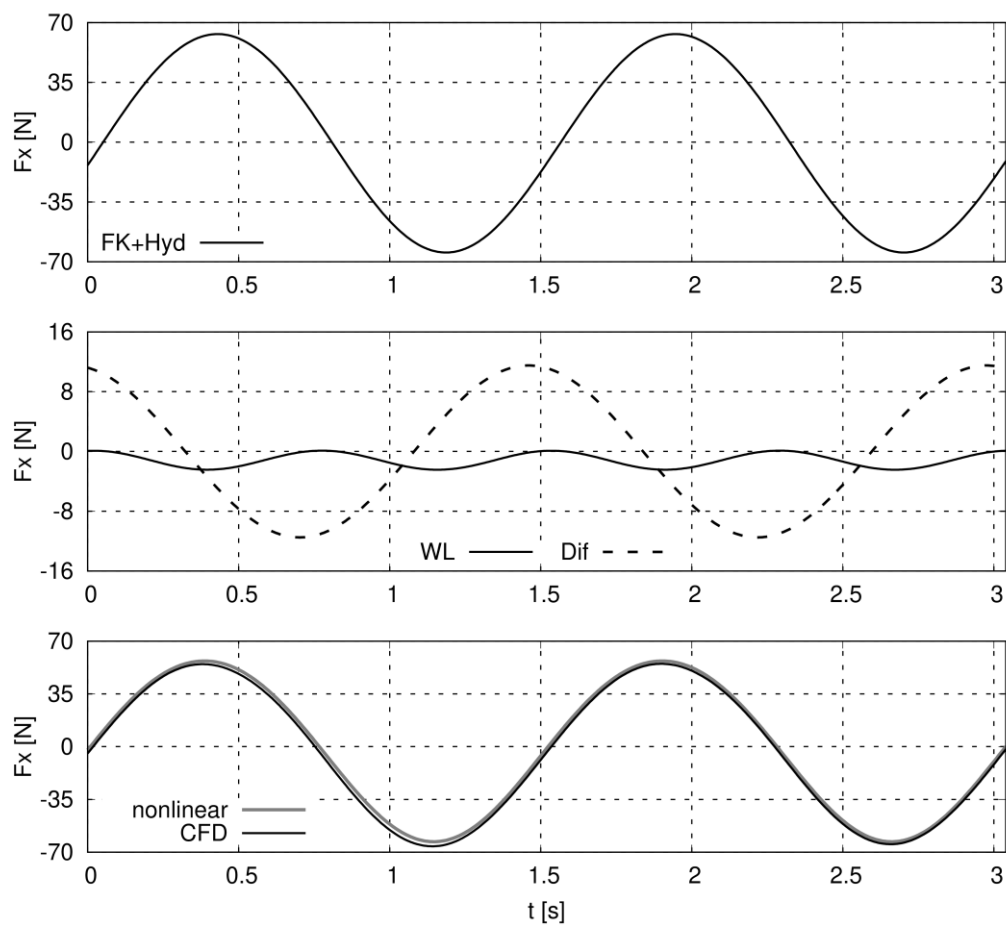
Figure 130: Illustration of the radiation and diffraction induced changing wetted surface according to the waterline integral (left). Improved consideration of the changing wetted hull surface with the correct hull normal vectors (right).

7 Appendix

7.1 Weakly-Nonlinear Hydrodynamic Forces at the Fixed VLCC Tanker

Comparisons of the hydrodynamic forces and moments at the fixed VLCC tanker advancing at a forward speed according to $F_n = 0.142$ in a long, medium and short wave according to $\lambda/L_{PP} = 1.62, 1.0$ and 0.54 (head waves).

7.1.1 Results for $\lambda/L_{PP} = 1.62$



7.1 Weakly-Nonlinear Hydrodynamic Forces at the Fixed VLCC Tanker

Figure 131: Time histories of longitudinal forces for the fixed KVLCC2 tanker ($F_n = 0.142$) in head waves of $\lambda/L = 1.62$ and a wave amplitude of 3m. "FK+Hyd" denotes combined nonlinear Froude-Krylov and hydrostatic forces, "Rad" denotes radiation forces, "Dif" denotes diffraction forces and "nonlinear" denotes the total hydrodynamic force compared to CFD results.

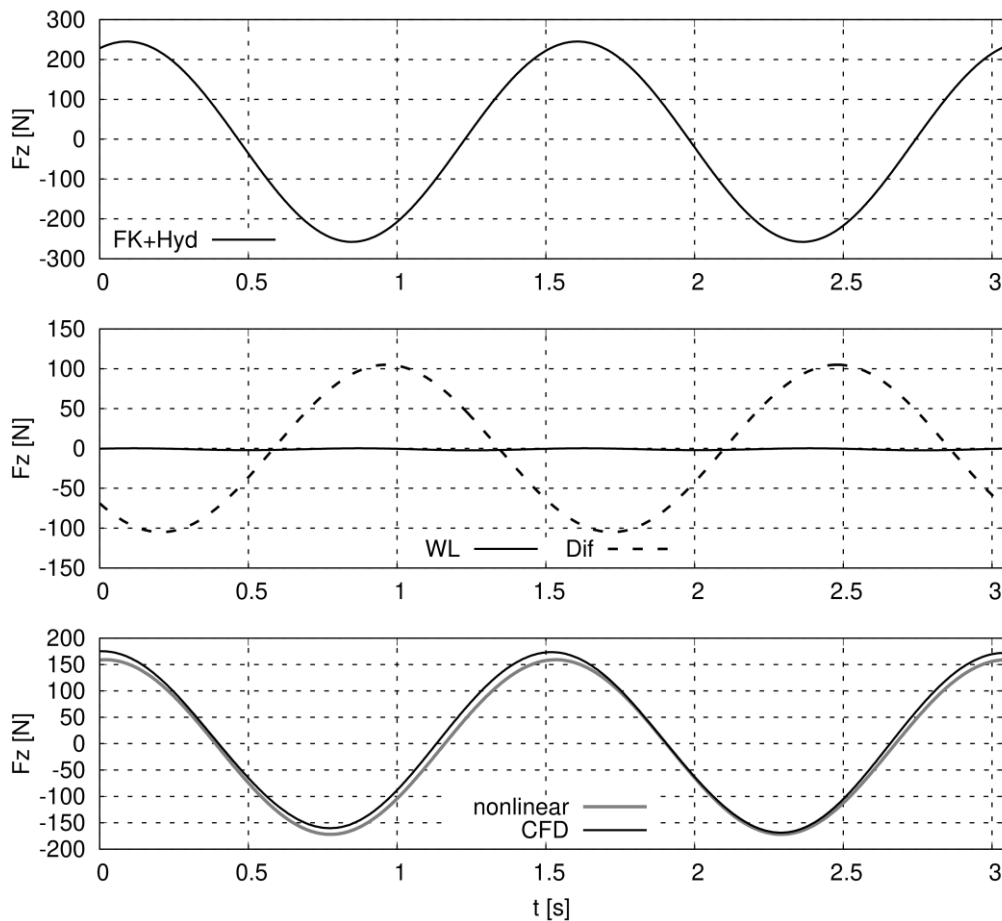


Figure 132: Time histories of vertical forces for the fixed KVLCC2 tanker ($F_n = 0.142$) in head waves of $\lambda/L = 1.62$ and a wave amplitude of 3m. "FK+Hyd" denotes combined nonlinear Froude-Krylov and hydrostatic forces, "Rad" denotes radiation forces, "Dif" denotes diffraction forces and "nonlinear" denotes the total hydrodynamic force compared to CFD results.

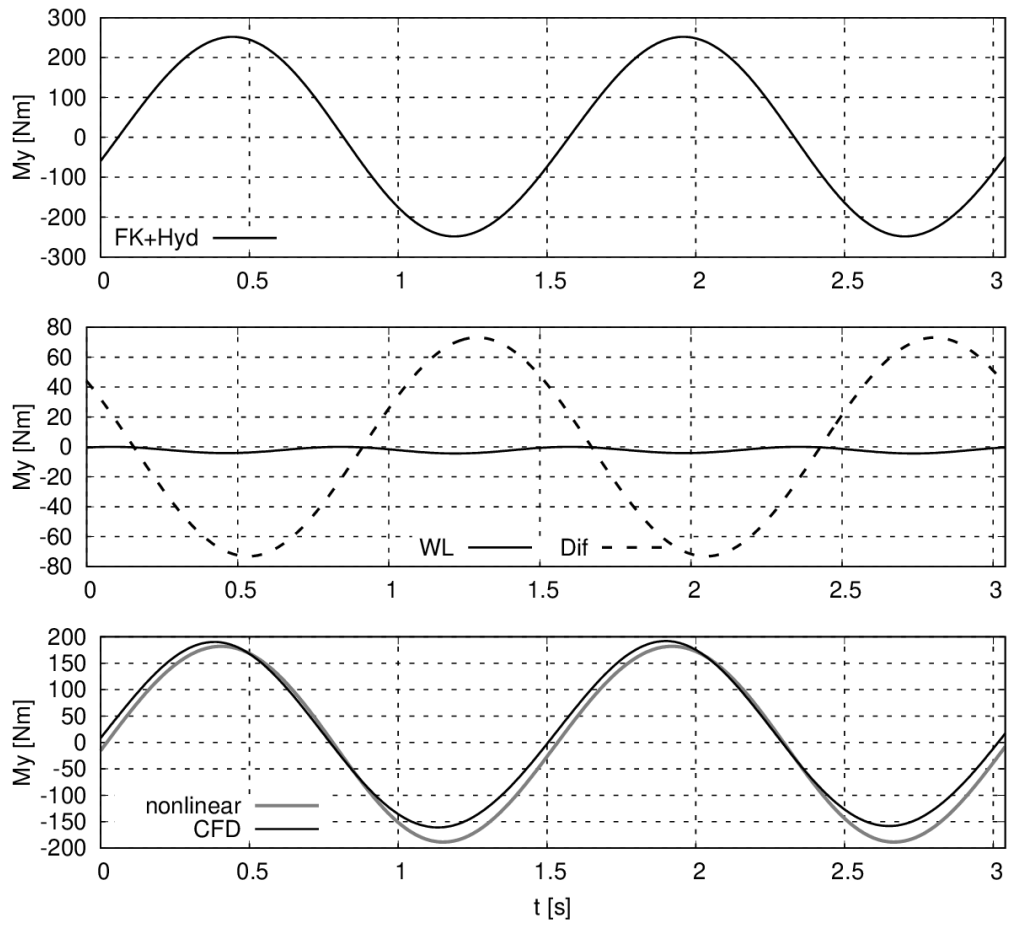


Figure 133: Time histories of pitch moment for the fixed KVLCC2 tanker ($F_n = 0.142$) in head waves of $\lambda/L = 1.62$ and a wave amplitude of 3m. "FK+Hyd" denotes combined nonlinear Froude-Krylov and hydrostatic forces, "Rad" denotes radiation forces, "Dif" denotes diffraction forces and "nonlinear" denotes the total hydrodynamic force compared to CFD results.

7.1.2 Results for $\lambda/L_{PP} = 1.0$

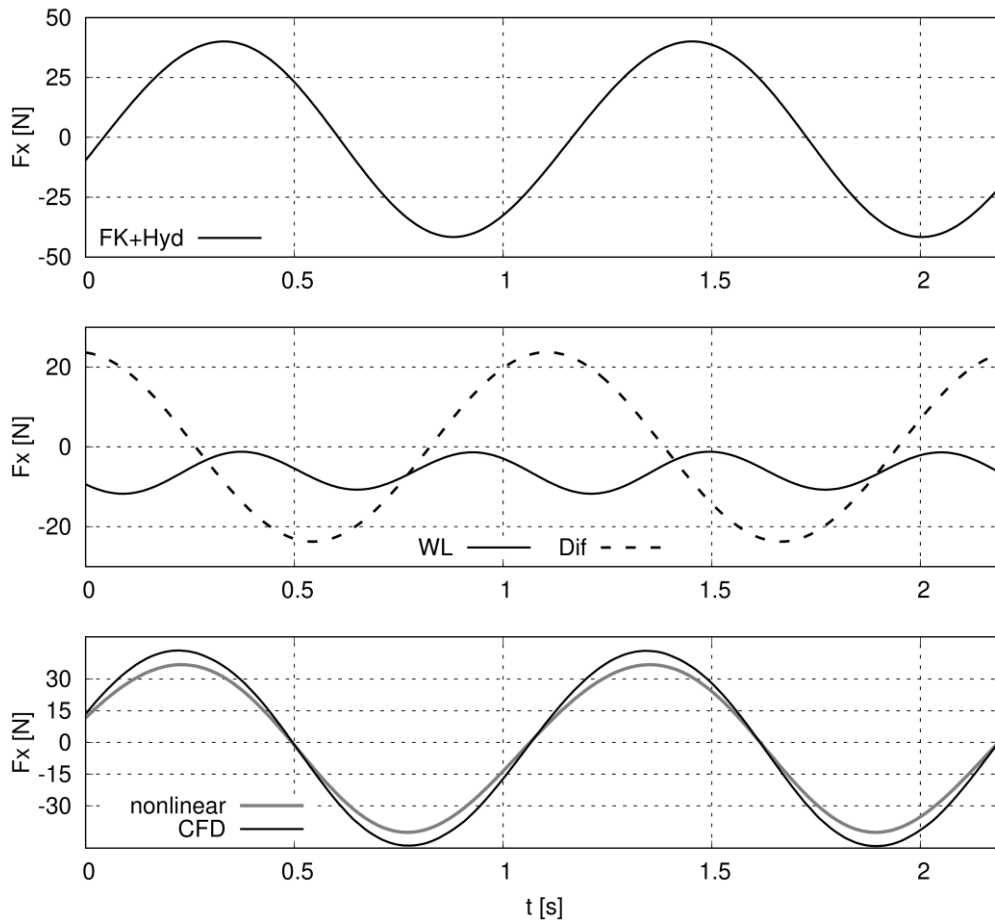


Figure 134: Time histories of longitudinal forces for the fixed KVLCC2 tanker ($F_n = 0.142$) in head waves of $\lambda/L = 1.0$ and a wave amplitude of 3m. "FK+Hyd" denotes combined nonlinear Froude-Krylov and hydrostatic forces, "Rad" denotes radiation forces, "Dif" denotes diffraction forces and "nonlinear" denotes the total hydrodynamic force compared to CFD results.

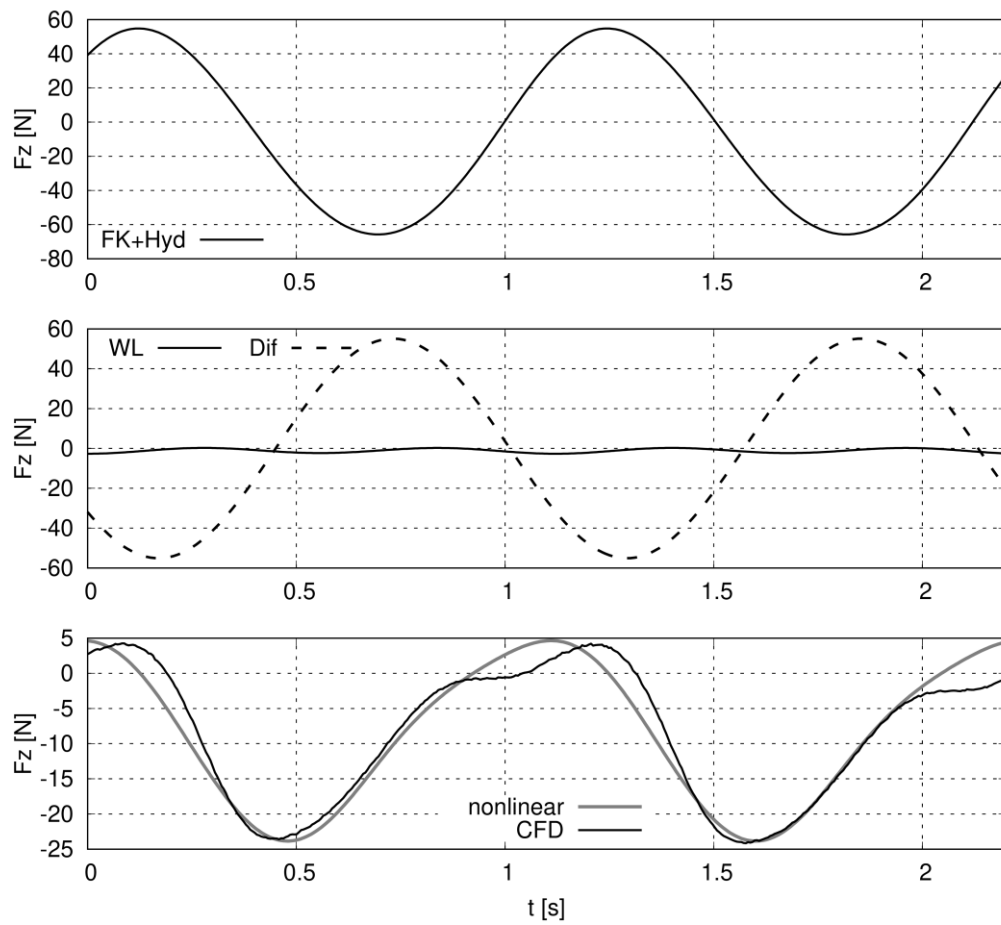


Figure 135: Time histories of vertical forces for the fixed KVLCC2 tanker ($F_n = 0.142$) in head waves of $\lambda/L = 1.0$ and a wave amplitude of 3m. "FK+Hyd" denotes combined nonlinear Froude-Krylov and hydrostatic forces, "Rad" denotes radiation forces, "Dif" denotes diffraction forces and "nonlinear" denotes the total hydrodynamic force compared to CFD results.

7.1 Weakly-Nonlinear Hydrodynamic Forces at the Fixed VLCC Tanker

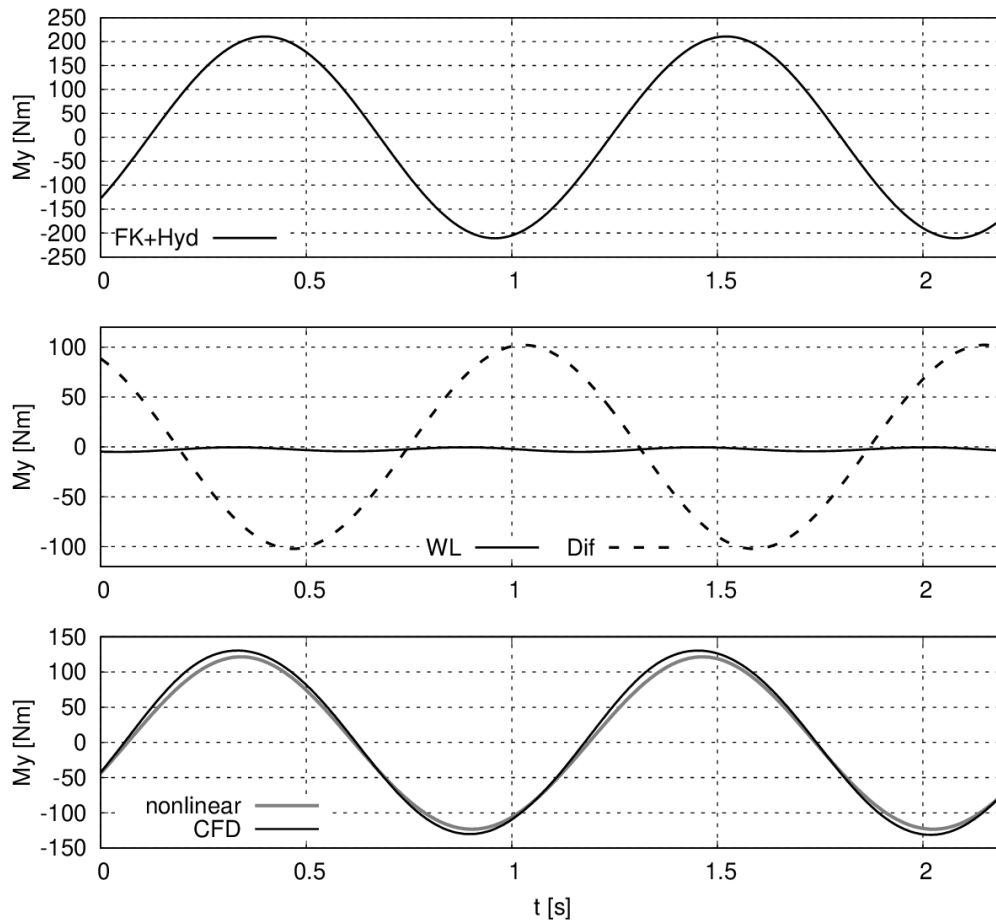


Figure 136: Time histories of pitch moment for the fixed KVLCC2 tanker ($F_n = 0.142$) in head waves of $\lambda/L = 1.0$ and a wave amplitude of 3m. "FK+Hyd" denotes combined nonlinear Froude-Krylov and hydrostatic forces, "Rad" denotes radiation forces, "Dif" denotes diffraction forces and "nonlinear" denotes the total hydrodynamic force compared to CFD results.

7.1.3 Results for $\lambda/L_{PP} = 0.54$

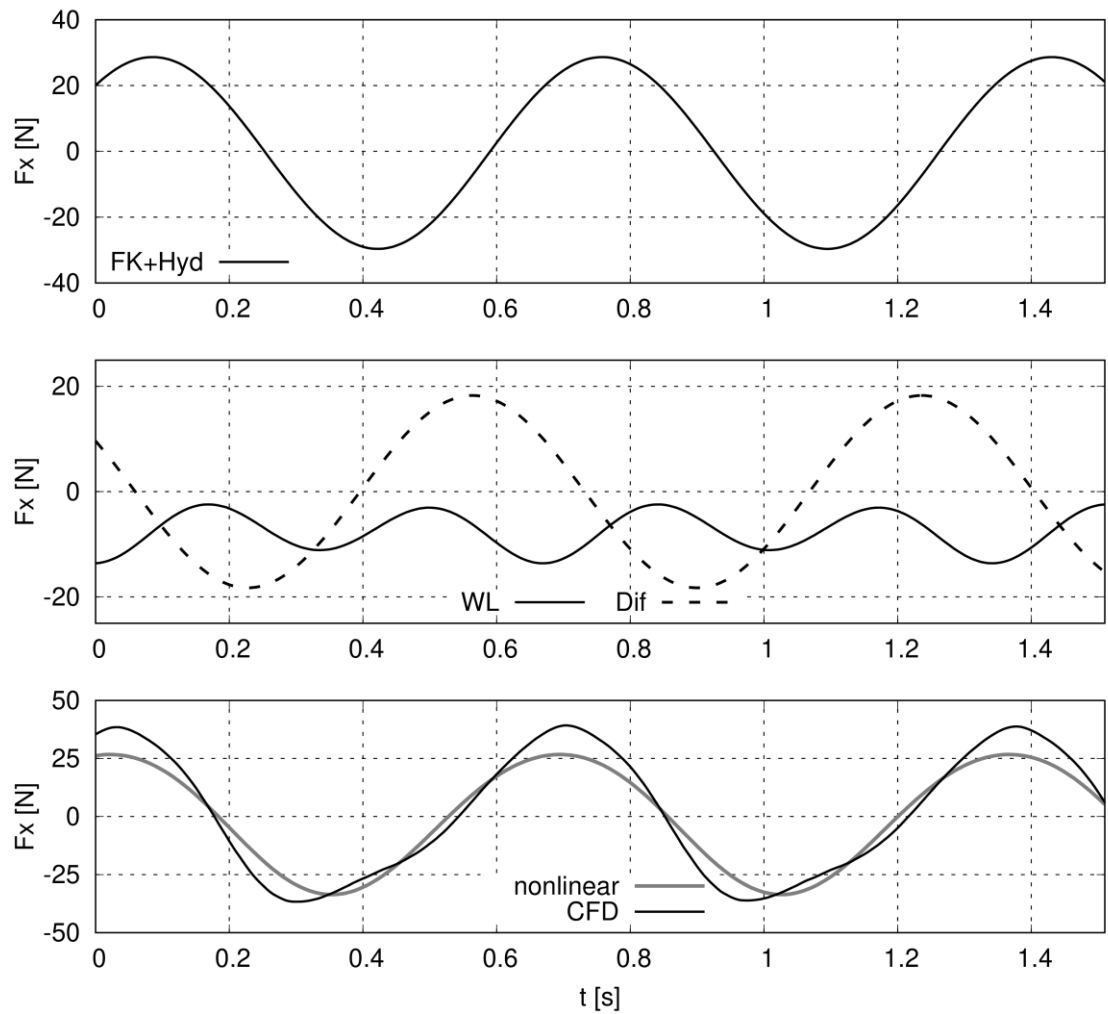


Figure 137: Time histories of longitudinal forces for the fixed KVLCC2 tanker ($F_n = 0.142$) in head waves of $\lambda/L = 0.54$ and a wave amplitude of 3m. "FK+Hyd" denotes combined nonlinear Froude-Krylov and hydrostatic forces, "Rad" denotes radiation forces, "Dif" denotes diffraction forces and "nonlinear" denotes the total hydrodynamic force compared to CFD results.

7.1 Weakly-Nonlinear Hydrodynamic Forces at the Fixed VLCC Tanker

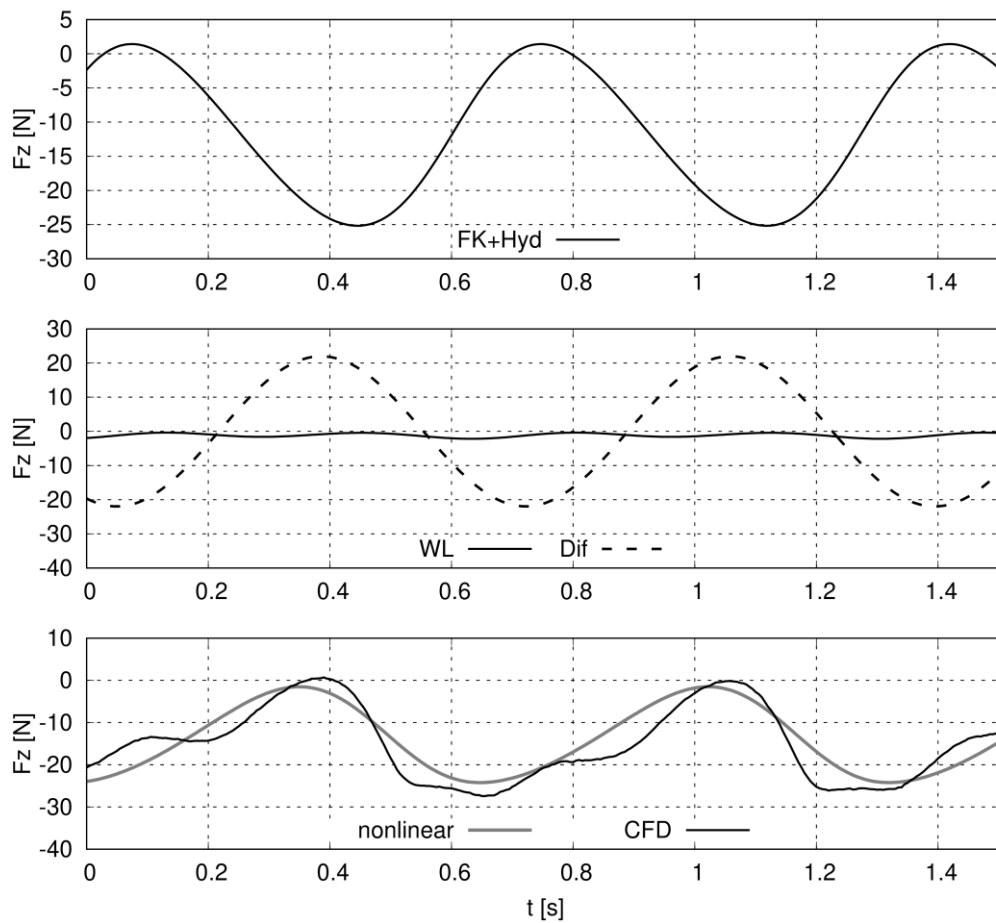


Figure 138: Time histories of vertical forces for the fixed KVLCC2 tanker ($F_n = 0.142$) in head waves of $\lambda/L = 0.54$ and a wave amplitude of 3m. “FK+Hyd” denotes combined nonlinear Froude-Krylov and hydrostatic forces, “Rad” denotes radiation forces, “Dif” denotes diffraction forces and “nonlinear” denotes the total hydrodynamic force compared to CFD results.

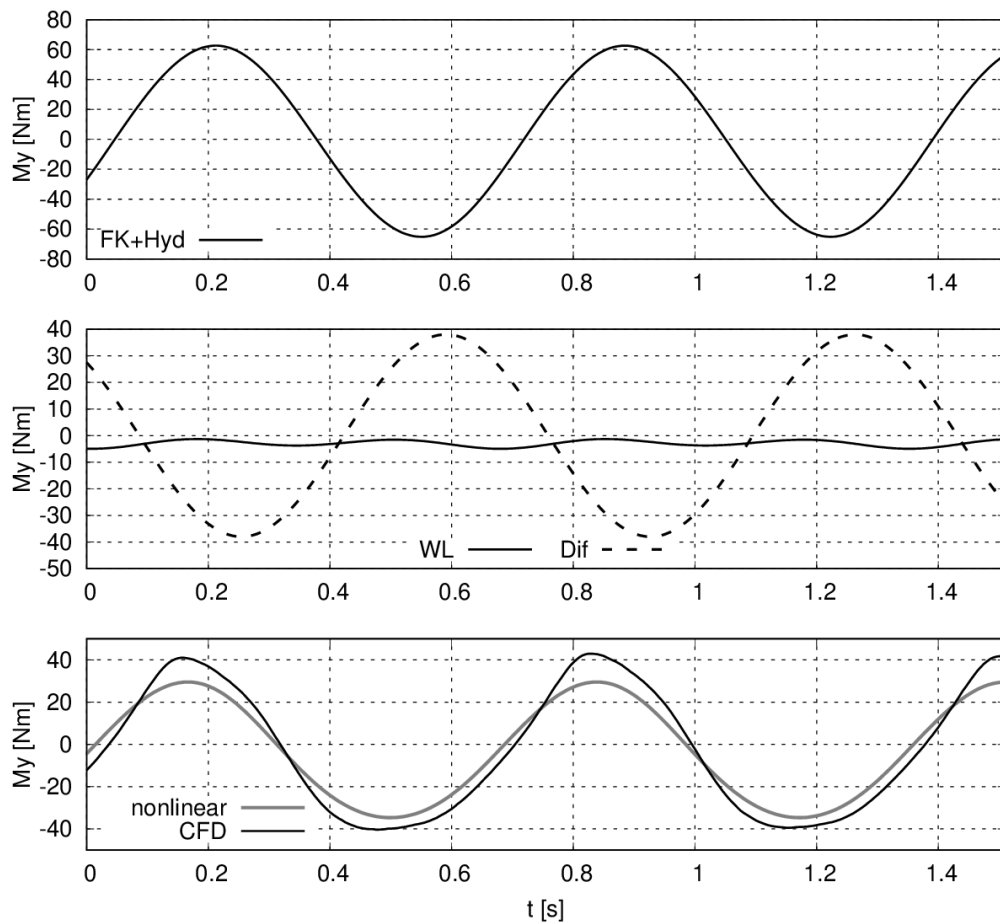


Figure 139: Time histories of pitch moment for the fixed VLCC2 tanker ($F_n = 0.142$) in head waves of $\lambda/L = 0.54$ and a wave amplitude of 3m. "FK+Hyd" denotes combined nonlinear Froude-Krylov and hydrostatic forces, "Rad" denotes radiation forces, "Dif" denotes diffraction forces and "nonlinear" denotes the total hydrodynamic force compared to CFD results.

7.2 Weakly-Nonlinear Hydrodynamic Forces at the Moving VLCC Tanker

Comparisons of the hydrodynamic forces and moments at the moving VLCC tanker advancing with a forward speed according to $F_n = 0.142$ in a long, medium and short wave according to $\lambda/L_{pp} = 1.84, 1.0$ and 0.54 (head waves).

7.2.1 Results for $\lambda/L_{PP} = 1.84$

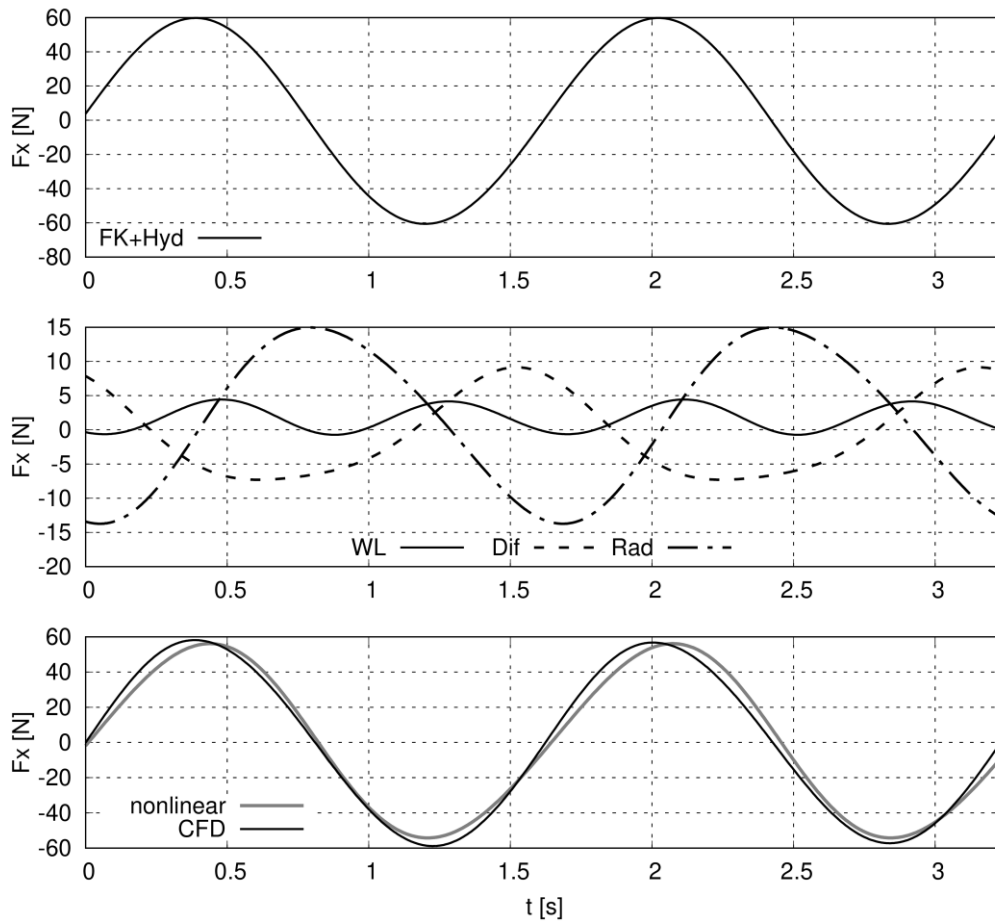


Figure 140: Time histories of longitudinal forces for the moving KVLCC2 tanker ($F_n = 0.142$) in head waves of $\lambda/L = 1.84$ and a wave amplitude of 3m. "FK+Hyd" denotes combined nonlinear Froude-Krylov and hydrostatic forces, "Rad" denotes radiation forces, "Dif" denotes diffraction forces and "nonlinear" denotes the total hydrodynamic force compared to CFD results.

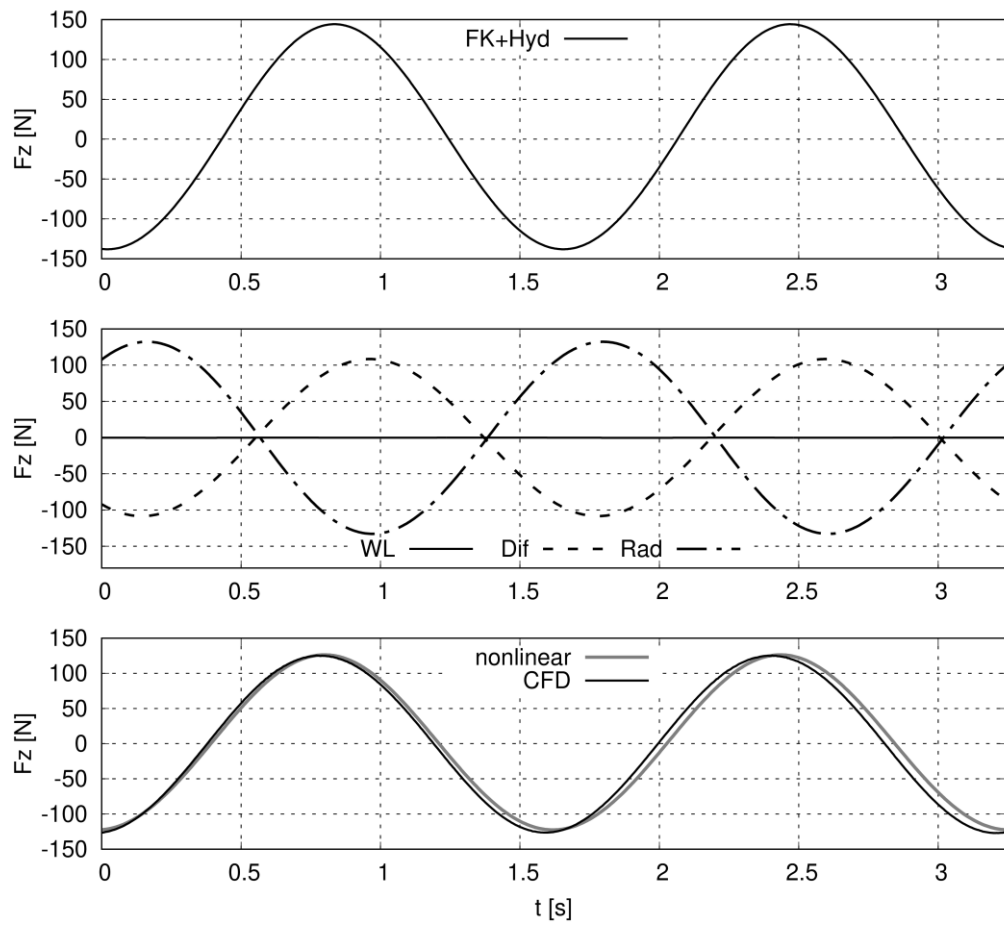


Figure 141: Time histories of vertical forces for the moving KVLCC2 tanker ($F_n = 0.142$) inhead waves of $\lambda/L = 1.84$ and a wave amplitude of 3m. "FK+Hyd" denotes combined nonlinear Froude-Krylov and hydrostatic forces, "Rad" denotes radiation forces, "Dif" denotes diffraction forces and "nonlinear" denotes the total hydrodynamic force compared to CFD results.

7.2 Weakly-Nonlinear Hydrodynamic Forces at the Moving VLCC Tanker

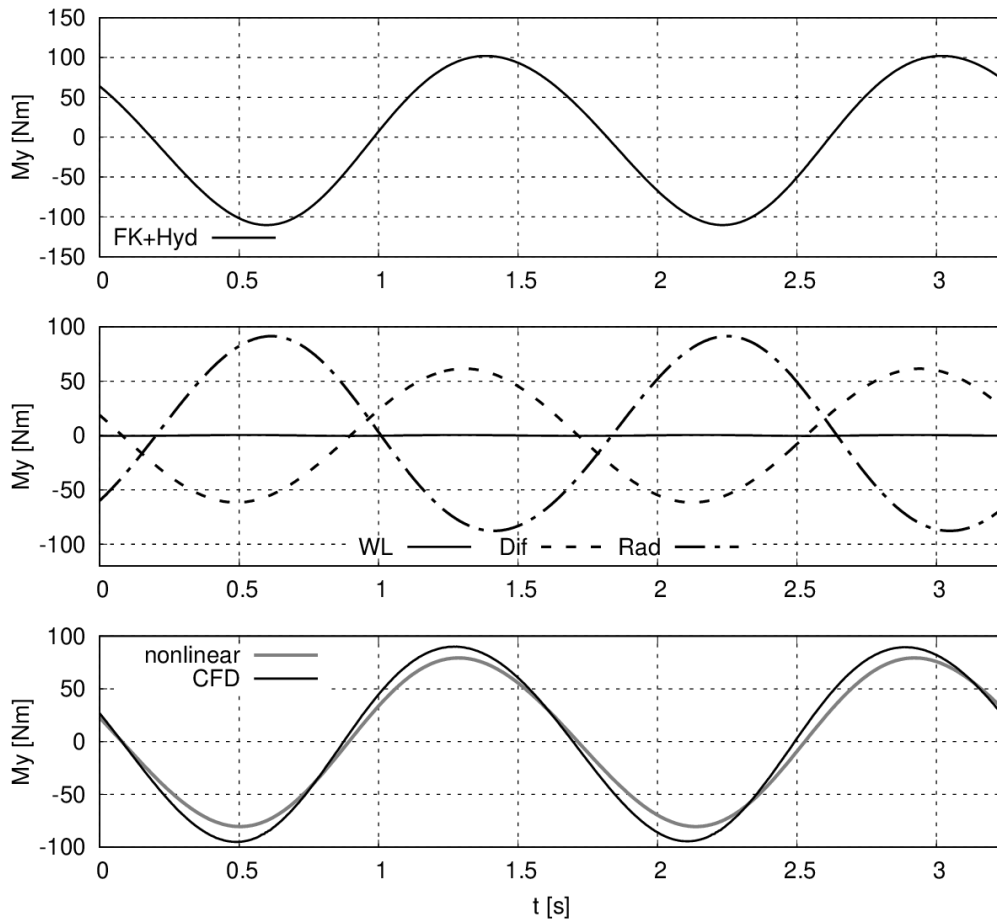


Figure 142: Time histories of pitch moment for the moving KVLCC2 tanker ($F_n = 0.142$) in head waves of $\lambda/L = 1.84$ and a wave amplitude of 3m. "FK+Hyd" denotes combined nonlinear Froude-Krylov and hydrostatic forces, "Rad" denotes radiation forces, "Dif" denotes diffraction forces and "nonlinear" denotes the total hydrodynamic force compared to CFD results.

7.2.2 Results for $\lambda/L_{PP} = 1.0$

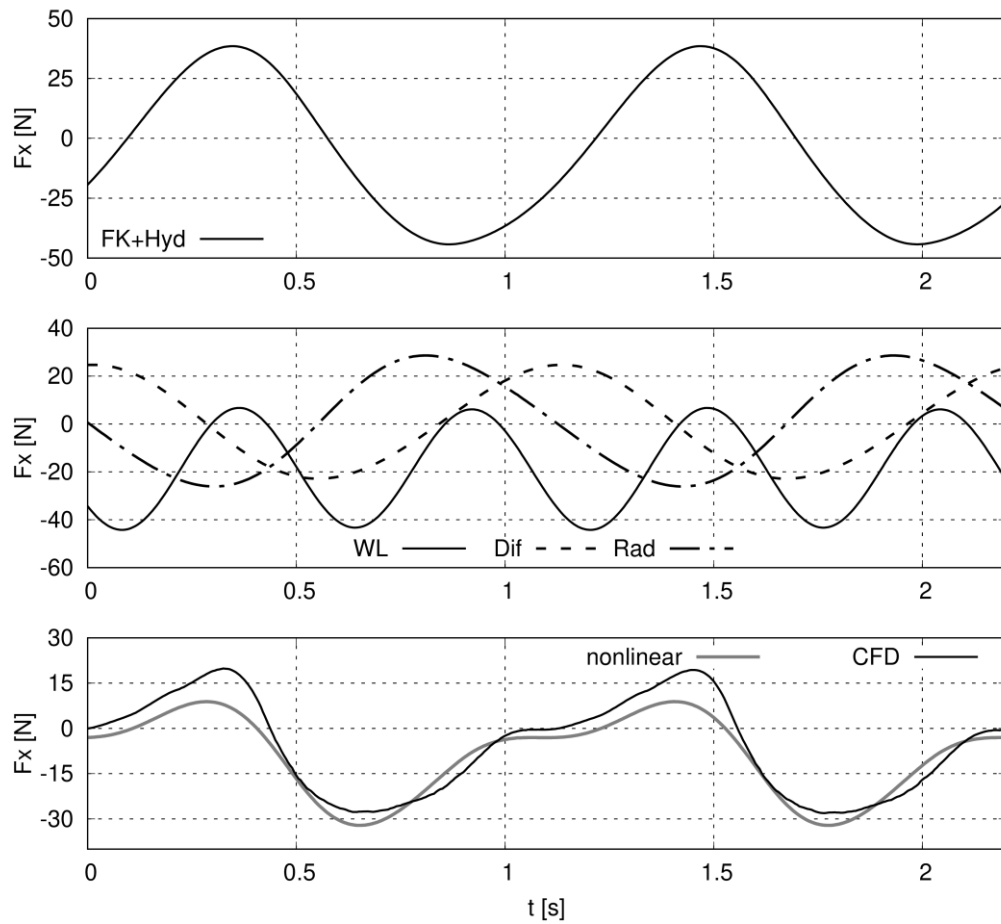


Figure 143: Time histories of longitudinal force for the moving KVLCC2 tanker ($F_n = 0.142$) in head waves of $\lambda/L = 1.0$ and a wave amplitude of 3m. “FK+Hyd” denotes combined nonlinear Froude-Krylov and hydrostatic forces, “Rad” denotes radiation forces, “Dif” denotes diffraction forces and “nonlinear” denotes the total hydrodynamic force compared to CFD results.

7.2 Weakly-Nonlinear Hydrodynamic Forces at the Moving VLCC Tanker

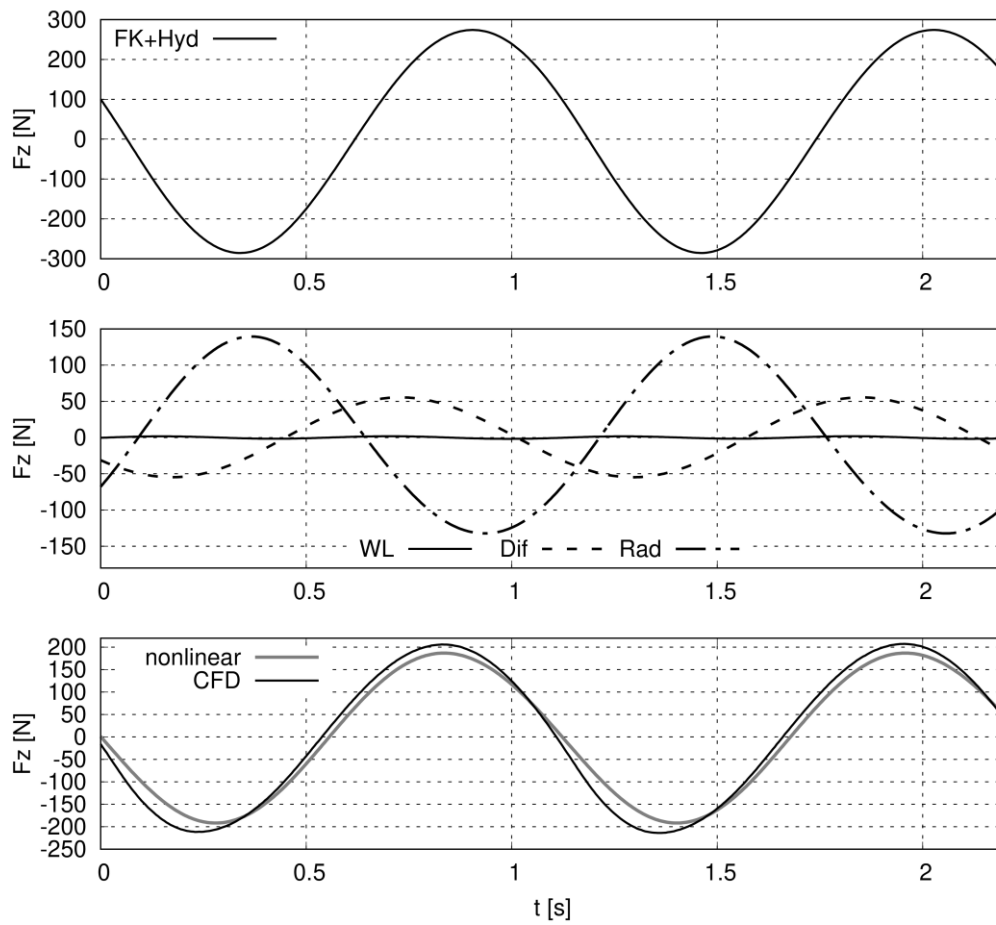


Figure 144: Time histories of vertical forces for the moving KVLCC2 tanker ($F_n = 0.142$) in head waves of $\lambda/L = 1.0$ and a wave amplitude of 3m. "FK+Hyd" denotes combined nonlinear Froude-Krylov and hydrostatic forces, "Rad" denotes radiation forces, "Dif" denotes diffraction forces and "nonlinear" denotes the total hydrodynamic force compared to CFD results.

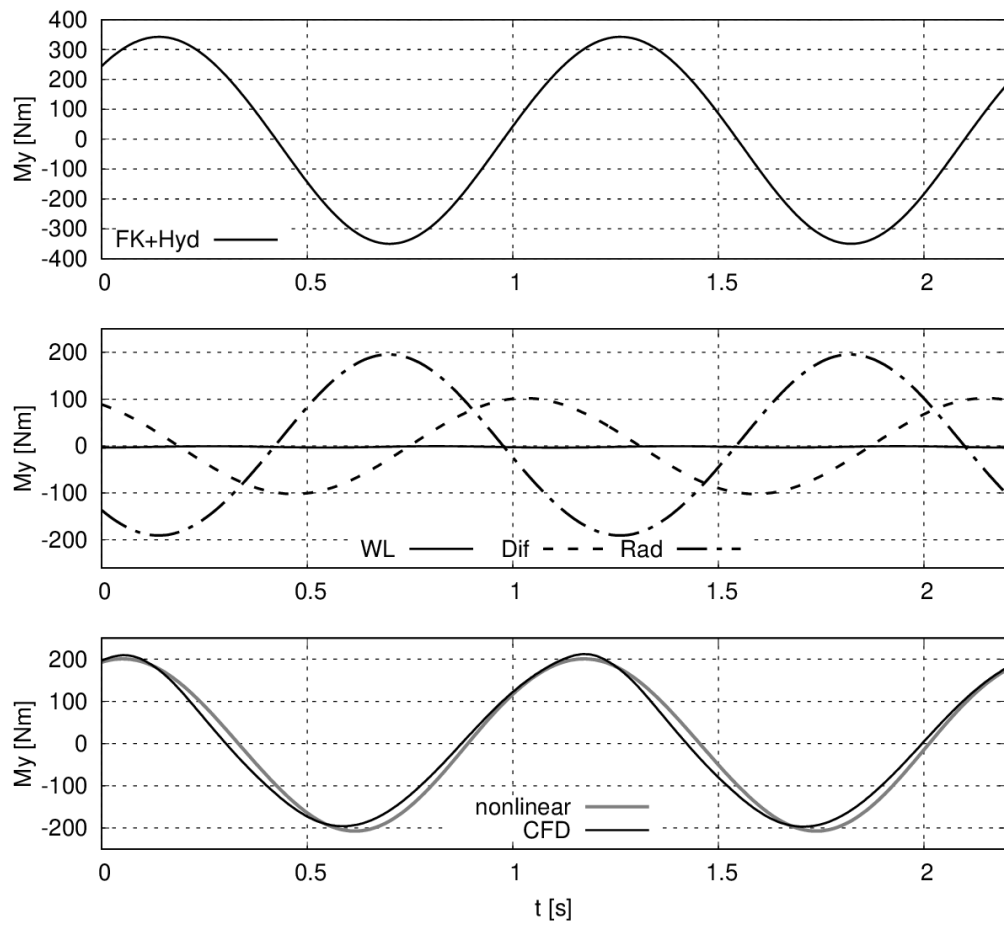


Figure 145: Time histories of pitch moment for the moving KVLCC2 tanker ($F_n = 0.142$) in head waves of $\lambda/L = 1.0$ and a wave amplitude of 3m. “FK+Hyd” denotes combined nonlinear Froude-Krylov and hydrostatic forces, “Rad” denotes radiation forces, “Dif” denotes diffraction forces and “nonlinear” denotes the total hydrodynamic force compared to CFD results.

7.2.3 Results for $\lambda/L_{PP} = 0.54$

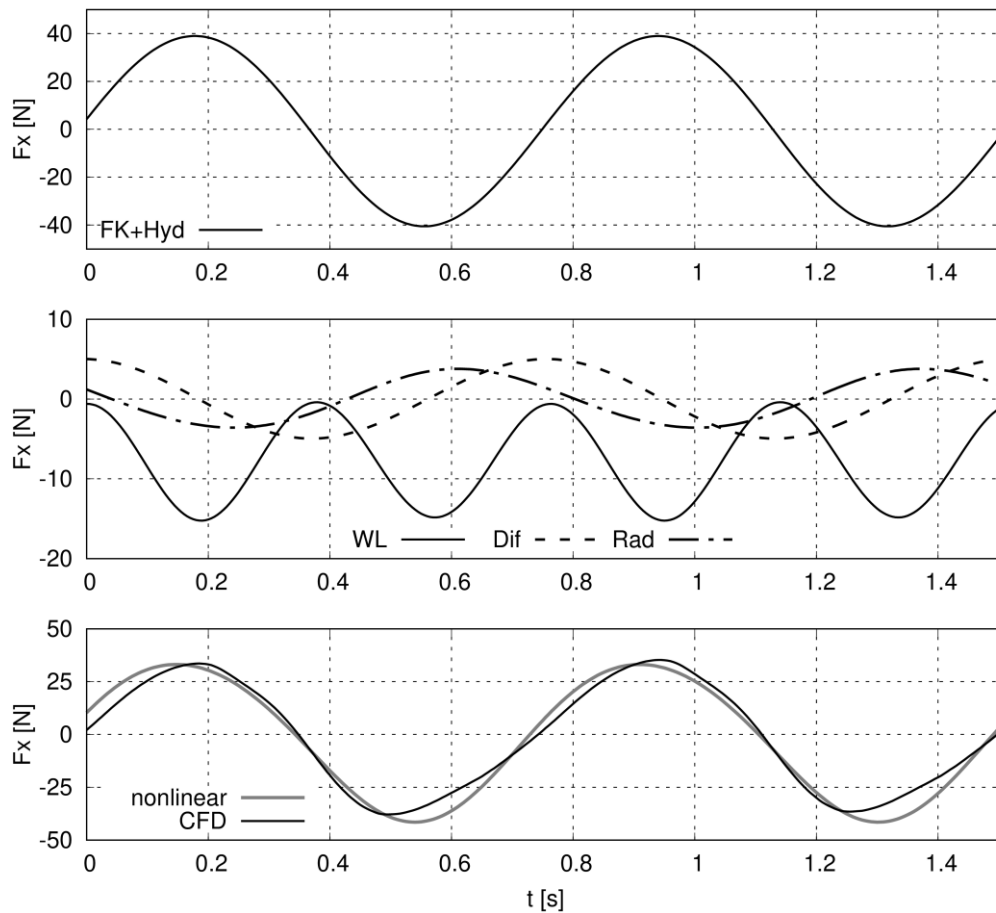


Figure 146: Time histories of longitudinal force for the moving KVLCC2 tanker ($F_n = 0.142$) in head waves of $\lambda/L = 0.54$ and a wave amplitude of 3m. "FK+Hyd" denotes combined nonlinear Froude-Krylov and hydrostatic forces, "Rad" denotes radiation forces, "Dif" denotes diffraction forces and "nonlinear" denotes the total hydrodynamic force compared to CFD results.

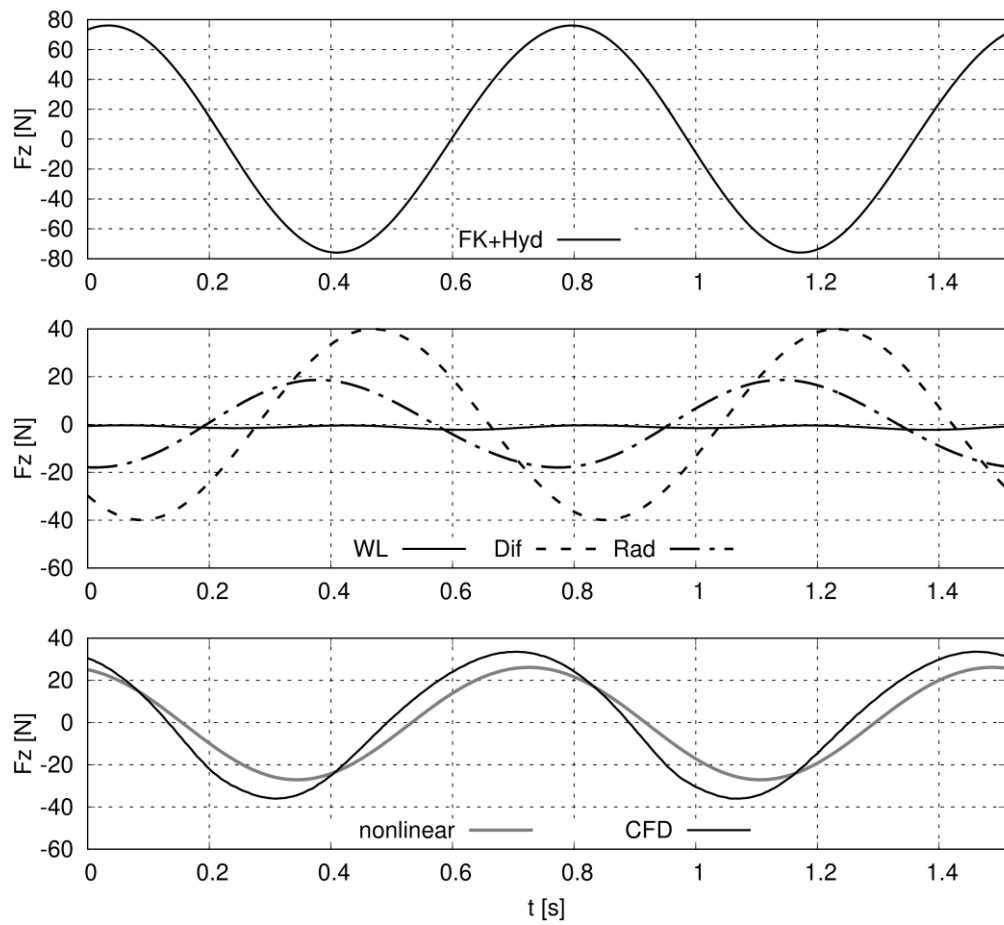


Figure 147: Time histories of vertical forces for the moving KVLCC2 tanker ($F_n = 0.142$) in head waves of $\lambda/L = 0.54$ and a wave amplitude of 3m. "FK+Hyd" denotes combined nonlinear Froude-Krylov and hydrostatic forces, "Rad" denotes radiation forces, "Dif" denotes diffraction forces and "nonlinear" denotes the total hydrodynamic force compared to CFD results.

7.2 Weakly-Nonlinear Hydrodynamic Forces at the Moving VLCC Tanker

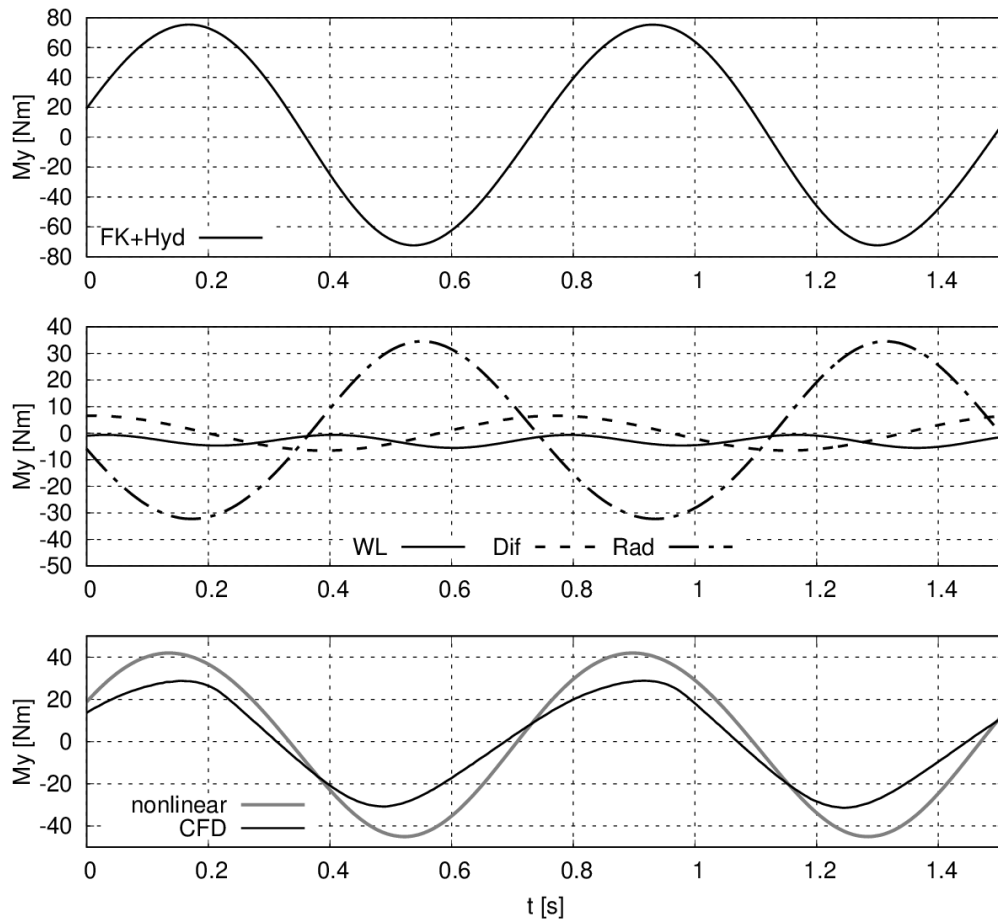


Figure 148: Time histories of pitch moment for the moving KVLCC2 tanker ($F_n = 0.142$) in head waves of $\lambda/L = 0.54$ and a wave amplitude of 3m. “FK+Hyd” denotes combined nonlinear Froude-Krylov and hydrostatic forces, “Rad” denotes radiation forces, “Dif” denotes diffraction forces and “nonlinear” denotes the total hydrodynamic force compared to CFD results.

8 Bibliography

Andersen, I. M. V., and Jensen, J. J. ,(2015), *Extreme Value Prediction of the Wave-induced Vertical Bending Moment in Large Container Ships*. Proceedings of the 7th International Conference on Hydroelasticity in Marine Technology, pp. 389–402, Split, Croatia.

Bathe, K-J ,(1996), *Finite Element Procedures*, Prentice Hall.

Beck R.F., and Reed A.M. ,(2001), *Modern computational methods for ships in a seaway*. Trans SNAME (109), pp. 1–51.

Bertram, V. ,(1990), *A Rankine Source Method for the Forward-Speed Diffraction Problem*. Schriftenreihe Schiffbau, Technische Universität Hamburg-Harburg, Hamburg, Germany.

Bertram, V. ,(2000), *Practical ship hydrodynamics*, Butterworth+Heinemann. Oxford.

Bertram, V., and Thiart, G. ,(1998), *A Rankine panel method for ships in oblique waves*. Euromech (374), pp. 157–165, Poitiers, Oxford.

Bishop, R. E. D., and Price, W. G. ,(1979), *Hydroelasticity of Ships*, Cambridge University Press, Cambridge.

Boese, P. ,(1970), *A Simple Method for the Calculation of Resistance Increase of a Ship in a Seaway*. Ship Technology Research (17(86)), Cambridge.

Bulian G., and Francescutto, A. ,(2013), *Second Generation Intact Stability Criteria: on the validation of codes for direct stability assessment in the framework of an example application*. Polish Maritime Research (4(80)), pp. 52–61. DOI: 10.2478/pomr-2013-0041.

Chang, M-S. ,(1977), *Cumputation of Three-Dimensional Ship-Motions with Forward Speed*. Second International Conference on Numerical Ship Hydrodynamics, pp. 124–135, Berkeley, USA.

Craig, M., Piro, D., Schambach, L., Mesa, J., Kring, D., and Maki, K. ,(2015), *A comparison of fully-coupled hydroelastic simulation methods to predict slam-induced whipping*, In Proc. 7th Int. Conf. on Hydroelasticity in Marine Technology, Split, Croatia.

Cummins, W. ,(1962), *The Impulse Response Function and Ship Motions*. Schiffstechnik (9), pp. 101–109.

Dean, R. G.,and Dalrymple, R. A. ,(1991), *Water Wave Mechanics For Engineers and Scientists*, World Scientific Publishing Co. Pte. Ltd., Singapore.

Dvorkin, E. N.,Celentano, D.,Cuitino, A.,and Giola, G. ,(1989), *A Vlasov Beam Element*. Computers & Structures (33(1)), pp. 187–196.

el Moctar, B.,Kaufmann, J.,Ley, J.,Oberhagemann, J.,Shigunov, J.,and Zorn, T. ,(2010), *Prediction of Ship Resistance and Motions using RANSE*. In Proc. of Gothenburg Workshop 2010 (495–505).

el Moctar, B.,Sprenger, F.,Schellin, T. E.,and Papanikolaou, A. ,(2016), *Numerical and Experimental Investigations of Ship Maneuvers in Waves*. 35th Int. Conf. on Ocean, Offshore and Arctic Engineering, Busan, South Korea.

el Moctar, O.,Ley, J.,Oberhagemann, J.,and Schellin, T. E. ,(2017), *Nonlinear Computational Methods for Hydroelastic Effects of Ships in Extreme Seas*. Ocean Engineering (130), pp. 659–673. DOI: 10.1016/j.oceaneng.2016.11.037.

el Moctar, O.,Oberhagemann, J.,and Schellin, T. E. ,(2011), *Free Surface RANS Method for Hull Girder Springing and Whipping*. Trans. SNAME (119), pp. 48–66.

el Moctar, O.,Schellin, T. E.,and Söding, H. ,(2021), *Numerical Methods for Seakeeping Problems*, Springer International Publishing.

Faltinsen, O. M.,Minsaas, K.,Liapis, N.,and Skjördal, S. O. ,(1980), *Prediction of resistance and propulsion of a ship in a seaway*. In: 13th Symposium on Naval Hydrodynamics, pp. 505–529.

Ferreira González, D.,Göttsche, U.,Netzband, S.,and Abdel-Maksoud, M. ,(2020), *Advances on simulation of wave-body interactions under consideration of the nonlinear free water surface*. Ship Technology Research (69), pp. 27–40. DOI: 10.1080/09377255.2020.1836551.

Ferziger, J. H.,and Peric, M. ,(2010), *Numerische Strömungsmechanik*, Springer Verlag.

- Fonseca, N., and Guedes Soares, C. ,(2004), *Experimental investigation of the nonlinear effects on the vertical motions and loads of a containership in regular waves*. Journal of Ship Research (48(2)), pp. 118–148.
- Fonseca, N., and Soares, C. C. ,(1998), *Time-Domain Analysis of Large-Amplitude Vertical Ship Motions and Wave Loads*. Journal of Ship Research (42(2)), pp. 139–153.
- Gaul, G. E., Kögel, M., and Wagner, M. ,(2003), *Boundary Element Methods for Engineers and Scientists*, Springer Verlag, Heidelberg.
- Gerritsma, J., and Beukelman, W. ,(1972), *Analysis of the resistance increase in waves of a fast cargo ship*. Int. Shipb. Progr. (19), pp. 285–293.
- Graefe, A. von ,(2014), *A Rankine Source Method for Ship-Ship Interaction and Shallow Water Problems*. Doctoral Thesis, University of Duisburg-Essen, Duisburg.
- Grammatikopoulos, A., Banks, J., and Temarel, P. ,(2020), *Prediction of the vibratory properties of ship models with realistic structural configurations produced using additive manufacturing*. Marine Structures (73).
- Guevel, P., and Bougis, J. ,(1982), *Ship Motions with Forward Speed in Infinite Depth*. Int. Shipb. Progr. (29), pp. 103–117.
- Guo, B., Steen, S., and Deng, G. ,(2012), *Seakeeping prediction of KVLCC2 in head waves with RANS*. Applied Ocean Research (35), pp. 56–67.
- Hachmann, D. ,(1991), *Calculation of pressures on a ship's hull in waves*. Journal of Ship Technology Research (38), pp. 111–133.
- Hänninen, S. K. ,(2014), *Second Harmonic Wave Loads as Springing Excitation of a Large Cruise Ship in Short and Steep Head Waves*. PhD Thesis, Aalto University.
- Hirdaris, S. E., Price, W. G., and Temarel, P. ,(2003), *Two- and Three-Dimensional Hydroelastic Modeling of a Bulker in Regular Waves* (16(8)), pp. 627–658.
- Hong, S., Y., and Kim, B., W. ,(2014), *Experimental investigations of higher-order springing and whipping-WILS project*. Int. J. Nav. Archit. Ocean Eng., pp. 1160–1181. DOI: 10.2478/IJNAOE-2013-0237.

Hong, S., Y., Kim, B., W., and Nam, B., W. ,(2012), *Experimental Study on Torsion Springing and Whipping of Large Container Ship*. International Journal of Offshore and Polar Engineering (22), pp. 97–107.

Huang, Y. ,(1998), *Nonlinear Ship Motions by a Rankine Panel Method*. Massachusetts. Ph.D. Dissertation, Cambridge, MA.

Ikeda, Y., Himeno, Y., and Tanaka, N. ,(1978), *Components of Roll Damping of Ship at Forward Speed*. Report of Department of Naval Architecture University of Osaka Prefecture.

ISSC ,(2018), *Proceedings of the 20th International Ship and Offshore Structures Congress (ISSC 2018)*, IOS Press BV, Netherlands, Amsterdam.

ITTC ,(2021), *Final Report and Recommendations to the 29th ITTC*. Seakeeping Committee.

Iwashita, H., and Ito, A. ,(1992), *The Green Function Method for SHip Motions*. Ship Technology Research (39), pp. 3–21.

Jensen, J. J., and Dogliani, M. ,(1996), *Wave-induced ship hull vibrations in stochastic seaways*. Marine Structures (9(3)), pp. 353–387.

Jiao, J., and Yu, H. ,(2019), *Time-domain numerical and segmented model experimental study on ship hydroelastic responses and whipping loads in harsh irregular seaways*. Ocean Engineering (185), pp. 59–81.

Journee, J.M.J ,(2001), *Verification and Validation of Ship Motion Program SEAWAY*. Ship hydromechanics laboratory. Report1213a, Delft University of Technology.

Kahl, A., and Menzel, W. ,(2008), *Full-Scale Measurements on a PanMax Containership*. Ship Repair Technology Symposium Proceedings, pp. 59–66, Newcastle upon Tyne.

Kashiwagi, M. ,(1995), *Prediction of Surge and Its Effect on Added Resistance by Means of the Enhanced Unified Theory*. Transactions of West-Japan Society of Naval Architects (89), pp. 77–89.

Kashiwagi, M. ,(2009), *Impact of hull design on added resistance in waves application of the enhanced unified theory*. Proceedings of the 10th International Marine Design Conference, pp. 521–535, Trondheim, Norway.

Kashiwagi, M. ,(2011), *Hydrodynamic Study on Added Resistance Using Unsteady Wave Analysis*. 34th Weinblum Memorial Lecture.

Kim, K.-H.,Joncquez, S.,Kim, Y.-H.,and Bingham, H. ,(2010), *Numerical analysis on added resistance of ships in time-domain*. In: Proceedings 25th International Workshop on, Harbin, China.

Kim, M.,Hizir, O.,Turan, O.,Day, S.,and Incecik, A. ,(2016), *A study on ship speed loss due to added resistance in a seaway*. Proceedings of the 26th International Ocean and Polar Engineering Conference, pp. 527–534, Rhodes, Greece.

Kim, M.,Hizir, O.,Turan, O.,and Incecik, A. ,(2017), *Numerical studies on added resistance and motions of KVLCC2 in head seas for various ship speeds*. Ocean Engineering (140), pp. 466–476.

Kim, Y.,Kim, K.-H.,Kim, J.-H.,Kim, T.,and Seo, M.-G. ,(2011), *Time domain analysis of nonlinear motion responses and structural loads on ships and offshore structures: development of WISH programs*. Int. Journal Naval Architecture Ocean Eng. (3), pp. 37–52.

Kim, Y.,Kim, K.-H.,and Kim, Y. ,(2009), *Springing analysis of a seagoing vessel using fully coupled BEM–FEM in the time domain*. Ocean Engineering (36), pp. 785–796.

Kim, Y. C.,Kim, K. S.,Kim, J.,Kim, Y. S.,Van, S. H.,and Jang, Y. H. ,(2015), *Calculation of added resistance in waves for KVLCC2 and its modified hull form using RANS-based method*. Proceedings of the 25th International Offshore and Polar Engineering (924–930), Hawaii, USA.

King, B. ,(1987), *Time-Domain Analysis of Wave Exciting Forces on Ships and Bodies*. University of Michigan. Doctoral Thesis.

Know, Y. J. ,(2008), *Speed loss due to added resistance in wind and waves*. Nav. Archit, pp. 14–16.

Lakshmyarayanan, P. A.,and Temarel, P. ,(2019), *Application of CFD and FEA coupling to predict dynamic behaviour of a flexible barge in regular head waves*. Marine Structures (65), pp. 308–325.

Lakshmyarayanan, P. A.,Temarel, P.,and Chen, Z. ,(2015), *Coupled fluid-structure interaction to model three-dimensional dynamic behaviour of ship in waves*. Proceedings

of 7th International Conference on Hydroelasticity in Marine Technology, pp. 623–636, Split, Croatia.

Le Méhauté, B. ,(1976), *An Introduction to Hydrodynamics & Water Waves*, Springer Science+Business Media, New York.

Lee, Y.,White, N.,Wang, Z.,Tong, J.,Xiao, Y.,and Li, Q. ,(2014), *Springing Loads and Fatigue Assessment on Large Container Ships*, Proc. 24th Int. Ocean and Polar Eng. Conf. (ISOPE), Busan, South Korea.

Ley, J.,and el Moctar, O. ,(2014), *An Enhanced 1-Way Coupling Method to Predict Elastic Global Hull Girder Loads*. Paper No. OMAE2014-24199, Proc. 33rd ASME Int. Conf. on Ocean, Offshore and Arctic Engineering OMAE2014, San Francisco, USA.

Ley, J.,el Moctar, O.,Oberhagemann J.,and Schellin, T. E. ,(2014a), *Assessment of Loads and Structural Integrity of Ships in Extreme Seas*, Proc. 30th Symposium on Naval Hydrodynamics, Hobart, Tasmania, Australia.

Ley, J.,Sigmund, S.,and el Moctar, B. ,(2014b), *Numerical prediction of the added resistance of ships in waves*. International Conference on Ocean, Offshore and Arctic Engineering.

Liu, S.,and Papanikolaou, A. ,(2014), *Time Domain Simulation of Nonlinear Ship Motions Using an Impulse Response Function Method*. Journal of Ship Research (42(2)).

Liu, S.,and Papanikolaou, A. ,(2016), *Fast Approach to the Estimation of the Added Resistance of Ships in Head Waves*. Ocean Engineering (112), pp. 211–225.

Liu, S.,Papanikolaou, A.,and Zaraphonites, G. ,(2011), *Prediction of added resistance of ships in waves*. Ocean Engineering (38), pp. 641–650.

Lui, S.,Sprenger, F.,Papanikolaou, A.,Dafermos, G.,and Zaraphonitis, G. ,(2020), *Experimental and numerical studies on linear and nonlinear seakeeping phenomena of the DTC ship in regular waves* (68), pp. 41–61. DOI: 10.1080/09377255.2020.1857007.

Lyu, W.,and el Moctar, O. ,(2017), *Numerical and experimental investigations of wave-induced second order hydrodynamic loads*. Ocean Engineering (131), pp. 197–212.

- Malenica, S., Senjanovic, I., Tomasevic, S., and Stumpf, E. ,(2007), *Some Aspects of Hydroelastic Issues in the Design of Ultra Large Container Ships*, Proceedings of the 22nd International Workshop on Water Waves and Floating Bodies, Plitvice, Croatia.
- Malenica, Š., and Derbanne, Q. ,(2012), *HYDRO-ELASTIC ISSUES IN THE DESIGN OF ULTRA LARGE CONTAINER SHIPS – TULCS PROJECT*. Hydroelasticity in Marine Technology, pp. 233–246, Tokyo, Japan.
- Mao, W., Li, Z., Ogeman, V., and Ringsberg, J. W. ,(2015), *A regression and beam theory based approach for fatigue assessment of containership structures including bending and torsion contributions*. Marine Structures (41), pp. 244–266.
- Maron, A., and Kapsenbeerg, G. ,(2014), *Design of a Ship Model for Hydroelastic Experiments in Waves*. J. Nav. Arch. and Ocean Eng. (6). Online verfügbar unter <http://dx.doi.org/10.2478/IJNAOE-2013-235>.
- Maruo, H. ,(1960), *The drift force on a body floating in waves*. Journal of Ship Research.
- Maruo, H. ,(1963), *Resistance in waves*. Soc. Nav. Archit. Jpn. 8 60th anniversary Series.
- Matusiak, J. ,(2007), *On certain types of ship responses disclosed by the two-stage approach to ship dynamics*. Arch Civil Mech Eng. (7), pp. 151–166.
- Matusiak, J. ,(2011), *On the non-linearities of ship's restoring and the Froude-Krylov wave load part*. Int J Naval Archit Ocean Eng (3), pp. 111–115.
- Mei, C.C., Stiassnie, M., and Yue, D.K.-P. ,(2005), *Theory and Applications of Ocean Surface Waves*. Part 1: Linear Aspects, World Scientific Publishing Co. Pte. Ltd., London.
- Nakos, D., and Sclavounos, P. ,(1991), *Ship Motions by a Three-Dimensional Rankine Panel Method*. Eighteenth Symposium in Naval Hydrodynamics, pp. 21–39.
- Noblesse, F., and Yang C. ,(2015), *A Simple Green Function for Diffraction-Radiation of Time-Harmonic Waves with Forward Speed*. Ship Technology Research (51), pp. 35–52. DOI: 10.1179/str.2004.51.1.005.
- Oberhagemann, J. ,(2016), *On Prediction of Wave-Induced Loads and Vibration of Ship Structures with Finite Volume Fluid Dynamic Methods*. Doctoral Thesis, University of Duisburg-Essen, Duisburg.

-
- Ogilvie, T. ,(1964), *Recent progress toward the understanding and prediction of ship motions*. Proc. of the 5th Symposium on Navan Hydrodynamics (112), pp. 3–79, Bergen, Norway.
- Ogilvie, T.,and Tuck, E. ,(1969), *A rational strip theory of ship motions: part i*. University of Michigan. Tech. report.
- O'Kelly, M.E.J. ,(1961), *Normal Modes in Damped Systems*. Thesis, California Institute of Technology, Pasadena, California.
- Orlowitz, E.,and Brandt, A. ,(2014), *Operational modal analysis for dynamic characterization of a Ro-Lo ship*. Journal of Ship Research (58(4)), pp. 1–9.
- Paik K.-J.,Carrica PM.,Lee D.,and Maki K. ,(2009), *Strongly coupled fluid–structure interaction method for structural loads on surface ships*. Ocean Engineering (36), pp. 1346–1357.
- Papanikolaou, A.,Zaraphonitis, G.,Bitner-Gregersen, E.,Shigunov, V.,el Moctar, O.,Guedes Soares, C. et al. ,(2016), *Energy efficient safe SHIP OPERAtion (SHOPERA)*. Transportation Research (14), pp. 820–829. DOI: 10.1016/j.trpro.2016.05.030.
- Papanikolaou, A.,Zaraphonitis, G.,Bitner-Gregersen, E.,Shigunov, V.,el Moctar, O.,Guedes Soares, G. et al. ,(2015), *Energy Efficient Safe Ship Operation*. Proceedings of the SNAME World Maritime Conference, Providence, USA.
- Papanikolaou, A. D.,and Schellin, T. E. ,(1993), *A Three-Dimensional Panel Method for Motions and Loads on Ships with Forward Speed*. Ship Technology Research (39), Bergen, Norway.
- Park, D.-M.,Lee, J.-H.,Jung, Y.-W.,Lee, J.,Kim, Y.,and Gerhardt, F. ,(2019), *Experimental and numerical studies on added resistance of ship in oblique sea conditions*. Ocean Engineering (186).
- Pavazza, R. ,(2005), *Torsion of thin-walled beams of open cross-section with influence of shear*. Int. J. Mech. Sci. (47(7)), pp. 1099–1122.
- Pawlowski, J. ,(1992), *A Nonlinear Theory of Ship Motions in Waves*. Proc. 19th Symp. on Naval Hydrodynamics, Seoul, Korea.

Pedersen, P. T. ,(1985), *Torsional response of containerships*. Journal of Ship Research (29(3)), pp. 194–205.

Piehl, H. ,(2016), *Ship Roll Damping Analysis*. University of Duisburg-Essen. Dissertaion.

Prpić-Oršić, J.,and Faltinsen, O. M. ,(2012), *Estimation of ship speed loss and associated CO2 emissions in a seaway*. Ocean Engineering (44).

Przemieniecki, J. S. ,(2012), *Theory of Matrix Structural Analysis*, Dover Publications, Mineola, New York.

Rajendran, S.,Fonseca, N.,and Guedes Soares, C. ,(2015), *Calculation of vertical bending moment acting on an ultra large containership in large amplitude waves*. Proceeding of the 34th International Conference on Offshore Mechanics and Arctic Engineering. OMAE 2015-42405.

Rajendran, S.,Fonseca, N.,and Soares, C. G. ,(2016), *A numerical investigation of the flexible vertical response of an ultra large containership in high seas compared with experiments*. Ocean Engineering (122), pp. 293–310.

Riesner, M.,Chillcce, G.,and el Moctar, O. ,(2018a), *Rankine source time domain method for nonlinear ship motions in steep oblique waves*. Ships and Offshore Structures. DOI: 10.1080/17445302.2018.1498568.

Riesner, M.,and el Moctar, O. ,(2018), *A time domain boundary element method for wave added resistance of ships taking into account viscous effects*. Ocean Engineering (162), pp. 290–303.

Riesner, M.,and el Moctar, O. ,(2021a), *A numerical method to compute global resonant vibrations of ships at forward speed in oblique waves*. Applied Ocean Research (108). DOI: 10.1016/j.apor.2020.102520.

Riesner, M.,and el Moctar, O. ,(2021b), *Assessment of Wave Induced Higher Order Resonant Vibrations of Ships at Forward Speed*. Journal of Fluids and Structures (103). DOI: 10.1016/j.jfluidstructs.2021.103262.

Riesner, M.,el Moctar, O.,and Schellin, T.E ,(2018b), *Design Related Speed Loss and Fuel Consumption of Ships in Seaways*. 4th International Conference on Maritime Technology and Engineering.

Riesner, M., Graefe, A. von, Shigunov, V., and el Moctar, O. ,(2016), *Prediction of Non-Linear SHip Responses in Waves Considering Forward Speed Effects*. Ship Technology Research (63(3)), pp. 135–145. DOI: 10.1080/09377255.2016.1221607.

Riesner, M., Ley, J., and el Moctar, O. ,(2018c), *An Efficient Approach to Predict Wave-Induced Global Hydroelastic Ship Response*. 8th International Conference on HYDROELASTICITY IN MARINE TECHNOLOGY, Seoul, Korea.

Robert, M., Monroy, C., Reliquet, G., Ducoin, A., Guillerm, P., and Ferrant, P. ,(2015), *Hydroelastic response of a flexible barge investigated with a viscous flow solver*. In Proc. 7th Int. Conf. on Hydroelasticity in Marine Technology, Split, Croatia.

Sadat-Hosseini, H., Carrica, P., Kim, H., Toda, Y., and Stern, F. ,(2010), *URANS Simulation and Valiation of Added Resistance and Motions of the KVLCC2 Crude Carrier with Fixed and Free Surge Conditions*. A Workshop on CFD in Ship Hydrodynamics, Gothenburg.

Sadat-Hosseini, H., Wu, P.-C., Carrica, P. M., Kim, H., Toda, Y., and Stern, F. ,(2013), *CFD Verification ad Validation of Added Resistance and Motions of KVLCC2 with Fixed and Free Surge in Short and Long Head Waves*. Ocean Engineering (59), pp. 240–273.

Salvesen, N. ,(1978), *Added resistance of ships in waves*. J. Hydrodyn (12(1)), pp. 24–34.

Salvesen, N., Tuck, E. O., and Faltinsen, O. ,(1970), *Ship motions and Sea loads*. SNAME Trans. (78), pp. 250–287.

Schanz, M., and Steinbach, O. ,(2007), *Boundary Element Analysis*, Springer Verlag, Heidelberg.

Schellin, T. E., Shigunov, V., Troesch A., Kim D.-H., and Maki, K. ,(2015), *Prediction of loads for ship structural design*. Naval Eng J. (127), pp. 103–134.

Seng S., and Jensen, J. J. ,(2012), *Slamming simulations in a conditional wave*. Proc. 31th Int. Conf. on Ocean, Offshore and Arctic Eng, Rio de Janeiro, Brazil.

Senjanović, I., Malenica, Š., Tomašević, S., and Rudan, S. ,(2007a), *Methodology of Ship Hydroelasticity Investigation*. Brodogradnja : Teorija i Praksa Brodogradnje i Pomorske Tehnike 58 (2), pp. 133–145.

- Senjanović, I., Malenica Š., and Tomasevic, S. ,(2007b), *Investigation of Ship Hydroelasticity*. Faculty of Mechanical Engineering and Naval Architecture, University of Zagreb (35), pp. 523–535.
- Senjanović, I., Vladimir, N., and Timić, M. ,(2011), *Investigation of torsion, warping and distortion of large container ships*. Ocean Systems Engineering (1(1)), pp. 73–93.
- Senjanović, I., Tomašević, S., and Vladimir, N. ,(2009), *An advanced theory of thin-walled girders with application to ship vibrations*. Marine Structures (22), pp. 387–437.
- Sigmund, S. ,(2019), *Performance of Ships in Waves*. Dissertation. DOI: 10.17185/dupublico/70021, DuEPublico. Duisburg.
- Sigmund, S., and el Moctar, O. ,(2017), *Numerical and experimental investigation of propulsion in waves*. Ocean Engineering (144), pp. 35–49.
- Sigmund, S., and el Moctar, O. ,(2018a), *Advanced numerical and experimental investigation of added resistance of different ship types in short and long waves*. Ocean Engineering (147), pp. 51–67.
- Sigmund, S., and el Moctar, O. ,(2018b), *Numerical and experimental investigation of added resistance of different ship types in short and long waves*. Ocean Engineering (147), pp. 51–67. DOI: 10.1016/j.oceaneng.2017.10.010.
- Söding, H. ,(1993), *A Method for Accurate Force Calculation in Potential Flow*. Ship Technology Research (40(4)), pp. 76–186.
- Söding, H. ,(2009a), *Berechnung der stationären oder langsam veränderlichen Schiffsumströmung in GLRankine*. Internal Report.
- Söding, H. ,(2009b), *Computation of Springing Transfer Functions*. Journal of Engineering for the Maritime Environment (223(3)), pp. 291–304.
- Söding, H. ,(2020), *Fast accurate seakeeping predictions*. Ship Technology Research. DOI: 10.1080/09377255.2020.1761618.
- Söding, H., and Bertram V. ,(2009), *A 3-d Rankine Source Seakeeping Method*. Ship Technology Research (56), pp. 50–68.

Söding, H., Graefe, A. von, Shigunov, V., and el Moctar, O. ,(2012), *Rankine Source Method for Seakeeping Predictions*. Proc. 31th Int. Conf. on Ocean, Offshore and Arctic Eng. OMAE2012-83450.

Söding, H., Shigunov, V., Schellin, T.E, and el Moctar, B. ,(2014), *A Rankine Panel Method for Added Resistance of Ships in Waves*. Journal of Offshore Mechanics and Arctic Engineering (136).

Sportelli, M., and Huijsmans, R. ,(2012), *Added resistance in short waves: a ray theory approach*. In: 27th International Workshop on Water Waves and Floating Bodies.

Sprenger, F., and Fathi, D. ,(2015), *Report on Model Tests at Marintek*. Deliverable D3.3, Energy Efficient Safe Ship Operation - SHOPERA.

Sprenger, F., Maron, A., Delefortrie, G., van Zwijnsvoorde, T., Cura-Hochbaum, A., Lengwinat, A., and Papanikolaou, A. ,(2017), *Experimental Studies on Seakeeping and Manoeuvrability in Adverse Conditions*. Journal of Ship Research, SNAME Publ. DOI: 10.5957/JOSR.170002.

Stern, F., Wang, Z., Yang J., Sadat-Hosseini, H., Mousaviraad M., Bhushan S. et al. ,(2015), *Recent progress in CFD for naval architecture and ocean engineering*. J Hydrodyn Ser B. (27), pp. 1–23.

Storhaug, G. ,(2014), *The measured contribution of whipping and springing on the fatigue and extreme loading of container vessels*. Int. J. Nav. Archit. Ocean Eng. (6), pp. 1096–1110, Netherlands, Amsterdam. DOI: 10.2478/IJNAOE-2013-0233.

Storhaug, G., and Kahl, A. ,(2015), *Full scale measurements of torsional vibrations on Post-Panamax container ships*, In Proc. 7th Int. Conf. on Hydroelasticity in Marine Technology, Split, Croatia.

Storhaug, G., and Kahl, A. ,(2016), *Hull monitoring closing the gap between the design and operation*, In Proc. 6th Int. Maritime Conference on Design for Safety, Hamburg, Germany.

Storhaug, G., Laanemets, K., Edin, I., and Ringsberg, J. W. ,(2017), *Estimation of damping from wave induced vibrations in ships*, Proceedings of the 6th International Conference on Marine Structures (MARSTRUCT2017), Lisbon, Portugal. pp. 121-130.

Telste, J., and Noblesse, F. ,(1986), *Numerical Evaluation of the Green Function of Water-Wave Radiation and Diffraction*. Journal of Ship Research (30), pp. 69–84, Schiffstechnik.

Timoshenko, S. P., and Goodier, J. N. ,(1970), *Theory of elasticity*, McGraw-Hill, New York.

Valanto, P., and Hong, Y. P. ,(2015), *Experimental Investigation on Ship Wave Added Resistance in Regular Head, Oblique, Beam and Following Waves*. Proc. of the 25th International Ocean and Polar Engineering Conference, Hawaii, USA.

Vlasov, VZ. ,(1961), *Thin-walled elastic beams*, Israel Program for Scientific Translation Ltd., Jerusalem.

Wheeler, JD. ,(1970), *Method for Calculating Forces Produced by Irregular Waves*. J. Petroleum Technology (22(3)), pp. 359–367.

Woernle, C. ,(2011), *Mehrkörpersysteme*. Eine Einführung in die Kinematik und Dynamik von Systemen starrer Körper, Springer-Verlag, Berlin, Heidelberg.

Wu, G. X., and Eatock-Taylor, R. ,(1987), *A Green's Function Form for SHIP Motions at Forward Speed*. Int. Shipb. Progr. (34), pp. 189–196.

Wu, J.-S., and Ho, C.-S. ,(1987), *Analysis of Wave-Induced Horizontal-and-Torsion-Coupled Vibrations of a Ship Hull*. Journal of Ship Research (31(4)), pp. 235–252.

Wu, M. K., and Moan, T. ,(1996), *Linear and nonlinear hydroelastic analysis of high-speed vessel*. Journal of Ship Research (40(2)), pp. 149–163.

Wu, YS., Maeda, H., and Kinoshita, T. ,(1997), *The second order hydrodynamic actions on a flexible body*, Seisan-Kenkyu.

Zaho, R., and Faltinsen, O. M. ,(1989), *A discussion of the m_j -terms in the wave-current-body interaction problem*. Proc. 4th International Workshop on Water Waves and Floating Bodies.

DuEPublico

Duisburg-Essen Publications online

UNIVERSITÄT
DUISBURG
ESSEN

Offen im Denken

ub | universitäts
bibliothek

Diese Dissertation wird via DuEPublico, dem Dokumenten- und Publikationsserver der Universität Duisburg-Essen, zur Verfügung gestellt und liegt auch als Print-Version vor.

DOI: 10.17185/duepublico/75903

URN: urn:nbn:de:hbz:465-20220602-110712-2

Alle Rechte vorbehalten.